

PROBING COHERENCE PROPERTIES OF STRONGLY INTERACTING BOSE GASES

Dissertation
zur Erlangung des Doktorgrades
an der Fakultät für Mathematik, Informatik und Naturwissenschaften
Fachbereich Physik
der Universität Hamburg

vorgelegt von
Jonas Daniel Siegl

Hamburg, im Oktober
2018

Gutachter der Dissertation	Prof. Dr. Henning Moritz Prof. Dr. Ludwig Mathey
Zusammensetzung der Prüfungskommission	Prof. Dr. Nils Huse Prof. Dr. Ludwig Mathey Prof. Dr. Henning Moritz Prof. Dr. Roman Schnabel Prof. Dr. Klaus Sengstock
Vorsitzender der Prüfungskommission	Prof. Dr. Roman Schnabel
Vorsitzender des Fach-Promotionsausschusses PHYSIK	Prof. Dr. Wolfgang Hansen
Leiter des Fachbereichs PHYSIK	Prof. Dr. Michael Potthoff
Dekan der Fakultät MIN	Prof. Dr. Heinrich Graener

Abstract

This thesis reports on experiments studying the coherence properties of strongly interacting homogeneous gases of bosonic ${}^6\text{Li}$ dimers confined to two dimensions. The main results of these studies are first measurements of the momentum distribution and the density-density correlation function after time of flight.

The momentum distribution is measured via a matter wave focusing technique where the momentum space is mapped to real space by letting the gas expand into a harmonic potential. We observe a fast depopulation of the low-momentum modes for prolonged hold times in an optical dipole trap and extract the temperature from the high-momentum modes. The depopulation occurs with only minor increase in measured temperature, indicating that a non-equilibrium description might be required. Additionally, we present how the phase correlation function can be obtained from the momentum distribution and discuss the influence of finite size effects.

Properties of the phase correlation function are inferred from the measurement of the density-density correlation function after short time of flight. During expansion, the in situ phase fluctuations of the gas transform into density fluctuations and thus produce an observable density pattern. By fitting the extracted density-density correlation function with theoretical predictions, the scaling exponent of the phase correlation function can be obtained if a power law decay is assumed. We measure the scaling exponent for extended hold time in an optical dipole trap and observe a downward trend. However this trend of the scaling exponent is inconsistent with the behavior of the high-momentum modes, which indicate constant or slightly increasing temperature. We discuss the numerical analysis and possible issues in detail and arrive at the conclusion that non-equilibrium effects likely render the employed theoretical framework inadequate.

Zusammenfassung

Diese Arbeit beschreibt experimentelle Untersuchung der Kohärenzeigenschaften von stark wechselwirkenden, homogenen Gasen aus bosonischen ${}^6\text{Li}$ Dimeren, deren Kinematik auf zwei Dimensionen beschränkt ist. Das Hauptresultat der Untersuchung stellt die erste Messung der Impulsverteilung und der Dichte-Dichte Korrelationsfunktion nach kurzer freier Expansion dar.

Die Impulsverteilung wird mithilfe einer Materiewellenfokussierung gemessen, wobei eine Abbildung vom Impuls- in den Ortsraum während der freien Expansion in einem harmonischen Potential stattfindet. Wir beobachten eine schnelle Abnahme der Anzahl der Moden mit niedrigem Impuls, wenn das Gas längere Zeit in einer optischen Dipolfalle gehalten wird und bestimmen die Temperatur aus der Verteilung der höheren Impulse. Wir beobachten eine Abnahme der Moden mit niedrigem Impuls ohne signifikante Steigerung der Temperatur. Dies deutet darauf hin, dass das System sich nicht im thermischen Gleichgewicht befindet. Außerdem wird dargelegt, wie aus der Impulsverteilung die Korrelationsfunktion der Phase bestimmt werden kann und welchen Einfluss die endliche Größe der Probe auf diese hat.

Die Eigenschaften der Korrelationsfunktion der Phase werden aus der Messung der Dichte-Dichte Korrelationsfunktion nach kurzer Expansionszeit abgeleitet. Die in situ Phasenfluktuationen werden während der freien Expansion in Dichtefluktuationen umgewandelt, wodurch ein beobachtbares Dichtemuster entsteht. Der Exponent der Korrelationsfunktion kann unter der Annahme, dass sie einem Potenzgesetz genügt, durch einen Fit mit einer theoretischen Vorhersage an die Dichte-Dichte Korrelationsfunktion bestimmt werden. Wir bestimmen den Exponenten in Abhängigkeit der Haltezeit in einer optischen Dipolfalle und beobachten einen fallenden Trend. Dieses Ergebnis ist jedoch inkompatibel mit dem Verhalten der Verteilung der höheren Impulse, welches auf eine konstante oder leicht steigende Temperatur hindeutet. Wir diskutieren die zu diesem Ergebnis führende numerische Analyse und mögliche Einwände eingehend und kommen zu dem Resultat, dass höchstwahrscheinlich Nichtgleichgewichtseffekte die Anwendbarkeit der zugrundeliegenden theoretischen Beschreibung limitieren.

CONTENTS

1	Introduction	3
I Preparation 9		
2	From 3D to 2D in the Laboratory	11
2.1	Trapping and cooling	11
2.2	Reaching kinematic 2D	12
2.3	High resolution imaging	14
3	The coherence properties of 3D and 2D Bose gases	17
3.1	The ideal 3D gas	18
3.1.1	Recapitulation of relevant statistical mechanics	18
3.1.2	The density of states	20
3.1.3	3D Bose-Einstein condensation	20
3.1.4	3D coherence properties	23
3.2	The ideal 2D gas	24
3.2.1	2D Bose-Einstein condensation?	25
3.2.2	2D coherence properties	26
3.3	Interacting trapped 3D Bose gases	28
3.3.1	Coherence in interacting trapped 3D Bose gases	29
3.3.2	Condensation of interacting trapped 3D Bose gases	30
3.3.3	Superfluidity in interacting trapped 3D Bose gases	31
3.3.4	Tuning the interactions	32
3.3.5	Effective two-dimensional scattering	34
4	Coherence of the trapped interacting quasi-2D Bose gas	37
4.1	Coherence in the interacting 2D Bose gas	37
4.2	The KT transition	44
5	Experimental Context	49
5.1	Superfluidity in two dimensions	49
5.2	Coherence measurements on single layers	53
5.3	Quantitative theoretical analysis of the interference pattern after ToF	55
6	Experimental tools and methods	57
6.1	Accessing the momentum $n(k)$ after $T/4$ ToF	57
6.2	Reducing vertical expansion with a brake pulse	59
II Results 63		
7	Momentum distribution and first order correlation function of interacting 2D Bose gases	65
7.1	Challenges extracting the momentum distribution from a $T/4$ measurement	67
7.2	Momentum distribution of a 2D ${}^6\text{Li}$ gas	71
7.3	Extracting the temperature of a homogeneous gas	73
7.4	Interpretation of the results	74
7.5	Towards experimental access to the first order correlation function	81
8	A new tool: Accessing coherence via short ToF	87
8.1	Key idea, interference as a phase probe	87
8.1.1	Prior work this thesis builds upon	89
8.1.2	Relation of density ripples to in situ coherence	91

8.2	Analysis of density-density correlations after time of flight	95
8.2.1	Density correlation functions of the experimental system	95
8.2.2	Numerical Correlation Analysis	95
8.3	Time dependence of the coherence from short ToF	98
8.3.1	What can we learn directly from G_2 ?	98
8.3.2	Model theory	100
8.3.3	Quantitative analysis	103
8.4	Possible issues with the theoretical description	110
8.4.1	Applicability of the used theoretical ansatz	111
8.4.2	Probable necessity for non-equilibrium description	113
8.4.3	Technical causes	114
9	Managing systematic errors	115
9.1	Setting the experimental parameters	115
9.1.1	Focus	115
9.1.2	Detuning calibration and optimal intensity	118
9.1.3	Density calibration	119
9.1.4	Magnification calibration	120
9.2	Compensation of systematic errors	123
9.2.1	Absorption image acquisition procedure	123
9.2.2	Influence of the imaging system	123
9.2.3	Compensating for in situ density fluctuations	133
9.3	Technical details of the implemented analysis	134
9.3.1	Verification of compensation and fitting routines	135
9.3.2	Verification of image preparation and correlation analysis routines	137
9.3.3	Fit limits	139
9.3.4	Size the of region of interest	140
9.4	Advantages of analyzing g_2 instead of the PSD	141
10	Conclusion and Outlook	143
A	Detailed derivation of simulated density-density correlation function after time of flight	147
B	Detailed numerical analysis procedure	151
B.1	Image preparation	152
B.2	Correlation analysis	154
B.3	In situ propagation and fitting of g_2	156
C	In situ temperature determination of a homogeneous gas	159
	LIST OF ACRONYMS	160
	LIST OF FIGURES	163
	LIST OF TABLES	164
	ACKNOWLEDGEMENTS	177

1

INTRODUCTION

We spend our lives in three spatial dimensions and our way of thinking is intimately connected to this dimensionality which we take for granted. In our everyday lives we hardly ever encounter objects which can be considered to be of lower dimensionality, since even for objects as thin as aluminum foil, the electrons can still move freely in the third direction.

However, physical systems exist, where the motion in the third direction is frozen out and which exhibit a very different behavior than their 3D counterparts. A few hundred atomic layers of liquid helium adsorbed on a surface represent such a two-dimensional system: When the temperature is lowered below 1.22 K, the film turns superfluid, with a sudden jump in superfluid density¹ not present in bulk ^4He . Much more common, in fact ubiquitous, are *two-dimensional electron gases (2DEGs)* which can be found in every semiconductor device that includes a MOSFET*. Another prominent man-made two-dimensional material, promising great technological potential, is graphene, a single layer of carbon atoms forming a hexagonal grid. This material has many astonishing properties not present in its bulk counterpart, found e. g. in the common pencil.

Over 80 years ago, R. Peierls already realized² that the dimensionality of a system has a profound impact on its properties. He argued that the high degree of order in crystals is not at all trivial, since in lower dimensions perturbations could add up and destroy the symmetry over large distances. Thirty years later, P. Hohenberg³, N. Mermin and H. Wagner⁴ pointed out that in low dimensional systems of infinite continuous symmetry the existence of true long-range order, typically intimately associated with superfluidity, is precluded. This is due to the fact in addition to the movement of the particles being restricted to two dimensions, the density of states does not vanish when approaching zero energy, in contrast to 3D systems. Hence, even for arbitrarily small finite temperature there exist very low energy and thus long wavelength excitations that destroy true long-range order, the property associated with many phase transitions in 3D, such as the freezing of water or Bose-Einstein condensation. A BEC[†] is a remarkable superfluid state driven purely by quantum statistics in which the wave functions of many indistinguishable particles begin to overlap below a critical temperature to form a single macroscopic wave function.

However, V. Berezinskii⁵, J. Kosterlitz and D. Thouless⁶ realized that despite the lack of true long-range order, interacting 2D systems can nevertheless undergo a transition to a superfluid state. This transition is of a novel type: Above the transition, free vortices proliferate, whereas below the transition, vortices of opposite circulation bind into

¹ D. Bishop and J. Reppy: *Phys. Rev. Lett.*, vol. 40, (1978)

*MOSFET: metal-oxide-semiconductor field-effect transistor. A 2DEG is present when in inversion mode.

² R. Peierls: *Helv. Phys. Acta*, vol. 7, (1934)

³ P. C. Hohenberg: *Phys. Rev.*, vol. 158, (1967)

⁴ N. D. Mermin and H. Wagner: *Phys. Rev. Lett.*, vol. 17, (1966)

[†]BEC: Bose-Einstein condensate

⁵ V. L. Berezinskii: *J. Exp. Theor. Phys.*, vol. 32, (1971)

⁶ J. M. Kosterlitz and D. J. Thouless: *J. Phys. C*, vol. 6, (1973)

pairs, hence effectively screening each other in the far-field. Yet, the remaining phononic excitations are still sufficient to destroy true long-range order but not superfluidity. For their theoretical discoveries of this topological phase of matter, J. Kosterlitz and D. Thouless were awarded the Nobel Prize in physics in 2016.

The peculiar phase transition into a regime of quasi-long-range order first came into reach with experiments on thin films of helium¹ and over time, this behavior has been observed in a wide range of other physical systems ranging from 2DEGs⁷, exciton-polariton systems^{8–11} to photonic lattices¹².

With the advent of the first Bose-Einstein condensate in 1995¹³ and degenerate ultracold Fermi gases^{14–16} shortly after, widely tunable and very clean quantum mechanical model systems were realized. Here, unlike e. g. in helium films, the interactions, the density, and the dimensionality can be tuned. To freeze out the vertical degree of freedom, a strong vertical confinement is needed, making excitations in this direction energetically inaccessible. A formal definition of this criterion is to require the energy spacing of the confining trap, $\hbar\omega$, to be much larger than both the thermal, $k_B T$, and the interaction energy, gn , i. e. $\hbar\omega \gg k_B T$ and $\hbar\omega \gg gn^*$. This was accomplished for weakly interacting bosons in 2001^{17,18} and for interacting fermions in 2010¹⁹.

Motivated by the first direct observation of the *Kosterlitz-Thouless* (KT) transition showing the proliferation of vortices in ultracold gases in the group of J. Dalibard²⁰, the phase coherence of ultracold two-dimensional systems were studied in greater detail in that and subsequent works^{21–25}, observing evidence for quasi-long-range order^{20,26}. The interest stems from the fact that phase coherence is one of the defining features of the transition. Being of infinite order, the KT transition is rather peculiar, displaying no discontinuity in any thermodynamic function. However, the phase coherence changes qualitatively, from a thermal gas with an exponentially decaying phase correlation function to an algebraically decaying function with no associated length scale in the *Berezinskii-Kosterlitz-Thouless* (BKT) phase. Superfluid flow is intimately connected with this surprisingly high degree of coherence and only breaks down when the thermal excitations are strong enough to excite singular vortices, i. e. the “phase landscape” is changed globally.

This thesis presents measurements of the phase coherence properties of an ultracold 2D gas of composite bosons with high precision for the first time in a homogeneous box potential, expanding on prior work^{22,27,28}. The phase coherence is made accessible in a homodyne detection scheme exploiting the self interference of the sample during *time of flight* (ToF) in the far and in the near field of the expansion. Using matter wave focusing²⁶ in the far field, the momentum distribution $n(k)$ is measured, from which the phase correlation function g_1 is computed. During short ToF, the gas is left to interfere with itself in the near field, transforming the phase fluctuations partially into density fluctuations, creating a density amplitude pattern. The density-density correlation function g_2 of this pattern is intimately connected

¹ D. Bishop and J. Reppy: *Phys. Rev. Lett.*, vol. 40, (1978)

⁷ P. Minnhagen: *Rev. Mod. Phys.*, vol. 59, (1987)

⁸ D. Snoke: *Science*, vol. 298, (2002),
⁹ L. V. Butov: *Phys. Status Solidi C*, vol. 238, (2003),¹⁰ J. Kasprzak et al.: *Nature*, vol. 443, (2006),¹¹ A. Amo et al.: *Nature Physics*, vol. 5, (2009)

¹² G. Situ and J. W. Fleischer: *Observation of all-optical Berezinskii-Kosterlitz-Thouless crossover in a photonic lattice*, (2012)

¹³ M. H. Anderson et al.: *Science*, vol. 269, (1995)

¹⁴ B. DeMarco and D. S. Jin: *Science*, vol. 285, (1999),¹⁵ A. G. Truscott et al.: *Science*, vol. 291, (2001),¹⁶ F. Schreck et al.: *Phys. Rev. A*, vol. 64, (2001)

*Here k_B is the Boltzmann constant, T the temperature, g the interaction parameter (tunable) and n the density of the gas

¹⁷ M. Greiner et al.: *Phys. Rev. Lett.*, vol. 87, (2001),¹⁸ A. Görlitz et al.: *Phys. Rev. Lett.*, vol. 87, (2001)

¹⁹ K. Martiyanov et al.: *Phys. Rev. Lett.*, vol. 105, (2010)

²⁰ Z. Hadzibabic et al.: *Nature*, vol. 441, (2006)

²¹ P. Cladé et al.: *Phys. Rev. Lett.*, vol. 102, (2009),²² J.-Y. Choi et al.: *Phys. Rev. Lett.*, vol. 110, (2013),²³ M. G. Ries et al.: *Phys. Rev. Lett.*, vol. 114, (2015),²⁴ V. Schweikhard et al.: *Phys. Rev. Lett.*, vol. 99, (2007),²⁵ T. Plisson et al.: *Phys. Rev. A*, vol. 84, (2011)

²⁰ Z. Hadzibabic et al.: *Nature*, vol. 441, (2006),²⁶ P. A. Murthy et al.: *Phys. Rev. Lett.*, vol. 115, (2015)

²² J.-Y. Choi et al.: *Phys. Rev. Lett.*, vol. 110, (2013),²⁷ R. Desbuquois: *Thermal and superfluid properties of the two-dimensional Bose gas*, (2013),²⁸ S. Pres: *BKT - phase transition in a strongly interacting 2D Bose gas*, (2014)

²⁶ P. A. Murthy et al.: *Phys. Rev. Lett.*, vol. 115, (2015)

to the phase correlation function g_1 and can hence be used to gain insights into the latter.

These density ripples are akin to the speckle pattern produced by the self interference of a laser beam reflected off a rough surface. Here, varying phase delays are imprinted by reflections off the surface irregularities, leading to a random intensity pattern when they interfere. Although the spatial distribution of the noise pattern changes from realization to realization, the intensity-intensity correlation can be extracted to gain insights into the phase correlations and thus the surface. In the case of our quantum gas, the correlations of the changing density noise after time of flight yield information about the phase of the in situ wave functions.

In order to derive information about the phase distribution, we fit theoretical predictions for the density-density correlation function g_2 with realistic phase correlation functions g_1 as input to the experimentally determined density correlations. Due to the large usable area of the homogeneous gas, a remarkably high data quality can be reached and hence excellent fits to individual theory curves are obtained. However, the observed trend when holding the gas in a dipole trap for varying time contradicts our expectations for a superfluid gas being heated during the hold time and crossing the *KT* transition boundary to the normal regime. The assumption that longer hold times lead to increasing temperature seems plausible since the momentum distribution shows a clear depopulation of low-momentum modes. Then, an increase in temperature is expected to be accompanied by an increase in phase fluctuations in situ and therefore increased density fluctuations after short *ToF*. Yet, the algebraic fits indicate a reduction of total phase fluctuations. The analysis arriving at this surprising contradiction is provided in detail in this work. The joint analysis of momentum distribution and short *ToF* interference pattern suggests that the comparison with the theory employed is most likely limited by non-equilibrium effects caused by strong heating due to e. g. insufficient background vacuum pressure.

This thesis is separated into two parts, the theoretical support is introduced in *Part I*, in preparation for the discussion of the experimental results presented in *Part II* and is further organized as follows:

Part I

- In Chapter 2, the experimental apparatus is introduced and the experimental procedure used to create a degenerate two-dimensional gas of composite bosons is summarized.
- In Chapter 3 we introduce the basic concepts of coherence and superfluidity and establish the qualitative difference between 3D and 2D regarding the phase transitions. First, the coherence properties of the three-dimensional ideal gas are discussed as an instruc-

tive example and compared to the two-dimensional case. Subsequently, interactions are introduced and the resulting superfluidity is discussed on the basis of the Landau criterion.

- Chapter 4 discusses the coherence properties of two-dimensional interacting Bose gases in greater detail and presents the theoretical framework from which these are derived. We show how the KT-phase transition can be explained by the creation of free vortices.
- In Chapter 5, a short overview of the previous experimental studies relevant for this work is given, from the first experiments on superfluid ^4He films to the studies of coherence and superfluidity in 2D systems of ultracold atoms. The theoretical foundation for this work is introduced briefly.
- Chapter 6 highlights two methods required to study the momentum distribution experimentally, namely the matter wave focusing technique, enabling the access of phase properties, and the reduction of the expansion perpendicular to the 2D plane by a brake pulse, ensuring high resolution optical imaging.

Part II

- In Chapter 7, we present the first measurements of the momentum distribution $n(k)$ of a single homogeneous 2D layer of composite bosons, demonstrating the challenges associated with extracting the first order correlation function g_1 due to the strong impact of the imaging system. Further, the experimental results are interpreted assuming a heating process for prolonged hold time in an optical trap.
- Chapter 8 introduces the measurements of the coherence properties via the analysis of the self-interference patterns appearing after short time of flight. The analysis is presented in detail and the results are interpreted. Possible issues, especially when also considering the measured momentum distribution, are pointed out.
- In Chapter 9, we present the calibration and compensation procedures performed in order to limit the dependence of the measurements on systematic errors.

PUBLICATIONS IN THE CONTEXT OF THIS THESIS

- **Two-Dimensional Homogeneous Fermi Gases**
K. Hueck, N. Luick, L. Sobirey, J. S., T. Lompe, and H. Moritz
Phys. Rev. Lett, 120(6), 060402-1 (2018)
- **Calibrating high intensity absorption imaging of ultracold atoms**
K. Hueck, N. Luick, L. Sobirey, J. S., T. Lompe, H. Moritz, L. W. Clark, and C. Chin
Opt. Express, 25(8), 8670–8679 (2017)
- **Probing superfluidity of Bose-Einstein condensates via laser stirring.**

V. P. Singh, W. Weimer, K. Morgener, J. S., K. Hueck, N. Luick, H. Moritz, and L. Mathey
Phys. Rev. A, 93(2), 1–14 (2016)

- **Critical Velocity in the BEC-BCS Crossover**

W. Weimer, K. Morgener, V. P. Singh, J. S., K. Hueck, N. Luick, L. Mathey, and H. Moritz
Phys. Rev. Lett., 114(9), 1–5 (2015)

Part I

PREPARATION

2

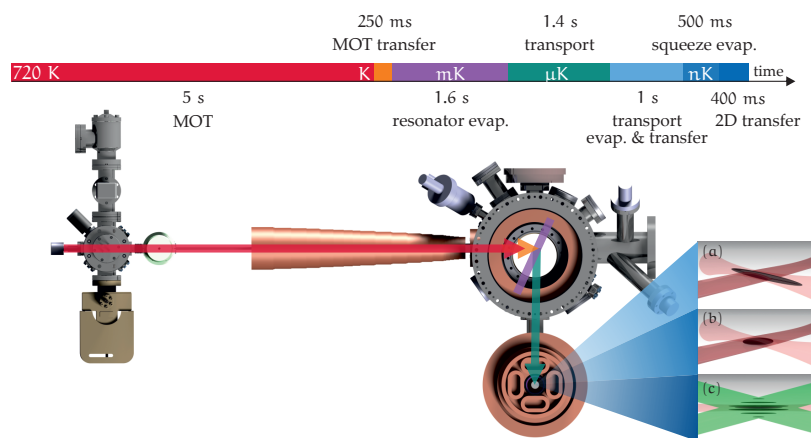
FROM 3D TO 2D IN THE LABORATORY

2.1	Trapping and cooling	11
2.2	Reaching kinematic 2D	12
2.3	High resolution imaging	14

This chapter outlines the process of creating an interacting 2D gas of composite bosons. It will cover the most important aspects of the trapping, cooling and squeezing of a cloud of ^6Li to reach a highly anisotropic degenerate gas. For additional details pertaining to the construction of the experimental apparatus and the technical specifics in the preparation of a degenerate two-dimensional sample, refer to the theses of W. Weimer²⁹ and K. Morgener³⁰. For a more detailed description of the experimental setup required to obtain the homogeneous density and the applied process see the thesis of K. Hueck³¹.

2.1 TRAPPING AND COOLING

A technical drawing of the most important elements in trapping and cooling neutral lithium atoms is presented in Fig. 2.1. The process of creating a degenerate gas in this experimental apparatus can be conceptually divided into four stages. In a fifth step, detailed in the next section, the vertical degree of freedom is frozen out. The process ends with an absorption image of the studied gas, destroying the sample. Hence, the complete sequence of creating, cooling an imaging is repeated approximately every 13 s.



The sequence is as follows:

²⁹ W. Weimer: *Probing superfluid properties in strongly correlated Fermi gases with high spatial resolution*, (2014)

³⁰ K. H. Morgener: *Microscopy of 2D Fermi Gases Exploring excitations and thermodynamics*, (2014)

³¹ K. Hueck: *A homogeneous, two-dimensional fermi gas. Measurements in Position- and Momentum-Space*, (2017)

Figure 2.1: Overview of the trapping and cooling procedure. Fermionic lithium is evaporated (left) at $\approx 720\text{ K}$ and subsequently decelerated by the Zeeman slower (middle) in order to be captured in the MOT. After multiple forced evaporation steps, the cooled gas is transported into the experiment cell pictured on the bottom. Here the sample is transferred into a highly anisotropic attractive dipole trap (a to b) and subsequently loaded into a single node of a blue detuned lattice (c). During this cycle, the temperature of the gas is reduced by about twelve orders of magnitude in less than 13 seconds. Figure is adapted from³⁰.

³⁰ K. H. Morgener: *Microscopy of 2D Fermi Gases Exploring excitations and thermodynamics*, (2014)

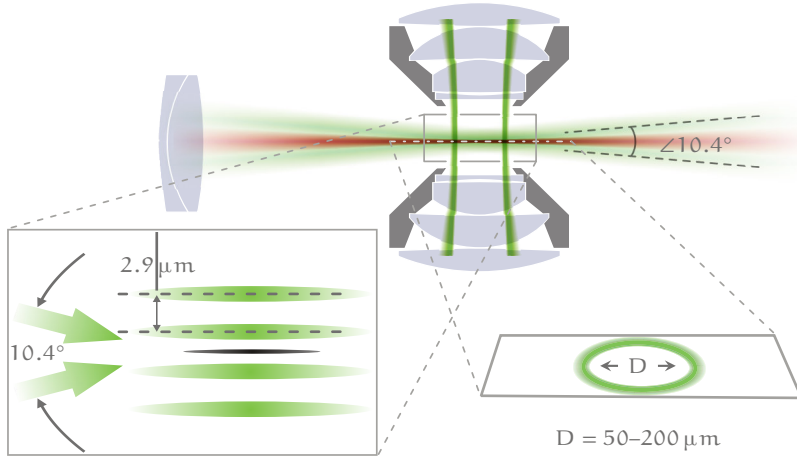
- In the first step, fermionic ${}^6\text{Li}$ is evaporated at approximately $450\text{ }^\circ\text{C}$ in a high vacuum oven chamber. This creates a jet of hot gas of approximately 1400 m/s in a mixture containing mostly the lowest two hyperfine states.
- Second, the jet of hot ${}^6\text{Li}$ gas is decelerated in a Zeeman slower. Here, collisions with counter-propagating photons reduce the velocity of the atoms. The magnetic field decreases along the direction of travel so that the changing Doppler shift is compensated by the Zeeman shift, which ensures that the slowed atoms are constantly in resonance with the counter-propagating laser light.
- Third, the slowed atoms are captured and cooled in a *magneto optical trap* (MOT). A MOT consists of a magnetic quadrupole field and six beams of near resonant laser light from all spatial directions. This results in a spatial and velocity dependent radiation force which confines the atoms to the center of the trap and reduced the average temperature of the gas to be on the order of one mK. Roughly 50×10^6 atoms are captured and after evaporative cooling in a resonator dipole trap approximately 10×10^6 atoms are ready to be transported out of the MOT chamber.
- In a fourth step, the atoms are transferred into a far detuned dipole trap with movable focus and transported to the experiment cell. This octagonal non-magnetic cell with good optical access features a high resolution imaging system and magnetic field coils in close proximity in order to reach high magnetic fields. At this point, the number of ${}^6\text{Li}$ atoms has been reduced to approximately 1×10^6 but the temperature has also decreased to $\approx 100\text{ }\mu\text{K}$.

The lithium isotope employed is fermionic and hence requires an interacting spin mixture for effective cooling. However, only negligible interaction between the spin states exists naturally. Hence, the interaction is facilitated by coupling the scattering properties of the two hyperfine states of ${}^6\text{Li}$ via a magnetic field, a so called Feshbach resonance. The existence of this Feshbach resonance allows us to tune the interaction strength from repulsion to attraction and when working at a magnetic field of 834 G , the scattering length even diverges enabling efficient evaporative cooling in a strongly interacting many-body state. Further details pertaining to the scattering properties of ultracold lithium can be found in Section 3.3.4.

2.2 REACHING KINEMATIC 2D

The final step in preparing a single layer of two-dimensional composite bosons is performed in the experiment cell. A pre-cooled Fermi gas containing two hyperfine states is transferred into an oblate pancake shaped dipole trap with an aspect ratio of ≈ 10 . Here, a magnetic field close to the Feshbach resonance is applied and the trap depth is lowered, thus removing the fastest atoms by evaporation. This results

in atom numbers on the order of 3×10^5 at a temperature of approximately 100 nK. Next, a radial confinement is provided by a repulsive



ring potential generated by a cascade of three axicons and projected into the gas by a high-resolution objective. This potential cuts away the outer high-entropy region of the cloud which is subsequently removed from the observation volume by switching off the radial magnetic confinement. In order to reach kinematic 2D and freeze out the movement in the vertical direction, strong axial confinement is applied by means of an optical lattice formed by two blue-detuned laser beams intersecting at an angle of 10.4° .

To transfer the atoms into a single layer, we re-compress the gas axially by increasing the laser power in the oblate trap, thus reducing the width of the cloud below the lattice spacing of $2.9 \mu\text{m}$. The wide lattice spacing allows the loading of a single layer, containing approximately 90% of the atoms. The relative number of atoms in adjacent layers is ascertained by a matter wave focusing technique which magnifies the separation before imaging. If need be, the relative population of the layers can be adjusted by changing the position of the oblate trap relative to the lattice nodes. Subsequently, the magnetic fields are reduced to form the bosonic molecules and a homogeneous 2D Bose gas is obtained. The single homogeneous 2D layer is confined axially by the lattice potential with a trap frequency of $(12.4 \pm 0.1) \text{ kHz}$ and radially by the ring potential. A weak magnetic field curvature is used to counteract the anticonfinement introduced by the lattice potential.

If the confinement in the vertical direction is sufficient, all the atoms occupy the lowest oscillator mode and are thus only able to move laterally, a situation sketched in Fig. 2.3. For the temperatures of our experiment, the level spacing in comparison to the available thermal energy E_T is approximately $\frac{\hbar\omega_z}{k_B T} \approx 5$, thus suppressing the thermal excitation of higher levels significantly. For an interacting system to be considered two-dimensional, the energy associated with the interaction must also be well below the confinement energy, which is also reasonably well satisfied with a ratio of level spacing to mean field interaction energy of $\frac{\hbar\omega_z}{g_{2D}n_{2D}} \approx 6.8$. Thus, a single homogeneous 2D

Figure 2.2: Sketch of the setup used to reach the kinematic 2D regime. In the center, the two microscope objectives above and below the ^6Li gas are depicted. In order to freeze out the vertical motion, we shine in two blue detuned laser beams at an enclosing angle of 10.4° (lower left). This results in a comparatively wide lattice spacing of $2.9 \mu\text{m}$ which is sufficient to load a single layer of compressed ^6Li atoms into a single node. The homogeneous density is facilitated by the application of a repulsive ring potential created by a cascade of three axicons. The size of the resulting box potential can be freely tuned in between $50\text{--}200 \mu\text{m}$ by varying the magnification of the image. Figure is adapted from^{30,31}.

³⁰ K. H. Morgener: *Microscopy of 2D Fermi Gases Exploring excitations and thermodynamics*, (2014), ³¹ K. Hueck: *A homogeneous, two-dimensional fermi gas. Measurements in Position- and Momentum-Space*, (2017)

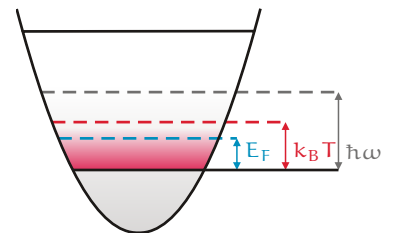


Figure 2.3: Schematic illustrating the confinement of the ultracold gas to the lowest oscillator level. Note that the Fermi energy E_F as well as the thermal energy $k_B T$ are well below the oscillator spacing $\hbar\omega_z$. Hence, all motion is frozen out in the direction of the confinement. Figure is adapted from³⁰.

³⁰ K. H. Morgener: *Microscopy of 2D Fermi Gases Exploring excitations and thermodynamics*, (2014)

layer of composite bosons is attained.

2.3 HIGH RESOLUTION IMAGING

The complete experimental apparatus contains a multitude of components, many of them essential for the measurements presented in this work. However, due to the pivotal role of the imaging system in acquiring the data to be analyzed, it is highlighted in the following.

The experiment is performed in an octagonal ultra high vacuum cell sandwiched between two magnetic field coils. Concentric to the coils, two high resolution microscope objectives are positioned such that the upper objective can be used to imprint arbitrary potentials onto the 2D quantum gas and the lower objective is used to acquire an absorption image. During the imaging, the gas is illuminated through the upper objective with an approximately homogeneous beam of resonant laser light on the so called D_2 line of atomic lithium, i. e. between the states with spectroscopic notation: $2^2S_{1/2} \leftrightarrow 2^2P_{3/2}$. Hence, depending on the exact detuning, the population in the lower or upper hyperfine state can be measured. A sketch of the imaging system, without the magnetic field coils, is shown in Fig. 2.4.

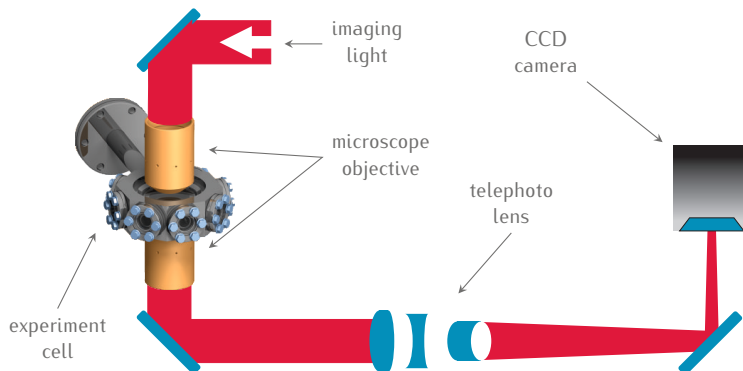


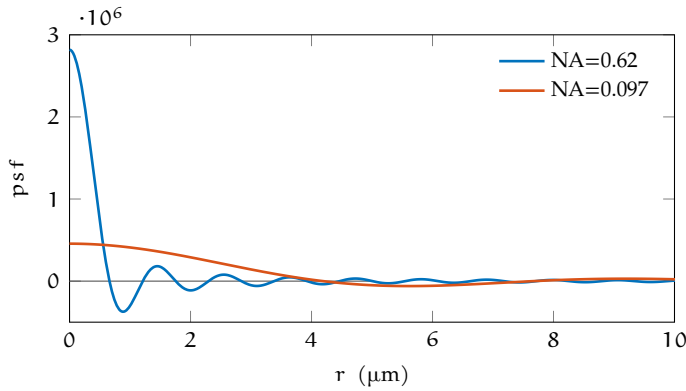
Figure 2.4: Sketch of the high resolution imaging setup used for manipulation and imaging. Two $NA=0.62$ microscope objectives are installed above and below the experiment cell in order to achieve high resolution imaging and the ability to impart detailed arbitrary potentials. The imaging beam is subsequently focused onto a highly efficient CCD camera by a large telephoto lens, thus decreasing the necessary beam length. Note that the pictured steel cell has since been replaced by a glass cell after the completion of the presented experiments. A more detailed schematic can be found in Section 9.2.2. Figure is adapted from³⁰.

When the gas is released from the trap, it expands quickly in the highly confined direction. On the one hand, this process is beneficial to suppress interactions during time of flight due to the rapidly decreasing density. On the other hand, the available *depth of field* (DoF) is limited to less than $\pm 2 \mu\text{m}$ due to the large *numerical aperture* (NA) of the microscope of $NA=0.62$. This DoF is quickly exceeded by the expanding atoms. Hence, the theoretical diffraction limited resolution of $\approx 700 \text{ nm}$ cannot be reached due to the blur acquired from atoms out of focus.

Fortunately, the size of the observable features expected in this experiment are typically on the order of multiple micrometers which allows us to trade lateral resolution for DoF by reducing the NA. Since the size of the expected density features increases with the square root of the time of flight, $L_{\text{lateral}} \propto \sqrt{t_{\text{ToF}}}$ but the axial extent of the cloud increases approximately linear for small *time of flight* (ToF), $L_{\text{axial}} \propto t_{\text{tof}}$,

³⁰ K. H. Morgener: *Microscopy of 2D Fermi Gases Exploring excitations and thermodynamics*, (2014)

the compromise between time of flight and resolution can be optimized. To this end, the numerical aperture is reduced to values of ≈ 0.1 by placing an iris diaphragm in the Fourier plane in the imaging path, limiting the available wave vectors of the light field to $|\mathbf{k}| < |\mathbf{k}|_{\text{iris}}$. Hence, the lateral resolution is decreased to approximately $4 \mu\text{m}$ but the depth of field is increased up to $\pm 67 \mu\text{m}$. Although most of the imaged atoms are therefore in focus, we have lost lateral resolution and hence small lateral features are stronger effected by the influence of the imaging system. This is illustrated best in the broadening of the *point spread function* (PSF), shown in Fig. 2.5. However, since this effect is known it can be compensated for in the quantitative analysis of the absorption image, which is presented in more detail in Section 9.2.2.



The size of the expanding cloud only deviates noticeably from linear for ToF larger than $T/4 \approx 9 \text{ ms}$ due to the anti-Helmholtz configuration of the magnetic field coils introducing an axial deconfinement.

Figure 2.5: The effect of reducing the lateral resolution via the placement of an iris diaphragm in the dark field. The result of the suppressed high frequencies yields an effective numerical aperture of $\text{NA}=0.097$ which in turn leads to a much broader and shallower PSF shown in red (dashed) compared to the original $\text{NA}=0.62$ shown in blue. Note, the curves have been normalized to unit area instead of volume to ensure comparable amplitudes.

3

THE COHERENCE PROPERTIES OF 3D AND 2D BOSE GASES

- 3.1 The ideal 3D gas 18
- 3.2 The ideal 2D gas 24
- 3.3 Interacting trapped 3D Bose gases 28

This work focuses on the study of ultracold strongly correlated 2D gases, their phase coherence properties and the possibly associated superfluidity. Remarkably, the superfluid *Bose-Einstein condensate* (BEC) can only exist in more than two dimensions. It turns out that in 1D, dynamical superfluidity is notably absent³² and 2D is the marginal dimension for frictionless flow. Hence, it is instructive to consider ultracold 3D gases first, where the concepts of condensation and superfluidity are much easier understood. The line of reasoning will loosely follow the excellent review of Z. Hadzibabic and J. Dalibard³³.

First, an infinite homogeneous 3D Bose gas at low temperatures is considered and it is shown that the gas undergoes a phase transition to a regime where the ground state is macroscopically populated below a critical temperature $T_{\text{crit}} > 0$. This is due to the rapid decrease of the *density of states* (DoS) towards low energies and thus an insufficient number of excited states for the particles to inhabit. Hence, they will condense into the ground state and form a BEC where the constituent wave functions exhibit identical phase. Thus, investigating the coherence of the phase over a distance x by means of the first order phase correlation function $G_1(x)$, yields a constant value. The gas exhibits *long-range order* (LRO).

In case of inter-particle interaction, the condensate will exhibit superfluidity, i. e. frictionless flow below a critical velocity $v_c > 0$. This velocity is given by the minimal slope of the Bogoliubov dispersion relation, i. e. the group velocity of the lowest excitation. The Landau criterion³⁴ states that below this velocity the gas is energetically stable under small perturbations. Thus, in a 3D Bose gas, the onset of condensation and superfluidity coincide.

In contrast, in an infinite homogeneous 2D gas at low temperatures, a macroscopic population of the ground state for all temperatures except $T = 0$ is notably absent. This is due to a constant DoS even for the energy approaching zero, which enables the distribution of the particles to the excited states at any temperature $T > 0$. Hence, there exists no BEC in an infinite homogeneous 2D system for any finite temperature.

Investigating the phase of the order parameter, one can show that in an infinite 2D system a continuous symmetry can not spontaneously

³² A. Y. Cherny et al.: *Front. Phys.*, vol. 7, (2012)

³³ Z. Hadzibabic and J. Dalibard: *Riv. Nuovo Cimento*, vol. 34, (2011)

³⁴ L. Landau: *Phys. Rev.*, vol. 60, (1941)

be broken. This implies that for any distance $x \rightarrow \infty$, the correlation function $G_1(x)$ vanishes for any finite temperature. This has been shown for the 2D Heisenberg model by N. Mermin and H. Wagner⁴, applied to 2D quantum field theory³⁵ and rigorously proven for any 2D system by P. Hohenberg³. Thus, a uniform two-dimensional system does not exhibit LRO.

A qualitatively different behavior occurs if the particles of the 2D Bose gas are interacting with each other. Below a critical temperature T_{KT} , the correlation function $G_1(x)$ changes from an exponential decay to an algebraic decay $G_1(x) \propto (\xi/x)^\eta$, where ξ is the healing length and η is called the scaling exponent. Since the correlations decay with no associated length scale this situation is called *quasi-long-range order* (QLRO). Surprisingly, this gas is nevertheless superfluid. In fact, the occurrence of a superfluid density n_s is intimately linked to the existence of QLRO since both only break down when free vortices proliferate, as will be detailed in Section 4.2.

Interestingly, an unusual phase transition accompanies the change from exponential to algebraic decay of phase correlations as explained by the theory of V. Berezinskii³⁶, J. Kosterlitz and D. Thouless⁶. It is remarkable in the sense that the change from a high-temperature normal state to a low-temperature superfluid state does not involve any spontaneous symmetry breaking. This quantum phase transition revolves around another source of phase fluctuations: vortices. As will be shown later, the unbinding of vortices of opposite charge defines the transition from a superfluid to a normal fluid.

In the following, the concepts of condensation and coherence are described in more detail. Initially, infinite ideal homogeneous 3D and 2D gases are compared and then interactions are introduced. Concluding, the 2D case will be examined in the presence of a trapping potential and some finite size effects will be discussed.

3.1 THE IDEAL 3D GAS

In this section, the mean occupancy of a state $b(\epsilon)$ is briefly derived and subsequently used to show the effect of Bose-Einstein condensation in 3D. This yields the basis for the discussion of the coherence properties in Section 3.1.4.

3.1.1 Recapitulation of relevant statistical mechanics

The framework of classical statistical mechanics can be used to describe many of the important properties of cold gases also when approaching low temperatures.

An interactionless atomic gas can be adequately described by the grand partition function

$$\mathcal{Z}(z, \epsilon, \beta) = \prod_{\nu} (1 \pm z e^{-\beta \epsilon_{\nu}})^{\pm d_{\nu}} \quad \text{with} \quad \mu = \left(\frac{\partial U}{\partial N_{\nu}} \right)_{S, V}. \quad (3.1)$$

Here, it is multiplied over every microstate ν with the inverse temper-

⁴ N. D. Mermin and H. Wagner: *Phys. Rev. Lett.*, vol. 17, (1966)

³⁵ S. Coleman: *Commun. Math. Phys.*, vol. 31, (1973)

³ P. C. Hohenberg: *Phys. Rev.*, vol. 158, (1967)

³⁶ V. Berezinskii: *J. Exp. Theor. Phys.*, vol. 34, (1971)

⁶ J. M. Kosterlitz and D. J. Thouless: *J. Phys. C*, vol. 6, (1973)

ature $\beta = 1/k_B T$, the fugacity $z = e^{\beta\mu}$ and the degeneracy of each state d_ν . The chemical potential of the reservoir, for example, can be defined as the partial derivative of the internal energy U evaluated at constant entropy S and volume V . Since Bose and Fermi gases satisfy different statistics the minus sign is taken for bosons and the plus sign for fermions. It is useful to introduce the grand potential from which many basic properties of the gas can be derived

$$\mathcal{Q}(z, \epsilon, \beta) = \ln(\mathcal{Z}(z, \epsilon, \beta)) = \sum_{\nu} \pm d_{\nu} \ln(1 \pm z e^{-\beta \epsilon_{\nu}}). \quad (3.2)$$

An *equation of state* (EOS) like the total number of particles, can be attained by differentiating the grand potential with respect to z

$$N = z \frac{\partial}{\partial z} \mathcal{Q}(z, \epsilon, \beta) = \sum_{\nu} \pm d_{\nu} (e^{\beta \epsilon_{\nu} - \mu} \pm 1)^{-1}. \quad (3.3)$$

From this, the mean occupancy of a single-particle state ν with energy ϵ_{ν} can be seen to be

$$b(\epsilon_{\nu}) = (e^{\beta(\epsilon_{\nu} - \mu)} + \gamma)^{-1}. \quad (3.4)$$

The constant γ describes the nature of the distribution of the particles:

$$\gamma = +1 \quad \text{Fermi-Dirac}$$

$$\gamma = 0 \quad \text{Maxwell-Boltzmann}$$

$$\gamma = -1 \quad \text{Bose-Einstein}$$

Note, if $\epsilon_0 = 0$ is chosen as the minimum energy of the single-particle spectrum, one immediately requires $-\infty \leq \mu \leq 0$ for the Bose-Einstein distribution since the occupation has to be positive semidefinite. For the other distributions, the chemical potential can take on either sign. The different behaviors of the distributions for small $\beta(\epsilon_{\nu} - \mu)$ are shown in Fig. 3.1. In the limit of high excitations, or $e^{\beta(\epsilon - \mu)} \gg 1$, all distributions approach the Maxwell-Boltzmann distribution.

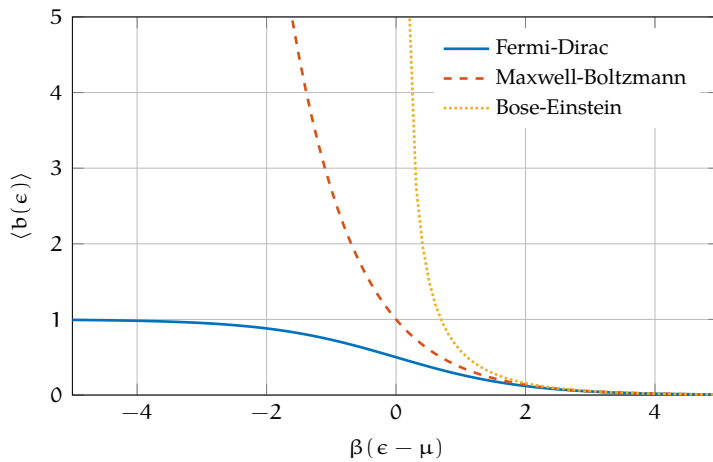


Figure 3.1: Comparison of mean particle occupancy $\langle b(\epsilon) \rangle$ for different particle statistics in dependence of the energy ϵ shifted by the chemical potential μ and scaled by the inverse temperature $\beta = 1/k_B T$. Note that only the Fermi-Dirac distribution (blue) is bounded and approaches 1 for $\epsilon \ll \mu$, the Bose-Einstein distribution (yellow, dotted) diverges for $\epsilon \rightarrow \mu$ while both approach the Maxwell-Boltzmann distribution (red, dashed) for high excitations i. e. $\epsilon \gg \mu$.

Analogous to the approximation made in the Thomas-Fermi model, if the temperature of the system is sufficiently high or the size is sufficiently large, the spacing of the single-particle energy levels becomes

small enough to replace the sum over discrete excited states by an integral over the energy weighted by the density of states $g(\epsilon)$. Hence, the particle number can be written as

$$N_{\text{excited}} \approx N = \sum_{\nu} \pm d_{\nu} b(\epsilon_{\nu}) \approx \int_0^{\infty} b(\epsilon) \text{DoS}(\epsilon) d\epsilon. \quad (3.5)$$

Here, $b(\epsilon_{\nu})$ denotes the probability that a state is populated and the density of states $\text{DoS}(\epsilon)$, describes the states that are available. Replacing the discrete sum in Eq. (3.5) with an integral is a good approximation if the density of states is large. For a vanishing density of states, this approximation breaks down.

The mean occupancy depends on the nature of the considered particles and their properties. The density of states in contrast, depends on the properties of the system the particles are in.

3.1.2 The density of states

The **DoS** is given by the space a particle inhabits in phase space. According to Heisenberg's uncertainty principle, the minimal phase-space volume is quantized to $(2\pi\hbar)^3$. Let $V = \Delta x \Delta y \Delta z$ be the real-space volume a particle occupies and $V_m = 4/3\pi p^3$ be the volume a particle with momentum up to p occupies in momentum space. As a function of the energy $\epsilon = p^2/2m$, the total number of states can be written as

$$\# \text{States}(\epsilon) = \frac{V \frac{4}{3}\pi p^3}{(2\pi\hbar)^3} = V \frac{\sqrt{2}}{3\pi^2\hbar^3} (m\epsilon)^{3/2}. \quad (3.6)$$

For simplicity, no internal degrees of freedom are considered here, effectively setting a multiplicative constant to unity. From this, the **DoS** for a homogeneous 3D system can be calculated by taking the derivative with regard to the energy

$$\text{DoS}(\epsilon) = \frac{d}{d\epsilon} \# \text{States}(\epsilon) = V \frac{\sqrt{2}}{2\pi^2\hbar^3} (m)^{3/2} \sqrt{\epsilon}. \quad (3.7)$$

In other dimensions, substitution with the appropriate volume element leads to the respective density of states. The **DoS** can usually be written as a power law of ϵ

$$\text{DoS}(\epsilon) = \zeta_{\alpha} \epsilon^{\alpha-1}, \quad (3.8)$$

where ζ_{α} is a constant. The exponent α depends on the dimensionality of the system. For the homogeneous case in d dimensions $\alpha = d/2$ and for the harmonically trapped gas in d dimensions $\alpha = d$.

3.1.3 3D Bose-Einstein condensation

The effect of condensation of bosons to the ground state can already be seen by investigating Eq. (3.5). Replacing the total number of particles N by the total number density $n_{\text{tot}} = N/V$ the equation reads

$$n_{\text{tot}} = \frac{N}{V} = \frac{1}{V} \int_0^{\infty} d\epsilon b(\epsilon) \text{DoS}(\epsilon) = C \int_0^{\infty} d\epsilon \frac{\sqrt{\epsilon}}{e^{\beta(\epsilon-\mu)} - 1}, \quad (3.9)$$

with the constant $C = m^{3/2}/\sqrt{2\pi^2\hbar^3}$. The particle density as a function of chemical potential and temperature is thus attained by evaluating the integral on the right hand side. Since this type of integral yields a special function called the polylogarithm, it is instructive to study some its elementary properties. It turns out, for example, that the value of the integral is finite for any finite $T > 0$ and thus facilitates the creation of a Bose-Einstein condensate. Additional details can be found in Extra 3.1.

Extra 3.1: The polylogarithm

The polylogarithm appears naturally as the closed form solution of Bose-Einstein and Fermi-Dirac type integrals with positive α and the fugacity $z = e^{\beta\mu}$

$$\mp \text{Li}_\alpha(\mp z) = \frac{\beta^\alpha}{\Gamma(\alpha)} \int_0^\infty d\epsilon \frac{\epsilon^{\alpha-1}}{\frac{e^{\beta\epsilon}}{z} \pm 1}$$

Here $\Gamma(\alpha)$ is the Gamma function, i.e. the extension of $\Gamma(n) = (n-1)!$ to real and complex numbers. The upper sign is chosen for fermions and the lower sign for bosons. The polylogarithm is in general defined for arbitrary complex z and α but in terms of a physical quantity like the particle density n only a non-negative and real valued polylogarithm is meaningful. For bosons, this restricts the argument z to the interval $0 \leq z \leq 1$. This coincides with the requirement $-\infty \leq \mu \leq 0^-$

and thus $z \rightarrow 1$ the $\text{Li}_{3/2}$ has a finite value of $\zeta(3/2) \approx 2.612$ at $z = 1$ whereas $\text{Li}_{1/2}$ diverges. ζ denotes the Riemann Zeta function, a solution of Eq. (3.10) for the special case of $z = 1$.

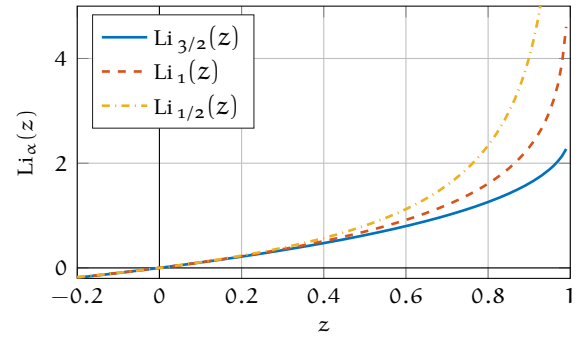


Figure 3.2: Plot of the polylogarithm for $\alpha = 3/2$ (solid blue line), $\alpha = 1$ (dashed red line) and $\alpha = 1/2$ (dot-dashed yellow line).

Using the polylogarithm to solve Eq. (3.9) the total particle density n_{tot} is found to be

$$n_{\text{tot}} = \frac{\Gamma(3/2)C}{\beta^{3/2}} \text{Li}_{3/2}(z). \quad (3.10)$$

This result can be simplified by replacing the Gamma function with its numerical value $\Gamma(3/2) = \sqrt{\pi}/2$ and realizing that the prefactors can be written with the thermal de Broglie wavelength $\lambda_T = \sqrt{2\pi\hbar^2\beta/m}$ as

$$n_{\text{tot}} = \frac{1}{\lambda_T^3} \text{Li}_{3/2}(z). \quad (3.11)$$

Now, when adding particles to the system to increase the density, the chemical potential has to increase from $\mu_{\text{min}} = -\infty \rightarrow \mu_{\text{max}} = 0$. The polylogarithm is a monotonically increasing function, thus this is synonymous with increasing $z = 0 \rightarrow z = 1$. Since $\text{Li}_{3/2}(z = 1) \approx 2.612$, the achievable density seems to be bounded. This is certainly unphysical.

The error must lie with the only approximation applied. Replacing the sum in Eq. (3.5) with an integral is only viable for a finite density of states. Since for the 3D case the DoS($E \rightarrow 0$) $\rightarrow 0$ the contribution

of the ground state is effectively ignored. Taking the ground state correctly into account yields a first order correction to the total density in Eq. (3.9)

$$\begin{aligned} n_{\text{tot}} &= \frac{1}{V} \frac{1}{e^{\beta(\epsilon_0 - \mu)} - 1} + C \int_0^\infty \frac{\sqrt{\epsilon}}{e^{\beta(\epsilon - \mu)} - 1} d\epsilon \\ &= \frac{1}{V} \frac{1}{1/z - 1} + \frac{1}{\lambda_T^3} \text{Li}_{3/2}(z) \\ &= n_{\text{ground}} + n_{\text{excited}}. \end{aligned} \quad (3.12)$$

Setting the energy of the ground state $\epsilon \equiv 0$ one sees immediately that the first term, representing the particles in the ground state, n_{ground} diverges for $z \rightarrow 1$ while the second term, representing the particles in the excited states, n_{excited} is bounded. Thus, when the excited states are saturated, the additional particles are accommodated in the ground state. Ultimately, a significant part of all particles inhabit the ground state. This is known as a BEC.

It will be shown in the next section that the same calculation for a 2D Bose gas shows that the excited state population is not bounded. Hence all particles remain in the excited states and the ground state exhibits no macroscopic population for any finite temperature.

The dependence of the fugacity and the chemical potential on temperature can be extracted by solving Eq. (3.9) numerically and is plotted in Fig. 3.3. A universally useful property in the description of condensation phenomena is the phase-space density $D = n\lambda_T^d$ with d being the dimension. The phase-space density describes the occupation of a phase-space volume cell. Thus, there exists a critical phase-space density $D_{\text{crit}} = \text{Li}_{3/2}(z = 1) \approx 2.612$ above which the particles begin to condensate.

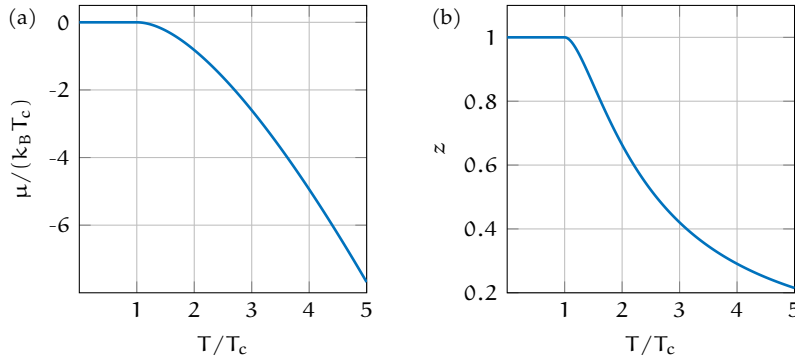


Figure 3.3: (a) Chemical potential μ and (b) fugacity $z = e^{\beta\mu}$ obtained from numerical solution of Eq. (3.9)³⁷ in dependence of reduced temperature T/T_c in the thermodynamic limit. Note that the chemical potential is $\mu \leq 0$ for non-interacting bosons and only approaches 0 at $T = T_c$. Thus, the fugacity is also bounded.

In addition to increasing the density, the change in chemical potential can also be facilitated by a change in temperature. Hence, it is possible to populate the ground state macroscopically by lowering the temperature of the system. The critical temperature T_c below which the ground state is significantly populated is

$$T_c = \frac{n_{\text{tot}}^{2/3} 2\pi\hbar^2}{\xi(3/2)^{2/3} k_B m}. \quad (3.13)$$

With this, the fraction of particles in the ground state can be written as

$$\frac{n_{\text{ground}}}{n_{\text{tot}}} = 1 - \left(\frac{T}{T_c}\right)^{3/2}. \quad (3.14)$$

As can be seen in Fig. 3.4, the discontinuous slope of the ground state fraction indicates that the Bose-Einstein condensation is a second order phase transition.

3.1.4 3D coherence properties

The condensate has additional interesting properties apart from the macroscopic population of the ground state, for example, its coherence properties. To measure the degree of coherence of a system – such as the coherence of the constituent wave functions – the first order correlation function can be used. If a system is fully coherent, the information at point \mathbf{x} is sufficient to describe the properties of the system at point \mathbf{x}' and vice versa. For a translationally invariant system, all observables only depend on the distance between two points $x = |\mathbf{x} - \mathbf{x}'|$ and the first order correlation function can be retrieved from the momentum distribution by a Fourier transform

$$G_1(\mathbf{x}) = \frac{1}{(2\pi)^3} \int_{-\infty}^{\infty} b(\mathbf{k}) e^{i\mathbf{k}\mathbf{x}} d\mathbf{k}. \quad (3.15)$$

Details on the derivation for a homogeneous system can be found in Extra 7.4 in Chapter 7.

Extra 3.2: Definition of the Fourier Transform

There exist a multitude of conventions to define the Fourier transform. The definition for the Fourier transform used in this thesis is

$$F(\mathbf{k}) = \int_{-\infty}^{+\infty} d^d \mathbf{x} f(\mathbf{x}) e^{-i\mathbf{k}\mathbf{x}}$$

and for the inverse Fourier transform

$$f(\mathbf{x}) = \frac{1}{(2\pi)^d} \int_{-\infty}^{+\infty} d^d \mathbf{k} F(\mathbf{k}) e^{i\mathbf{k}\mathbf{x}},$$

with the dimensionality d .

In the following, $G_1(x)$ is calculated from $n(\mathbf{k})$ to show the appearance of LRO in a three-dimensional BEC.

With Eq. (3.15), the first order correlation function of the infinite homogeneous 3D Bose-Einstein condensate can be calculated via substitution of the free particle dispersion relation into the energy distribution $b(\epsilon(\mathbf{k}))$ given by

$$b(\epsilon(\mathbf{k})) = \frac{1}{e^{\beta(\epsilon(\mathbf{k})-\mu)} - 1}, \quad \text{with} \quad \epsilon(\mathbf{k}) = \frac{\hbar^2 \mathbf{k}^2}{2m}. \quad (3.16)$$

These relations are evaluated readily in the limits of low and high phase-space density, i. e. the non-degenerate and the degenerate limit, respectively.

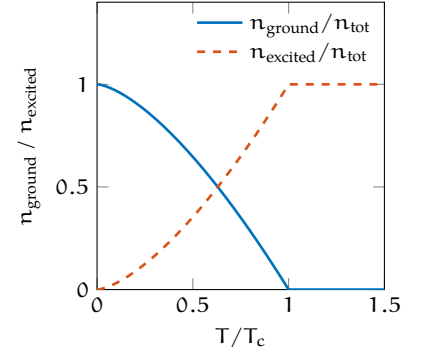


Figure 3.4: Fraction of particles in the ground state $n_{\text{ground}}/n_{\text{tot}}$ (blue) and in the excited states $1 - n_{\text{ground}}/n_{\text{tot}}$ (red, dashed) in dependency of reduced temperature T/T_c , see Eq. (3.14).

NON-DEGENERATE LIMIT

In a non-degenerate gas, the polylogarithm is approximately $\text{Li}_\alpha(z) \approx z$ and thus, Eq. (3.11) yields $z \approx n\lambda_T^3 \ll 1$. In this regime $|\mu| \gg k_B T$ and all momentum states are weakly occupied, hence

$$b(\mathbf{k}) \approx ze^{-\beta\epsilon(\mathbf{k})} \approx n\lambda_T^3 e^{-k^2\lambda_T^2/4\pi} \ll 1. \quad (3.17)$$

Since the Fourier transform of a Gaussian is again a Gaussian, the correlation function $G_1(x)$ reads

$$G_1(x) \approx 2\pi n e^{-\pi x^2/\lambda_T^2}. \quad (3.18)$$

Thus, thermal gases exhibit only short-range correlations which decay on the length scale $\lambda_T/\sqrt{\pi}$.

DEGENERATE LIMIT

In the presence of a condensate, the ground state has to be separated out before replacing the sum over single-particle states with an integral. Due to the divergence of the ground state population $b(\mathbf{k} \rightarrow 0) \approx \delta(\mathbf{k}) \cdot b_0$ the first order correlation function for distances larger than λ_T is then given by³⁸

$$G_1(x) \approx \frac{\langle b_0 \rangle}{V} + \frac{1}{(2\pi)^3} \int_{-\infty}^{\infty} d^3k b(\mathbf{k}) e^{i\mathbf{k}\cdot\mathbf{x}} \quad (3.19)$$

$$\approx \frac{\langle b_0 \rangle}{V} + \frac{m}{\beta 2\hbar^2} \frac{e^{-x/l_c}}{x}, \quad \text{for } x \gg \lambda_T \quad (3.20)$$

with the mean ground state occupation $\langle b_0 \rangle$ and the characteristic decay length $l_c = \hbar/\sqrt{2m|\mu|}$. The second term in Eq. (3.20) vanishes for $x = |\mathbf{x} - \mathbf{x}'| \rightarrow \infty$ but due to the significant occupation of the ground state the first term does not. Hence, in a degenerate infinite ideal 3D Bose gas, the first order correlation function shows a finite degree of coherence for all distances. For such a system, knowledge of point \mathbf{x} enables conclusions about the properties at *any* point \mathbf{x}' . Such systems with finite coherence over infinite distances are said to exhibit **LRO**. Since the influence of dimensionality on the gas is of interest here, this process is now repeated for an ideal two-dimensional Bose system.

³⁸ K. Huang: *Statistical mechanics*, (1987)

3.2 THE IDEAL 2D GAS

This section aims to illustrate the profound change introduced by reducing the dimensionality from 3D to 2D on the example of an ideal gas. To contrast the 3D Bose gas to the 2D case, this section will follow the structure of Section 3.1 in brevity. Where similar, details of the derivation are left to the reader or where appropriate presented in separate boxes denoted *Extra* which can be skipped. It is shown that not only condensation, and hence a true **BEC**, is precluded in 2D but also that the coherence vanishes for any uniform system of finite temperature manifested in the absence of long-range order.

3.2.1 2D Bose-Einstein condensation?

Here, the thermodynamic calculations are reiterated for the two-dimensional case, showing that the difference in the density of states precludes the existence of a macroscopic population of the ground state, i. e. a BEC.

The grand potential function is again the starting point and differentiation with respect to the fugacity z yields the total atom number as

$$N = z \frac{\partial}{\partial z} Q(z, \epsilon, \beta) = \sum_{\nu} \pm d_{\nu} (e^{\epsilon_{\nu} - \mu} \pm 1)^{-1}. \quad (3.21)$$

The Thomas-Fermi approximation is applied and the sum is replaced by an integral, hence the total atom number is given by

$$N = \int_0^{\infty} d\epsilon \frac{\text{DoS}(\epsilon)}{e^{\beta(\epsilon - \mu)} - 1}. \quad (3.22)$$

Extra 3.3: Density of states of a homogeneous system in two dimensions

In two dimensions, the minimal phase-space cell size is quantized to be $(2\pi\hbar)^2$. Let $A = \Delta x \Delta y$ be the real space area a particle occupies and $A_m = \pi p^2$ be the area in momentum space a particle with momentum up to p occupies. As a function of the energy $\epsilon = p^2/2m$ the total number of states can be written as

$$\# \text{ States}(\epsilon) = \frac{A\pi p^2}{(2\pi\hbar)^2} = \frac{Am}{2\pi\hbar^2} \epsilon.$$

From this, the density of states for a homogeneous 2D system can be calculated by taking the derivative with respect to the energy

$$\text{DoS}(\epsilon) = \frac{d}{d\epsilon} \# \text{ States}(\epsilon) = \frac{Am}{2\pi\hbar^2}.$$

Repeating the procedure for the 2D case, see Extra 3.3, the DoS is found to be

$$\text{DoS}(\epsilon) = \frac{Am}{2\pi\hbar^2} = \text{constant with resp. to } \epsilon \quad (3.23)$$

with $A = \Delta x \Delta y$ denoting the real space area the system occupies. Note that in contrast to 3D, the density of states in 2D does not depend on the energy but is constant. Hence, the approximation made in Eq. (3.22) is valid even for low energy states. If this result is inserted into Eq. (3.22) and divided by A it yields the 2D number density

$$n_{2D} = \frac{N}{A} = \frac{m}{2\pi\hbar^2} \int_0^{\infty} d\epsilon \frac{1}{e^{\beta(\epsilon - \mu)} - 1}. \quad (3.24)$$

Again, the solution to this type of integral is the polylogarithm. For $\alpha = 1$, the polylogarithm reduces to the normal logarithm. Thus, it can be written with the help of the thermal de Broglie wavelength $\lambda_T = \sqrt{2\pi\hbar^2\beta/m}$ as

$$n_{2D} = \frac{1}{\lambda_T^2} \text{Li}_1(z) = -\frac{1}{\lambda_T^2} \ln(1 - z). \quad (3.25)$$

Thus, when particles are added to the system, the fugacity increases, i. e. $z \rightarrow 1$.

This result already displays one major difference between 2D and 3D systems. Whereas in 3D the $Li_{3/2}$ in Eq. (3.11) is bounded, the logarithm in Eq. (3.25) diverges at $z = 1$. (See for comparison Extra 3.1). Thus, *all* particles can be accommodated in the excited states. In two dimensions, a valid solution for Eq. (3.25) almost always exists. Only at $T = 0$, there exists no solution and the ground state will have macroscopic population. This shows that due to a different dependence of the density of states on the energy, Bose-Einstein condensation does not occur in the ideal infinite 2D Bose gas. Next, it is explored if the coherence properties also exhibit such a drastic difference.

Extra 3.4: Ground state population in large 2D systems

Unlike the 3D case, it is not necessary to separate out the ground state in Eq. (3.25) under the condition that $2\pi\hbar^2/(Am) \ll |\mu| \ll k_B T$. This box will present a rough outline why this is the case. In the above regime, $b_0 = b(\mathbf{k} = 0) \approx k_B T/|\mu|$ and with $T_{2D} = 2\pi\hbar^2 n_{2D}/mk_B$ the chemical potential can be approximated as

$$|\mu| = \left| k_B T \ln(1 - e^{-T_{2D}/T}) \right| \approx k_B T e^{-T_{2D}/T}.$$

Thus, the ground state population is approximated by $b_0 \approx e^{T_{2D}/T}$. For this to be on the order

of the total number of particles N , the temperature T would have to obey

$$b_0 \approx e^{T_{2D}/T} \stackrel{!}{=} N \Rightarrow T = \frac{T_{2D}}{\ln(N)}.$$

In the thermodynamic limit $N \rightarrow \infty$, $A \rightarrow \infty$ and $N/A = \text{constant}$, hence the necessary temperature will become increasingly small. For finite temperature the ground state is therefore not significantly occupied and Bose-Einstein condensation can not occur in a uniform two-dimensional gas in the limit of a large system.

3.2.2 2D coherence properties

To evaluate the coherence of the two-dimensional system, the first order correlation function is again employed. In analog to Section 3.1.4 it is instructive to treat the degenerate and the non-degenerate limit separately.

NON-DEGENERATE LIMIT

Analogous arguments to those that lead to Eq. (3.17), here $z \approx n_{2D}\lambda_T^2$, lead in the two-dimensional case to

$$b(\mathbf{k}) \approx ze^{-\beta\epsilon(\mathbf{k})} \approx n_{2D}\lambda_T^2 e^{-k^2\lambda_T^2/4\pi} \ll 1 \quad (\forall \mathbf{k}). \quad (3.26)$$

Hence, a fast Gaussian decay of the correlation function on the length scale $\lambda_T/\sqrt{\pi}$ is again expected for the normal regime

$$G_1(x) \approx 2\pi n_{2D} e^{-\pi x^2/\lambda_T^2}. \quad (3.27)$$

DEGENERATE LIMIT

For a gas with $n\lambda_T^2 > 1$, one can see from Eq. (3.25) that $z \approx 1$ and $\beta|\mu| \approx e^{-n\lambda_T^2} \ll 1$. Thus, the phase-space density is approximately

$n\lambda_T^2 \approx \ln(k_B T/|\mu|)$. The occupation of high-energy states in the degenerate gas, with $\beta\epsilon \gg 1$, is small and the occupation is – similar to the case of the non-degenerate gas – approximated by the Boltzmann distribution

$$b(\mathbf{k}) \approx e^{-\beta\epsilon(\mathbf{k})} = e^{-k^2\lambda_T^2/4\pi} \ll 1, \quad \text{for } k^2 \gg 4\pi/\lambda_T^2. \quad (3.28)$$

However, the occupation of the low energy states in the degenerate gas is large and for $\beta\epsilon \ll 1$, $\beta\mu \ll 1$ and $\mu = -|\mu|$ the approximation of the exponential in the denominator of the Bose-Einstein distribution for small argument leads to a Lorentzian

$$\begin{aligned} b(\mathbf{k}) &= (e^{\beta(\epsilon(\mathbf{k})-\mu)} - 1)^{-1} \\ &\approx (1 + \beta(\epsilon(\mathbf{k}) - \mu) - 1)^{-1} \\ &= \frac{k_B T}{\epsilon(\mathbf{k}) + |\mu|} \\ &\approx \frac{4\pi}{\lambda_T} \frac{1}{|\mathbf{k}|^2 + k_c^2} \gg 1, \quad \text{for } |\mathbf{k}|^2 \ll 4\pi/\lambda_T^2, \end{aligned} \quad (3.29)$$

where $k_c = \sqrt{2m|\mu|}/\hbar$ and the energy distribution is $\epsilon(\mathbf{k}) = \frac{\hbar^2|\mathbf{k}|^2}{2m}$. Consequently, the correlation function for the degenerate 2D gas is bimodal. The Fourier transform of the momentum space distribution, $b(\mathbf{k})$ of Eq. (3.29), is proportional to the modified first order Bessel function of the second kind $K_0(k_c x)$. This results in correlations dominated by Gaussian decay for short distances of up to $\approx \lambda_T$ but for larger distances the correlations decay approximately exponential. Thus, similar to the 3D case in Eq. (3.20) the correlation function for large distances is approximately given by

$$G_1(x) \propto \frac{e^{-x/l_c}}{\sqrt{x}}. \quad (3.30)$$

From the definition of the correlation length $l_c \approx \lambda_T e^{n_{2D}\lambda_T^2/2}/\sqrt{4\pi}$, one can immediately see that for increasing phase-space density $n_{2D}\lambda_T^2$, the correlation increases exponentially but the first order correlation function still vanishes in the limit $x \rightarrow \infty$. Hence, the 2D system does not exhibit LRO which has been shown to be true for any uniform two-dimensional system with continuous symmetry by N. Mermin, H. Wagner⁴ and P. Hohenberg³. However, although Eq. (3.30) shows that the correlation function vanishes for $x \rightarrow \infty$, for any finite system the correlation length eventually becomes larger than the system size which has important consequences for real world systems.

⁴ N. D. Mermin and H. Wagner: *Phys. Rev. Lett.*, vol. 17, (1966)

³ P. C. Hohenberg: *Phys. Rev.*, vol. 158, (1967)

Table 3.1: Overview of ideal gas properties for different dimensionality.

	Ideal 3D Gas	Ideal 2D Gas
Condensation	Yes	No
Long Range Order	Yes	No
Superfluidity	No	No

It is obvious that neglecting real world effects such as those introduced by interparticle interaction or an external trapping potential reduces

the mathematical complexity in a theoretical description but unfortunately simultaneously results in rather unexciting coherence properties for the two-dimensional system, which are summarized in Table 3.1.

3.3 INTERACTING TRAPPED 3D BOSE GASES

Since experimentally accessible quantum gases are neither infinite nor ideal the influence of a trapping potential and the interparticle interactions must be taken into account. Most magnetic and optical dipole traps can be reasonably well approximated by a harmonic potential. Thus, harmonic trapping will be considered in the examples. If interactions between particles are introduced, the system becomes much more complex. For strong interactions, the system becomes analytically intractable and thus it is very challenging to develop an adequate theory. For the presented experiment however, the interactions between particles can be treated to first order in a mean field approximation and the condensate wave function $\psi(\mathbf{x})$ obeys the finite temperature *Gross-Pitaevskii equation* (GPE)

$$\left(-\frac{\hbar^2}{2m} \nabla^2 + V(\mathbf{x}) + U(\mathbf{x}) [|\psi(\mathbf{x})|^2 + 2n_T(\mathbf{x})] - \mu \right) \psi(\mathbf{x}) = 0. \quad (3.31)$$

Here, $V(\mathbf{x})$, $U(\mathbf{x})$, μ are the trapping potential, the two-body interaction potential and the chemical potential, respectively. The $n_T(\mathbf{x})$ represents the density of thermal atoms interacting with the condensate. For a cold gas, the dominant interaction is s-wave scattering, as explained in Section 3.3.4. Then, the interaction potential can be replaced by an effective contact interaction potential that reads

$$U(\mathbf{x}) = \frac{4\pi\hbar^2}{m} a_{3D} \delta^3(\mathbf{x}) = g\delta^3(\mathbf{x}), \quad (3.32)$$

with the Dirac delta function δ , the s-wave scattering length a_{3D} and the effective interaction parameter g ³⁹. The derivations presented here have been developed originally for weak interactions $\tilde{g} \ll 1$ but more sophisticated methods⁴⁰ have validated the approach – at least qualitatively – even for the interaction strengths relevant to the experiment presented in this thesis.

The addition of interactions to the system is far reaching, whilst condensation still occurs and the LRO of the order parameter is also preserved, a new property arises: superfluidity. In preparation for the discussion of 2D systems, these properties are briefly reviewed highlighting the phase correlation function g_1 . Note that in 3D the effect of interactions on the coherence at long distances is minor and the onset of superfluidity is still accompanied by condensation and LRO. However, the same cannot be said for 2D systems. Here, interactions have a profound impact on the phase correlations and hence drive the normal to superfluid transition despite the fact that condensation and LRO cease to exist.

³⁹ C. J. Pethick and H. Smith: *Bose-Einstein Condensation in Dilute Gases*, (2008)

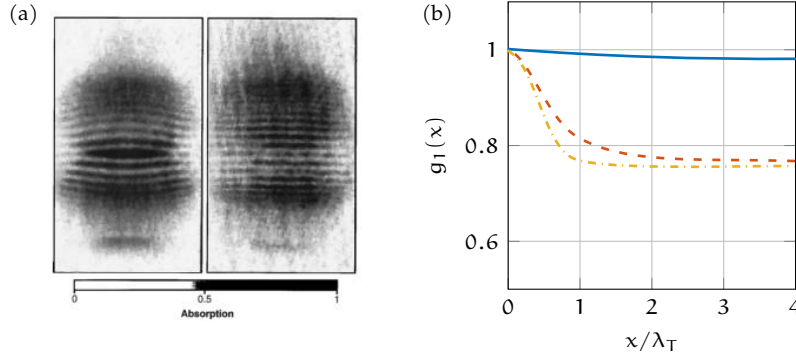
⁴⁰ M. Holzmann et al.: *Phys. Rev. A*, vol. 81, (2010)

3.3.1 Coherence in interacting trapped 3D Bose gases

The first order correlation function $G_1(\mathbf{x}, \mathbf{x}')$ for a trapped system cannot be expressed in terms of the difference $|\mathbf{x} - \mathbf{x}'|$ anymore and acquires a dependence on the position in the trap. To define a local measure of coherence, the normalized first order correlation function

$$g_1(\mathbf{x}, \mathbf{x}') = \frac{G_1(\mathbf{x}, \mathbf{x}')}{\sqrt{G_1(\mathbf{x}, \mathbf{x})}\sqrt{G_1(\mathbf{x}', \mathbf{x}')}} \quad (3.33)$$

is introduced. The most notable property of g_1 is its relation to the achievable contrast in interference experiments. This fact has been used for example by M. Andrews et al.⁴¹ to show that the observation of high-contrast interference fringes is evidence for the spatial coherence of 3D condensates when brought into superposition. Figure 3.5a shows a density image with clear interference, confirmation of a finite g_1 for the size of the condensate. For experiments in interacting trapped Bose gases, the normalized first order correlation function displays no qualitative change in behavior. Similar to the ideal gas, the correlation function decreases for separations larger than the thermal wavelength but much smaller than the total size of the condensate, confer Fig. 3.5b for a theoretical calculation of the decay of g_1 with particle separation. The first order correlation function of interacting 3D condensates approaches the condensate fraction for large relative distances and thus also exhibits LRO.



⁴¹ M. Andrews et al.: *Science*, vol. 275, (1997)

Figure 3.5: (a) The occurrence of interference fringes is direct evidence for spatial coherence i.e. a finite first order correlation function g_1 in the experiment of M. Andrews et al.⁴¹ (b) Theoretical calculation of a volume averaged $\bar{g}_1(x)$ (red dashed) for a degenerate interacting Bose gas as well as the local $g_1(x)$ (blue). Additionally the fast decay of the Maxwell-Boltzmann distributed uncondensed atoms is plotted (yellow, dash dotted). Note the strong decay on the length scale of λ but the finite value of g_1 due to the existence of a Bose-Einstein condensate. Figure a) adapted from M. Andrews⁴¹. Figure b) adapted from M. Naraschewski and R. Glauber⁴².

⁴¹ M. Andrews et al.: *Science*, vol. 275, (1997)

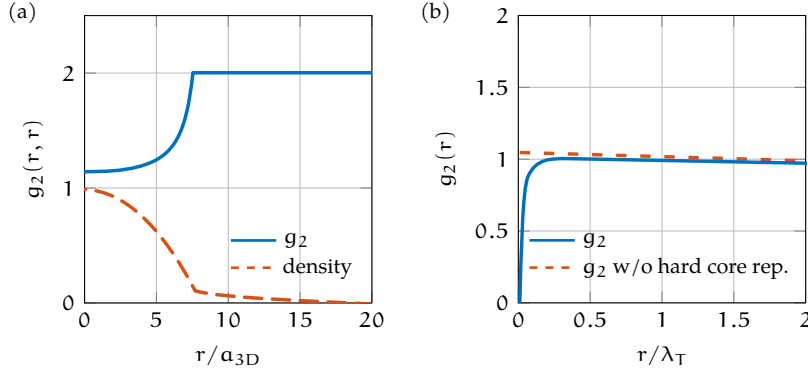
⁴² M. Naraschewski and R. J. Glauber: *Phys. Rev. A*, vol. 59, (1999)

An additional measure applicable to the degree of coherence is the value of the normalized second order correlation function $g_2(\mathbf{x}, \mathbf{x}')$ which will be introduced more rigorously in Chapter 8. Put roughly, this function describes the possibility to find two particles at positions \mathbf{x} and \mathbf{x}' . For bosonic gases, g_2 generally increases with decreasing temperature and thus increasing coherence length ξ_c . This can be used to explain the bosonic bunching from i.e. the familiar Hanbury Brown and Twiss experiment⁴³ or the cold atom analog of the group of A. Aspect⁴⁴. Interestingly, the presence of a coherent condensate – analogous to the coherent state of a laser beam – suppresses the probability of two particles in close vicinity since all atoms are distributed maximally random. Accordingly, g_2 is decreased in the condensate as can be seen in Fig. 3.6a. Additionally, if repulsive interactions are

⁴³ R. Hanbury Brown and R. Q. Twiss: *Nature*, vol. 178, (1956)

⁴⁴ M. Schellekens et al.: *Science*, vol. 310, (2005)

present in the system the mean field calculation of M. Naraschewski and R. Glauber⁴² show a further reduction for very short distances, see Fig. 3.6b. Despite the fact that the hard core repulsion of two atoms is a local effect, the change in the density-density correlation function can be observed over much greater distances. However, the length scales of interest in this work are many times larger than the thermal wavelength and thus the effects of hard core repulsion are ignored.



⁴² M. Naraschewski and R. J. Glauber: *Phys. Rev. A*, vol. 59, (1999)

Figure 3.6: (a) The normalized second-order correlation function is a measure of local second-order coherence. Plotted is g_2 (solid line) for a harmonically trapped interacting gas with temperature $T = 0.8T_c$. For comparison, the red (dashed) curve shows the total density distribution in arbitrary units. (b) Normalized volume integrated second order correlation function for an interacting trapped Bose gas at $T/T_c = 0.5$ (solid line). The dashed line omits the hardcore repulsion. Due to the presence of a considerable condensate fraction, a large degree of second-order coherence is attained i. e. the curve remains close to unity. The existence of quasiparticle excitations leads to a remarkably slow decrease of the correlation function. Figure adapted from M. Naraschewski and R. Glauber⁴².

⁴² M. Naraschewski and R. J. Glauber: *Phys. Rev. A*, vol. 59, (1999)

3.3.2 Condensation of interacting trapped 3D Bose gases

The condensation properties of interacting Bose gases depend subtly on the consequences of the trapping potential. Whereas calculations have shown that a repulsive infinite uniform Bose gas condenses at marginally higher temperature due to a slight increase in local density by *critical fluctuations*^{45,46} the trapped interacting Bose gas behavior shows the contrary⁴⁷. The repulsion reduces the density of the particles in the center of the trap and therefore also the phase-space density. To pass the condensation point at a phase-space density of $n\lambda^3 \approx 2.6124$ lower temperatures have to be achieved. This intuitive result has been quantitatively derived in first order in a_{3D} and reads

$$\frac{T_c - T_c^{\text{ideal}}}{T_c^0} \approx -1.326 \frac{a_{3D}}{l_{\text{osc}}} N^{1/6}, \quad (3.34)$$

with the harmonic oscillator length l_{osc} and the atom number N . The left hand term consists of the critical temperature of the interacting trapped Bose gas T_c of the ideal trapped Bose gas T_c^0 and the temperature of the ideal homogeneous Bose gas T_c^{ideal} . The dominant effect of the trapping potential in comparison to the critical fluctuations has been verified for typical trap frequencies down to $\omega_{\text{trap}}/2\pi \approx 9 \text{ Hz}$ ⁴⁸. Since the increase of the critical temperature due to critical fluctuations in interacting gases is much smaller than the reduction due to the repulsion in inhomogeneous traps, it can usually be neglected.

⁴⁵ G. Baym et al.: *Phys. Rev. Lett.*, vol. 83, (1999), ⁴⁶ S. Pilati et al.: *Phys. Rev. Lett.*, vol. 100, (2008)

⁴⁷ S. Giorgini et al.: *Phys. Rev. A*, vol. 54, (1996)

⁴⁸ F. Gerbier et al.: *Phys. Rev. Lett.*, vol. 92, (2004)

3.3.3 Superfluidity in interacting trapped 3D Bose gases

The introduction of interactions has the most drastic effect on the viscosity of the Bose condensate. The usual Landau criterion³⁴ states that a superfluid with elementary excitation spectrum $\epsilon(\mathbf{k})$ will become unstable against perturbations with velocity \mathbf{v} when $\epsilon(\mathbf{k}) = \mathbf{k} \cdot \mathbf{v}$ and the minimum v_{critical} satisfying this condition is the critical velocity.

$$v_{\text{critical}} = \min \frac{\epsilon(\mathbf{k})}{|\mathbf{k}|}. \quad (3.35)$$

Using the free particle dispersion relation of the ideal gas, $\epsilon = \hbar^2 \mathbf{k}^2 / (2m)$, it is immediately obvious that there exists no energy gap for excitations and thus $v_{\text{crit}} = 0$. The ideal 3D Bose gas is hence not superfluid. However, for an interacting homogeneous condensate near its ground state, the elemental perturbative excitations are described in good approximation by the Bogoliubov dispersion relation

$$\epsilon(\mathbf{k}) = \pm \sqrt{\frac{\hbar^2 |\mathbf{k}|^2}{2m} \left(\frac{\hbar^2 |\mathbf{k}|^2}{2m} + 2gn \right)}. \quad (3.36)$$

Assume energy and momentum conservation of a scattering event with an impurity of mass M

$$\frac{M |\mathbf{v}_{\text{before}}|^2}{2} = \frac{M |\mathbf{v}_{\text{after}}|^2}{2} + \hbar\omega(\mathbf{k}), \quad (3.37)$$

$$M\mathbf{v}_{\text{before}} = \hbar\mathbf{k} + M\mathbf{v}_{\text{after}}, \quad (3.38)$$

with the velocities \mathbf{v}_x before and after the collision. Now, the limit $|\mathbf{k}| \rightarrow 0$ immediately yields a minimal velocity v_{critical} of an impurity to excite the condensate

$$v_{\text{critical}} = \sqrt{\frac{gn}{m}}. \quad (3.39)$$

Here, m and n are the mass and the density of the condensed particles respectively. Any scattering on an impurity below the critical velocity does not excite the condensate, it is thus superfluid. The relation to the interaction parameter g shows the direct dependence of superfluidity on the presence of interactions. Superfluidity has been shown to also occur in trapped gases⁴⁹ in which case this simple derivation of the critical velocity gains a position dependence via $n(x)$ by means of a local-density approximation.

The coherence properties for 3D Bose gases are – apart from the remarkable onset of superfluidity – only changed quantitatively by the introduction of interactions. In contrast, for 2D Bose gases, in addition to the onset of superfluidity, the coherence properties are altered fundamentally which is subject of the following chapter. Since the treatment of the interactions has been presented in terms of the interaction parameter g , it is now discussed how this parameter relates to the microscopic scattering process in ultracold ⁶Li in terms of the scattering length. Additionally, the process of controlling the interactions via a Feshbach resonance is introduced.

³⁴ L. Landau: *Phys. Rev.*, vol. 60, (1941)

⁴⁹ C. Raman et al.: *Phys. Rev. Lett.*, vol. 83, (1999)

3.3.4 Tuning the interactions

The control of interparticle interactions is an exceptional feature of ultracold atom systems, playing a pivotal role in every stage of our experiment, from the efficient evaporative cooling, to the creation of bosonic dimers. To this end, the interaction of the two lowest hyperfine states of ${}^6\text{Li}$ with an external magnetic field, a so called Feshbach resonance, is exploited. Since the general quantum mechanical treatment of scattering is somewhat arduous, only an abbreviated summary of the basic concepts relevant for this work is given, which follows the excellent review J. Dalibard⁵⁰.

The non-degenerate densities of the atomic vapors used in the experiment are extremely dilute with configuration volumes of $n_{3D}\lambda_{dB}^3 \ll 1$, hence it is reasonable to restrict the treatment to binary collisions. Here, two distinguishable particles are assumed in the derivations, in the case of ultracold ${}^6\text{Li}$, for example the two lowest hyperfine states.

Every two-body problem can be reduced to two one-body problems. The center of mass motion turns out to be trivial while the interesting physics are contained in the relative wave function $\Psi_{\mathbf{k}}(\mathbf{r} = \mathbf{r}_1 - \mathbf{r}_2)$ and in the interaction potential $V(\mathbf{r})$. Hence, we seek the solution of the Schrödinger equation

$$\left[\frac{\mathbf{p}^2}{2m_-} + V(\mathbf{r}) \right] \Psi_{\mathbf{k}}(\mathbf{r}) = E_{\mathbf{k}} \Psi_{\mathbf{k}}(\mathbf{r}), \quad (3.40)$$

where $m_- = m/2$ is the reduced mass of the particles of mass m and $E_{\mathbf{k}} = \hbar^2 \mathbf{k}^2 / (2m_-)$. For any radially symmetric potential $V(r)$, far from the scattering center the wave function can be written with $|\mathbf{r}| = r$ and $|\mathbf{k}| = k$ as

$$\Psi_{\mathbf{k}}(\mathbf{r}) \propto \underbrace{e^{i\mathbf{k}\cdot\mathbf{r}}}_{\text{incoming plane wave}} + f(k, \theta) \underbrace{\frac{e^{i\mathbf{k}\cdot\mathbf{r}}}{r}}_{\text{scattered spherical wave}}. \quad (3.41)$$

Here, the scattering amplitude $f(k, \theta)$ describes the probability of scattering for any momentum k and angle θ . Now, the scattering cross section $\sigma(k)$, a value proportional to the probability that a scattering event occurs, can be calculated by integrating over all solid angles Ω

$$\sigma(k) = \int_{\Omega} |f(k, \theta)|^2 d\Omega. \quad (3.42)$$

For central potentials, as is the case here, there is no θ dependence and the incoming and scattered wave functions can be expanded in an angular momentum basis in so called partial waves, one for each angular momentum number $l = 0, 1, 2, 3, \dots$ ⁵²

$$\sigma_l(k) = \frac{4\pi}{k^2} (2l + 1) \sin^2(\delta_k). \quad (3.43)$$

Here, the effect of the potential is to introduce phase shifts δ_k for each partial wave. However, the contribution of higher partial waves is approximately zero since the collisional energies available in an ultracold gas are very low. This is intuitively understood when considering the

⁵⁰ J. Dalibard: *Collisional dynamics of ultra-cold atomic gases*, (1999)

The assumption of dominant binary collisions breaks down with onset of degeneracy, i.e. $n_{3D}\lambda_{dB}^3 > 1$. In degenerate gases, three-body collisions can actually present the dominant scattering channel⁵¹.

⁵¹ E. Burt et al.: *Phys. Rev. Lett.*, vol. 79, (1997)

Note that only a single angle is required since the scattering process is confined to a plane due to the conservation of angular momentum.

⁵² J.J. Sakurai: *Modern Quantum Mechanics, Revised Edition*, (1995)

relative angular momentum $L = \mathbf{p} \cdot \mathbf{d}$ of two particles colliding with an impact parameter d , sketched in Fig. 3.7. In order to scatter, their impact parameter must be less than the range of interaction, given by the van der Waals radius, i. e. $d \lesssim r_{\text{vdW}}$. In order to significantly admix higher partial waves with $l > 0$, an angular momentum of $L \gtrsim \hbar$ is required and hence relative momenta of $p > L/d \approx \hbar/r_{\text{vdW}}$.

The van der Waals radius for ${}^6\text{Li}$ is on the order of 50 \AA and thus the required relative momenta would correspond to temperatures orders of magnitude higher than typically found in ultracold atoms experiments

$$k_{\text{B}}T = \frac{p}{2m} \sim \frac{\hbar^2}{r_{\text{vdW}}^2 2m} \gtrsim 1000 \mu\text{K}. \quad (3.44)$$

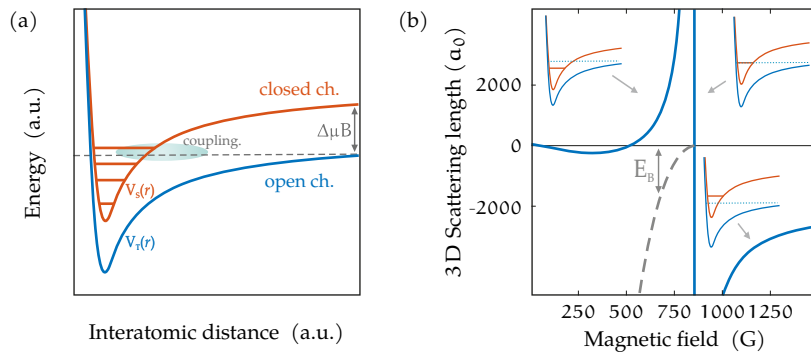
Hence, the scattering in ultracold gases is dominated by the $l = 0$, or *s-wave scattering*. The low energy behavior of the total scattering cross section can now be simplified by realizing that the phase shifts introduced by the scattering potential are directly proportional to k , i. e. $\delta_k \propto k^{2l+1}$ ⁵²

$$\lim_{k \rightarrow 0} \sigma_0(k) = 4\pi a_{3\text{D}}^2. \quad (3.45)$$

Hence, the scattering process can be described by a single number, the *s-wave scattering length* $a_{3\text{D}}$, defined by

$$a_{3\text{D}} = - \lim_{k \rightarrow 0} \frac{\tan(\delta_0(k))}{k}. \quad (3.46)$$

This is the foundation of the introduction of interactions via an effective interaction parameter, used at the start of this section. Where we use the approximation that the scattering is due to a point-like interaction potential $V_{\text{mf}}(\mathbf{r}) = g_{3\text{D}}\delta(\mathbf{r})$ with $g_{3\text{D}} = \frac{4\pi\hbar^2}{m} a_{3\text{D}}$. In alkali atoms, the phase shifts and thus the scattering length can be controlled via the interaction with a magnetic field making use of a Feshbach resonance.



In a Feshbach resonance, two atoms in one spin state are brought into resonance with a molecular bound state in a different spin state. The different magnetic moments μ_B of the spin states enable us to tune their relative energies via an external magnetic field and shift the energetically available *open channel* into resonance with a bound state in the *closed channel* as depicted in Fig. 3.8a. Shifting the bound state energy above or below the free continuum allows us to set the *s-wave*

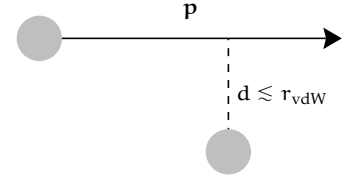


Figure 3.7: Sketch of two atoms colliding, depicting the impact parameter d . For the two atoms to interact, their impact parameter d must be less than their van der Waals interaction radius r_{vdW} . Figure adapted from R. Fletcher⁵³.

⁵³ R. J. Fletcher: *Bose-Einstein Condensation and Superfluidity in Two Dimensions*, (2015)

⁵² J. J. Sakurai: *Modern Quantum Mechanics, Revised Edition*, (1995)

For fermions, the two-body wavefunction must be such that the spatial wave function is anti-symmetric. However, since the *s-wave scattering* solution is symmetric, scattering between two identical fermions is strongly suppressed at low temperatures. Hence, spin-polarized mixtures are non-interacting and spin mixtures must be used in order to tune the interactions.

Figure 3.8: (a) The two-channel model of the Feshbach scattering resonance. Here, the relative Lennard-Jones scattering potential $V(\mathbf{r})$ is sketched for the open and the closed channel. A bound state in the closed channel can be brought into degeneracy with the continuum of the open channel via an external magnetic field acting on the magnetic moments, $\Delta\mu_B$. (b) Scattering length $a_{3\text{D}}$ of the lowest two hyperfine states of ${}^6\text{Li}$ in dependence of an external magnetic field in units of the Bohr radius a_0 . How the bound state in the closed channel is tuned while crossing the resonance is sketched in the insets. At the Feshbach resonance, the scattering length diverges when the bound state is brought into degeneracy and below it a bound state E_B exists, facilitating the association of dimers. Figure adapted from K. Morgener³⁰.

³⁰ K. H. Morgener: *Microscopy of 2D Fermi Gases Exploring excitations and thermodynamics*, (2014)

scattering length to an arbitrary value, described in the proximity of the resonance approximately by

$$a_{3D} \approx a_{bg} \left(1 - \frac{\Delta B}{B - B_0} \right). \quad (3.47)$$

Here, a_{bg} is the off-resonant background scattering length, B_0 the position and ΔB the width of the Feshbach resonance, sketched for ${}^6\text{Li}$ in Fig. 3.8b. Note that these considerations are made under the assumption of a 3D scattering process. This assumption is still valid for most of the 2D systems of ultracold gases since the confinement length scale l_z is typically much larger than the scattering length and hence the scattering itself can be considered three-dimensional. This breaks down however for very large scattering lengths, i. e. when approaching the Feshbach resonance. In any case, it can be illuminating to describe the scattering process strictly two-dimensional since it turns out that even if the microscopic scattering is three-dimensional, many of the asymptotic phenomena are driven by 2D physics.

3.3.5 Effective two-dimensional scattering

The scattering amplitude introduced in the prior section contains the physics of the collision process. If the scattering is considered strictly two-dimensional, the 3D amplitude ($f(k)_{3D}$) has to be replaced by the 2D amplitude ($f(k)_{2D}$)³³ with the 2D scattering length a_{2D}

$$f(k)_{3D} = -\frac{a_{3D}}{1 + ik a_{3D}} \longrightarrow f(k)_{2D} \approx \frac{4\pi}{-\ln k^2 a_{2D}^2 + i\pi}. \quad (3.48)$$

Note that while the 3D amplitude approaches a finite value for vanishing momenta, the 2D amplitude does not. Hence, the scattering process in 2D is in general momentum dependent. If the 2D scattering length is rewritten in terms of the 3D scattering length, the vertical confinement oscillator length l_z , and $\kappa \approx 3.5$

$$a_{2D} = l_z \sqrt{\kappa} e^{-\sqrt{\frac{\pi}{2}} \frac{l_z}{a_{3D}}}, \quad (3.49)$$

a mapping from 3D to 2D is obtained and the 2D scattering amplitude can be written as

$$f(k) \approx \frac{4\pi}{\sqrt{2\pi} \frac{l_z}{a_{3D}} - \ln \kappa k^2 l_z^2 + i\pi}. \quad (3.50)$$

For the presented experiment, the l_z/a_{3D} term in the denominator dominates over the logarithm and imaginary part. Hence, the scattering amplitude is approximately k -independent in a regime far away from the Feshbach resonance and is thus typically written as

$$f(k) \equiv \tilde{g} \approx \sqrt{8\pi} \frac{a_{3D}}{l_z} \quad (3.51)$$

The removal of the confinement in this abstraction allows the description of a real world, i. e. 3D, system in terms of 2D physics. The dimensionless interaction parameter \tilde{g} for example allows a convenient

³³ Z. Hadzibabic and J. Dalibard: *Riv. Nuovo Cimento*, vol. 34, (2011)

comparison of experiments with varying confinement and scattering length but identical 2D low-momentum scattering dynamics. The interaction parameters used in the [GPE](#) above are thus defined as follows

$$g_{3D} = \frac{4\pi\hbar^2}{m} a_{3D} \quad \text{and} \quad g_{2D} = \frac{\hbar^2}{m} \tilde{g}. \quad (3.52)$$

Note that the introduction of the confinement has subtle effects such as the existence of a bound state for all energies. However, these effects are small for the interaction parameters the experiment is performed at. However, the accurate description of an ultracold gas closer to resonance is still an issue under discussion.

4

COHERENCE OF THE TRAPPED INTERACTING QUASI-2D BOSE GAS

- 4.1 Coherence in the interacting 2D Bose gas 37
- 4.2 The KT transition 44

The coherence properties of interacting 2D Bose gases show a significant departure from the ideal gas case. An infinite two-dimensional Bose gas can not undergo Bose-Einstein condensation for any finite temperature. This implies that the first order correlation function always vanishes for distances much larger than the thermal de Broglie wavelength. In 2016, the Nobel Prize in Physics has been awarded to M. Kosterlitz, D. Thouless and D. Haldane for their work involving the coherence properties of interacting two-dimensional Bose gases which exhibit much richer physics compared to the ideal gas approximation. These effects include for example the extension of the criticality to the whole region below the critical point and not only close to it. This critical phase is characterized by a non-vanishing and only slowly decaying first order correlation function $G_1(x) \propto x^{-\eta}$, with the scaling exponent η . Additionally, the transition into this critical region is marked by an unusual – infinite order – phase transition. This *Kosterlitz-Thouless (KT)* transition, named after M. Kosterlitz and D. Thouless, is driven by the creation and unbinding of vortex pairs having opposite rotation.

The phenomena of this unique regime have been theoretically investigated by V. Berezinskii, M. Kosterlitz and D. Thouless and are hence known as BKT-physics. Ultracold gases proved to be a versatile model system to study BKT-physics and the associated phase transition. First investigated in the group of J. Dalibard in 2006/2007^{20,54}. Later, the coherence properties for bosonic gases were studied in the groups W. Phillips in 2009²¹ and Z. Hadzibabic⁵⁵ and for fermionic gases in the group of S. Jochim in 2015²⁶. Additionally, the superfluid properties of bosonic gases have been studied in the groups of J. Dalibard⁵⁶, H. Perrin⁵⁷ and Y. Shin, where vortices have also been observed⁵⁸.

4.1 COHERENCE IN THE INTERACTING 2D BOSE GAS

This work concerns the analysis of two-dimensional Bose gases after time of flight. Examples of the data to be analyzed is given in Fig. 5.5, where the expansion of a single highly oblate cloud of ultracold bosons can be seen. The in situ image (left) does not show

²⁰ Z. Hadzibabic et al.: *Nature*, vol. 441, (2006), ⁵⁴ P. Krüger et al.: *Phys. Rev. Lett.*, vol. 99, (2007)

²¹ P. Cladé et al.: *Phys. Rev. Lett.*, vol. 102, (2009)

⁵⁵ R. J. Fletcher et al.: *Phys. Rev. Lett.*, vol. 114, (2015)

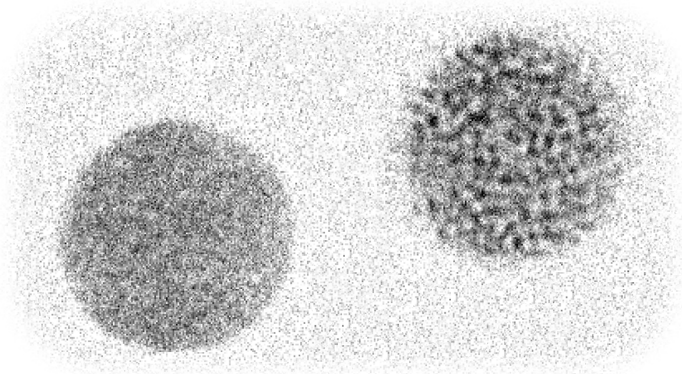
²⁶ P. A. Murthy et al.: *Phys. Rev. Lett.*, vol. 115, (2015)

⁵⁶ R. Desbuquois et al.: *Nature Physics*, vol. 8, (2012)

⁵⁷ C. De Rossi et al.: *New J. Phys.*, vol. 18, (2016)

⁵⁸ J.-Y. Choi et al.: *Phys. Rev. Lett.*, vol. 109, (2012)

any significant density modulations. In contrast, the absorption image taken after a short time of flight (right) shows strong density fluctuations. The result is clearly incompatible with the expansion of a true *Bose-Einstein condensate* (BEC) since the constant phase over the extent of the condensate would not lead to any density modulation. On the other hand, a thermal gas can also be ruled out since the length scale of density fluctuations is incompatible with the de Broglie wavelength λ_T at the given time of flight⁵⁹. As will be shown later, the assumption



⁵⁹ D. E. Miller et al.: *Phys. Rev. A*, vol. 71, (2005)

Figure 4.1: From left to right: In situ density distribution, after 1 ms time of flight. Note the formation of density ripples which have been formed by the transformation of phase excitations into density ripples.

of coherence governed by BKT physics below the transition temperature T_{KT} is in good agreement with the experimental data. A 2D Bose gas has quasi-long-range order, i. e. the phase only decays algebraically $G_1(x) \propto x^{-\eta}$. The scaling exponent η vanishes for $T = 0$ and increases with T towards $\eta = 0.25$. Hence at higher temperatures the coherence decays faster. At the transition point $\eta = 0.25$, the scaling exponent is still small and thus a high degree of phase coherence is sustained also for distances much larger than λ_T .

In a simplified picture one could imagine the 2D condensate as a collection of patches of constant phase i. e. numerous smaller BECs with different but constant phase. Then, expansion during time of flight would lead to constructive and destructive interference where the patches overlap thus creating the observed density modulation.

Absorption images similar to Fig. 5.5 and Fig. 5.5 allow us to extract the scaling exponent η and hence theoretically a measure for the superfluid density n_s . In order to establish the theoretical foundation, the algebraic decay of phase correlations in 2D Bose gases will be introduced. The transformation of phase correlations to density correlations will be dealt with formally in Section 4.1.

THE GOAL OF THE ENSUING DISCOURSE is the formal derivation of the power law scaling of the first order correlation function i. e. $G_1(x) \propto n_0 |\chi/\xi|^{-\eta}$. This derivation will follow the formulation of L. Mathey⁶⁰ based on the theoretical foundation provided by C. Mora and Y. Castin⁶¹ and is inspired by the review of Z. Hadzibabic and J. Dalibard⁶².

The mean field Bogoliubov treatment of a 2D Bose gas is known to fail due to infrared divergences⁶³. These divergences appear since the basic operator of any quantum mechanical study, the density, is

⁶¹ C. Mora and Y. Castin: *Phys. Rev. A*, vol. 67, (2003)

⁶² Z. Hadzibabic et al.: *New J. Phys.*, vol. 10, (2008)

⁶³ J. O. Andersen et al.: *Phys. Rev. Lett.*, vol. 88, (2002)

defined as

$$\hat{n} = \hat{\Psi}(\mathbf{x})^\dagger \hat{\Psi}(\mathbf{x}). \quad (4.1)$$

For the regime of quasi-condensates, a small parameter for perturbation is that the fluctuations of n are only minuscule

$$\frac{\langle \hat{n}(\mathbf{x})^2 \rangle - \langle \hat{n}(\mathbf{x}) \rangle^2}{\langle \hat{n}(\mathbf{x}) \rangle^2} \ll 1. \quad (4.2)$$

To evaluate the expectation value of $\hat{n}(\mathbf{x})^2$ however, the field operators need to be normal ordered and thus a Dirac distribution is introduced at the origin $\delta(0)$

$$\langle \hat{n}(\mathbf{x})^2 \rangle = \delta(0) \hat{n}(\mathbf{r}) + \langle \hat{\Psi}^\dagger \hat{\Psi}^\dagger \hat{\Psi} \hat{\Psi} \rangle. \quad (4.3)$$

Hence, the density fluctuations are infinite for any point with nonvanishing density n . It has been shown by C. Mora and Y. Castin that a self consistent theory is obtained by formulating the Gross-Pitaevskii equation in second quantization on a discretized lattice of length l . Thus turning the Dirac distribution $\delta(0)$ into a Kronecker $\delta_{x,x'}$ and limiting the density variance to a finite value for any dimension d

$$\text{var}[\hat{n}(\mathbf{x})] = \langle \hat{\Psi}^\dagger \hat{\Psi}^\dagger \hat{\Psi} \hat{\Psi} \rangle - \hat{n}(\mathbf{x})^2 + \frac{\hat{n}(\mathbf{x})}{l^d}. \quad (4.4)$$

With this approach, the divergence at $x = 0$ is removed and as it turns out, the limit $x \rightarrow 0$ can even be taken safely.

Therefore, the discretized lattice operators b_i are defined from the field operators $\hat{\psi}(\mathbf{x})$ as

$$\hat{\psi}(\mathbf{x}) \rightarrow \frac{1}{l^{d/2}} b_i. \quad (4.5)$$

Here, l is the discretization length, d the dimension of the system and b_i annihilates a particle at site i . The density is then represented by

$$\hat{\psi}(\mathbf{x})^\dagger \hat{\psi}(\mathbf{x}) \rightarrow \frac{1}{l^d} b_i^\dagger b_i. \quad (4.6)$$

With these replacements, the mean field Hamiltonian for a pure condensate in continuous space

$$\begin{aligned} H = \int d^2x \left(\frac{\hbar^2}{2m} \nabla \hat{\psi}(\mathbf{x}) \nabla \hat{\psi}(\mathbf{x}) \right. \\ \left. + \frac{g}{2} \hat{\psi}(\mathbf{x})^\dagger \hat{\psi}(\mathbf{x})^\dagger \hat{\psi}(\mathbf{x}) \hat{\psi}(\mathbf{x}) \right. \\ \left. - \mu \hat{\psi}(\mathbf{x})^\dagger \hat{\psi}(\mathbf{x}) \right) \end{aligned} \quad (4.7)$$

becomes

$$\begin{aligned} H = -t \sum_{\langle ij \rangle} (b_j^\dagger b_i + b_j b_i^\dagger) \\ + \frac{U}{2} \sum_i b_i^\dagger b_i^\dagger b_i b_i \\ - \mu \sum_i b_i^\dagger b_i. \end{aligned} \quad (4.8)$$

Here, the hopping energy is given by $t = \hbar^2/(2ml^2)$ and the on-site interaction energy by $U = g/l^d$. Additionally, the chemical potential was shifted by a constant via the substitution: $\mu - \hbar^2/(ml^2) \rightarrow \mu$. Investigating the phase of a condensate becomes more accessible in a density-phase representation of the operators. To this end, the lattice operators b_i and b_i^\dagger are separated into a density operator $\sqrt{n_i}$ and an operator A that is connected to the phase of the wave functions, as will become evident later

$$b_i = A_i \sqrt{n_i} \quad (4.9)$$

$$b_i^\dagger = \sqrt{n_i} A_i^\dagger. \quad (4.10)$$

The b_i have to satisfy the usual commutation relations of bosonic ladder operators and thus operate on the Fock states $|n\rangle_i$ with particle number n at lattice point i as

$$b_i |n\rangle_i = \sqrt{n} |n-1\rangle_i \quad (4.11)$$

$$b_i^\dagger |n\rangle_i = \sqrt{n+1} |n+1\rangle_i. \quad (4.12)$$

If one inserts the above replacements into Eq. (4.6) and recognizes that the action of the $\sqrt{n_i}$ operator is $\sqrt{n_i} |n\rangle_i = \sqrt{n} |n\rangle_i$, then a short calculation reveals that A_i acts on the number states as

$$A_i |n\rangle_i = (1 - \delta_{n,0}) |n-1\rangle_i. \quad (4.13)$$

Together with an analogous relation for A_i^\dagger this leads to the exact relations

$$A_i A_i^\dagger = \mathbb{1}, \quad A_i^\dagger A_i = \mathbb{1} - |0\rangle_i \langle 0|, \quad [A_i, A_i^\dagger] = |0\rangle_i \langle 0|, \quad (4.14)$$

where $\mathbb{1}$ is the identity operator and $|0\rangle_i \langle 0|$ represents the projection onto the vacuum state at lattice point i . As is immediately obvious from the second term in Eq. (4.14), the operator A_i is not Hermitian. An approximation must be made since any observable must be Hermitian and the commutation relation $[n_i, \theta_i] = i/l^d$ of the phase operator θ_i and the density n_i must be satisfied as well. A Hermitian operator is obtained if the states $|0\rangle_i$ do not contribute to the behavior of the system and the projection is thus zero. This is the case for any density fluctuation δn which is small compared to the mean density itself, i. e. $\langle \delta n_i^2 \rangle \ll \langle n_i \rangle^2$. A simple phase operator that obeys the required conditions in good approximation can be defined by $A_i = e^{i\theta_i}$ and $A_i^\dagger = e^{-i\theta_i}$.

Next, we expand the density operator around the square root of its expectation value n_0 , i. e. $n_i = n_0 + \delta n_i$ and expand the Hamiltonian to second order in both the phase and density fluctuations. The calculation is presented in detail in⁶¹ and the result reads

$$H \approx \sum_{\langle ij \rangle} \left(t n_0 (\theta_i - \theta_j)^2 + \frac{t}{4n_0} (\delta n_i - \delta n_j)^2 \right) + \sum_i \frac{U}{2} \delta n_i^2. \quad (4.15)$$

⁶¹ C. Mora and Y. Castin: *Phys. Rev. A*, vol. 67, (2003)

To diagonalize the Hamiltonian, the phase and density operators are replaced by their Fourier transforms normalized to the number of condensed atoms N_0

$$\theta_i = \frac{1}{\sqrt{N_0}} \sum_{\mathbf{k}} e^{i\mathbf{k}\cdot\mathbf{x}_i} \theta_{\mathbf{k}} \quad (4.16)$$

$$\delta n_i = \frac{1}{\sqrt{N_0}} \sum_{\mathbf{k}} e^{i\mathbf{k}\cdot\mathbf{x}_i} \delta n_{\mathbf{k}}. \quad (4.17)$$

With these replacements, the second order Hamiltonian, Eq. (4.15), now reads

$$H = \sum_{\mathbf{k}} \left(n_0 \epsilon_{\mathbf{k}} \theta_{\mathbf{k}}^\dagger \theta_{\mathbf{k}} + \frac{\epsilon_{\mathbf{k}}}{4n_0} \delta n_{\mathbf{k}}^\dagger \delta n_{\mathbf{k}} + \frac{U}{2} \delta n_{\mathbf{k}}^\dagger \delta n_{\mathbf{k}} \right) \quad (4.18)$$

A Bogoliubov-style transformation of the phase and density fluctuation operators using the Fourier transform of the lattice operators $b_i = 1/\sqrt{N_0} \sum_{\mathbf{k}} e^{i\mathbf{k}\cdot\mathbf{x}_i} b_{\mathbf{k}}$

$$\delta n_{\mathbf{k}} = \sqrt{n_0} (u_{\mathbf{k}} + v_{\mathbf{k}}) (b_{\mathbf{k}} + b_{-\mathbf{k}}^\dagger) \quad (4.19)$$

$$\theta_{\mathbf{k}} = \frac{1}{2i\sqrt{n_0}} (u_{\mathbf{k}} - v_{\mathbf{k}}) (b_{\mathbf{k}} - b_{-\mathbf{k}}^\dagger) \quad (4.20)$$

and the usual quasiparticle excitation relations

$$u_{\mathbf{k}}^2 = \frac{\hbar\omega_{\mathbf{k}} + \frac{\hbar^2\mathbf{k}^2}{2m} + gn}{2\hbar\omega_{\mathbf{k}}} \quad (4.21)$$

$$v_{\mathbf{k}}^2 = \frac{-\hbar\omega_{\mathbf{k}} + \frac{\hbar^2\mathbf{k}^2}{2m} + gn}{2\hbar\omega_{\mathbf{k}}} \quad (4.22)$$

$$v_{\mathbf{k}} u_{\mathbf{k}} = -\frac{V_{\mathbf{k}} n}{2\hbar\omega_{\mathbf{k}}} \quad (4.23)$$

results in the diagonal Hamiltonian

$$H = \sum_{\mathbf{k}} \hbar\omega_{\mathbf{k}} b_{\mathbf{k}}^\dagger b_{\mathbf{k}} + \text{constant}, \quad (4.24)$$

where $\hbar\omega_{\mathbf{k}}$ is the dispersion relation

$$\hbar\omega_{\mathbf{k}} = \left[\frac{\hbar^2\mathbf{k}^2}{2m} \left(\frac{\hbar^2\mathbf{k}^2}{2m} + 2V_{\mathbf{k}} n \right) \right]^{1/2}. \quad (4.25)$$

The formulation in a density-phase notation of the lattice operators reduces the complexity of the evaluation of the first order correlation function of a homogeneous system significantly. Now, G_1 can be written as

$$G_1(\mathbf{x}_i) \equiv \langle \hat{\psi}^\dagger(\mathbf{x}) \hat{\psi}(0) \rangle \approx \frac{1}{\mathcal{V}^d} \langle b_i^\dagger b_0 \rangle \approx \frac{n_0}{\mathcal{V}^d} \langle e^{-i\theta_i} e^{i\theta_0} \rangle. \quad (4.26)$$

Using the moment generating function of any independent Gaussian distributed random variable, confer Extra 4.1, the evaluation of the expectation value in Eq. (4.26) can be pulled into the exponential and

The approximately equal sign " \approx " for the second order approximated Hamiltonian will from now on be replaced by the equal "=" symbol for clarity.

thus the first order correlation function at distance i from the origin is simplified to

$$G_1(i) \propto e^{-\langle(\theta_i - \theta_0)^2\rangle/2}. \quad (4.27)$$

From this, it becomes obvious that the difficulty in evaluating the first order correlation function is reduced to evaluating the following expression

$$\langle(\theta_i - \theta_0)^2\rangle = \langle(\theta_0 - \theta_i)(\theta_0 - \theta_i)\rangle. \quad (4.28)$$

Extra 4.1: Expected value of the exponential of a normally distributed random variable

Let X be a normally distributed random variable with mean μ and variance σ^2 . Then, the expected value of its exponential or its moment generating function is

$$\langle e^X \rangle = \int_{-\infty}^{+\infty} dx e^x \cdot \frac{1}{\sqrt{2\pi\sigma^2}} e^{-(x-\mu)^2/(2\sigma^2)}.$$

Completion of the square in the exponential yields

$$\langle e^X \rangle = \frac{1}{\sqrt{2\pi\sigma^2}} \int_{-\infty}^{+\infty} dx e^{-\frac{1}{2\sigma^2}(x-(\sigma^2+\mu))^2 + \frac{\sigma^2}{2} + \mu}.$$

Here, the exponential containing the mean and variance can be pulled out of the integral. The remaining integral can be rewritten as an integral

over a standard probability density which is normalized to be equal to unity

$$\langle e^X \rangle = e^{\mu + \frac{\sigma^2}{2}} \cdot \underbrace{\frac{1}{\sqrt{2\pi\sigma^2}} \int_{-\infty}^{+\infty} dx e^{-\frac{1}{2\sigma^2}(x-(\sigma^2+\mu))^2}}_{=1}.$$

Since for any quantum mechanical operator the variance σ^2 is calculated as⁶⁴

$$\text{Var}(\hat{O}) = \langle \hat{O}^2 \rangle - \underbrace{\langle \hat{O} \rangle^2}_{\mu} = \sigma^2,$$

it becomes obvious that for any independent operator \hat{u} of mean $\mu = 0$ and Gaussian distribution, e. g. the phase operator θ_i , the following expression is true

$$\langle e^{i\hat{u}} \rangle = e^{-\frac{1}{2}\langle \hat{u}^2 \rangle}.$$

This problem is most easily solved in momentum space. Hence, a replacement of the phase operators by their Fourier transform

$$\theta_i = 1/\sqrt{N_0} \sum_{\mathbf{k}} e^{i\mathbf{k}x_i} \theta_{\mathbf{k}} \quad (4.29)$$

and

$$\theta_0 = 1/\sqrt{N_0} \sum_{\mathbf{k}} e^{i\mathbf{k}\cdot 0} \theta_{\mathbf{k}} = 1/\sqrt{N_0} \sum_{\mathbf{k}} \theta_{\mathbf{k}} \quad (4.30)$$

results in

$$\begin{aligned} \langle(\theta_i - \theta_0)^2\rangle &= \langle(\theta_0 - \theta_i)(\theta_0 - \theta_i)\rangle \\ &= \left\langle \frac{1}{N_0} \left(\sum_{\mathbf{k}} \theta_{\mathbf{k}} - \sum_{\mathbf{k}} e^{i\mathbf{k}x_i} \theta_{\mathbf{k}} \right) \left(\sum_{\mathbf{k}'} \theta_{\mathbf{k}'} - \sum_{\mathbf{k}'} e^{i\mathbf{k}'x_i} \theta_{\mathbf{k}'} \right) \right\rangle \\ &= \left\langle \frac{1}{N_0} \sum_{\mathbf{k}} (1 - e^{i\mathbf{k}x_i}) \theta_{\mathbf{k}} \sum_{\mathbf{k}'} (1 - e^{i\mathbf{k}'x_i}) \theta_{\mathbf{k}'} \right\rangle. \end{aligned} \quad (4.31)$$

To simplify the notation even further, Eq. (4.31) can be written as a double sum over \mathbf{k} and \mathbf{k}'

$$\langle(\theta_i - \theta_0)^2\rangle = \frac{1}{N_0} \sum_{\mathbf{k}, \mathbf{k}'} (1 - e^{i\mathbf{k}x_i}) (1 - e^{i\mathbf{k}'x_i}) \langle \theta_{\mathbf{k}} \theta_{\mathbf{k}'} \rangle. \quad (4.32)$$

⁶⁴ M. G. Bulmer: *Principles of Statistics*, (2012)

Here, moving the expectation value $\langle * \rangle$ around the operators is allowed by the monotone convergence theorem by B. Levi, which allows the exchange of summation and integration for any non-negative infinite series.

The next step is the evaluation of the expectation value of the phase operators, $\langle \theta_{\mathbf{k}} \theta_{\mathbf{k}'} \rangle$. As before, a transformation to the Bogoliubov basis $\theta = \frac{1}{2i\sqrt{n_0}}(u_{\mathbf{k}} - v_{\mathbf{k}})(b_{\mathbf{k}} - b_{-\mathbf{k}}^\dagger)$ simplifies the expression and enables easier computation. The expectation value of the phase operators in momentum space is thus written as

$$\langle \theta_{\mathbf{k}} \theta_{\mathbf{k}'} \rangle = \frac{-1}{4n_0}(u_{\mathbf{k}} - v_{\mathbf{k}})(u_{\mathbf{k}'} - v_{\mathbf{k}'})\langle (b_{\mathbf{k}} - b_{-\mathbf{k}}^\dagger)(b_{\mathbf{k}'} - b_{-\mathbf{k}'}^\dagger) \rangle. \quad (4.33)$$

The term consisting of the lattice operators $b_{\mathbf{k}}$ can be further simplified by expansion, subsequent reordering and the use of the bosonic commutation relations to

$$\langle (b_{\mathbf{k}} - b_{-\mathbf{k}}^\dagger)(b_{\mathbf{k}'} - b_{-\mathbf{k}'}^\dagger) \rangle = -\delta_{\mathbf{k}, -\mathbf{k}'}(2n_{\mathbf{k}} + 1). \quad (4.34)$$

Here, $b_{\mathbf{k}}^\dagger b_{\mathbf{k}} = n_{\mathbf{k}}$ represents the momentum distribution. If Eq. (4.34) is inserted into Eq. (4.33) and the Kronecker delta is evaluated, the sum of exponentials yields a cosine term which results in

$$\langle (\theta_i - \theta_0)^2 \rangle = \frac{1}{N_0} \sum_{\mathbf{k}} \frac{1}{2n_0} (1 - \cos(\mathbf{k}\mathbf{x}))(u_{\mathbf{k}} - v_{\mathbf{k}})^2 (2n_{\mathbf{k}} + 1). \quad (4.35)$$

Since the above expression is true for any dimension, we transform the discrete sum over \mathbf{k} into an integral $\sum_{\mathbf{k}} \rightarrow \left(\frac{1}{2\pi}\right)^2 \int d^2\mathbf{k}$ and approximate the terms on the right hand. For non-zero temperature and weak interaction energy, i. e. $k_B T > gn$, the momentum distribution can be approximated by $n_{\mathbf{k}} \approx k_B T / (\hbar\omega_{\mathbf{k}})$ and for small momenta the relation $(u_{\mathbf{k}} - v_{\mathbf{k}})^2 \approx \sqrt{2}/(\xi|\mathbf{k}|)$ holds. Hence, the expectation value of the phase operators can be written as

$$\langle (\theta_i - \theta_0)^2 \rangle = \frac{1}{\rho_0} \frac{2mk_B T}{\hbar^2} \frac{1}{(2\pi)^2} \int_{-k_{\max}}^{k_{\max}} d^2\mathbf{k} \frac{(1 - \cos(\mathbf{k}\mathbf{x}))}{k^2} \quad (4.36)$$

$$\approx \frac{1}{\rho_0} \frac{mk_B T}{\hbar^2} \frac{1}{\pi} \ln(k_{\max}x) \quad (4.37)$$

Here, we introduced a short-range cut-off $k_{\max} \approx 1/\xi$ and the real space density $\rho_0 = n_0/l^d$. The logarithmic dependence can be seen intuitively, since the integral has only significant contributions from excitations with $|\mathbf{k}| > 1/|\mathbf{x}|$, thus we can approximate $1 - \cos(\mathbf{k} \cdot \mathbf{x}) \approx 1$. Inserting Eq. (4.36) into Eq. (4.26) yields the desired single particle first order correlation function

$$G_1(|\mathbf{x}|) \propto \rho_0 (k_{\max}|\mathbf{x}|)^{-\eta}. \quad (4.38)$$

The result is a formula that does not depend on the discretization length l and as such the limit $l \rightarrow 0$ can be made safely without divergences. From Eq. (4.38) it is immediately clear that the phase correlations of an interacting 2D Bose gas at low temperatures decay

The exact relation $\nabla^2 \int d^2\mathbf{k} (1 - \cos(\mathbf{k} \cdot \mathbf{x})) \mathbf{k}^{-2} = (2\pi)^2 \delta(\mathbf{x})$ lets us infer the logarithmic dependency.

The expression $\rho = n/l$ does not diverge since both n as well as l approach zero in the thermodynamic limit.

much slower than exponential at large distances. This is not inconsistent with the Mermin-Wagner theorem since the correlations vanish for extremely large distances $|x| \rightarrow \infty$. In the degenerate case, however, the exponent in Eq. (4.38) is never greater than $1/4$ and therefore the decay is extremely slow and a significant degree of coherence remains. Hence, this state is, as Y. Kagan, B. Svistunov and G. Shlyapnikov⁶⁵ describe it, a quasi-condensate, i. e. a condensate with fluctuating phase. See for example Fig. 4.2 for a graphic representation of the algebraic decay compared to the case of a true Bose-Einstein condensate with constant phase and a thermal gas with exponential decay. Interestingly, although the algebraic decay of G_1 is a defining characteristic of the interacting 2D Bose gas and the change in functional form from algebraic to exponential decay is the defining feature of the KT transition of a 2D Bose gas, the above derivations does not elucidate the source of the phase transition at all. The conditions for validity of the discrete model require only variations of the phase between two neighboring points to be small. As it turns out, this precludes the existence of vortices, the driving force behind the KT transition.

4.2 THE KT TRANSITION

We explicitly assumed small density fluctuations $\langle \delta n^2 \rangle \ll \langle n \rangle^2$ and a slowly varying phase gradient $\nabla\theta \ll 1$ to reach the approximation of the Hamiltonian in Eq. (4.15). By doing so, phononic excitations were included but not vortex excitations which exhibit a phase jump across the vortex core and a vanishing density at the vortex core. This section will describe the concept of a vortex and vortex pairs in a 2D bosonic condensate and how the creation and unbinding of these vortex pairs is responsible for the unusual phase transition in 2D Bose gases.

Since a full thermodynamic description of the role of vortices in 2D gases is rather involved, a more intuitive picture is presented in order to illustrate how vortices drive the KT transition. To this end, we will estimate the Helmholtz free energy of a single vortex in a condensate. The sign of the free energy enables us to reason if a vortex excitation is energetically possible, i. e. if energy is gained or lost when creating a free vortex. The free energy is defined as $F = U - TS$, where U is the total internal energy and T and S are the temperature and entropy, respectively. The temperature is a parameter and hence the internal energy and the entropy need to be obtained. For a weakly interacting gas, the internal energy is reasonably well approximated by the kinetic energy $U \approx E_{\text{kin}} = \frac{m}{2}v^2$. Thus, we require the velocity v which is defined via the phase gradient

$$\mathbf{v} = \frac{\hbar}{m}\nabla\theta. \quad (4.39)$$

For any well behaved, i. e. continuously twice-differentiable, scalar field Φ , it is true that $\nabla \times \nabla\Phi = 0$. Thus, it is implied that the velocity field must be curlless

$$\nabla \times \mathbf{v} = 0. \quad (4.40)$$

⁶⁵ Y. Kagan et al.: *J. Exp. Theor. Phys.*, vol. 66, (1987)

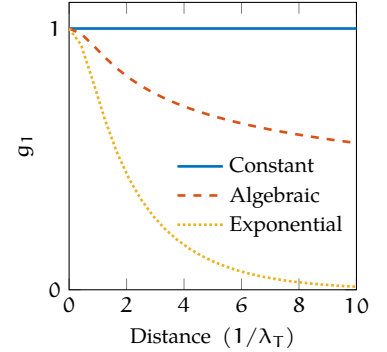


Figure 4.2: The phase correlation function g_1 for constant phase (blue) compared to algebraic (red, dashed) and exponential (yellow, dotted) decay. Note the relatively slow decay and finite value at distances of many λ_T for the algebraic decay. Here, a short-range cut-off was introduced into the algebraic decay, confer Chapter 8.

However, if the gas contains points of vanishing density, the phase is not necessarily well behaved and it is possible for the phase to wind around that density defect in multiples of 2π with

$$\Delta\theta = \oint ds \cdot \nabla\theta = 2\pi l_{\text{wind}}, \quad (4.41)$$

where the winding number l_{wind} counts the number of turns. Without loss of generality, a circular system of size R is assumed, which will tend towards infinity later on. Then, the kinetic energy of a free vortex, i. e. a condensate that is described by the ansatz $\psi = \sqrt{n}e^{il_{\text{wind}}\varphi}$ with density n and azimuthal coordinate φ , is given by the *Gross-Pitaevskii equation* (GPE) in cylindrical coordinates

$$E = \int_0^Z dz \int_0^R 2\pi r dr \left(\frac{\hbar^2}{2m} \left(\frac{d\sqrt{n}}{dr} \right)^2 + \frac{\hbar^2 l_{\text{wind}}^2}{2mr^2} \sqrt{n}^2 + \frac{g}{2} \sqrt{n}^4 \right). \quad (4.42)$$

Here, integration over the z direction is readily performed and since the second term in the integrand dominates, the remaining terms will be discarded. A common estimate of the radial integration is based on the fact that the vortex under consideration has vanishing density n at $r = 0$ and for distances on the order of the healing length, the density has approached the bulk value of the superfluid density $n(r = \xi) \approx n_s$. Thus, the integral is considerably simplified by approximating the density n_s as constant over the interval $[\xi, R)$ and omitting the first and third term

$$E \approx Z \int_{\xi}^R 2\pi r dr \frac{\hbar^2 l_{\text{wind}}^2}{2mr^2} n_s = Z \frac{\pi \hbar^2 n_s l_{\text{wind}}^2}{m} \ln \left(\frac{R}{\xi} \right). \quad (4.43)$$

From this, it is apparent that the energy of a free vortex diverges logarithmically with the system size R . Note that it is assumed that only the superfluid component rotates under the phase gradient of the vortex which is reasonable since the normal component does not have any phase stiffness and is thus not affected directly by the presence of a vortex.

Since the goal is to compute the free energy $F \approx E_{\text{kin}} - TS$ of a vortex, with the internal energy E_{kin} which we have calculated above, the remaining step is to estimate the entropy S .

The number of possible states a single vortex of size $\pi\xi^2$ can occupy in a system of size πR^2 is approximately given by the ratio $\frac{\pi R^2}{\pi\xi^2}$. Thus, the entropy of a single vortex can be estimated as

$$S = k_B \ln \left(\frac{\pi R^2}{\pi\xi^2} \right) = 2k_B \ln \left(\frac{R}{\xi} \right). \quad (4.44)$$

The combination of Eq. (4.43) and Eq. (4.44) for a system size of $Z = 1$ leads to the free energy associated with one singly charged free vortex,

i. e. $l_{\text{wind}} = 1$

$$\frac{F}{k_B T} = \frac{E}{k_B T} - S \quad (4.45)$$

$$= \rho_s \frac{\pi \hbar^2}{m k_B T} \ln \left(\frac{R}{\xi} \right) - 2k_B \ln \left(\frac{R}{\xi} \right) \quad (4.46)$$

$$= \frac{1}{2} (\rho_s \lambda_T^2 - 4) \ln \left(\frac{R}{\xi} \right) \quad (4.47)$$

From Eq. (4.47), it is clear that the free energy associated with the creation of a free vortex changes sign at $\rho_s \lambda_T^2 = 4$. Since the logarithmic term diverges for large system size, this indicates two strongly contrasting regimes. If the phase-space density is greater than 4, i. e. $\rho_s \lambda_T^2 > 4$, the free energy is large and positive. Thus, the creation of a free vortex is strongly suppressed and the system is stable against vortex excitations. If $\rho_s \lambda_T^2 < 4$ instead, the free energy is large and negative. Hence, the system becomes unstable against excitations of a free vortex since the appearance of a free vortex reduces ρ_s and thus increases the possibility for the creation of additional free vortices even further. Via this runaway process, the condensate density will be ultimately reduced to zero. That means, in contrast to 3D, there cannot exist a 2D condensate with densities between 0 and $4/\lambda_T^2$. This fact is referred to as the *superfluid jump* or *universal jump*. This remarkably

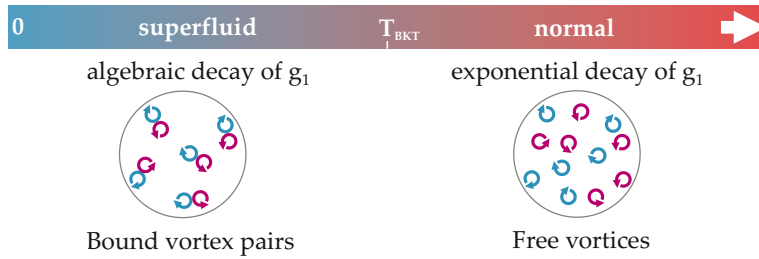
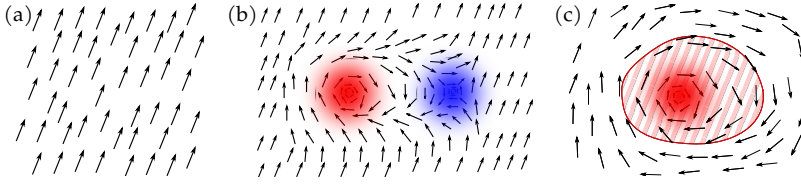


Figure 4.3: Sketch of the proliferation of free vortices when crossing the KT transition. For $T < T_{\text{KT}}$, a superfluid phase exists where vortices only exist in bound pairs, hence not disturbing the phase globally. With quasi-long-range order maintained, the correlations decay only algebraically. When $T > T_{\text{KT}}$, free vortices proliferate which destroy phase correlations even for small distances, hence the first order correlation function g_1 decays exponentially.

simple estimate based on a self consistency argument accurately predicts the phase-space density at the transition temperature T_{KT} . Unfortunately, the direct calculation of T_{KT} itself is more involved since it depends on the exact nature of the short-range physics. Also, the presented argument does not capture the microscopic reason for the proliferation of a free vortex. At any non zero temperature, pairs of tightly bound vortices with opposite rotation are continuously excited and annihilated, sketched on the left side of Fig. 4.3. As the energy of a vortex pair is finite and its entropy in this regime is still divergent, the free energy of vortex pairs is always negative and the system is stable. As the temperature is increased, the number as well as the size of the vortex pairs increases. When the pair size becomes comparable to the distance between pairs, the vortices effectively screen the attractive interaction within a vortex pair and thus increase the size of the vortex pair even further. As T_{KT} is approached from below, this leads eventually to the break up of the vortex pairs and results in a plasma of free vortices destroying even quasi-long-range order and with it superfluidity, sketched on the right side of Fig. 4.3.



One remarkable feature of this transition is precisely the absence of any significant thermodynamic features at the critical point. Since it is of infinite order, no sudden change in thermodynamic properties occurs. Only the decay of phase correlations changes its functional form. This is the reason why this kind of transition is called a *topological* phase transition, illustrated in Fig. 4.4. In this context, it is related to the fact that as long as the phase of the condensate can be described *locally* by a suitable order parameter which varies smoothly over the extent of the condensate it is topologically identical to the Bose-Einstein condensate with *long-range order* (LRO). Long wavelength phonons which destroy LRO do not alter the topology of the system. Whereas a free vortex affects the phase globally in the integration along any path through the condensate and thus cannot be unwound. This state, which includes free vortices, is topologically different from a BEC and thus not superfluid. Interestingly, the onset of superfluidity is not associated with the phenomenon of condensation, as is the case in 3D, but with the sudden change of phase topology.

More extensive treatments of the vortex dynamics at the KT phase transition – first analytically by D. Fisher et al.⁶⁷ for ultra weak interactions and later on by N. Prokof'ev et al.^{68,69} using Monte Carlo simulations – led to the numerical solution of the critical phase-space density D_c at the transition point given by

$$D_c = (n_{\text{total}} \lambda_T^2)_c = \ln \left(\frac{380 \pm 3}{\tilde{g}} \right), \quad (4.48)$$

where $g_{2D} = \hbar^2/m\tilde{g}$ denotes the effective long-wavelength interaction parameter. This result is formally only valid for the weak coupling limit, $\tilde{g} \ll 1$. Nevertheless, it is also a very good approximation for stronger interactions²⁶ almost up to the naive limit of the breakdown of Eq. (4.48) at $D_c > 4$ which would suggest a valid regime for the above expression for interaction parameters of $\tilde{g} \lesssim 7$. Thus, with the help of Eq. (4.48) it is possible to estimate the transition temperature for a given total density and interaction. The main differences highlighted in the prior chapters are presented in Table 4.1, which show the much richer physics of the interacting 2D system compared to its ideal or 3D counterparts.

	Interacting 3D Gas	Interacting 2D Gas
Condensation	Yes	If trapped
Long Range Order	Yes	Quasi
Superfluidity	Yes	Yes

Figure 4.4: Illustration how the proliferation of vortices alters the phase of the quasi-condensate. Here, the phase is represented by arrows. (a) When no vortices are present, the phase is ordered and only minor deviations occur. Note that the arrows on the edge are aligned, i. e. no circular path can be found that follows the orientation of the arrows. (b) A vortex (red) and antivortex (blue) pair does not destroy the arrows alignment globally. Despite the rotation in the close vicinity, a path enclosing the pair cannot be found by following the orientation of the arrows. Hence, the phase canvas is only disturbed locally, quasi-long-range order is maintained. (c) A single free vortex alters the phase canvas globally, when traversing a closed path around the core, a phase of 2π will be picked up. At the vortex core, the arrows must point either into (or out of) the page, hence changing the topology of the phase canvas due to the presence of a "hole". Figure is adapted from⁶⁶.

⁶⁶ A. J. Beekman: *Vortex duality in higher dimensions*, (2011)

⁶⁷ D. S. Fisher and P. C. Hohenberg: *Phys. Rev. B*, vol. 37, (1988)

⁶⁸ N. Prokof'ev et al.: *Phys. Rev. Lett.*, vol. 87, (2001), ⁶⁹ N. Prokof'ev and B. Svistunov: *Phys. Rev. A*, vol. 66, (2002)

²⁶ P. A. Murthy et al.: *Phys. Rev. Lett.*, vol. 115, (2015)

Table 4.1: Overview of interacting gas properties for different dimensionality.

5

EXPERIMENTAL CONTEXT

- 5.1 Superfluidity in two dimensions 49
- 5.2 Coherence measurements on single layers 53
- 5.3 Quantitative theoretical analysis of the interference pattern after ToF 55

5.1 SUPERFLUIDITY IN TWO DIMENSIONS

The unusual phenomena of two-dimensional superfluid systems of bosons, or fermions, have been the focus of scientists even before direct optical access to single layers of particles has been possible. Thus, a short overview of relevant studies on two dimensional systems will be given in addition to an excerpt of the work in the context of this thesis. First, the early experimental studies of the KT type phase transition on 2D layers of superfluid bosons, in this case a film of liquid ^4He , are presented. Then, the pioneering work on 2D Bose gases in the field of ultracold atoms will be introduced. A short presentation of the studies of coherence and superfluidity in 2D systems of ultracold atoms follows, separated into the experiments concerning bosons and those regarding fermions. Subsequently, the theoretical framework for the analysis of the phenomena observed during this work will be introduced.

SUPERFLUIDITY IN 2D HELIUM FILMS

Already in 1978, D. Bishop and J. Reppy showed in an impressive experiment on a film of superfluid ^4He adsorbed on a torsional oscillator that there exists a “fundamental difference between the onset phenomena in two- and three-dimensional superfluids”¹. This supplies strong support for the validity of the Kosterlitz-Thouless picture of the nature of the phase transition. In their experiment, a thin film of ^4He is adsorbed on a torsional pendulum and subsequently cooled below the critical temperature for the onset of superfluidity. While the pendulum is driven close to its resonance frequency, the oscillation period and dampening is measured. Once the adsorbed helium turns superfluid it contributes no longer to the inertia of the pendulum and hence the observed period and dissipation changes. They observe a sudden change in the period shift and a strong peak in the dissipation which can be fitted accurately with a dynamic theory by V. Ambegaokar, B. Halperin, D. Nelson, and E. Siggia⁷⁰. This theory expands on the static theory developed by J. Kosterlitz and D. Thouless^{6,71} and is based on

¹ D. Bishop and J. Reppy: *Phys. Rev. Lett.*, vol. 40, (1978)

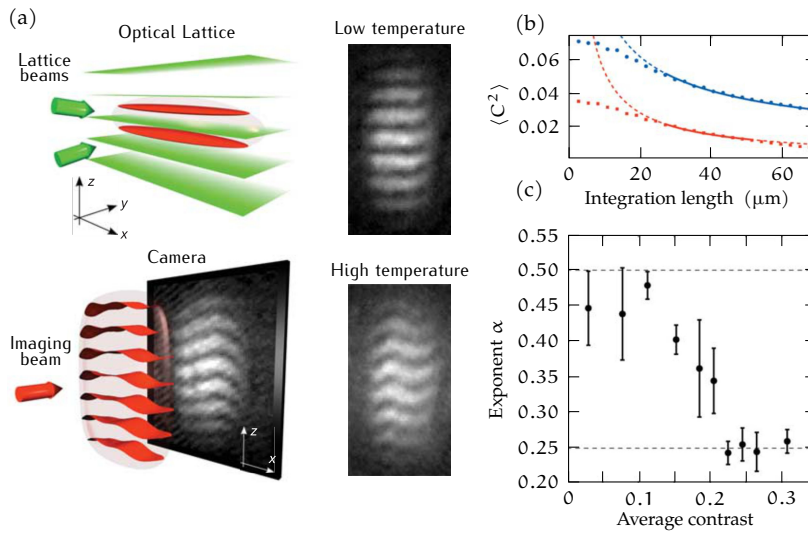
⁷⁰ V. Ambegaokar et al.: *Phys. Rev. Lett.*, vol. 40, (1978)

⁶ J. M. Kosterlitz and D. J. Thouless: *J. Phys. C*, vol. 6, (1973), ⁷¹ J. M. Kosterlitz: *J. Phys. C*, vol. 7, (1974)

the creation and dissipation associated with the movement of 2D vortices. The fit parameters show excellent agreement with the theoretical value for the superfluid density at the transition temperature T_c derived in a previous chapter to be $n_s \lambda_T(T_c)^2 = 4$. Despite the good agreement to experiments with torsional oscillators (M. Chester and L. Yang⁷²) and the propagation of third sound (R. Hallock, J. Mochel, I. Rudnick⁷³) with the theory proposed by Kosterlitz and Thouless, no insight into the microscopic driving mechanism could be gained.

PIONEERING WORK ON COHERENCE OF BOSONIC 2D QUANTUM GASES

Almost 30 years later, measurements on ultracold atomic gases could elucidate for the first time the connection between the vanishing algebraic phase decay and the proliferation of vortices. In the pioneering work of J. Dalibard et al., multiple 2D layers of weakly interacting ^{87}Rb atoms at very low temperatures interfere during ballistic expansion^{20,74,75}. During expansion the atom clouds overlap and the wave functions begin to interfere. After a short time of flight, the expanded clouds are imaged and a 2D interference pattern similar to the those depicted in Fig. 5.1a is recorded. The resultant interference pattern is



⁷² M. Chester and L. C. Yang: *Phys. Rev. Lett.*, vol. 31, (1973)

⁷³ I. Rudnick: *Phys. Rev. Lett.*, vol. 40, (1978)

²⁰ Z. Hadzibabic et al.: *Nature*, vol. 441, (2006), ⁷⁴ Z. Hadzibabic et al.: *Phys. Rev. Lett.*, vol. 93, (2004), ⁷⁵ S. Stock et al.: *Phys. Rev. Lett.*, vol. 95, (2005)

Figure 5.1: (a) Probing the coherence of 2D atomic gases using matter wave heterodyning. (b) Examples of average integrated interference contrast (C^2) are shown for low (blue circles) and high (red squares) temperature in dependence of the integration length. From these curves, the decay exponent α is determined. (c) Emergence of quasi-long-range order in a 2D gas, as shown by the sudden decrease of the exponent α with increasing average contrast. The dashed lines indicate the theoretically expected values of α above and below the *Kosterlitz-Thouless* (KT) transition in a uniform system. Figure adapted from²⁰.

²⁰ Z. Hadzibabic et al.: *Nature*, vol. 441, (2006)

fitted with a sinusoidal function and the extracted local contrast is integrated over a variable length L_x in the x -dimension to yield the integrated contrast $\langle C^2(L_x) \rangle$, proposed by A. Polkovnikov et al⁷⁶. Absolute values in agreement with the theoretical description have been measured over the *KT* transition. The integrated contrast along the x -axis, for a system of two identical but independent condensates that has expanded into the z -axis and in which the length $L_x \gg L_y$ is given by

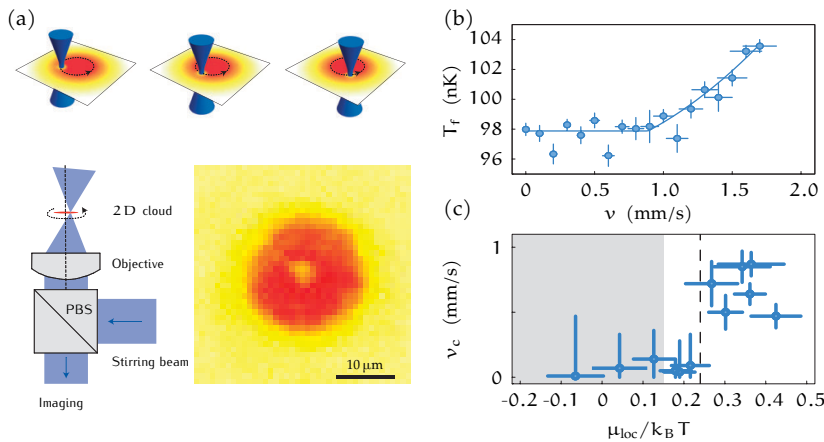
$$\langle C^2(L_x) \rangle \approx \frac{1}{L_x} \int_0^{L_x} dx (g_1(x, 0))^2. \quad (5.1)$$

⁷⁶ A. Polkovnikov et al.: *Proc. Natl. Acad. Sci. U.S.A.*, vol. 103, (2005)

For temperatures above the critical point, for which the phase correlations decay exponentially, the scaling of the fringe contrast is inversely proportional to the integration distance, $\langle C^2(L_x) \rangle \propto (1/L_x)^{2 \cdot 0.5}$. However, for temperatures below the critical point, $T < T_c$, the exponent α is defined in the same manner as the scaling exponent derived in Chapter 4 and varies as $0 < \alpha < \alpha_c = 0.25$. Thus, at and below the phase transition, the integrated contrast scales as $\langle C^2(L_x) \rangle \propto (1/L_x)^{2 \cdot \alpha}$. The observed sudden jump in the averaged contrast in Fig. 5.1c from $\alpha \approx 0.5$ to $\alpha \approx 0.25$ shows strong indication that the phase transition has been reached. Since the exact relation between the superfluid density ρ_s and the condensate density ρ_c is not completely understood in 2D atomic gases, it is not clear if the superfluid regime has been explored. Thus, the convergence of the measured exponent to the critical value of ≈ 0.25 might be explained by the inequality of condensate and superfluid density, the inhomogeneity of the sample or attributed to residual heating in the trapping potential. A sharp dislocation in the interference pattern recorded close to T_c provides evidence for the occurrence of the *universal jump in superfluid density* and the involvement of free vortices in the crossover region. Subsequently, also the critical atom number of an array of weakly interacting ^{87}Rb atoms has been studied⁵⁴. The results rule out the application of the conventional *Bose-Einstein condensate* (BEC) theory of ideal gases to the interacting Bose gases used in the experiments.

SUPERFLUIDITY OF SINGLE BOSONIC LAYERS

The dynamical properties of single layer Bose systems were studied by R. Desbuquois⁵⁶, again in the group of J. Dalibard. They provide the first direct observation of superfluidity in ultracold 2D gases by stirring a sample with a repulsively tuned laser beam, as sketched in Fig. 5.2a. A gas of approximately $N = 35\,000 - 90\,000$ weakly interacting ^{87}Rb atoms is prepared in a harmonic trap with an aspect ratio of ≈ 56 and interaction parameter $\tilde{g} = 0.093$.



⁵⁴ P. Krüger et al.: *Phys. Rev. Lett.*, vol. 99, (2007)

⁵⁶ R. Desbuquois et al.: *Nature Physics*, vol. 8, (2012)

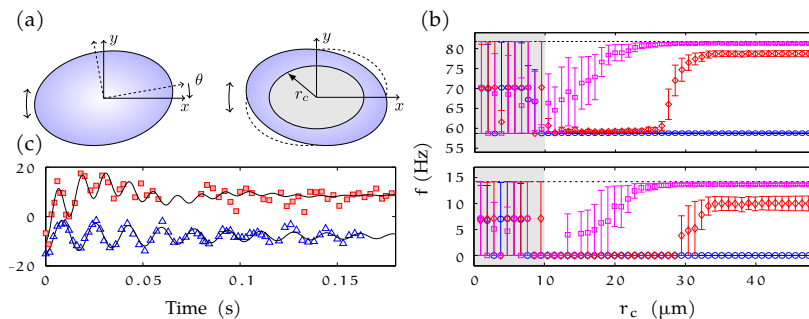
Figure 5.2: (a) A trapped 2D gas of ^{87}Rb atoms is perturbed by a focused laser beam, which moves at constant velocity on a circle centered on the cloud. (b) Typical curves of the temperature after stirring the laser beam at varying velocities in the superfluid regime (c) The critical velocities v_c obtained [...], plotted versus the single parameter $\mu_{\text{loc}}/k_B T$. The gray shaded area represents the expected superfluid region, whereas the dashed line indicates the measured transition point. Figure adapted from⁵⁶.

⁵⁶ R. Desbuquois et al.: *Nature Physics*, vol. 8, (2012)

After stirring, the temperature and chemical potential of the cloud is determined via a Hartree-Fock fit to the thermal wings. When the

stirrer lies well in the expected superfluid region, a final temperature T_f curve similar to Fig. 5.2b is recorded. Here, a sharp bend can be observed close to $v = 1$ mm/s which is identified as the critical velocity, below which there is no dissipation. For large stirring radii, when the stirrer is well in the normal regime, no such sharp bend can be observed. This type of measurement is repeated for different values of the universal ratio $\mu_{\text{loc}}/k_B T$, which is implied by the scale invariance of the weakly interacting Bose gas. Here, μ_{loc} is the chemical potential in the local density approximation. When the thusly extracted critical velocities are plotted versus $\mu/k_B T$, a sharp discontinuity can be observed indicating the transition from the normal to the superfluid phase, see Fig. 5.2c. Here, the gray shading represents the theoretical prediction for the superfluid region, the authors attribute the small discrepancy to the non-zero width of the stirrer which has also recently been shown to impact the absolute value of the critical velocity⁷⁷.

A symmetric but simultaneously very different approach to the measurement of local superfluidity via global observables in single 2D layers has been pursued by the group of H. Perrin⁵⁷. A similar weakly interacting Bose gas in the quasi-2D regime is prepared in a highly oblate elongated harmonic trap at an aspect ratio of ≈ 40 and interaction parameter $\tilde{g} \approx 0.1056$. After preparation, the trap is rotated suddenly by 10° which excites a so called *scissor mode*, sketched on the left side of Fig. 5.3a. This mode exhibits characteristic frequencies for the nearly collisionless thermal and hydrodynamic, i. e. superfluid, fraction. Examples of the oscillations extracted from the cloud average $\langle xy \rangle$ after varying hold time can be seen in Fig. 5.3c. Here, the red open squares (blue open triangles) show the response of the thermal (superfluid) fraction, respectively. The fit to the observed oscillations with a simple model retrieves frequencies on a lower and an upper branch, $[0, \omega_-]$ and $[\omega_{\text{hd}}, \omega_+]$, respectively. As soon as a non-superfluid fraction is present, the scissor mode frequency is expected to shift from $0 \rightarrow \omega_-$ and $\omega_{\text{hd}} \rightarrow \omega_+$, which can be clearly observed in Fig. 5.3b.



In a second step, the cloud was not averaged as a whole, although a signal was still observable, but only on a region around the center, depicted on the right side of Fig. 5.3a. When extending this region

⁷⁷ V. P. Singh: *Probing Superfluidity of Ultracold Bose Gases via Laser Stirring and Noise Correlations*, (2017)

⁵⁷ C. De Rossi et al.: *New J. Phys.*, vol. 18, (2016)

Figure 5.3: (a) Sketch of the experimental setup and procedure. The gas is set into motion by rotating the trap 10° . At first, the complete cloud is analyzed and subsequently only a an area around the center with equi-density radii r_c . (b) High frequency (top) and low frequency (bottom) component extracted in the analysis for three decreasing superfluid fractions (blue circles, red diamonds and pink squares, respectively)(c) Examples of the oscillations extracted from the cloud average $\langle xy \rangle$ for varying hold time. The red open squares (blue open triangles) show the response of the thermal (superfluid) fraction respectively. Figure adapted from⁵⁷.

⁵⁷ C. De Rossi et al.: *New J. Phys.*, vol. 18, (2016)

from the center on equi-density lines to radii r_c , a very clear transition can be observed in Fig. 5.3b. The experiment was performed for varying superfluid fraction which results in no shift towards higher frequencies when no thermal part is present (blue circles), a sharp bend when the normal-superfluid boundary is well defined (red diamonds) and a gradual transition when the fractions are not clearly separated (pink squares). With this, the authors have demonstrated a novel method to study the superfluid to normal boundary and also provided evidence that the coupling of the two fluids induces “damping rates larger than the usual Landau damping” for the superfluid. Recently, this approach has been extended to forgo the dependency on scattering theory in favor of a model free method based on principal component analysis⁷⁸.

⁷⁸ R. Dubessy et al.: *AIP Conf. Proc.*, vol. 1936, (2018)

5.2 COHERENCE MEASUREMENTS ON SINGLE LAYERS

Studies on a single layer of very weakly interacting ($\tilde{g} = 0.02$) ^{23}Na atoms in a quasi 2D geometry in the group of D. Phillips²¹ have shown indication of the emergence of a trimodal phase in the thermal to superfluid crossover after time of flight. Low inter-particle interaction and direct imaging access to the 2D plane allowed the azimuthal average of density and thus the observation of an intermediary quasi-condensate component. By applying a Raman pulse in a Ramsey-like sequence, an in situ interference image of two copies of the Bose gas is obtained. Similar to the work of J. Dalibard, an averaged contrast over the central interference fringes is extracted and a slower than thermal decay of the normalized first order correlation function can be observed.

²¹ P. Cladé et al.: *Phys. Rev. Lett.*, vol. 102, (2009)

IMAGING THE MOMENTUM PROPERTIES VIA MATTER WAVE FOCUSING

The research on single 2D layers of highly confined bosons was extended to a flexible ^6Li system in the group of S. Jochim²³. The interaction strength of the ^6Li dimers can be controlled by means of a Feshbach resonance. Using direct perpendicular imaging access to the 2D plane and magnetically focusing the expanding gas, an averaged momentum distribution can be measured²⁶. From this, a Fourier transform produces the normalized first order correlation function, see Fig. 5.4a. A qualitative change in the decay of g_1 can be observed when increasing the sample temperature across the phase transition, here the shape of g_1 changes from linear to sub-linear in the shown logarithmic plot. The fitted decay follows the expected power law scaling until a thermal gas is produced. The thermal gas shows clearly a better agreement with exponential decay as can be seen in Fig. 5.4b, where a lower χ^2 value indicates a better fit. Additionally, the trap averaged scaling exponents were fitted along the Bose-Einstein to Bardeen-Cooper-Schrieffer crossover with no discernible difference between attractive and repulsive interactions, shown in Fig. 5.4c. Remarkably, the comparison of the critical central phase-space density D_0 , with

²³ M. G. Ries et al.: *Phys. Rev. Lett.*, vol. 114, (2015)

²⁶ P. A. Murthy et al.: *Phys. Rev. Lett.*, vol. 115, (2015)

bosonic quantum Monte Carlo simulations showed excellent agreement even for large interaction parameters of $\tilde{g}=2.76$ and only breaks down for interaction parameters well into the strongly-interacting regime at $\tilde{g}=7.75$, cf. Fig. 5.4d and e.

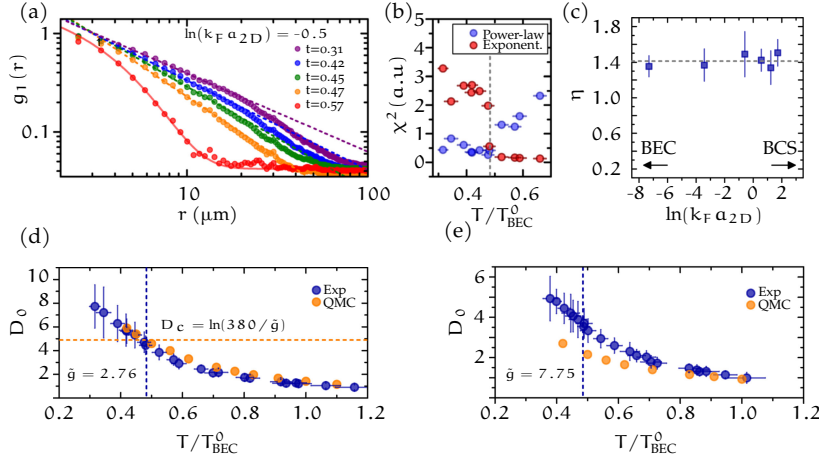


Figure 5.4: (a) First order correlation function g_1 for different temperatures $t = T/T_{\text{BEC}}^0$. At high temperatures, correlations decay exponentially, whereas at low temperatures algebraic decay is observed by the authors. (b) The qualitative change in decay is visible in the χ^2 error for both exponential (red circles) and algebraic fits (purple circles). From this, the transition temperature (dashed line) could be determined. (c) The critical exponent η_c stays approximately constant for all $\ln(k_F a_{2D})$. (d) and (e) Peak phase space density D_0 . Both panels show experimental data (purple circles) and simulated data for bosons (yellow circles) for the coupling strengths $\tilde{g} = 2.76$ and $\tilde{g} = 7.75$ respectively. The vertical dashed lines indicate the corresponding critical temperatures. Even at $\tilde{g} = 2.76$ excellent agreement between experiment and simulation can be observed verifying the relation $D_c = \ln(380/\tilde{g})$ at this interaction strength. For higher interaction, however, the simulation is seen to deviate from the measured results. Figure adapted from²⁶.

²⁶ P. A. Murthy et al.: *Phys. Rev. Lett.*, vol. 115, (2015)

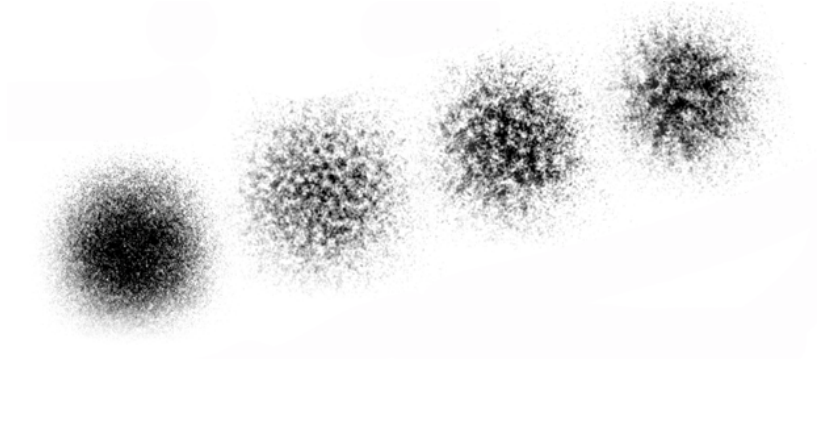
⁵⁸ J.-Y. Choi et al.: *Phys. Rev. Lett.*, vol. 109, (2012), ⁷⁹ J.-Y. Choi et al.: *Phys. Rev. Lett.*, vol. 111, (2013), ⁸⁰ S.-W. Seo et al.: *Phys. Rev. A*, vol. 89, (2014)

²⁷ R. Desbuquois: *Thermal and superfluid properties of the two-dimensional Bose gas*, (2013)

Figure 5.5: Density images after freely expanding for varying time. Demonstrating the formation of density ripples from in situ phase fluctuations. From left to right: In situ density distribution, 1 ms, 2 ms and 3 ms time of flight.

PHASE PROPERTIES ACCESSIBLE VIA INTERFERENCE AFTER SHORT TIME OF FLIGHT

The interference property of degenerate gases has recently been the focus to gain insight into the quasi-condensates coherence, since direct imaging of the quasi-condensates phase is still technically impossible. Multiple attempts of the group of Y. Shin have notably shown that the *self interference* of a 2D quasi-condensate exhibits distinct density ripples after short time of flight and requires a large degree of precision and imaging calibration as well as compensation^{58,79,80}, which will be expanded on in Chapter 8. Inspired by their work and the results published in R. Desbuquois' doctoral thesis²⁷, which indicated the possibility to use the phase interference to probe the first order correlation function, the experiment presented in this work was realized.



We achieved direct high resolution access to one highly confined 2D layer of bosonic ${}^6\text{Li}$ dimers after short time of flight, which presents the opportunity to accurately measure the normalized density-density correlation function $g_2(\mathbf{x})$. Using a theoretical prediction of the time

propagation of *in situ* phase fluctuations developed by V. Singh and L. Mathey, we are able to infer the functional form and possibly the scaling exponent of the first order correlation function $g_1(x)$ locally. The absorption images displayed in Fig. 5.5 show an expanding ultracold cloud of bosonic ${}^6\text{Li}$ dimers at increasing time of flight, studied in our group for harmonically trapped gases by N. Luick⁸¹. While the *in situ* density distribution is smooth, density ripples form after short time of flight. These density fluctuations stem from the time propagation of the phase fluctuations initially present in the gas. In doing so, the phase correlations are translated into density correlations. The increasing length scale of the density correlations for longer time of flight, samples the inherent phase correlations at different length scales – and thus momenta – in resemblance to the Talbot effect.

Due to the recent development of a single homogeneous 2D layer of ${}^6\text{Li}$ in our group, the experiment is extended to attempt the quantitative study of the interference pattern in larger detail, due to the increased *signal-to-noise ratio* (SNR) and good optical access.

5.3 QUANTITATIVE THEORETICAL ANALYSIS OF THE INTERFERENCE PATTERN AFTER TOF

Many of the recent quantitative analyses of self interference images after short *time of flight* (ToF) are based on the work of A. Imambekov⁸², which has been extended and applied to ultracold 2D ${}^{87}\text{Rb}$ and ${}^6\text{Li}$ systems by the group of L. Mathey⁸³. The dependency of the density ripples on the ToF can be regarded qualitatively as a realization of the Talbot effect, i. e. a time dependent sampling of the dominant momentum contribution. Phase excitations with larger spatial wavelength and thus smaller momenta require a longer time to permeate the condensate and build up a significant interference pattern. Hence, at each point in time, there exists a wavelength that reaches maximum interference amplitude and therefore highest visibility. In contrast to the interference pattern of Bose-Einstein condensates, the time dependence is not linear but the dominant visible length scale varies as $\lambda_1 \propto \sqrt{t}$. This is a first indication of the power law decay of phase correlations in a 2D Bose gas.

However, the quantitative analysis of the density-density correlation function is only made possible by the detailed computation of the propagation of the *in situ* phase-phase correlation function with ToF⁸⁴. Due to the pivotal role of these numerical results for this work, an outline will be presented in Section 8.1.2 as well as a full derivation in Appendix A.

⁸¹ N. Luick: *Local probing of the Berezinskii – Kosterlitz – Thouless transition in a two-dimensional Bose gas*, (2014)

⁸² A. Imambekov et al.: *Phys. Rev. A*, vol. 80, (2009)

⁸³ L. Mathey et al.: *Phys. Rev. A*, vol. 79, (2009)

⁸⁴ V. P. Singh and L. Mathey: *Phys. Rev. A*, vol. 89, (2014)

6

EXPERIMENTAL TOOLS AND METHODS

- 6.1 Accessing the momentum $n(k)$ after $T/4$ ToF 57
 6.2 Reducing vertical expansion with a brake pulse 59

All the experiments on ultracold gases require excellent control and detection in order to elucidate the elusive quantum mechanical processes of the microscopic particles. Naturally, the presented study builds upon the achievements and technical developments of the community, two of which are pivotal to the ensuing analysis and hence warrant a detailed description. Two methods will be presented in this section which highlight the versatility of the ultracold atom systems and fully optical control but also the high demands on precision when dealing with the ultra small. First, a cornerstone of cold atom systems, the measurements of the momentum distribution after *time of flight* (ToF), is presented in the case of expansion into a static magnetic field for a quarter of the trapping period, akin to the focusing of a light beam in a gradient index lens.

Second, it is explained how high optical resolution can be maintained during expansion by illuminating the sample with a highly anisotropic laser beam for a short amount of time, effectively stopping the axial expansion without disturbing the measured quantities.

6.1 ACCESSING THE MOMENTUM $N(k)$ AFTER $T/4$ TOF

ANALOGOUS to the focus of a collimated light beam at infinity, that represents the light field in terms of its k -vector, or momentum, a quantum gas released from a trap also displays its momentum distribution after – ideally – infinite expansion. In practice, an expansion time t much longer than the inverse of the trapping frequency $t \gg 1/\omega_{\text{trap}}$ suffices to yield a good approximation to the true momentum distribution.

The focus of the light beam can be brought to a finite distance with the help of a lens, acting on the phase of the light field. Similarly, an atom cloud can be focused by an electro-magnetic field, imprinting a parabolic phase profile onto it, thus completing the transformation to momentum space in a finite amount of time⁸⁵.

Alternatively, free evolution in a harmonic trap yields the same result. Here, the phase shift is not imprinted only once but continuously, similar to the effect of a gradient index lens. Since the amount of time after which the gas has reached the focus is precisely a quar-

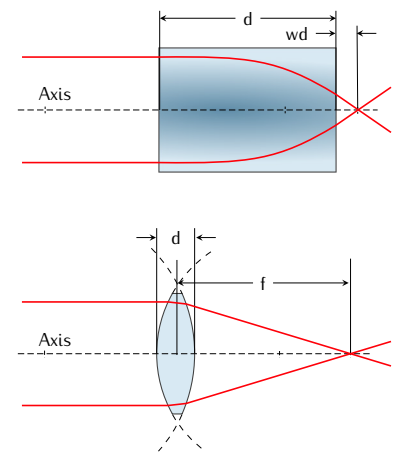


Figure 6.1: Illustration showing the similarity of the expansion into a magnetic field to the passing of a laser beam through a gradient index lens (top). In contrast to the application of a single magnetic or optical pulse analogous to the focusing via a conventional lens (bottom). Note that the result is identical although the thickness d is different and the focal length f is replaced by the working distance wd .

⁸⁵ P. A. Murthy et al.: *Phys. Rev. A*, vol. 90, (2014)

ter of the trapping period T of the magnetic trap, these measurements will henceforth be referred to as $T/4$ -measurements.

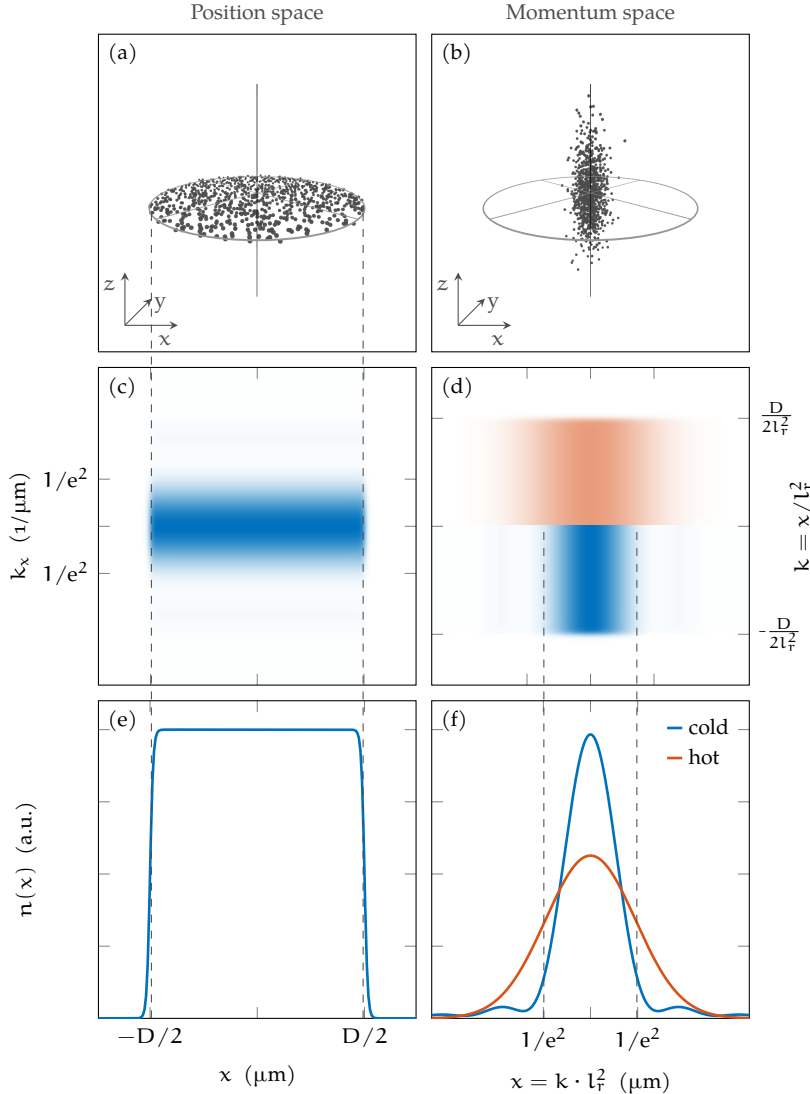


Figure 6.2: Outline of the method used for imaging the momentum distribution. The upper two panels ((a) and (b)) show an artists impression of the evolution of the atom cloud during the matter wave focusing procedure. The originally disk-shaped 2D cloud compresses radially due to the radially harmonic potential and maps its momentum to position space. For a cold gas, most of the particles end up close to the origin, i.e. with small momenta. During this process, the gas expands vertically due to the original confinement, interaction energy and deconfining magnetic field. The circular frame represents the size of the cloud in situ. This detrimental effect is considered in the following section. The second row of panels ((c) and (d)) show a sketch of the x -axis phase space distribution during the procedure. The horizontal axis indicates the x position while the vertical axis indicates the k_x momentum distribution. Initially, the gas is well defined in position space (left panel) with boundaries at half the diameter D and exhibits an unknown momentum distribution estimated here via Hankel transform of the expected algebraically decaying phase correlation function g_1 of a quasi-condensate. The point where the momentum distribution has decayed to $1/e^2$ of its maximum value is given on the vertical axis. A vertical integration over the phase space density akin to the process of imaging is shown below in (e) which shows the boundary of the cloud in position space indicated by dashed lines. Panel (d) shows the phase space distribution mapped onto position space (rotated) for the same quasi-condensate (blue) and a thermal gas (red) which exhibits a much broader momentum distribution. Note that due to the rotation, the momentum distribution is now imaged when integrating vertically over the phase space density. The result is shown below in (f). Here, the momentum distributions of both gases are compared and the points where the momentum distribution has decayed to $1/e^2$ of its maximum amplitude are indicated by dashed lines.

THE method is outlined in Fig. 6.2. We start with 6.2a, a homogeneous 2D gas in position space. The corresponding phase-space representation – reduced to a the x coordinate for convenience – is plotted below in 6.2c. Here, the momentum is plotted vertically and is estimated by Hankel transforming the expected first order correlation function with algebraic decay. Since absorption imaging is only able to probe the location and not the momentum of the atoms, it can be thought of as an integration of the phase-space density distribution in the vertical direction. This would result in the integrated density $n(x)$ shown in 6.2e for the in situ case.

The dipole traps are turned off and the gas is left to expand ballistically for a quarter of the trapping period T into a weakly confining magnetic trap. This results in a drastically different situation. Now, an atom distribution as shown in 6.2b is imaged. Due to the focusing

effect of the magnetic trap, the gas is mapped from position space to momentum space. In our setup, the gas also expands drastically in the vertical, or z direction due to the tight prior confinement, interaction energy and the deconfining effect of the applied magnetic field.

The matter wave focusing corresponds to a rotation in phase space, as visualized in 6.2d for a hotter (red) and a colder (blue) gas. The position of the atoms after the focusing procedure reflects the momentum they had in situ. If an atom had no momentum, it would have been accelerated towards the center and arrive there after a time of $T/4$. If the atom had a certain momentum, it could travel further outwards during $T/4$. Hence, the distance from the center of the magnetic trap becomes a measure of the atoms momentum.

Since a hotter gas consists of a larger percentage of high momentum particles, the imaged momentum distribution will be broader. The momentum distribution of a cold gas (blue) is shown in the lower half and a distribution of a thermal gas (red) – with more weight at higher momenta – is shown in the upper half of 6.2d. In analogy to the dependence of the focus of the beam profile of a laser beam on its wavefront just before the focusing lens, the shape of the matter focus of a coherent Bose gas reflects the fluctuations in the wave functions phase, or in other words, its momentum.

Imaging the cloud after $T/4$ is equivalent to a vertical integration of 6.2d and thus results in the momentum distributions shown in 6.2f. The colors of the plot correspond to the colors used in 6.2d. Now, each location corresponds to an in situ momentum and the x -axis can be converted to display the momentum via $k = x/l_r^2$, with l_r being the radial harmonic oscillator length of the magnetic focusing trap. For a more in-depth look at the employed technique see Hueck et al.⁸⁶ and Murthy et al.⁸⁵.

From figure 6.2f, one can immediately see that there is a significant qualitative difference between the momentum distributions of a cold gas (blue) and a hot gas (red). The quantitative analysis of the acquired images yields insights into global phase properties of the trapped gas and – theoretically – the extraction of the phase correlation function g_1 . However, since the functional form of $n(k)$ is usually required in large detail, high precision imaging of extended gases is desirable, which presents unique challenges.

6.2 REDUCING VERTICAL EXPANSION WITH A BRAKE PULSE

COMPLETELY free expansion, the simplest way of achieving a $T/4$ measurement uses the experimental sequence depicted on the right of Fig. 6.3. In the used phase-space representation, the vertical axis indicates the z -position of a particle and the horizontal axis the z -momentum. Hence, a free expansion is visualized as a shearing motion where the atoms with negative momentum move straight downwards and the atoms with positive momentum move straight upwards. The in situ phase-

⁸⁶ K. Hueck et al.: *Phys. Rev. Lett.*, vol. 120, (2018)

⁸⁵ P. A. Murthy et al.: *Phys. Rev. A*, vol. 90, (2014)

space distribution is illustrated in gray (dashed) and the final phase-space distribution after the $T/4$ time is plotted in red. A projection onto position space is plotted to its left (also in red). Due to the significant amount of particles beyond the *depth of field (DoF)*, the resultant *effective point spread function (PSF_{eff})* (also in red, towards the center of the figure) is quite broad.

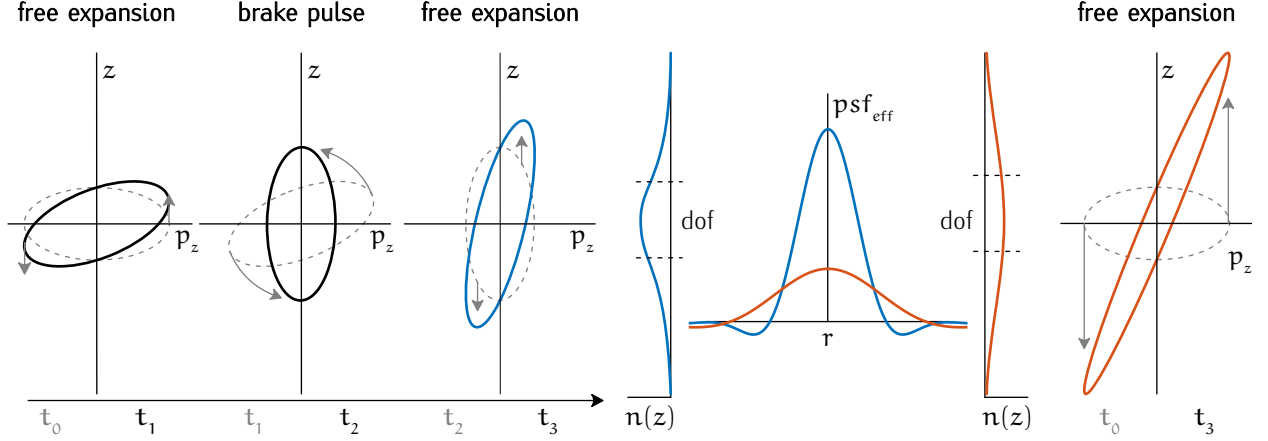


Figure 6.3: Comparison of two methods used for imaging the momentum distribution. Completely free expansion (right side) is contrasted with the application of a brake pulse (left side). Here, a phase-space representation, with the z position on the ordinate and the momentum p_z on the abscissa is used. The initial distribution is sketched as a horizontal ellipse (dashed), which represents all individual atoms phase-space values. Whilst the gas is left to expand freely until the radial spatial distribution is mapped onto the momentum distribution, the gas also freely expands vertically in the z direction. This is represented by a vertical shearing in phase space which results in the elongated ellipse shown in red (solid). This distribution is projected leftwards which yields the vertical density profile (red). The cloud hence extends well beyond the DoF indicated by two dashed lines which leads to a broad PSF_{eff} (red) and hence strongly reduced x, y resolution. In contrast, the sequence including the brake pulse is shown from left to right. When the gas expands only briefly to reduce scattering (vertical shearing motion depicted in leftmost image), subsequently vertically decelerated in an optical harmonic potential (rotation until vertical) and finally left to expand freely (blue) until the radial momentum distribution is obtained, the resulting vertical density profile (blue) is largely contained within the DoF. Hence a much narrower PSF_{eff} and thus higher x, y resolution is obtained. Axes are scaled such that the total energy of each particle is equal to the distance to the origin.

To increase the resolution of the images, the PSF_{eff} must be reduced in width, which can be achieved by decreasing the amount of particles beyond the DoF, i. e. reducing the vertical expansion. To this end, the dipole potentials used to trap the cloud can also be used to stop the vertical expansion. This is achieved by the application of a strong vertical confinement for a time on the order of a quarter of its vertical trapping period. Hence, ideally stopping the vertical expansion of the particles by removing the vertical momenta without effecting the radial momenta. The pulse of light is henceforth referred to as the *brake pulse*. It turns out that the optimal reduction in vertical expansion can be achieved in our system when the brake pulse is applied for $125 \mu\text{s}$ with a power of 100 mW . Due to the large aspect ratio of $\omega_z/\omega_r \approx 50$, the radial momentum distribution can be considered unchanged. Here, the radial trapping frequency is estimated as the average of the Cartesian trapping frequencies, i. e. $\omega_r = \sqrt{\omega_y \omega_x}$.

The free expansion \rightarrow brake pulse \rightarrow free expansion sequence is depicted on the left side of Fig. 6.3. At first, the gas is left to expand freely for a very short time of $\approx 20 \mu\text{s}$ which causes the aforementioned shearing motion from t_0 (gray dashed) to t_1 (black, solid). Then, the brake pulse is enabled, which results in a rotation in phase space until the ellipse is oriented vertically, ideally stopping the vertical expansion during t_1 (gray, dashed) to t_2 (black). Subsequently, the gas is left to evolve the rest of the $T/4$ time, t_2 (gray, dashed) to t_3 (blue) which corresponds to another vertical shear. The projection of the density of the expanded gas in the z -direction is plotted to the right of the last step (blue). Since the atoms lie mostly within the DoF, the PSF_{eff} (also in blue) is greatly reduced as can be seen in the compar-

ison. Thus, reducing the vertical expansion by the application of a brake pulse significantly increases the achievable resolution of a microscope and hence enables the detailed analysis of e. g. complex momentum distributions. Note that the initial free expansion is greatly magnified in the illustration, due to its otherwise minuscule visible effect on the drawn ellipse. The resultant relative sizes are appropriate nonetheless.

COMBINING the presented tools, allows us to perform a high precision measurement of the global phase of a cold atom system. Since the phase in two-dimensional Bose systems is highly non-trivial and expected to yield interesting insights we apply these methods to our homogeneous 2D Bose gas in the following chapter.

Part II

RESULTS

7 | MOMENTUM DISTRIBUTION AND FIRST ORDER CORRELATION FUNCTION OF INTERACTING 2D BOSE GASES

- 7.1 Challenges extracting the momentum distribution from a T/4 measurement 67
- 7.2 Momentum distribution of a 2D ${}^6\text{Li}$ gas 71
- 7.3 Extracting the temperature of a homogeneous gas 73
- 7.4 Interpretation of the results 74
- 7.5 Towards experimental access to the first order correlation function 81

Homogeneous systems are particularly well suited for the measurements of nonlocal observables such as the momentum distribution since, *time of flight* (ToF) measurements do not mix parts of the cloud with different phase-space density.

Our experimental system, as introduced in Chapter 5 and shown in Fig. 7.1, mimics a homogeneous 2D quantum gas very well. With a root mean square density variation of only 8.6% and a diameter of $\approx 139 \mu\text{m}$, the system is in good approximation homogeneous and large enough so that finite size effects do not play a major role.

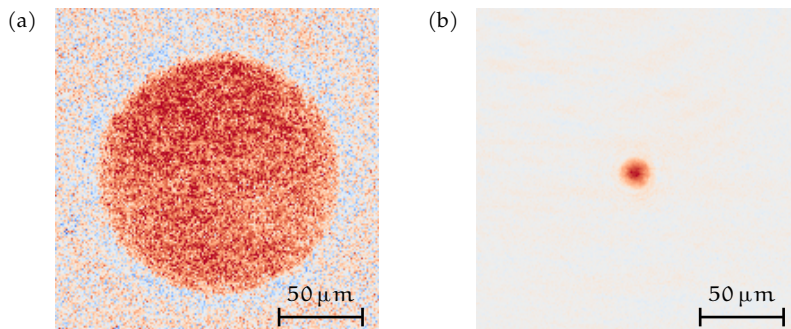


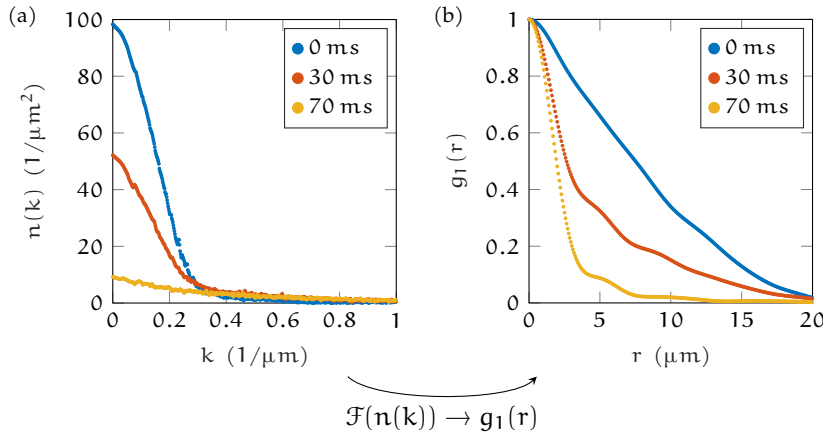
Figure 7.1: (a) Exemplary density distribution $n(\mathbf{x})$ of our homogeneous sample (Averaged over ca. 20 realizations). (b) Sample of the 2D image of $n(\mathbf{k})$ for a relatively cold gas. Note the difference in size. Also, the color has been rescaled to accommodate the approximately 50 fold density.

The momentum distribution is accessed via a matter wave focusing technique^{85,87} which is very similar to the optical focusing of a plane wave. This expansion into a harmonic magnetic field maps the wave function of the gas from position-space to momentum-space in a finite amount of time. This type of measurement will be referred to as T/4 since the evolution in the potential for a quarter of the traps period T is exploited. The details of this measurement and how a brake pulse can be used to improve the experimental accuracy for interacting gases is presented in Section 6.1 and Section 6.2 respectively.

An example of a momentum distribution of a comparatively cold gas is shown in Fig. 7.1b. As can be seen from the scale, the resulting

⁸⁵ P. A. Murthy et al.: *Phys. Rev. A*, vol. 90, (2014), ⁸⁷ S. Tung et al.: *Phys. Rev. Lett.*, vol. 105, (2010)

object is very small and thus high resolution imaging would be desirable. To achieve high resolution, the object has to be located within the *depth of field (DoF)* of the imaging objective and hence a gas with very low thickness is beneficial. Since the scattering rate shortly after release out of the trap is still significant, fast expansion perpendicular to the image plane is required, in order to reduce the density and hence interactions. This results in a larger cloud size in the direction of the imaging axis. Hence, for the times needed to perform the measurement, parts of the gas extend far beyond the DoF and therefore introduce blur. Thus, a compromise between the introduction of systematic errors due to scattering and the reduction of resolution by a large cloud extent has to be found. How experimental effects can be accounted for and how this impacts the extraction of G_1 is discussed in Section 7.1. Azimuthal averages of the density in momentum space $n(\mathbf{r})$ are plotted in Fig. 7.2a. Here, the holding time in the 2D trap has been varied and a significant decline in amplitude can be observed for hold times on the order of 50 ms, which will be discussed in Section 7.4.



Increasing the trapping potential would decrease the time needed for a $T/4$ measurement and therefore reduce the expansion. However, it reduces the width of the distribution simultaneously, thus requiring even greater resolution with even smaller DoF

Figure 7.2: (a) Azimuthal averages of $n(k)$ of a bosonic gas after varying hold time. From 0 ms (blue) over 30 ms (red) to 70 ms (yellow). Note the quickly decreasing amplitude. (b) The Fourier transformation with respect to $k = \frac{r}{l_F}$ yields the normalized g_1 without any corrections due to scattering or the imaging system. It is immediately obvious that the decay increases quickly for longer hold times (same colors as in (a)).

For a homogeneous system, the momentum distribution $b(k)$ is directly related to the first order correlation function $G_1(x)$ by a Fourier transform (cf. Eq. (3.15))

$$G_1(x) = \frac{1}{(2\pi)^2} \int_{-\infty}^{+\infty} b(k) e^{ikx} dk. \quad (7.1)$$

Hence, it should in principle be possible to directly visualize the algebraic decay of the phase correlations of a 2D system below the critical point by imaging its momentum distribution. Three correlation functions extracted in this way are shown in Fig. 7.2b. Directly after preparation with a hold time of $< 20 \mu\text{s}$, after a hold time of 10 ms, and after a hold time of 70 ms. It is clearly visible that the gas held for prolonged time exhibits much faster decay than the gas that was originally prepared. The theoretical and experimental issues pertaining the extraction of the first order correlation function will be discussed in Section 7.5.

In summary, both, the $n(k)$ and the $g_1(r)$ show that the momentum distribution and hence the phases of the constituent wave functions are mutated during the holding process. Reasons for the decay can be numerous, some possible scenarios will be discussed in more detail in Section 7.4. These scenarios include heating of a thermal equilibrium state by three-body loss processes, a quench into an unstable supercritical phase, or loss of atoms out of the trapping volume. Especially heating comes to mind when the reduction of coherence length is observed, thus the change in experimentally accessible temperature is measured during the holding period which will be discussed in Section 7.3. Interestingly, it appears that heating might only be partially responsible for the decay in coherence.

In the following, the methods employed to acquire momentum distributions $n(k)$ via matter wave focusing and the associated experimental challenges will be discussed. The evolution of the momentum distribution in dependence of hold time is presented and analyzed. Subsequently, the normalized first order correlation function g_1 is calculated using the momentum distribution. Finally, the method of extracting the temperature is explained in detail, before proceeding with the interpretation of the results.

7.1 CHALLENGES EXTRACTING THE MOMENTUM DISTRIBUTION FROM A $T/4$ MEASUREMENT

When performing a $T/4$ type measurement, there are two aspects of the method that need to be addressed even if one assumes that most sources of systematic errors, like stray fields, have been accounted for. First, imaging an expanded gas might introduce errors due to the finite extent and limited optical resolution. Second, interatomic scattering during ToF might redistribute the momentum. To address the former, we employ a so called brake pulse. This technique is presented in more detail in Section 6.2, in essence, it reduces the vertical size of the cloud by decelerating the expanding particles. The effect of the brake pulse on the imaged momentum distribution $n(k)$ is shown in Fig. 7.3. It is immediately obvious that even the application of the brake pulse does not reproduce the expected momentum distribution accurately. However, reducing the vertical expansion during ToF yields a result closer resembling the theoretical prediction. Thus, the smallest vertical expansion possible seems to be optimal when imaging the momentum distribution. However, due to the reduced size, the density and therefore also the scattering rate are increased. Thus, in order to judge if the improved imaging at the expense of increased scattering is a worthwhile compromise it is relevant to estimate the influence of collisions.

INCREASED DENSITY COUNTERACTS THE ADVANTAGES of higher imaging resolution by the increased occurrence of scattering events. Here, an estimate of the expected scattering events during ToF is provided. If the scattering process is to be assumed three-dimensional, an estimate

A full discussion of the applicability of 2D or 3D scattering physics or the precise nature of the scattering states themselves is not within the scope of this work and is an ongoing field of research, see e. g.⁸⁸.

⁸⁸ J. P. Kestner and L. M. Duan: *Phys. Rev. A*, vol. 74, (2006)

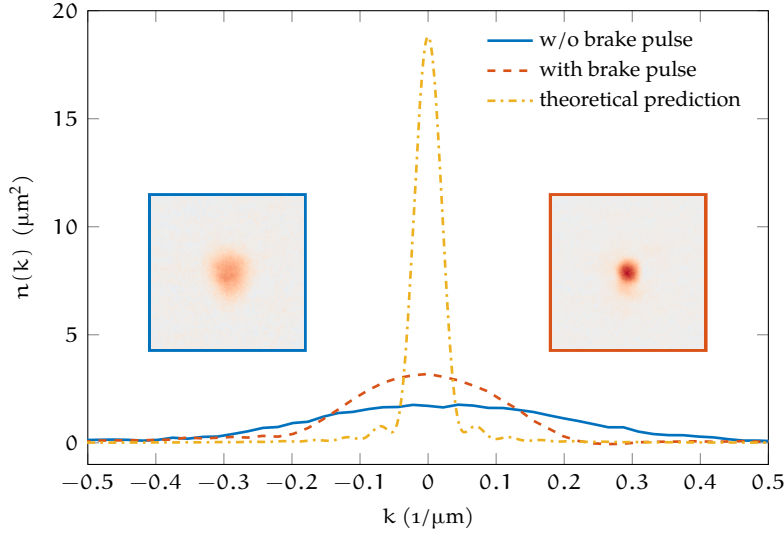


Figure 7.3: Comparison of the measured $n(k)$ with and without the application of a brake pulse. The image of the completely free expansion is shown framed in blue to the left. The image of the T/4 sequence with a braking pulse is shown framed in red to the right. The corresponding cut through the center of the image are shown in the center in blue and red (dashed), respectively. A theoretical $n(k)$ of a degenerate 2D Bose gas obtained from a phase correlation function with algebraic decay with $\eta = 0.125$ is shown for comparison in yellow (dash-dotted). The theoretical prediction is obtained via numerical Hankel transform of g_1 during which the finite sample boundaries are considered, furthermore all curves have been normalized to unity area instead of unity volume, in order to yield amplitudes suitable for comparison.

of the scattering can be obtained from the scattering rate Γ , which can be written with the 3D density n_{3D} , the scattering cross section σ_{sc} , and the mean velocity of the scatterers v_{mean} as

$$\Gamma = n_{3D} \sigma_{sc} v_{mean}. \quad (7.2)$$

Since the expansion occurs at a magnetic field offset of ≈ 690 G, where the lithium atoms form dimers, we expect a low-energy dimer-dimer elastic cross section⁵⁰ of

$$\lim_{k \rightarrow 0} \sigma_{sc} = 8\pi a_{dimer}^2. \quad (7.3)$$

Here, a_{dimer} is the scattering length between dimers which D. Petrov et al.⁸⁹ showed to be $a_{dimer} = 0.6a_{3D}$, with a_{3D} being the atom-atom 3D scattering length. The chemical potential is the relevant energy scale for estimating the mean velocity for a cold, strongly interacting gas. Hence, in the present case, the sound velocity may be approximated⁹⁰ using the mean field chemical potential $\mu = g_{2D} \cdot n_{2D} = \hbar^2/m_{dimer} \cdot \tilde{g}n_{2D}$ as

$$v_{mean} = \sqrt{\frac{g_{2D} n_{2D}}{m_{dimer}}}. \quad (7.4)$$

Since we measure the 2D column density, it is necessary to estimate the 3D density. If one assumes that the density distribution in z -direction is in good approximation Gaussian, the central 3D density can be calculated from the 2D density by

$$n_{center} = \frac{n_{2D}}{l_z \sqrt{\pi}}. \quad (7.5)$$

With this, it is possible to compare the number of scattering events for both – the completely free expansion and the brake pulse – methods. The number of scattering events per unit time is given by the scattering rate Γ times the relation of the initial $1/\sqrt{e}$ density radius σ_z to the current (at time t) radius, which effectively relates the in situ density

⁵⁰ J. Dalibard: *Collisional dynamics of ultra-cold atomic gases*, (1999)

⁸⁹ D. S. Petrov et al.: *Phys. Rev. Lett.*, vol. 93, (2004)

⁹⁰ L. Salasnich et al.: *Phys. Rev. A*, vol. 88, (2013)

If the thermal velocity was taken as the relevant energy scale, this would not alter the result of this argument much since for our gas $k_B T \approx \mu$.

Extra 7.1: 3D from 2D density

$$\begin{aligned} n_{2D} &= \int_{-\infty}^{\infty} n_{3D}(x, y, z) dz \\ &= \int_{-\infty}^{\infty} n_{3D}(x, y) e^{-z^2/l_z^2} dz \\ &= n_{3D}(x, y) \int_{-\infty}^{\infty} e^{-z^2/l_z^2} dz \\ &= n_{3D}(x, y) l_z \sqrt{\pi} \end{aligned}$$

to the density after ToF,

$$N_{\text{diff}}(t) = \Gamma \cdot \frac{\text{initial cloud radius}}{\text{cloud radius at time } t} \quad (7.6)$$

$$= \Gamma \cdot \frac{\sigma_{\text{in situ}}}{\sigma_z(t)}. \quad (7.7)$$

Since the gas in the considered experiment populates only the ground state in the vertical harmonic trapping potential, the in situ $1/\sqrt{e}$ density radius is given by the harmonic oscillator length $\sigma_z = l_z/\sqrt{2}$. In first order, one can assume that the expanded density profile is approximated well by the scaled in situ density distribution given by ballistic expansion to be⁹¹

$$\sigma_z(t) = \sigma_{\text{in situ}} \cdot \sqrt{1 + (\omega_z t)^2}, \quad (7.8)$$

which corresponds well to the linear part of the measured unimpeded expansion radius shown in Fig. 7.4.

The total number of average scattering events per particle during expansion N_{total} can be calculated by integrating the differential scattering number $N_{\text{diff}}(t)$ from the time $t_0 = 0$ the particles are released to the time t_{image} an image is taken. It is thus given by

$$\begin{aligned} N_{\text{total}} &= \int_0^{t_{\text{image}}} N_{\text{diff}}(t) dt \\ &= \int_0^{t_{\text{image}}} \frac{1}{\sqrt{1 + (\omega_z t)^2}} dt + \text{higher order corrections.} \end{aligned} \quad (7.9)$$

An axial deconfinement of $\omega_- \approx i\sqrt{2} \cdot 20$ Hz, due to a magnetic field needed for curvature compensation along the radial direction, is present in the measurements shown and responsible for the deviation from linear expansion for larger ToF. The influence of the magnetic field is considered in the following discussion by a slight modification of the aforementioned formula shown in Extra 7.2. The calculated cloud radius is shown in dependence of the ToF in Fig. 7.5a for the theoretical expectation of a free expansion (blue), the fitted radius $\sigma_z(t)$ when expanding into the actual saddle potential without brake pulse (red) and an agnostic spline fit to the measured $1/\sqrt{e}$ waist radius when the brake pulse is applied. It is immediately obvious that the brake pulse slows down the expansion significantly, although at some point the deconfinement results in a deviation from the expected linear expansion.

The integrated scattering events, as described by Eq. (7.9), are plotted for all three cases using the same colors as in the prior plot in Fig. 7.5b. For both, the free expansion and the expansion into a saddle potential, it can be seen that the total number of scattering events is small and approaches ≈ 0.1 for 12 ms ToF. This amount of scattering is tolerable. Meanwhile, the application of the brake pulse increases the number of scattering events due to the increased density significantly to ≈ 0.54 but at least stays well below 1.

⁹¹ W. Ketterle et al.: *Making, probing and understanding Bose-Einstein condensates*, (1999)

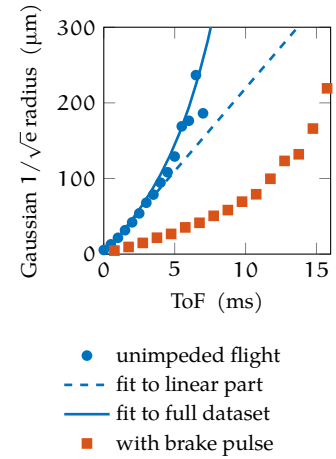


Figure 7.4: Measurement of the vertical expansion of the unimpeded cloud (blue, circles) compared to the application of a brake pulse (red, squares). The lines denote fits to the linear part (blue, dashed) with Eq. (7.8) and the complete dataset considering the anticonfinement (blue solid).

Extra 7.2: Deconfining potential

$$\begin{aligned} \sigma_z(t) &= \sigma_{\text{in situ}} \\ &\cdot \left[\cosh^2(\omega_- t) \right. \\ &\left. + \frac{\omega_z}{\omega_-} \sinh^2(\omega_- t) \right]^{1/2} \end{aligned}$$

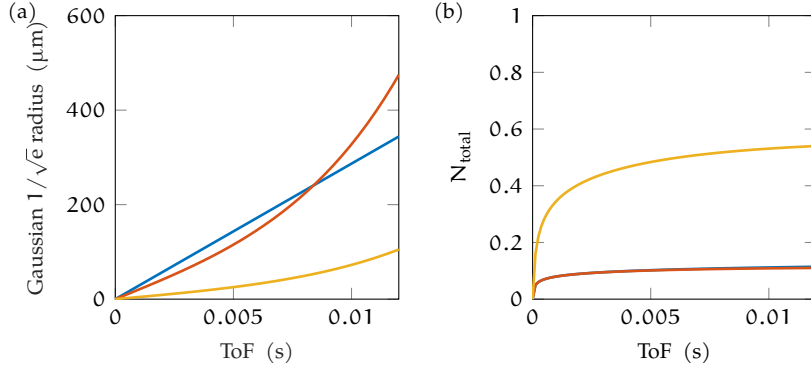


Figure 7.5: (a) The modeled vertical expansion for the case of a completely free expanding non-interacting Fermi gas (blue), an unimpeded expansion of a Bose gas with twice the fermionic mass into a deconfining potential (red) and the expansion of the same Bose gas when the brake pulse is applied (yellow). (b) The modeled average scattering events per particle integrated up to ToF. For the same three cases as in the left panel. The scattering events of the non-interacting Fermi gas (blue, if it scattered during ToF with α_{dimer}) and the unimpeded Bose gas (red) are virtually indistinguishable. Note that even for the impeded expansion (yellow) the scattering events stay below unity.

WEIGHTING THE ADVANTAGES of applying the brake pulse against the drawbacks, it is not clear which path to take. The increased resolution enables more accurate reconstruction of the actual density whereas the scattering introduces unknown systematic errors. Since the estimate of the number of scattering events during the expansion is still below 1, we use the data from the measurement with the brake pulse applied and neglect the scattering in the following in the quantitative analysis of the shape of $n(k)$. We have verified the dependence of the amplitude of $n(k)$ (see Fig. 7.9b) on the hold time against the time dependent amplitude without brake pulse and found the relative decay to be compatible.

ADDITIONAL CARE must be taken in the analysis, since slight misalignments in the brake pulse and dipole trap lead to a vertical displacement of the whole cloud during ToF. Eight distributions are shown that represent prototypical shapes observed in absorption imaging in Fig. 7.6. Many of the images show a single peak of significant amplitude similar to the one shown in ((e) to (g)). This kind of momentum distribution is expected for a cold 2D quantum gas having a lateral extent that is much smaller than a thermal Gaussian. The strong peak at $k = 0$ reflects the significant population of small momenta. The images ((a),(d)) show oddly shaped distributions of no apparent symmetry which we attribute to imaging out of focus and at an angle. Note that some images exhibit multiple maxima. The shape and size of these maxima are similar to those images showing only a single maximum, which might indicate that the imaging is indeed correct and the maxima represent two discrete populations of two opposite but equal k -modes. Possible explanations include the presence of vortices or solitons. However, the investigation of this signal is beyond the scope of this work but might be the focus of future study.

To focus on the data without these anomalous behaviors we take a large number of images and postselect the regular density distributions indicating a proper center of mass position. For comparison, samples of the momentum distributions after unimpeded ToF, i.e. without brake pulse, are given in Fig. 7.7. Here, the the gas has al-

An imaging apparatus out of focus would result in the convolution of the data with an extended *point spread function* (PSF) and therefore reduced amplitude and increased width.

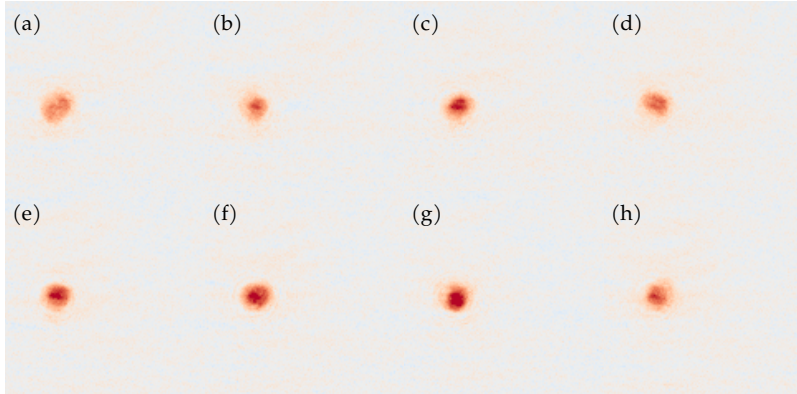


Figure 7.6: A sample of the momentum distributions, some of the images show a distortion which might be attributed to an acceleration of the particles out of focus by the brake pulse. Note that some of the distributions exhibit multiple maxima. At this point it is unclear if these represent any interesting physical phase excitation or are purely technical. The numbers shown in this plot do not represent the frequency of occurrence in the complete dataset but are comparable to Fig. 7.7.

ways expanded symmetrically around the plane of focus and shows less signs of asymmetry. However, since it has expanded significantly beyond the DoF the real momentum distribution has been convolved with a broad *effective point spread function* (PSF_{eff}) by the imaging system. This leads to much more consistent images but also eliminates the possibility to resolve multiple peaks as in Fig. 7.6.

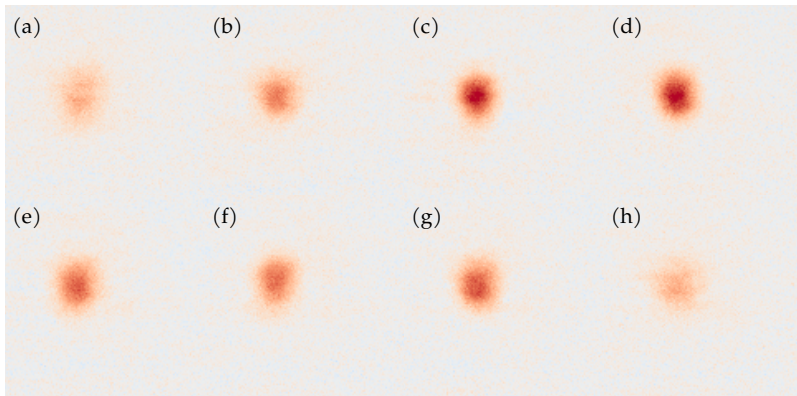


Figure 7.7: A sample of the momentum distributions for unimpeded expansion. Note that the momentum distributions are much broader compared to Fig. 7.6 but also much closer resemble the expected Gaussian-like shape. The optical density, however, is much lower. Thus, the color scale is reduced by a factor of 4 to ensure optimal visibility. The numbers shown in this plot do not represent the frequency of occurrence in the complete dataset but are comparable to Fig. 7.6.

IT MUST ALSO BE MENTIONED that the fits to the vertical expansion yield a trapping frequency $\omega_{z,\text{expansion}}$ which is about twice as large as the independently measured $\omega_z = (12.4 \pm 0.1)$ kHz. The latter measurements rely on the established method of exciting collective modes and the parametric heating by modulation of the trapping potential. Despite extensive search for systematic errors or physical causes, we are unable to bring those values into agreement. The only source of error in the measurement of the vertical expansion is the magnification. This has been repeatedly calibrated and all performed verifications are in excellent agreement. Therefore, the presented data and scattering integrals are assumed to be correct. If the scattering integral is calculated from ω_z it would increase by a factor of two.

7.2 MOMENTUM DISTRIBUTION OF A 2D ^6Li GAS

The momentum distribution of a 2D gas can be used to probe the dependency on a physical parameter. A straight forward method to vary a physical parameter of the quantum gas is to increase the holding

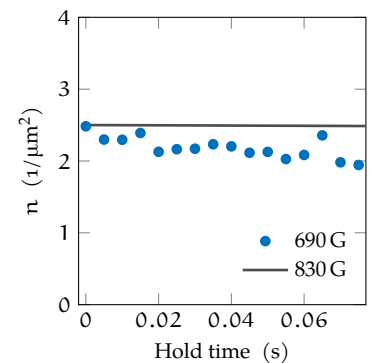


Figure 7.8: Measured mean density in dependence of the hold time in the dipole trap. At the studied magnetic field of 690 G (blue) and for comparison the fitted lifetime at 830 G (gray). The density decay from the T/4 measurements has been compensated for reduced detection due to detuning and particles leaving the detection volume.

time in the dipole traps. Two possible effects that impact the *equation of state* (EOS) of the trapped system are particle loss dN and a change in temperature dT . Therefore, both have been measured. The density loss has been found to be on the order of $0.29 \frac{\%}{\text{ms}}$ up to 70 ms, confer Fig. 7.8. The extraction of the experimentally accessible temperature, which has been found to only change moderately during the hold time, is described in more detail in Section 7.3.

In order to investigate the influence of hold time on a degenerate Bose gas, we prepare a dimerized Fermi gas at 690 G in the homogeneous trap geometry described in Chapter 2. The gas is kinematically frozen in the vertical direction and forms a 2D layer with temperature $T \approx 80$ nK and an average density of $n \approx 2.5 \frac{1}{\mu\text{m}^2}$. The chemical potential is thus $\mu/k_B \approx 85$ nK, both energy scales are below the harmonic oscillator spacing $\hbar\omega/k_B \approx 600$ nK. With these parameters, the gas is on the brink of degeneracy, if the weak-interaction estimate of the critical phase-space density $D_c \approx \ln(380/\bar{g}) \approx 6 \lesssim n\lambda_{dB}^2$ is still valid⁶⁸.

⁶⁸ N. Prokof'ev et al.: *Phys. Rev. Lett.*, vol. 87, (2001)

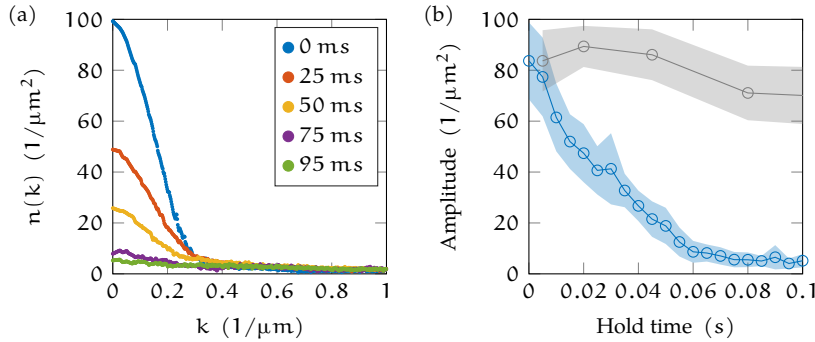


Figure 7.9: (a) Azimuthal averages of momentum distributions of a bosonic gas after different hold time. in situ (blue), 25 ms (red), 50 ms (yellow), 75 ms (violet), and 95 ms (green). Note the fast decrease in amplitude. (b) Maximum amplitude of the momentum distributions at 690 G after different hold time t (blue). Note the sharp decay for small times. The measured coherence decay close to the 3D Feshbach resonance at 830 G for comparison (gray). The shaded areas denote the statistical error bounds.

After preparation, the gas is held in the 2D dipole traps for a variable amount of time and subsequently a $T/4$ sequence is performed to image the momentum distribution. Examples of the measured momentum distributions are shown in Fig. 7.9a. For short hold times, a bimodal momentum distribution is observed, and the peak at low momenta, $k \leq 0.2/\mu\text{m}$, indicates coherence on a length scale of order $\approx 30 \mu\text{m}$. Note that the peak amplitude decreases quickly with increasing hold time. The peak amplitude versus hold time is plotted in Fig. 7.9b and a sharp decrease of the low- k population with time is immediately visible at 690 G, whereas the corresponding data taken close the 3D Feshbach resonance at 830 G exhibits a much slower decay. A common measure for degeneracy is the condensate fraction, which is the quotient of the number of atoms condensed in the ground state and the total number of atoms. Since no real condensate exists in two dimensions, a similar quantity, the *peak fraction*, is helpful to define in the interpretation. It indicates the number of atoms that occupy low-momentum modes with neither Gaussian nor exponential decay of coherence and hence possibly algebraic decay. The fraction of atoms contained within the peak is plotted in 7.10c. During the hold time, it decreases from $\approx 40\%$ to nearly zero, a much less drastic decay compared to the *peak amplitude* in Fig. 7.9b. This discrepancy is due to

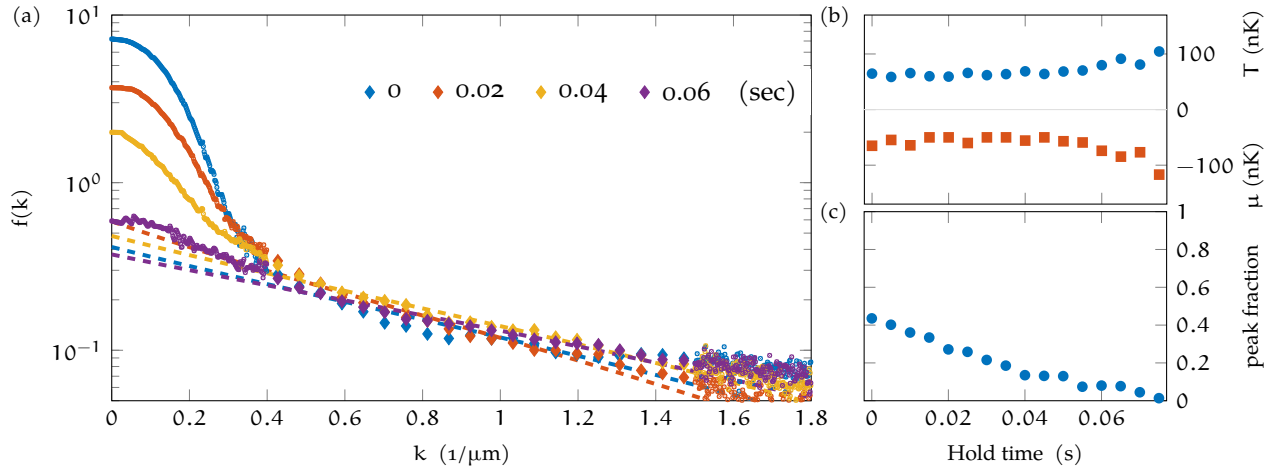
the geometry of the sample, the visually large peak amplitude is only present in a small k -area and thus does not actually lead to a large fraction of atoms contained in the peak. Nevertheless, the coherence loss occurs on relatively short time scales and remains the most prominent feature. The most straightforward explanation for this loss of coherence would lie in enhanced excitations due to an increased temperature, which destroy correlations. Hence, the accessible temperature of the system in dependence of holding time has been investigated.

7.3 EXTRACTING THE TEMPERATURE OF A HOMOGENEOUS GAS

A method to extract the temperature, which is applicable to the taken dataset, is to use the momentum distribution directly. For hotter gases, the thermal *wings* of the momentum distribution can be fitted by a Gaussian representing the Boltzmann population of the available states with energy ϵ , or alternatively, momentum k

$$f(k) = \frac{1}{e^{\beta(\epsilon(k)-\mu)} - 1} \approx A \cdot e^{-\frac{\beta\hbar^2}{2m}k^2}, \quad (7.10)$$

with the inverse temperature $\beta = 1/k_B T$, the particle mass m and an arbitrary amplitude A which is, in this approximation, not relevant for the extracted temperature.



As is evident from Fig. 7.9a, the signal above $k = 1/\xi \approx 1.4/\mu\text{m}$ is almost nonexistent. However, the Gaussian approximation of the momentum distribution given above is only valid in that region, where the kinetic energy dominates and the dispersion relation takes the simple form of $\epsilon = \frac{\hbar^2 k^2}{2m}$. Hence, we extend the ansatz to smaller k by including the full Bogoliubov dispersion relation

$$\epsilon(k) = \sqrt{\frac{\hbar^2 k^2}{2m} \left(\frac{\hbar^2 k^2}{2m} + 2g_{2D}n_{2D} \right)}. \quad (7.11)$$

With this extension, the exponential interval can be used to extract the temperature as well. The absolute accuracy of the extracted temperature suffers as a result, as mentioned by W. Ketterle et al., “[...]”

Figure 7.10: (a) Occupation $f(k)$ in logarithmic scale vs momentum k . Exemplary for four hold times 0, 0.02, 0.04 and 0.06 (blue, red, yellow, violet). The linear section of large diamonds is the fit interval, it has been boxcar averaged for the plot to improve visibility. (b) Temperature (blue, circles) and chemical potential (red, squares) versus hold time. Extracted by fitting the first term in Eq. (7.10) with the Bogoliubov dispersion relation Eq. (7.11). (c) The peak fraction (see text) versus hold time.

the systematic errors introduced by fitting too close to the condensate distribution are on the order of 2.⁹¹ Fortunately, the absolute value of T is only of secondary importance. To ascertain heating as the source of the decay of coherence, it is only necessary to investigate the relative change in temperature. Since the fitted momentum space density $n(k)$ is dependent on itself via the Fourier transform $\mathcal{F}\{n(k)\} = n_{2D}(r)$ in Eq. (7.11), the fitting process should in principle be repeated iteratively until the result has converged. However, the in situ density distribution for a homogeneous gas is easily determined and is, apart from fluctuations, not dependent on position. Thus, in this ansatz the interaction parameter g_{2D} and the position space density $n(r)$ are calculated beforehand and are assumed to be constant over the cloud.

To determine if the temperature of the gas changes, the momentum distributions are fitted with the above ansatz using a mean density of $n_{2D} = 2.5 \frac{1}{\mu\text{m}^2}$ and an interaction parameter of $g_{2D} \approx \frac{\hbar^2}{m} \cdot 0.87$. The data and corresponding fits are plotted for four hold times in Fig. 7.10a. Due to the logarithmic scale of the vertical axis, the approximately linear dependence of $f(k)$ is clearly visible. The fits to the linear regime yield temperatures T and chemical potentials μ which are shown in the 7.10b. As expected, both fit parameters increase in absolute value, the temperature by $\approx 40\%$ and the chemical potential by $\approx 50\%$ during ≈ 100 ms hold time. The decrease in chemical potential is compatible with the loss of atoms discussed earlier.

7.4 INTERPRETATION OF THE RESULTS

In summary, we observe that the peak occupation of low-momentum modes (peak fraction) decreases to $1/e$ (0.16) on a timescale of 37 milliseconds while the temperature increases by 3% and the density decreases by 10% during the same time.

There are at least two possible interpretations for the observed behavior. The first assumes that the gas is in thermal equilibrium and attributes the decrease of low-momentum modes and corresponding loss of coherence to heating, which causes the gas to cross the transition from a *Berezinskii-Kosterlitz-Thouless* (BKT) superfluid to a normal fluid. Possible sources for heating are three-body losses, collisions with particles in the background gas, parametric heating by intensity noise on the laser beams and other technical noise induced by the control of the magnetic fields and dipole traps.

Taking into account the rather short timescales on which the coherence is lost, non-equilibrium effects also have to be considered. These are particularly relevant in 2D gases since local excitations in form of vortices are topologically protected. When the time an excitation needs to travel across the sample is estimated by the speed of sound one finds that the time scales for thermalization are on the same order as the duration of the used preparation such as magnetic field sweeps or settling times. Hence, the gas might not be in complete thermal equilibrium yet.

⁹¹ W. Ketterle et al.: *Making, probing and understanding Bose-Einstein condensates*, (1999)

The fit of the chemical potential is coupled to the fitted temperature. Although the result is compatible with the measured in situ densities, due to the aforementioned systematic errors introduced, the *fitted* chemical potential is not used in the further analysis.

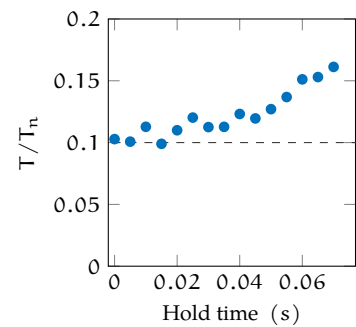


Figure 7.11: Extracted inverse phase-space density T/T_n in dependence of hold time

In the following, we discuss these possible interpretations and corresponding measurements in more detail. The energy associated with the absolute temperature of a cold gas by itself does not determine the momentum distribution, as can be seen from Eq. (7.11). Only in combination with the energy related to the density of the sample, a measure of degeneracy is obtained. The phase-space density would be a prime candidate. However, for better comparison, a common measure related to the phase-space density is used here instead, T/T_F . Here, the temperature T is compared to the Fermi temperature T_F , which is derived from the Fermi energy. Since the Fermi energy is not a well defined property of the present interacting Bose gas, this can be understood as a mapping to the temperature T_n of a non-interacting gas of fermions of the same density. With this, T/T_n in dependence of hold time can be calculated from the extracted temperatures as well as integrated densities divided by the in situ *box area*, shown in Fig. 7.11. From this, it is apparent that the decrease in density and the increase in temperature lead to an increase in T/T_n and thus to a decrease in phase-space density.

WHEN USING A QUANTITY SUCH AS TEMPERATURE, it is necessary for the system to be in thermodynamic equilibrium. This is usually the case for cold quantum gases since scattering processes redistribute the energy on much shorter time scales than those used for preparing the gas. Hence, all procedures can be assumed to be adiabatic and the gas is always in a thermalized state. This is not necessarily true for very cold 2D systems of interacting bosons if vortices are present, as V. Singh et al. have demonstrated⁹².

Hence, there are two possible avenues of interpretation, whether one assumes thermal equilibrium or not. First, the assumption of thermal equilibrium will be discussed. Subsequently, a plausible non-equilibrium scenario will be explored.

IN THERMAL EQUILIBRIUM, the extracted temperature is a valid measure of the distributed energy. Since T/T_n increases with hold time, the energy contained in the gas increases and the critical energy for degeneracy decreases. In combination, this could lead to the observed behavior, where the number of particles in the low-momentum peak vanishes with hold time. Assume that the *critical fraction*, that is the amount of particles that exhibit non-thermal physics is approximately

$$\frac{n_c}{n} = 1 - \frac{T}{T_{KT}}. \quad (7.12)$$

This is certainly an oversimplification, since the integral over the *density of states* (DoS) does not converge and thus the usual argument for this form is not applicable if the system were infinite. For finite systems however, the *Kosterlitz-Thouless* (KT) transition is always accompanied by a significant *Bose-Einstein condensate* (BEC) fraction and thus the approximation is better justified. The critical temperature

Extra 7.3: Origin of T_n

The phase-space density D for bosonic dimers of density n_{2D} introduced in 3.2 is

$$D = n_{2D} \lambda_{dB}^2 \\ = \frac{2\pi\hbar^2}{mk_B} \cdot \frac{n_{2D}}{T}.$$

When compared to the valid relation in Fermi systems of $T/T_F = 1/D$ one arrives at

$$\frac{1}{D} = \frac{mk_B}{2\pi\hbar^2} \cdot \frac{T}{n_D} = \frac{T}{T_F},$$

with $k_F = \sqrt{4\pi n_{2D}}$, usually defined for non-interacting fermions at $T = 0$. This is in essence a scaled comparison of the temperature T and the density n_{2D} . Since it reduces the ambiguity of what energy the temperature is actually compared to, we adopt the nomenclature

$$T/T_n = T/T_F.$$

⁹² V. P. Singh et al.: *Phys. Rev. A*, vol. 95, (2017)

The use of the word *adiabatic* in quantum mechanics⁹³ is slightly different than in classical thermodynamics. Whereas it usually denotes a process of a system *without heat or matter transfer* with its surroundings, here it signifies a *quasi-static* and *isoentropic* process, which is virtually reversible. In this sense, it does not randomly change the occupation numbers of the system and thus has been done *without heat transfer*.

⁹³ M. Born: *Nature*, vol. 119, (1927)

One can show³³ that for finite systems just below the critical temperature, there exist a condensed fraction on the order of $N^{-1/8}$. Since in practice $N \approx 40000$ one expects a sizable condensed fraction and Eq. (7.12) can be considered approximately as a *lower limit*.

³³ Z. Hadzibabic and J. Dalibard: *Riv. Nuovo Cimento*, vol. 34, (2011)

T_{KT} , necessary to evaluate the above expression, can be derived from

$$D_{\text{crit}} \approx \ln\left(\frac{380}{\bar{g}}\right) \approx 6 = n\lambda_{\text{dB,crit}}^2 \quad (7.13)$$

$$\Rightarrow T_{KT}(n = 2.5 \frac{1}{\mu\text{m}^2}) \approx 105 \text{ nK} \quad (\text{after preparation})$$

$$\Rightarrow T_{KT}(n = 1.7 \frac{1}{\mu\text{m}^2}) \approx 72 \text{ nK}. \quad (\text{after 60ms hold time})$$

Given these approximations, a significant decrease of *critical fraction* can be expected even for small changes in T/T_n , as is shown in Fig. 7.12.

If the temperature of the system increases, what are the sources of the additional thermal energy? Since the atoms are held in an optical dipole trap, a transfer of photon energy to the gas is possible. Laser intensity noise modulates the trapping potential which – at the right frequency – leads to a parametric heating process⁹⁴ where two quanta from the light field are transferred to kinetic energy in the gas. However, significant amplitude noise at twice the trap frequency, necessary for parametric heating, has not been observed in measurements of the laser power with high-speed photo diodes. Additionally, reference measurements on non-interacting Fermi gases have shown only negligible heating when subjected to a similar experimental procedure.

ANOTHER SOURCE OF HEATING are inelastic collisions between the particles in the system. During this process, energy from the internal structure of the scatterers can be transferred to kinetic energy, effectively heating the gas. In the case of the presented gas of an equal mixture of fermions forming bosonic dimers, the leading order process is a two dimer collision in either s-wave or low orbital momentum channels⁹⁵. During the approach of two dimers of approximate size a_{3D} , three of the constituent fermions engage in a three-body collision. One of the dimers relaxes into a deeply bound molecule with binding energy $E_B \gg \hbar^2/(ma_{3D}^2)$ while the other dimer dissociates into free fermions. The energy released by forming the deeply bound molecule is distributed to the scattering products which can subsequently scatter with the remaining particles of the gas and deposit this excess energy as heat. Due to the high velocity, and thus reduced scattering cross section, of the particles in the output channel of the scattering process, only a fraction of the total released energy is imparted as heat into the sample. Additionally, due to the geometry of the sample, most of the scattered particles leave the gas with only a low number of secondary scattering events. Since the particles are located in a thin layer, the output particles have a high probability to propagate into the large empty solid angle above and below the cloud. Therefore, the secondary scattering process is most likely to occur in close vicinity to the location of the original decay event and is thus a local excitation. In summary, a slight increase in temperature accompanying the observed atom loss is very plausible although the precise

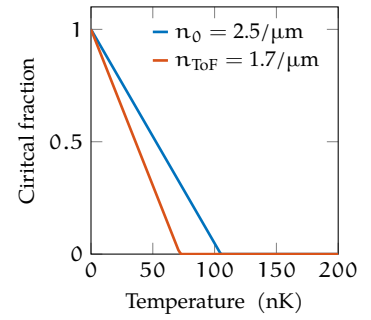


Figure 7.12: Model of the critical fraction in dependence of Temperature for two in situ densities. For the originally prepared system $n_0 = 2.5/\mu\text{m}^2$ (blue) and after 60 ms ToF $n_{\text{ToF}} \approx 1.7/\mu\text{m}^2$ (red, dashed).

⁹⁴ T. A. Savard et al.: *Phys. Rev. A*, vol. 56, (1997)

⁹⁵ D. S. Petrov et al.: *Phys. Rev. A*, vol. 71, (2005)

amount is difficult to estimate. It is important to note that this process necessarily combines heating with atom loss since both, the deeply bound molecule and the free fermions, escape the trap.

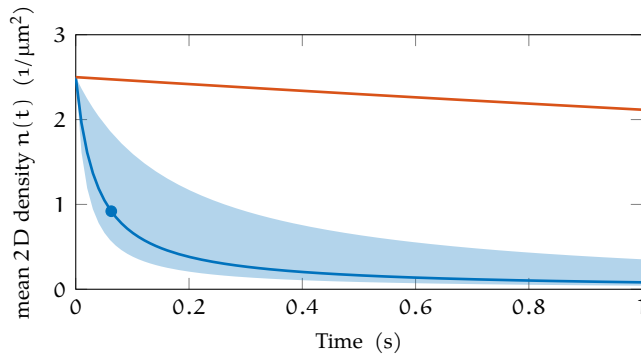
One body collisions with the background gas can also lead to heating by removing single particles from the sample and the thus ensuing reorganization cascade. If only scattering of particles within the sample is considered, the collisions must necessarily be inelastic or the scattering event must consist of multiple particles in order to lead to heating. Thus, three or more atoms must participate since the internal structure of the ^6Li atom can be neglected at this energy scale. Nonetheless, the loss rate can be modeled as a two-body decay since two dimers collide. Hence, the squared dimer density appears in the rate equations. The rate equations and solution for one- and two-body decay can be written as⁹⁶

$$\frac{dn}{dt} = -\alpha n - \beta_{dd} n^2, \text{ thus } n(t) = \frac{n_0}{e^{\alpha t} + \frac{\beta_{dd} n_0}{\alpha} (e^{\alpha t} - 1)}. \quad (7.14)$$

Here, α denotes the inverse one-body $1/e$ lifetime, β_{dd} the two-body loss coefficient for dimer-dimer relaxation and n_0 the mean density at $n(t=0) = n_0$. The one-body lifetime has been measured to be in excess of 6 s whereas the two-body loss coefficient is dependent on the scattering length a_{3D} by

$$\beta_{dd} = C \frac{\hbar r_{vdW}}{m} \left(\frac{r_{vdW}}{a_{3D}} \right)^{2.55}, \quad (7.15)$$

with the length of the characteristic van der Waals potential r_{vdW} and a system dependent parameter C . Fortunately, compatible values for these parameters have been independently determined experimentally^{97,98}. The available coefficient for our scattering length of $a_{3D} \approx 75 \text{ nm}$ is $\beta_{dd}(75 \text{ nm}) \approx 5 \times 10^{-18} / (\text{m}^3 \text{ s})$. According to T. Lompe, this value is assumed to be accurate up to a factor of 2*. Notwithstanding, the two-body scattering channel is still the dominant loss mechanism⁵¹ with a $1/e$ loss time on the order of 100 ms, as can be seen clearly in Fig. 7.13. Atom loss due to evaporation can be disregarded since the



interaction strength is ramped down from a much higher value during preparation. Thus the potential energy of the gas should be well below the trap depth.

This four-body decay can be thought of as a three-plus-one decay, due to the fact that when two large dimers scatter, the fourth atom does not participate in the relaxation process. Also, the Decay involving more than two-dimers is ignored here due to its diminished relative effect.

⁹⁶ M. Weidemüller: *Cold Atoms and Molecules*, (2009)

This dependency holds only if $a_{3D} \gg r_{vdW}$. Since for lithium, $r_{vdW} \approx 60 a_0$ this is valid for the regime of interest.

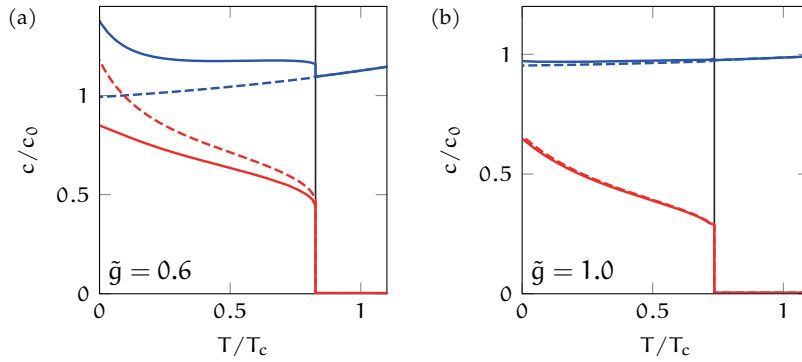
⁹⁷ T. Lompe: *Effimov Physics in a three-component Fermi gas*, (2011), ⁹⁸ S. Nakajima et al.: *Phys. Rev. Lett.*, vol. 105, (2010)

* Private communication, T. Lompe

⁵¹ E. Burt et al.: *Phys. Rev. Lett.*, vol. 79, (1997)

Figure 7.13: Expected combined one- and two-body decay (blue) of initial density with hold time. The shaded area denotes the error margin and the marker the $1/e$ time. Compare with only one-body loss (red).

AS ARGUED ABOVE, a decrease of the population of low-momentum modes is expected, yet the timescales are surprisingly short. The shortest time scale on which thermalization can be expected is proportional to the highest relevant energy, in this case the interaction energy $\mu = g_{2D}n_{2D} \approx 1.8 \text{ kHz} \cdot \hbar$ leading to a time scale of $t_\mu \approx 550 \mu\text{s}$. However, this is only the fastest timescale. A lower bound for the time it takes the gas to thermalize via the dissipation of locally deposited energy to the rest of the gas is given by the time an excitation needs to travel across the entire sample. For this, two phononic excitations need to be considered, an excitation in density and an excitation in entropy. These excitations hybridize below $k_B T_{\text{hyb}} \approx g_{2D}n_{2D}$ ⁹⁹ and the higher velocity is denoted *first sound*, whereas the lower velocity is denoted *second sound*. For temperatures well below the critical temperature, the entropy wave is faster than the density wave and for higher temperatures vice versa. However, for stronger interactions this hybridization is less pronounced since the thermal and entropic compressibility approach each other^{100–102}.



It is evident from the respective velocities plotted in Fig. 7.14, that for an interaction parameter of $\tilde{g} = 0.87$, and a temperatures close to the critical KT temperature, the zero-temperature Bogoliubov sound velocity c_0 is a reasonable approximation. This velocity is defined as the derivative of the chemical potential μ at constant volume V and temperature T and hence in the low temperature approximation given by⁹⁰

$$c_0 \approx \sqrt{\frac{n_{2D}}{m_{\text{dimer}}} \cdot \left(\frac{\partial \mu}{\partial n_{2D}} \right)_{V,T}} \approx \sqrt{\frac{n_{2D} g_{2D}}{m_{\text{dimer}}}}. \quad (7.16)$$

For the samples considered here, with a density of $n_{2D} \approx 2.5/\mu\text{m}^2$, this yields a maximum velocity for energy dissipation of $c_0 \approx 7.8 \frac{\mu\text{m}}{\text{ms}}$. Hence, a sound wave would need approximately 20 ms to traverse the entire sample of size $L \approx 139 \mu\text{m}$, slower than both, the 10 ms magnetic field ramp time used to go to the BEC regime as well as the 10 ms settling time following the ramp. Furthermore, the low-momentum modes that are considered here have momenta* $< 0.1/\mu\text{m}$ and therefore length scales of $\geq 63 \mu\text{m}$. Thus, it is likely that the system as a

Of course, the energy defined analogously to the Fermi energy, $E_n/k_B \approx 600 \text{ nK}$ as well as the zero point energy $\frac{\hbar\omega_z}{2k_B} \approx 300 \text{ nK}$ are much higher. However, these are not the relevant energy scales for thermalization in a gas of interacting bosons.

In the condensed matter context, lattice vibrations are known as phonons. Despite the absence of these vibrations, the excitations, reminiscent of acoustic phonons, with a linear dispersion relation are called phonons.

⁹⁹ L. Verney et al.: *EPL*, vol. 111, (2015)

¹⁰⁰ M. Ota and S. Stringari: *Phys. Rev. A*, vol. 97, (2018), ¹⁰¹ X. J. Liu and H. Hu: *Ann. Phys.*, vol. 351, (2014), ¹⁰² T. Ozawa and S. Stringari: *Phys. Rev. Lett.*, (2014)

Figure 7.14: First and second sound as a function of temperature in the hybridization region of a homogeneous 2D interacting Bose gas from (a) intermediate, $\tilde{g} = 0.6$, to (b) stronger interactions $\tilde{g} = 1.0$. The interaction strength of our experiment is $\tilde{g} \approx 0.87$ whereas the temperature is on the order of $T_c = T_{KT} \approx 100 \text{ nK}$. The upper blue and lower red solid lines correspond to first and second sound respectively. The upper blue and lower red dashed lines are approximated forms for independent density and entropy modes. The strong deviation from which for smaller interactions strength indicates a significant coupling between both modes. Figure adapted from M. Ota¹⁰⁰.

¹⁰⁰ M. Ota and S. Stringari: *Phys. Rev. A*, vol. 97, (2018)

⁹⁰ L. Salasnich et al.: *Phys. Rev. A*, vol. 88, (2013)

*The plot of $n(k)$ in Fig. 7.10 shows the measured width of the momentum distribution. During imaging a PSF_{eff} is convolved with the actual signal, see Section 9.2.2. The PSF_{eff} has a full width at half maximum (FWHM) of $\approx 6 \mu\text{m}$ to $8 \mu\text{m}$. Thus, the width imaged is mostly due to the PSF_{eff} . The expected size of $n(k)$ for a degenerate 2D Bose gas is $\approx 1 \mu\text{m}$ and therefore much smaller, as can be seen in Fig. 7.17a

whole is not fully equilibrated.

A possible interpretation is hence that the magnetic field ramp is non-adiabatic and that temperature and momentum distribution immediately after the ramp and settling time are still very similar to the momentum distribution the gas had initially, i. e. at 834 G, where the 3D scattering length diverges. Here, the critical phase-space density is decreased⁶⁸ and thus the critical temperature is much higher^{47,91}. Thus, the magnetic ramp corresponds effectively to a quench of a BKT superfluid with quasi-long-range order to a supercritical regime which now decays into a thermal gas. This would, in principle, explain our observation, since when the gas is held at 834 G no drastic reduction of low-momentum modes could be observed. Furthermore, if ramped slowly, a much reduced occupation of the low-momentum modes is observed.

Nevertheless, it is somewhat puzzling that the low-momentum modes exhibit faster decay than those at larger momenta. Typically, one would expect modes with larger momentum to thermalize faster since smaller length scales and higher energy scales are involved. A similar situation is discussed in two very relevant publications by the Mathey group^{92,103}. In the first, the authors investigate a similar quench of interactions numerically. They find that during the thermalization process intermediate states appear that exhibit algebraic decay albeit with a power law exponent larger than what is allowed and expected in equilibrium. In the second, they observe very slow thermalization across the interface between the superfluid and the thermal part in a spatially inhomogeneous gas. This lies in the fact that due to the reduced dimensionality, topologically protected vortex pairs have a much suppressed decay rate. The vortices must either annihilate with antivortices or drift towards low density regions where they can decay individually. There exists no definitive theoretical prediction of the timescale for the vortex drift for our exact parameters but the above mentioned simulations yield a decay time on the order of seconds and a reasonable agreement with the prediction of P. Fedichev and G. Shlyapnikov¹⁰⁴ which states for the decay rate τ^{-1}

$$\tau^{-1} \sim \frac{\hbar}{m_d R^2} (n_s a_{3D}^3) \frac{T}{\mu}. \quad (7.17)$$

Here, m_d is the mass of the bosonic dimer, μ the chemical potential and R the radius of disk that the vortex occupies. For an upper limit the superfluid density n_s is assumed to be the total density $n_s \approx n_{\text{total}} = 5.5/\mu\text{m}^3$ and $T \approx \mu$, see Fig. 7.10. The resultant timescale is on the order of hundreds of seconds for the limiting case of exactly one vortex and still on the order of a hundred milliseconds for a vortex of the smallest possible size of ξ_h and a more reasonable estimate of $n_s = 0.4n_{\text{total}}$.

The timescale for the annihilation of a vortex-antivortex pair is also dependent on the healing length of the Bose gas. Since this particular parameter is comparable to the experiment by J. Dalibard, we assume that the computed decay times of the above mentioned simulation of approximately 130 ms are also valid for our system.

⁶⁸ N. Prokof'ev et al.: *Phys. Rev. Lett.*, vol. 87, (2001)

⁴⁷ S. Giorgini et al.: *Phys. Rev. A*, vol. 54, (1996), ⁹¹ W. Ketterle et al.: *Making, probing and understanding Bose-Einstein condensates*, (1999)

⁹² V. P. Singh et al.: *Phys. Rev. A*, vol. 95, (2017), ¹⁰³ L. Mathey et al.: *Phys. Rev. A*, vol. 95, (2017)

¹⁰⁴ P. O. Fedichev and G. V. Shlyapnikov: *Phys. Rev. A*, vol. 60, (1999)

Estimating the relevant energy scale is not trivial since the vortex energy of a 2D system diverges as $E_v \approx \frac{\pi n_s \hbar^2}{m_d} \ln(1.464b/\xi_h)$, with b being the boundary of the area under consideration and ξ_h the healing length. In essence, single vortex decay is strongly suppressed by the trap geometry since there are no low-density areas and hence, the vortex has to travel the full distance to the edge of the homogeneous sample.

The annihilation of vortex-antivortex pairs is strongly suppressed in 2D systems^{105,106}, as well as stable against rotating away from the line of sight¹⁰⁷. Hence, due to the unique topology, vortices in 2D are exceptionally stable.

¹⁰⁵ S. Prabhakar et al.: *J. Phys. B*, vol. 46, (2013), ¹⁰⁶ S. J. Rooney et al.: *Phys. Rev. A*, vol. 84, (2011), ¹⁰⁷ P. C. Haljan et al.: *Phys. Rev. Lett.*, vol. 86, (2001)

Thus, if vortices are present due to the preparation or are created during, e. g. the dimer-dimer decay, it is probable that they have not fully dissociated in the course of our measurements. Therefore, the decay of the low-momentum modes might not solely be due to the heating in thermal equilibrium but also be driven by out of equilibrium dynamics.

THE NON-EQUILIBRIUM DYNAMICS could be numerous. Only two possible scenarios will be explored here since a detailed treatment of strongly interacting many-body non-equilibrium dynamics presents ongoing challenges, many of which are very difficult to solve. At the time of writing, the author is unaware of theoretical predictions for the dynamical structure factor of a strongly interacting Bose gas with our parameters. Hence, one possible explanation could be a *global quench* of the systems parameters – such as the scattering length – so that the system undergoes a time evolution in a new Hamiltonian $H'(t > t_0)$. Although, for a closed quantum system such as a trapped gas, this process is entirely unitary it is expected that for long times large systems exhibit a state that seems to have equilibrated¹⁰⁸.

In the presented measurement, the global magnetic field is changed quickly from the 3D Feshbach resonance of ≈ 834 G to the field of interest of ≈ 690 G. At the new field the critical entropy is lower than before and thus the system is suddenly quenched from the superfluid to the normal phase. The measurements taken by increasing the hold time might then sample the phase coherence of the dynamics at different times. At first, a large population of low-momentum modes can still be observed while for longer times, when the system has evolved to the ground state of the new governing Hamiltonian, a larger population of excited modes is exhibited.

Alternatively, the system could be driven locally out of equilibrium by e. g. a dimer-dimer decay. Depending on the type of excitation – for example phononic, particle or vortex like – these *local quenches* are limited by Lieb-Robinson bounds in their speed of information propagation. Thus, the system might exhibit excitations such as vortices for long times compared to the hold time without equilibrating. These excitations would destroy the low-momentum population which depends on correlations over large extents without being reflected in the experimentally accessible temperature.

Perturbations to the phase of the wave function of the many body state is the dominant excitation in low temperatures. Hence, in the following, the normalized first order phase correlation function $g_1(r)$ will be computed from the presented momentum distributions in order to examine if additional insight into the unexpectedly fast coherence decay can be gained.

¹⁰⁸ J. Eisert et al.: *Nature Physics*, vol. 11, (2015)

The total entropy of the system is expected to be conserved during the magnetic field ramp.

The dimer-dimer decay of four atoms has a decay channel with global orbital momentum of zero but since usually only three particles participate directly in the relaxation it is possible to impart the remaining rotational momentum onto the gas. Additionally, the scattering event creates a hole, facilitating vortex creation.

In the approximation of Bogoliubov quasiparticles, phase perturbations are the dominant excitations. This is due to the fact that the linear phase fluctuations are much cheaper in terms of energy than the highly suppressed density fluctuations of particle like excitations.

Extra 7.4: $g_1(\mathbf{r})$ as the Fourier transform of $n(\mathbf{k})$

In many experimental contexts, it will be difficult to determine the dependence of the correlation functions on all coordinates or – like in the present case – the problem does not depend on all degrees of freedom. It may then be more adequate to measure the volume integrated correlation function

$$G_1(\mathbf{r}) = \int_{-\infty}^{+\infty} d^2s \langle \hat{\psi}^\dagger(\mathbf{s}), \hat{\psi}(\mathbf{s} + \mathbf{r}) \rangle,$$

where the coordinate system has been shifted and \mathbf{x} and \mathbf{x}' have been replaced by the center of mass \mathbf{s} and the relative coordinate $\mathbf{r} = |\mathbf{x} - \mathbf{x}'|$, respectively. To see how the momentum distribution $n(\mathbf{k}) = \langle \hat{\psi}^\dagger(\mathbf{k})\hat{\psi}(\mathbf{k}) \rangle$ for a homogeneous system is related to G_1 , it is useful to insert the definition of the position space operators in terms of a Fourier transform of the momentum space operators

$$\hat{\psi}(\mathbf{x}) = \frac{1}{(2\pi)^2} \int_{-\infty}^{+\infty} d^2k e^{i\mathbf{k}\mathbf{x}} \hat{\psi}(\mathbf{k})$$

directly into the above equation:

$$\begin{aligned} G_1(\mathbf{r}) &= \int d\mathbf{s} \langle \frac{1}{(2\pi)^2} \int d^2k e^{-i\mathbf{k}\mathbf{s}} \hat{\psi}(\mathbf{k}), \dots \\ &\quad \frac{1}{(2\pi)^2} \int d^2k' e^{i\mathbf{k}'(\mathbf{s}+\mathbf{r})} \hat{\psi}(\mathbf{k}') \rangle \\ &= \frac{1}{(2\pi)^4} \int d\mathbf{k} \int d\mathbf{k}' \dots \\ &\quad \underbrace{\int d\mathbf{s} e^{-i(\mathbf{k}-\mathbf{k}')\mathbf{s}} e^{i\mathbf{k}'\mathbf{r}} \langle \hat{\psi}(\mathbf{k})\hat{\psi}(\mathbf{k}') \rangle}_{(2\pi)^2 \delta(\mathbf{k}, \mathbf{k}')} \\ &= \frac{1}{(2\pi)^2} \int d\mathbf{k} \int d\mathbf{k}' \delta(\mathbf{k}, \mathbf{k}') e^{i\mathbf{k}'\mathbf{r}} \langle \hat{\psi}(\mathbf{k})\hat{\psi}(\mathbf{k}') \rangle \\ &= \frac{1}{(2\pi)^2} \int d\mathbf{k} e^{i\mathbf{k}\mathbf{r}} \langle \hat{\psi}(\mathbf{k})\hat{\psi}(\mathbf{k}) \rangle. \end{aligned}$$

The limits of integration have been omitted for readability. The last line is precisely 2π times the Fourier transform of $n(\mathbf{k}) = \langle \hat{\psi}(\mathbf{k})\hat{\psi}(\mathbf{k}) \rangle$. This factor will be consumed by the normalization. For all translational invariant systems, the above equation can be simplified since the center of mass coordinate does not contribute and the integration yields a constant volume factor. Hence, $G_1(\mathbf{r}) \propto G_1(0, \mathbf{r})$, the true correlation function, over the the full lateral extend of our system.

7.5 TOWARDS EXPERIMENTAL ACCESS TO THE FIRST ORDER CORRELATION FUNCTION

A different perspective on the coherence properties displayed by the momentum distribution can be achieved by investigating its Fourier transform, the first order correlation function $g_1(\mathbf{r})$. Following the definition in Eq. (4.26), the first order correlation function can generally be written in operator notation as

$$G_1(\mathbf{x}, \mathbf{x}') = \langle \hat{\psi}^\dagger(\mathbf{x})\hat{\psi}(\mathbf{x}') \rangle. \quad (7.18)$$

Since most systems exhibit correlation only in an approximate way, the locally normalized first order correlation function

$$g_1(\mathbf{x}, \mathbf{x}') = \frac{G_1(\mathbf{x}, \mathbf{x}')}{\sqrt{G_1(\mathbf{x}, \mathbf{x})}\sqrt{G_1(\mathbf{x}', \mathbf{x}')}} \quad (7.19)$$

is used to define correlation of the complex field amplitude⁴². This

⁴² M. Naraschewski and R. J. Glauber: *Phys. Rev. A*, vol. 59, (1999)

normalization carries over to the translational invariant form $g_1(\mathbf{r}) \propto g_1(0, \mathbf{r})$ and will be used from here on.

TWO EXPERIMENTAL EFFECTS MUST BE CONSIDERED when applying the Fourier transform to yield the proper first order correlation function. First, the finite extent of the sample imparts a bias towards small distances and second, even an ideal imaging system with no aberrations is limited in its resolution by the finite aperture. Hence, both effects on g_1 are presented and methods for compensation are discussed.

Consider an ideal bosonic 2D system that stretches laterally to infinity. In such a system it is only possible to have a true BEC when the temperature vanishes. Since it is useful to compare the discussed effects on different correlation functions, three different temperatures are considered: At $T_0 = 0$ K, a true BEC is present with perfect coherence, above zero temperature but below the critical KT temperature $T_0 < T < T_{KT}$, the gas exhibits algebraic decay of coherence and for even larger temperatures $T_{\text{thermal}} \gg T_{KT}$, the decay will be exponential.

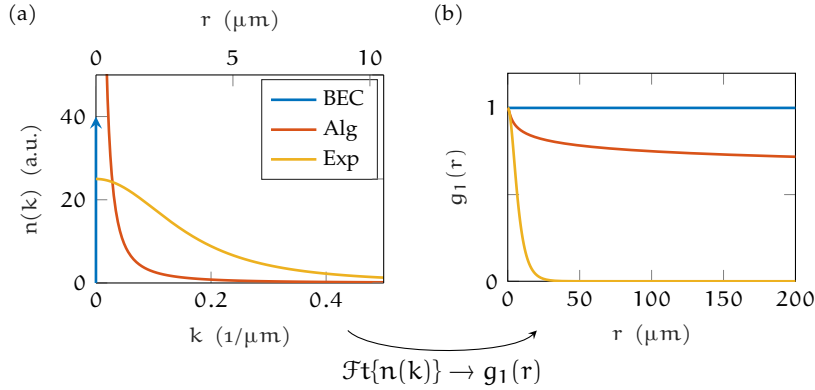


Figure 7.15: (a) Theoretical momentum distribution for a true BEC (blue) and a quasi-condensate with algebraic (red) and exponential (yellow) phase decay. The arrow represents a Dirac delta distribution. Since these distributions can be measured via matter wave focusing, the corresponding spatial dependency under typical experimental conditions is displayed on the upper axis. Note that both, the BEC and the algebraically decaying quasi-condensate require high imaging resolution due to their small scale. (b) Theoretical correlation functions corresponding to the momentum distributions shown in (a) with identical colors. Note the rather slow algebraic decay which exhibits a finite value even for large – but finite – values of r . The first order correlation function $g_1(r)$ is related to the momentum distribution $n(k)$ by a Fourier transformation.

The momentum distributions for these cases are plotted in Fig. 7.15a. All particles in the BEC (blue) populate only the lowest k -mode and $n(k)$ is thus a Dirac delta distribution. The widths of the algebraic and the exponential decay depend on the temperature, nevertheless, the thermal momentum distributions is often much broader in comparison. The corresponding normalized first order correlation function $g_1(r)$ is plotted in Fig. 7.15b. Here, a constant value of $g_{1,\text{BEC}} = 1$ indicates that the correlations do not decay. In comparison, the algebraic (red) and the exponential (yellow) correlation functions decay much faster. Note that even though $g_{1,\text{BKT}}$ vanishes at infinity, the gas exhibits significant coherence for length scales relevant in the laboratory.

The individual effects will be demonstrated on the simplest case of the true BEC and finally compared to both other cases.

ANY REAL SYSTEM HAS FINITE EXTENT. If the size of the system is restricted to a circular homogeneous layer of diameter $L = 139 \mu\text{m}$ (approximately the size of our prepared sample) the constituent wave functions end abruptly at the boundary. This can be modeled by multiplication with a Heaviside θ -function, i. e. $\psi(r) \rightarrow \psi(r) \cdot \theta(L/r - 1)$.

Inserting this into the definition of g_1 would lead to the correlation – $\langle *, * \rangle$ – of the original state multiplied with the correlation of the θ -functions

$$\langle \hat{\psi}^\dagger(\mathbf{r}), \hat{\psi}(\mathbf{r}) \rangle \longrightarrow \langle \hat{\psi}^\dagger(\mathbf{r}), \hat{\psi}(\mathbf{r}) \rangle \cdot \langle \theta(\mathbf{r}), \theta(\mathbf{r}) \rangle. \quad (7.20)$$

The autocorrelation of the Heaviside function can be calculated analytically even for two dimensional systems and resembles a pyramid with a smooth continuation to zero. Thus, even the correlation function of a perfect BEC shows significant decay if the system is finite, which is plotted in Fig. 7.16b. As a consequence, the original momentum distribution, in the shape of a delta distribution, is convolved with a squared Bessel function which broadens it significantly, as can be seen in Fig. 7.16a. The effect of a finite aperture is also easier under-

The effect of the finite size of the signal is exactly analogous to the way an aperture stop in optics leads to a decaying *transfer function* that limits the resolution by suppressing high frequencies.

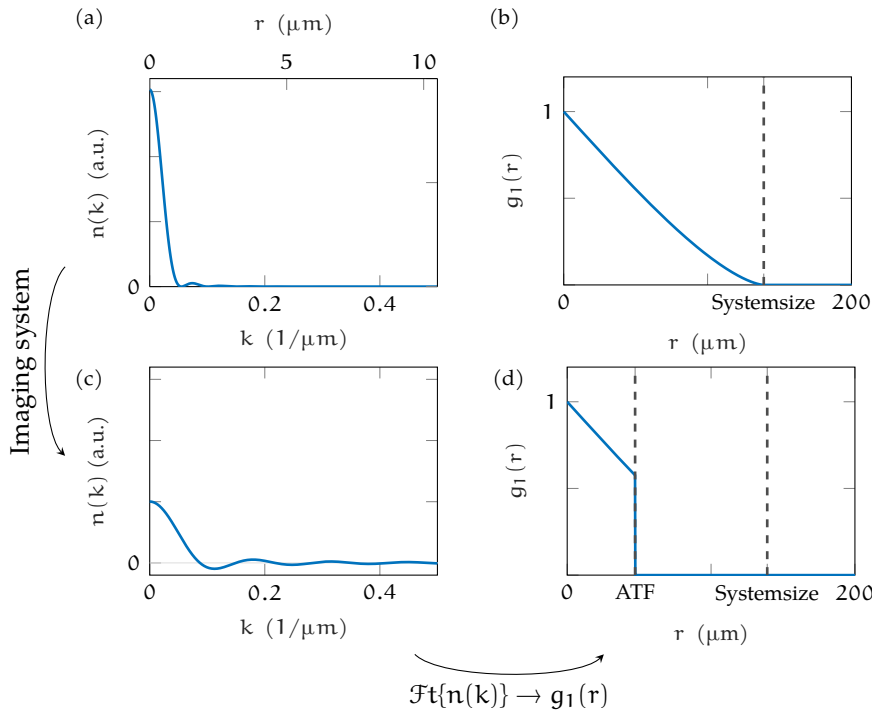


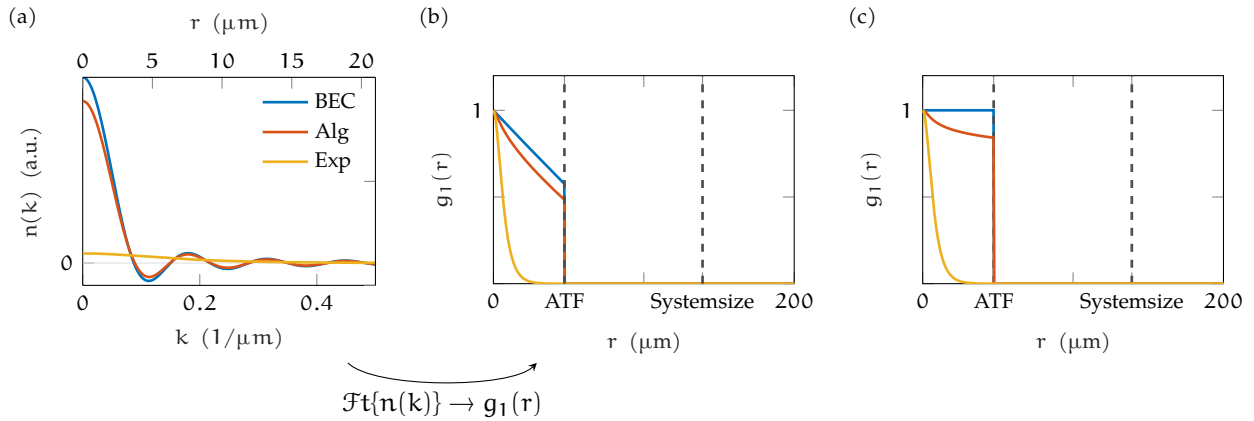
Figure 7.16: (a) Theoretical momentum distribution of a finite BEC. (b) Theoretical first order correlation function of a finite BEC. (c) Theoretical momentum distribution of a finite BEC considering the influence of imaging. (d) Theoretical correlation function of a finite BEC considering the influence of imaging. For details see the text.

stood in terms of g_1 . As is shown in Section 9.2.2, the *amplitude transfer function* (ATF) of non-aberrated coherent imaging cuts off the signal abruptly at some maximum value in reciprocal space. Since the real space coordinate after T/4-time represents the momentum space k , the r -coordinate after performing the Fourier transform is in the same reciprocal space as the ATF. Thus, the ATF sets an upper limit for the measurable correlation function. This is demonstrated for a numerical aperture of $NA = 0.12$ in Fig. 7.16d. This additional *high frequency cut-off* broadens the corresponding $n(k)$ even more, which can be seen in Fig. 7.16c. Note that although both, finite size and imaging, lead to a cutoff in g_1 , they are unrelated effects.

Remarkably, due to its origins in the absorption imaging, the sharp cutoff also leads to small negative values in the measured momentum distribution. These of course are an artifact of the measurement and hold no physical meaning.

NOT BOTH EFFECTS CAN BE FULLY CORRECTED during the analysis. The gradual suppression of longer distances due to the finite size can be

compensated by dividing g_1 with the known shape of the autocorrelator. None the less, where the suppression function vanishes, a reconstruction is impossible. Thus, no signal beyond the size of the system L or the resolution of the imaging system can be extracted. That means – for ideal imaging conditions – one cannot simply *deconvolve* an image with the *PSF* and improve the signal. In practice however, it is useful to compensate for the imaging system also, since a real-world *ATF* is usually not Heaviside-like but exhibits some structure due to aberrations or defocus.



The *point spread function* (PSF) is the two-dimensional Fourier transform of the *amplitude transfer function* (ATF) and hence a deconvolution with the former is identical to a division with the latter.

How the momentum distributions in Fig. 7.15a are impacted by the finite size and the imaging effects, is shown in Fig. 7.17. It is interesting to see that the signal of a BEC (blue) is almost indistinguishable from a BKT gas (red), only the exponential decay (yellow) is clearly distinct. The corresponding correlation functions show again that, apart from the exponential decay, the curves are very similar, which can be seen in Fig. 7.17b. When corrected for finite size, the curves of constant coherence and algebraic decay separate more and show distinguishable slopes, as can be seen in Fig. 7.17c. Interestingly, almost no benefit of the compensation can be observed for thermal gases due to the very short range of their correlations and thus comparatively large size in momentum space after $T/4$ time.

NOW, THE CORRECTED CORRELATION FUNCTION CAN BE COMPUTED FROM the momentum distributions presented in the prior section in Fig. 7.9a. For this, the azimuthally averaged momentum distributions are Hankel transformed* and subsequently divided by the finite size suppression function found in most Fourier optics books¹⁰⁹

$$\mathcal{H}(r) = \begin{cases} \frac{2}{\pi} \left[\arccos\left(\frac{r}{L}\right) - \frac{r}{L} \sqrt{1 - \left(\frac{r}{L}\right)^2} \right], & \text{if } r \leq L \\ 0, & \text{otherwise.} \end{cases} \quad (7.21)$$

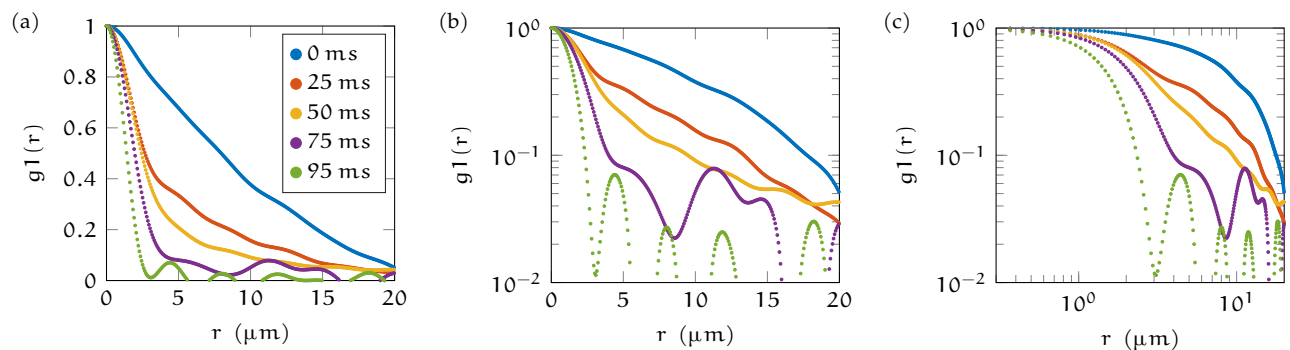
This results in the plots shown in Fig. 7.18a where a subset of the hold times is shown. To accommodate for the finite cloud size in imaging direction, the correlation function has also been divided by the *effective* ATF. Which is acquired by a weighted average of the measured

Figure 7.17: (a) Comparison of theoretical momentum distributions of finite systems with imperfect imaging. (b) Comparison of theoretical correlation functions of finite systems with imperfect imaging. (c) Comparison of corrected theoretical correlation functions of finite systems with imperfect imaging. For details see the text.

¹⁰⁹ J. W. Goodman: *Introduction to Fourier Optics*, (2005)

*Note that, for any two-dimensional space with rotational symmetry, the Fourier transform can be written in polar form and the rotational angle can be integrated out. This form is called Hankel transform of zeroth order and reduces the computational complexity. Therefore, it is used in some contexts in this work.

ATF over the cloud diameter. Already with the linear axis scaling, the corrected g_1 shows a visible difference between short and long hold times. The correlation decays slower for systems imaged immediately after preparation and faster if the system is held for an extended amount of time in the dipole traps. The areas of decay can be better differentiated if a logarithmic scale is chosen for the y-axis and one can identify areas of approximately linear slope for small r up to $\approx 14 \mu\text{m}$. A linear slope in a *semilog* plot signifies exponential decay. To identify possible algebraic decay, the same correlation functions are plotted with both axes scaled with the decadic logarithm. Here, a linear dependency identifies a power law decay. The interval above $\approx 14 \mu\text{m}$ could be considered linear and thus indicate slower than exponential decay. However, comparison to Fig. 7.17c shows globally much faster decay. For a BKT gas at the critical point, the decay is fastest but even there the slope does not exceed -0.25 . In a true analogue to a homogeneous 2D BKT gas, the first order correlation function should have decreased only marginally on the scale of the system size. In the present case, g_1 vanishes on the order of $20 \mu\text{m}$, only about a 7th of the system size. Hence, complete compatibility to the expected results of an infinite homogeneous system has not been found. Nonetheless, the results show an intriguing dependency of the first order correlation function on the hold time



Since g_1 is a measure of the phase correlation, a more direct investigation of the phase and its dependence on the hold time might reveal further information pertaining to the unexpected behavior of the first order correlation function described in this chapter. This will be the topic of the following chapter.

Figure 7.18: (a) A sample of the normalized first order correlation functions $g_1(r)$ in dependence of hold time. Note, for the equal time steps shown the longer hold times “bunch up”. (b) The same correlation functions as in (a) plotted with a decadic logarithmic ordinate. Here, straight lines denote exponential decay. (c) The same correlation functions as in (a) plotted with decadic logarithmic abscissa and ordinate. Here, straight lines denote power law decay.

8

A NEW TOOL: ACCESSING COHERENCE VIA SHORT TOF

- 8.1 Key idea, interference as a phase probe 87
- 8.2 Analysis of density-density correlations after time of flight 95
- 8.3 Time dependence of the coherence from short ToF 98
- 8.4 Possible issues with the theoretical description 110

The physical Fourier transformation of the matter wave focusing technique is an excellent tool to access the momentum distribution. With the relation $G_1 \sim \int n(\mathbf{k}) e^{i\mathbf{k}\cdot\mathbf{x}} d\mathbf{k}$ (see Eq. (3.15)), the mean first order – or phase – correlation function can in principle be extracted. As has been shown in the previous chapter, this is not without challenges. Hence, an alternative method that does not rely on long expansion times, and therefore does not suffer from reduced resolution, is desirable.

First, the well known method to probe phase via interference is revisited and examples of how it has been used to great effect in the context of ultracold gases are presented. It ensues a *back-of-the-envelope* style calculation to motivate how the density correlations we measure after different *time of flight* (ToF) can be related to the in situ phase correlations in order to determine the samples coherence.

Next, an example of the raw data obtained for two ToFs and an outline of the methodology used to obtain the density correlation function g_2 from it is presented in Section 8.2.

Subsequently, the presented method is used to investigate the coherence of a homogeneous sample held in a dipole trap, in Section 8.3. Here, an agnostic evaluation of the density correlations – with minimal theory – is made first, in order to develop an intuitive understanding for how the coherence develops with time. Finally, the underlying theory is explained conceptually, the full quantitative analysis of the density correlations in dependence of holding time, including all known corrections, is presented and the results interpreted.

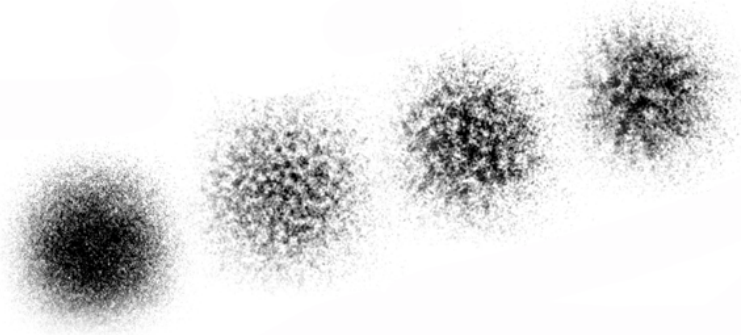
8.1 KEY IDEA, INTERFERENCE AS A PHASE PROBE

To introduce the method used in this experiment, it is helpful to reassert the concept of phase and how it impacts measurable quantities. In quantum mechanics, every state can be written in terms of wave functions – or their associated operators – in e. g. Slater determinants or permanents. Each single particle wave function ψ is commonly

written in amplitude-phase form

$$\psi(\mathbf{r}) = \sqrt{n(\mathbf{r})} \cdot e^{i\theta(\mathbf{r})}, \quad (8.1)$$

with a density amplitude \sqrt{n} and phase θ . Whereas the density is easily accessed in e. g. absorption imaging, the phase in the imaginary exponent is usually lost during this process. Unfortunately, there is no straightforward method to access the phase information since the definition of a suitable, i. e. Hermitian, phase operator to be used as an observable presents fundamental challenges¹¹⁰.



FORTUNATELY, the wave character of the above representation gives rise to a phenomenon by which the phase directly impacts the measurable density distribution: interference. To observe the effects of interference, a phase difference is required. Either a local oscillator with constant phase, in style of a heterodyne superposition, or a copy of the sample as in homodyne detection schemes can be used. In the present case of a cold Bose gas with, possibly, algebraically decaying coherence, phase differences within the gas are exploited, eliminating the need for two copies of the sample. This *self-interference* is achieved during short time of flight, during which parts of the cloud with different phases $\theta(\mathbf{r})$ mix and thus an interference pattern develops. The resulting density ripples are demonstrated in Fig. 8.1. This *quasi-condensate* can, roughly, be thought of as an ensemble of patches of approximately constant phase, where the phases of the different patches are only weakly correlated. The type of phase correlation and the resultant interference visibility is captured in the two-point correlation function $G_1(\mathbf{r}_1, \mathbf{r}_2, t)$, whose pivotal role in this analysis will become apparent later on. From the images above, it is obvious that the length scale of the density modulation increases with expansion time. It proves to be the case that the dominant size of the fluctuations after ToF contains information of in situ phase fluctuations at a certain length scale in analogy to the Talbot effect¹¹¹, this can already be understood in terms of a toy model that will be introduced at a later stage. On the one hand, if the sample were perfectly coherent, i. e. were a true *Bose-Einstein condensate* (BEC), no density modulation would develop. The density ripples form only due to the existence of

Density imaging effectively evaluates the expectation value by taking the square, $n = \psi^\dagger \psi$, hence the complex exponent is lost.

¹¹⁰ P. Carruthers and M. M. Nieto: *Rev. Mod. Phys.*, vol. 40, (1968)

Figure 8.1: During time of flight the non-constant phase of the cold interacting Bose gas develops into an interference pattern in form of density ripples. The time of flight increases from left to right: in situ, 1 ms, 2 ms to 3 ms.

¹¹¹ H. Talbot: *Philos. Mag.*, vol. 9, (1836)

excitations, which preclude constant phase. On the other hand, random excitations destroy the phase coherence and thus extinguish the interference pattern, similar to how a thermal light source does not exhibit extended interference fringes. Thus, reviewing the interference pattern of Fig. 8.1 it is already apparent that the samples initial phase distribution must exhibit coherence over some finite distance. Numerous experiments have leveraged interference to learn about coherence properties of degenerate quantum systems. This work builds upon these studies of ultracold bosons in lower dimensions, since all low-dimensional Bose gases share the significant departure from 3D physics.

8.1.1 Prior work this thesis builds upon

NATURALLY, QUASI 1D BOSE GASES HAVE BEEN STUDIED, for example in the group of K. Sengstock¹¹² in 2001, with techniques similar to the one employed in this work. In their experiment, a highly elongated cloud of weakly interacting ⁸⁷Rb atoms below the critical temperature T_c was left to expand for a time $t = 25$ ms. Upon imaging, parallel stripes have been observed in the density distribution. The occurrence of this interference pattern increased with stronger confinement and higher temperature. Hence, indicating pronounced phase fluctuations due to 1D low-energy axial excitations. Interference of two 1D samples in 2008¹¹³ and, more recently, the use of self-interference of a single cloud have been demonstrated in the Group of J. Schmiedmayer in 2010¹¹⁴ and 2016¹¹⁵. In the latter experiment, a one-dimensional gas of 10 000 ⁸⁷Rb atoms was evaporatively cooled until the system could be described by a macroscopic wave function with a fluctuating phase. Subsequently, the gas was coherently driven by a radio frequency pulse and parts of the system were coupled out to untrapped states. After 10.5 ms ToF, a density speckle pattern formed, from which the normalized autocorrelation function was computed. A comparison to simulated data was taken as evidence that, in contrast to predictions for such integrable systems, a reduction of temperature could be achieved by the outcoupling process.

THE STUDY OF TWO-DIMENSIONAL SYSTEMS IS AN ESSENTIAL PUZZLE PIECE since they represent an intermediate step between the theoretically accessible 1D and physically ubiquitous 3D systems. Of even greater importance might be the unique physics exhibited by 2D systems, since they are the only experimentally accessible system with an even number of dimensions.

A stack of multiple 2D layers was left to expand, overlap and interfere in a matter wave heterodyning experiment in the group of J. Dalibard in 2004⁷⁴. Also, a stack of two layers was used in an experiment demonstrating the *Kosterlitz-Thouless* (KT) transition²⁰ already described in more detail in Chapter 5. Of particular relevance for this work is that they saw evidence for the transition to a regime with al-

Similar to how the intensity interference contrast visibility $V = \frac{2\langle E_1 E_2 \rangle}{\langle E_1^2 + E_2^2 \rangle}$ of two superposed light beams, E_1 and E_2 depends on the cross term of the superposition

$$\begin{aligned} \langle I \rangle &= \langle (E_1 + E_2)^2 \rangle \\ &= \langle E_1^2 \rangle + \langle E_2^2 \rangle + 2 \underbrace{\langle E_1 E_2 \rangle}_{\sim g_1 = \langle \psi | \psi \rangle} \end{aligned}$$

the normalized first order correlation function g_1 determines the visibility of the interference of the wave function ψ .

¹¹² S. Dettmer et al.: *Phys. Rev. Lett.*, vol. 87, (2001)

¹¹³ S. Hofferberth et al.: *Nature Physics*, vol. 4, (2008)

¹¹⁴ S. Manz et al.: *Phys. Rev. A*, vol. 81, (2010)

¹¹⁵ B. Rauer et al.: *Phys. Rev. Lett.*, vol. 116, (2016)

⁷⁴ Z. Hadzibabic et al.: *Phys. Rev. Lett.*, vol. 93, (2004)

²⁰ Z. Hadzibabic et al.: *Nature*, vol. 441, (2006)

gebraically decaying coherence. This experimental setup produced a series of pioneering experiments for the study of the global coherence properties of highly oblate systems.

Vortices were also studied in a Josephson coupled 2D lattice of ^{87}Rb atoms in the *Berezinskii-Kosterlitz-Thouless* (BKT) regime in the group of E. Cornell in 2007²⁴. They provided strong evidence for the proliferation of thermally excited vortices by letting independent BECs interfere in an experiment inspired by the work of D. Scherer et al¹¹⁶.

The recent production of single 2D layers of ultracold atoms yields unparalleled optical access that enables the study of *local* properties. A high resolution microscope directly pointing at a single layer of a 2D system after ToF provides the possibility to determine local phase changes without averaging. For example, the extraction of the scaling exponents of the first order correlation function is much less error prone in single layers since short expansion times can be used which reduce the loss in resolution due to the gas extending beyond the *depth of field* (DoF).

PREVIOUS WORK ON SINGLE 2D LAYERS EMPLOYING INTERFERENCE include early investigations of density fluctuations performed by the group of Y. Shin. In the most recent work⁸⁰ they measured the power spectral density of an expanding 2D Bose gas after ToF and found that the “spectral peak positions are consistent with the numerical result [produced by I. Mazets¹¹⁷]”⁷⁹. It is instructive to recognize that their previous work and especially a subsequent comment by Tim Langen¹¹⁸ showed that for this type of measurement it is crucial to very carefully focus the imaging apparatus onto the sample. Otherwise, the free propagation of the light field through the gas, governed by the Helmholtz equation, can lead to qualitatively very similar effects compared to the free propagation of a matter wave field during ToF. The group of Y. Shin investigated the influence of this systematic error^{79,119} and also found that the defocusing present in the first published work⁵⁸ could indeed invalidate the experimental conclusions. Due to the importance of this effect, we have taken great care to focus the imaging system correctly¹²⁰ and describe the procedure in Section 9.1.1.

There have also been studies of single layers of kinematically 2D systems published outside of peer reviewed journals, in 2013, for example, in the group of J. Dalibard as part of the doctoral thesis by R. Desbuquois²⁷. The measurement of the power spectral density of a ^{87}Rb Bose gas at $\tilde{g} \approx 0.077$ in situ and after ToF indicated “that the dynamics of the degenerate two-dimensional Bose gas is dominated by phase fluctuations”. The recorded peak positions in the spectrum show quantitative agreement with the work of A. Imambekov⁸² supporting the conclusion that phonons are the primary fluctuation mechanism as well as indicating that density fluctuations increase in the thermal and critical regimes. Also, corrections to the power spectral density due to the in situ density fluctuations were presented, which we adopted to improve the comparison to the theoretical pre-

²⁴ V. Schweikhard et al.: *Phys. Rev. Lett.*, vol. 99, (2007)

¹¹⁶ D. R. Scherer et al.: *Phys. Rev. Lett.*, vol. 98, (2007)

⁸⁰ S.-W. Seo et al.: *Phys. Rev. A*, vol. 89, (2014)

¹¹⁷ I. Mazets: *Phys. Rev. A*, vol. 86, (2012)

⁷⁹ J.-Y. Choi et al.: *Phys. Rev. Lett.*, vol. 111, (2013)

¹¹⁸ T. Langen: *Phys. Rev. Lett.*, vol. 111, (2013)

⁷⁹ J.-Y. Choi et al.: *Phys. Rev. Lett.*, vol. 111, (2013), ¹¹⁹ S.-W. Seo et al.: *J. Korean Phys. Soc.*, vol. 64, (2014)

⁵⁸ J.-Y. Choi et al.: *Phys. Rev. Lett.*, vol. 109, (2012)

¹²⁰ A. Putra et al.: *Rev. Sci. Instrum.*, vol. 85, (2014)

²⁷ R. Desbuquois: *Thermal and superfluid properties of the two-dimensional Bose gas*, (2013)

⁸² A. Imambekov et al.: *Phys. Rev. A*, vol. 80, (2009)

diction.

Similar measurements have been performed on molecular ${}^6\text{Li}$ at $\tilde{g} \approx 0.6$ in the group of S. Jochim and published in the masters thesis of S. Pres²⁸. Here, they focused on the density-density correlation function in an effort to compare to the theoretical results of $g_2(\mathbf{r}, t)$ of the group of L. Mathey⁸⁴. A reduction of the anti-correlation for heated samples could be observed. Quantitative agreement has been impaired by the “very low signal” and the observed “strong correlation between the measured oscillation in the [density-density correlation] and the detuning of [the] imaging laser”. Additionally, the authors questioned if the strong interaction permits the comparison to a theory developed for weak interactions and purely ballistic expansion. The effects of strong interactions during ToF are relevant for the presented work as well, hence we have aimed to reduce the influence of scattering during expansion by a faster reduction in density, see Section 7.1.

Most of the prior studies have been performed on harmonically trapped Bose gases. There, the density gradient limits the viable area to extract a measurement for any given density and thus severely reduces the statistical sample size per realization. Hence, the homogeneous 2D gas presents a unique opportunity to increase the *signal-to-noise ratio* (SNR) significantly as well as to eliminate density dependent effects. Combined with the high degree of calibration of density, focus and detuning (see Chapter 9) the presented measurements offer the possibility of direct quantitative comparison. With this, the extraction of coherence parameters such as the scaling exponent η might be viable.

8.1.2 Relation of density ripples to in situ coherence

In order to extract any in situ phase properties from a density image after ToF, a relation of an observable quantity to the in situ wave function has to be found first.

A SIMPLIFIED TOY MODEL yields already rudimentary insight into the source of the density ripples that develop during time of flight and will be presented first. Subsequently, the theoretical ansatz will be introduced schematically. Since the complete derivation is relatively unwieldy, it will be presented in Appendix A.

Consider the following wave function of a Bose gas which omits density variations, i. e. $n(\mathbf{r}) \equiv 1$,

$$\psi(\mathbf{r}) = e^{i\theta(\mathbf{r})}. \quad (8.2)$$

Close to $T = 0$, the kinetic energy available for perturbations is only minimal. Hence, the phase gradient $\nabla\theta$ is small. In the small patch of interest, the exponent can then be written $\theta(\mathbf{r}) \approx \theta_{\text{mean}} + \delta\theta(\mathbf{r})$, where $\delta\theta \ll 1$ is a small fluctuation. This corresponds to a weak phase fluctuation. When the slowly varying phase is assumed to be constant, i. e. θ_{mean} , the exponential function can be approximated for small ar-

²⁸ S. Pres: *BKT - phase transition in a strongly interacting 2D Bose gas*, (2014)

⁸⁴ V. P. Singh and L. Mathey: *Phys. Rev. A*, vol. 89, (2014)

gument. Subsequently, if we neglect scattering, the propagation can be treated as non-interacting with the free time evolution operator as

$$\psi(\mathbf{r}, t) \approx 1 + i\delta\theta(\mathbf{r}) \cdot e^{-i\frac{\hbar k^2}{2m}(t-t_0)}. \quad (8.3)$$

Here, a free particle Hamiltonian $H = \frac{\hbar^2 k^2}{2m}$ with momentum $\hbar k$ and mass m has been assumed. This is valid when the expansion is presumed to occur on much faster timescales as the time between scattering events. In the following, we set $t_0 \equiv 0$. With this, fluctuations of density $n(\mathbf{r}) = n_{\text{mean}} + \delta n(\mathbf{r}) \propto |\psi(\mathbf{r})|^2$ take the form

$$\delta n(\mathbf{r}) = 2\delta\theta(\mathbf{r}) \sin\left(\frac{\hbar k^2}{2m}t\right) + \overbrace{\mathcal{O}(|\delta\theta|^2)}^{\text{small}}. \quad (8.4)$$

From this equation, it is immediately obvious that the in situ phase fluctuations $\delta\theta$ are present in the density image after ToF as density ripples. It is also evident that the visibility of the ripples is modulated with time t depending on the wavelength $\lambda = 2\pi/k$ of the phase fluctuation. This is analogous to the optical Talbot effect and already leads to a first conclusion about the phase of the 2D gas. If the phase fluctuation were of a single wavelength, e. g. $\delta\theta(\mathbf{r}) = \cos(\mathbf{k} \cdot \mathbf{r})$, the signal visibility would oscillate with ToF and show the highest SNR at odd multiples of $t = \frac{\pi m}{\hbar k^2}$. Since the contrast does not oscillate with ToF, there must be fluctuations at arbitrary momentum k , a first indication of slow and possibly algebraic decay of correlations.

AS IT TURNS OUT, not the complete knowledge of the local density fluctuations is necessary but only their correlation. The density-density correlation function $\langle n n \rangle$ is closely related to the four-point correlator G_2

$$G_2(\mathbf{r}_1, \mathbf{r}_2, \mathbf{r}_3, \mathbf{r}_4) = \langle \psi^\dagger(\mathbf{r}_1) \psi^\dagger(\mathbf{r}_2) \psi(\mathbf{r}_3) \psi(\mathbf{r}_4) \rangle. \quad (8.5)$$

Which, for homogeneous systems, can be simplified to only depend on a single distance \mathbf{r}

$$G_2(\mathbf{r}) = \underbrace{\langle \psi^\dagger(\mathbf{r}) \psi(\mathbf{r}) \rangle}_{n(\mathbf{r})} \underbrace{\langle \psi^\dagger(0) \psi(0) \rangle}_{n(0)} - n_{\text{mean}} \delta(\mathbf{r}), \quad (8.6)$$

with the average density n_{mean} . The above equation contains two terms on the right-hand side. The first denotes the experimentally accessible density-density correlations, whereas the second one represents a shot-noise contribution that results from the normal ordering of the bosonic field operators and will be ignored hereafter. Since the measurable density correlations, $\langle n(\mathbf{r}, t_{\text{ToF}}) n(0, t_{\text{ToF}}) \rangle$, only form after ToF and the in situ phase correlations $g_1(\mathbf{r}, t_0) = \langle \psi^\dagger(\mathbf{r}, t_0) \psi(0, t_0) \rangle$ are of interest, a model that relates the two is necessary. Fortunately, the discussion sparked by A. Polkovnikov⁷⁶ led A. Imambekov et al.^{82,121} to produce exactly that. These calculations have been extended and simulated for our 2D system by our collaborators in the group of L. Mathey⁸⁴. They derived an approximate analytical expression for the *power spectral density* (PSD) of an algebraically decaying quasi-condensate, which is simply the Fourier transform of the sought after density

Note that only the phase θ undergoes time evolution since this approximation can be interpreted as a superposition of the momenta 0 and $\pm k$. Here the $k = 0$ mode is associated with the local oscillator, the "1", therefore the Hamiltonian vanishes.

Note that this toy models purpose is mostly instructional. The ansatz in Eq. (8.4) erroneously exhibits density fluctuations also at $t = 0$, which will be disregarded due to their $\mathcal{O}(|\delta\theta|^2)$ dependency. Additionally, a small phase gradient does not guarantee a small phase amplitude $\delta\theta$ globally. This approximation is thus only valid on finite patches. Coincidentally, that is also an intuitive way of understanding a BKT quasi-condensate.

This expression holds true also for time dependent systems, the argument t has only been omitted for readability.

The delta function contribution results from the normal ordering of $G_2 = \langle \psi^\dagger \psi^\dagger \psi \psi \rangle$, listing the hermitian conjugates first. Using the usual bosonic commutation relation $[\psi(x), \psi(y)^\dagger] = \delta(x - y)$, the order can be permuted to $\langle \psi^\dagger \psi \psi^\dagger \psi \rangle$ at the cost of introducing the delta function δ .

⁷⁶ A. Polkovnikov et al.: *Proc. Natl. Acad. Sci. U.S.A.*, vol. 103, (2005)

⁸² A. Imambekov et al.: *Phys. Rev. A*, vol. 80, (2009), ¹²¹ A. Imambekov et al.: *Phys. Rev. A*, vol. 77, (2008)

⁸⁴ V. P. Singh and L. Mathey: *Phys. Rev. A*, vol. 89, (2014)

correlation function g_2

$$\mathcal{F}\{g_2(r, t) - 1\} = \text{psd}(k, t) \approx \frac{4\pi a \eta K_1(ak)}{k} \overbrace{\left(\frac{a^2}{a^2 + (k\hbar t/m)^2} \right)^\eta}^{g_{1,\text{alg}}^2(k\hbar t/m)} \cdot 2 \sin^2 \left(\frac{\hbar k^2}{2m} t \right). \quad (8.7)$$

Here, K_1 is the first order modified Bessel function of the second kind, $k = |\mathbf{k}|$ denotes the momentum of the excitations, a represents a short distance cut-off capturing short range physics like vortices. The above expression consists of three terms on the right-hand side. The first is purely the result of the introduced short range cut-off. The second term connects the density-density correlation function g_2 to the in situ phase properties via g_1 . The third term is the so called mean-field term, due to the fact that mean-field Bogoliubov theory can be used to derive it. In fact, it is precisely the square of the interference term of the density fluctuations derived earlier using simpler toy model. The correlation functions calculated from Eq. (8.7) already present the opportunity to gain approximate quantitative insight into the decay of a BKT gas. To better describe the true experimental conditions at $T \neq 0$ and especially $T \gtrsim T_{\text{BKT}}$ we solve the full integral expression numerically for the quantitative analysis since also in situ density fluctuations as well as exponential decay can be considered. Examples of the shape of g_2 for three different ToF of the algebraically Fig. 8.2(a) and exponentially Fig. 8.2(b) decaying phase correlations are given in Fig. 8.2. Here, the parameters (a, c) of the respective g_1 have been set to typical values for our experiment and the scaling exponent is $\eta = 0.125$, i. e. well in the algebraic regime. The parameter r_0 is on the order of the de Broglie wavelength of our sample. A more detailed explanation of these parameters and their requirements can be found in Section 8.3.2. The density correlation functions are – for these parameters – starkly different. The algebraic decay exhibits a distinct minimum that moves towards larger distances with increasing ToF, whereas the exponential decay exhibits no such minimum, a much larger amplitude at $r = 0$ and only minor change for the ToFs shown. Qualitative – and even quantitative – comparison of experimental g_2 to the theoretical curves allows to infer properties of the supplied in situ phase correlation functions g_1 .

The short distance cut-off close to $T = 0$ is $a \propto \xi_h$, with the healing length ξ_h and transitions continuously into $a = \lambda_{\text{dB}}^2 / (2\pi\xi_h)$, with the thermal de Broglie wavelength λ_{dB} , for finite temperatures.

For much smaller temperatures, the exponential decay also exhibits a pronounced minimum which vanishes for prolonged ToF. This can be seen from Eq. (8.14) since the time evolution is solely in the exponent and thus identical for all g_1 . For long ToF, this can be used as a differentiation between algebraic (slow) and exponential (faster) decay.

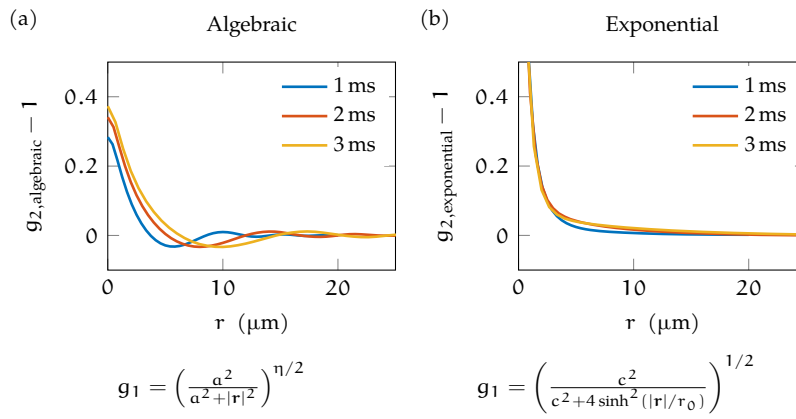


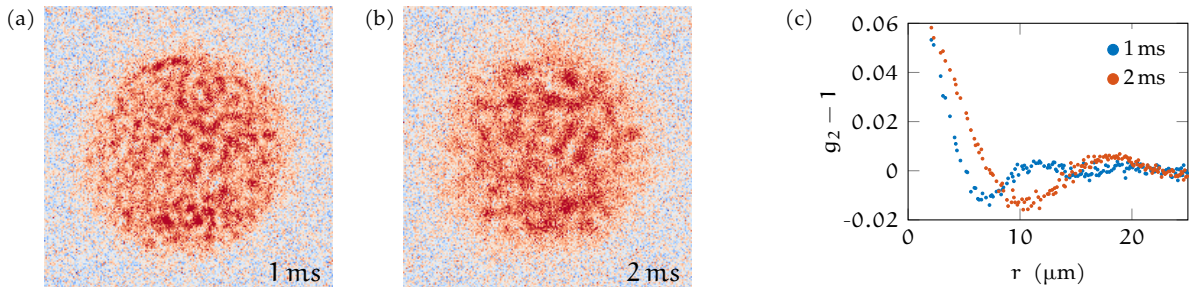
Figure 8.2: Plots of the normalized density-density correlation function g_2 after time of flight. (a) Examples of g_2 for algebraically decaying g_1 in dependence of the distance r are given for three different times of flight. For 1 ms (blue), 2 ms (red) and 3 ms (yellow). Note that the minimum shifts towards larger distances for longer time of flight. Typical values for the parameters were chosen and inserted in the formula given below the figure. (b) Examples of g_2 for exponentially decaying g_1 in dependence of the distance r are given for three different times of flight. For 1 ms (blue), 2 ms (red) and 3 ms (yellow). Note that no pronounced minimum is observable for the used parameters which are chosen to be typical for the presented experiment and inserted in the formula given below the figure.

8.2 ANALYSIS OF DENSITY-DENSITY CORRELATIONS AFTER TIME OF FLIGHT

A qualitative comparison of the measured g_2 with the theoretical prediction gives already first insights into the nature of the phase correlations present in the sample. To this end, examples of measured density correlation functions after ToF are shown and the method of extraction is explained. Subsequently, the measured g_2 is used to investigate the changes in phase correlation when the sample is held in an optical dipole trap for a variable amount of time. In Section 8.3.1, an agnostic analysis is performed in order to derive insights with the least amount of assumptions. At a later stage, the complete theoretical model and all known corrections for expected technical and physical effects are leveraged in an attempt to extract quantitative results in Section 8.3.3.

8.2.1 Density correlation functions of the experimental system

After the preparation of an ultracold bosonic cloud in a single 2D layer, the confining dipole traps are switched off abruptly. The gas is left to expand a variable amount of time and subsequently imaged. Typical absorption images for two ToFs are shown in Fig. 8.3. Even without detailed analysis, it is already apparent that the length scale of the density ripples increases with ToF as expected.



The extracted correlation function g_2 of the images is shown in Fig. 8.3c. Here, the shift in the dominant length scale can be seen even more clearly. Note that the density correlation functions are extracted from a single density image and still exhibit only negligible noise. The large amount of statistical samples is one of the advantages of the homogeneous gas since a very high SNR can be achieved from a single realization.

To utilize g_2 as a measurement tool, it is helpful to understand how it is obtained experimentally. The discussion of the physical implications of the measured density correlation functions for the studied system in dependence of the hold time is continued in Section 8.3.

8.2.2 Numerical Correlation Analysis

Obtaining a qualitative measure of the density correlations can be as simple as applying the 2D autocorrelation function of an image pro-

Figure 8.3: During time of flight the non-constant phase of the ultracold interacting Bose gas develops into an interference pattern in form of density ripples. (a) After 1 ms ToF the density ripples exhibit a characteristic length scale. (b) After 2 ms ToF the characteristic length scale has increased. (c) Extracted single-shot g_2 for the ToFs shown on the left. Different numerical apertures had to be chosen since otherwise the cloud would extend significantly beyond the DoF for longer ToF. How we compensate for this is detailed in Section 9.2.2.

cessing library to the image after ToF. To extract a quantitative measure, to be compared to theory, additional steps need to be performed in order to avoid effects introduced by the measurement or the computational analysis that are not immediately obvious.

The general process applied here is shown in form of a flow diagram in Fig. 8.4. Here, the performed steps are illustrated diagrammatically with the corresponding data visualized for selected steps, a more thorough description can be found as part of Appendix B.

A MEASUREMENT begins with the acquisition of a large number of absorption images of the quantum gas in situ and after 1 ms ToF. Usually 50 to 100 images are taken in order to allow for failed experimental cycles, or *shots*, and retain a sufficiently sized statistical sample. Of course, if the systems dependency on a physical parameter is investigated, this process is repeated for each value. For a typical experiment, this results in a dataset on the order of 10 000 files since each density image consists of three individual absorption images, for details see Section 9.2.1.

After a *region of interest* (RoI) has been selected to mask the areas where no atoms are present, the data is divided by the average density which is computed from the mean of all suitable images. Subsequently, the average of each individual realization is rescaled to unity to compensate for small drifts in average density. An example of a masked and normalized density image is shown labeled as ①.

When the preparation is completed, the offset is removed by subtracting the mean and subsequently each image is correlated with itself in a discrete 2D cross-correlation process labeled as *xcorr*. Since the image has been normalized, this step now yields the desired normalized correlation function $g_2 - 1$, which will be henceforth be used interchangeably with g_2 in this work due to the numerical benefit and notational convenience. However, the ideal second order correlation function requires an infinite domain or a sufficiently fast decaying signal in order to be compared to theoretical results. Neither is present in the experimental data. The autocorrelation process does not distinguish between correlations present in the gas or e. g. those present in the mask or the light field used for imaging. Since the mask is implemented as a multiplication with a Heaviside function, the extracted g_2 is also of multiplicative form $g_{2,\text{exp}} = g_{2,\text{ideal}} \cdot g_{2,\text{mask}}$.

The autocorrelation of the mask itself is shown in ②. Its large influence on $g_{2,\text{exp}}$ is obvious when compared to the *raw* autocorrelation of the masked image in ③, note the large difference in scale. The division of the correlation functions of the gas and the mask ④ reveals one obvious limitation even after correction: The correlation function is only defined within distances of twice the masks radius. Everything beyond that radius is purely numerical noise and even within the valid domain the noise is amplified towards the edge via the division by a small number. Note that the images shown in ② to ④ have twice the resolution of the raw image and are approximately radially symmetric.

Longer and shorter times of flight are also viable. The length scale observed depends on the ToF and hence has to be tuned to achieve optimal SNR to balance the decrease in resolution from the expansion in the imaging axis.

A *shot* is how the experimental procedure resulting in an absorption image and the destruction of the sample will be henceforth referred to.

Since the image is correlated with itself, i.e. the two inputs of the cross-correlation are identical, the process is known as *autocorrelation*.

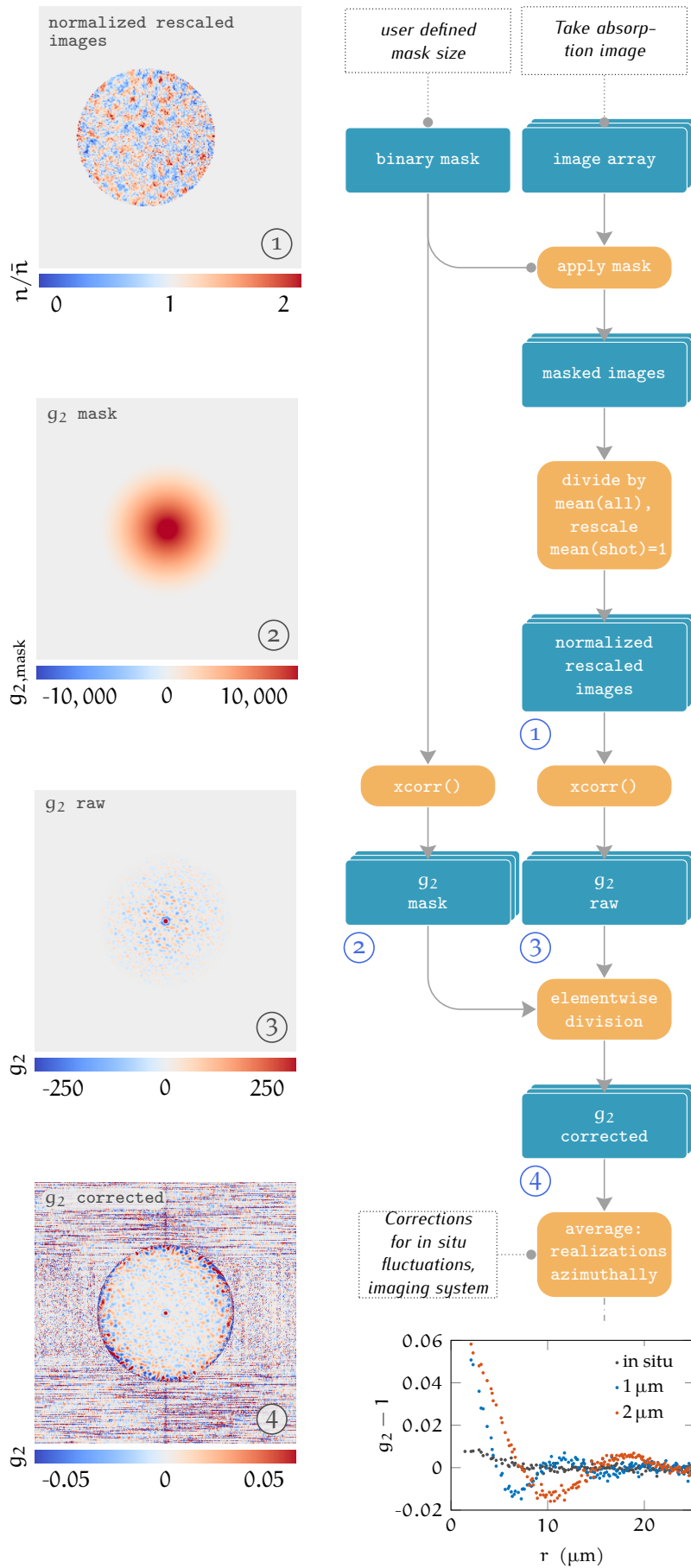


Figure 8.4: Outline of the image preparation used in the numerical analysis of g_2 . The flow chart presents the simplified procedure while examples for relevant intermediate steps are given to the left. Image preparation is the first step in the numerical analysis of the density correlation function g_2 . First, a ROI is defined by the user and subsequently applied as a binary mask to the array of density images. By division with the average density and rescaling to unit density per realization, the normalized and rescaled density distribution after ToF labeled ① is obtained. In a second step, the binary mask as well as the density image array is autocorrelated which yield the density-density correlation functions g_2 labeled ② and ③. The latter correlation function is divided by the former, hence the mask corrected g_2 is obtained, labeled ④. After subsequent azimuthal averaging, the corrections for the in situ fluctuations are applied to the data whilst the influence of the imaging system is considered by convolving the fit functions. Note that a constant offset of unity has been removed here in the density-density correlation function g_2 .

The image in ④ is averaged azimuthally by binning the radii of the pixels approximately every 100 nm, yielding a radial g_2 on an equidistant grid. Outliers are removed and the data is interpolated to facilitate high performance adaptive numerical fitting and easy comparison between different datasets.

Now, corrections to systematic errors introduced by the time of flight are applied. The measured in situ density-density fluctuations are propagated, $g_{2,\text{in situ}}(t = 0) \rightarrow g_{2,\text{in situ}}(t = \text{ToF})$ to the time the absorption image is taken and subtracted from the correlation function of the gas after ToF, i. e. $g_2 = g_{2,\text{tof}} - g_{2,\text{in situ}}(t = \text{ToF})$. For a more detailed explanation of the time propagation of in situ fluctuations see Section 9.2.3. The expansion into the magnetic field causes a minuscule compression radially and a significant expansion in the line of sight. The compression is compensated for by rescaling the correlation function radially whereas the reduction in resolution by the expansion cannot be reversed. Hence, the influence of the imaging system is in turn applied to the fit function by convolving with a suitable *point spread function* (PSF).

The result of this process is displayed in ⑤ for single realizations of two different ToFs and in situ. The result of the large homogeneous RoI is that a very large SNR can be achieved even for individual shots.

This tool in hand, we extract the density correlations from images taken after 1 ms ToF of a cold Bose gas held in a dipole trap for a variable amount of time, to investigate possible insights into the phase evolution.

8.3 TIME DEPENDENCE OF THE COHERENCE FROM SHORT TOF

To begin, a number of straightforward analyses of sample images are made to provide a rough assessment of the state of the gas. These analyses will evaluate the readily available values of density in situ and after ToF as well as, in a second step, the density correlation function g_2 that has been extracted via the method mentioned above.

8.3.1 What can we learn directly from G_2 ?

The first observation made is that the average density decreases by 20.2% during 70 ms hold time, as can be seen in Fig. 7.8. Here, the density is shown for each hold time in situ* and after ToF. Oddly, the measured average density after ToF shows approximately 5% reduction compared to the in situ density. We attribute this increased reduction to the expansion of the cloud beyond the DoF of our microscope. Details regarding the effect of the imaging system can be found in Section 9.2.2. For visual comparison, we have rescaled the density after ToF to the in situ density. This has no effect on the further statistical evaluation and correlation analysis since the density is normalized first. The in situ density is expected to be known well since we have calibrated the apparatus for this type of measurement, as is described

* *In situ* means in our case actually approximately 20 μs after the release of the trap. This short time delay ensures that the 3D density has been sufficiently reduced to suppress multi scattering effects of the imaging photons.

in Section 9.1.3.

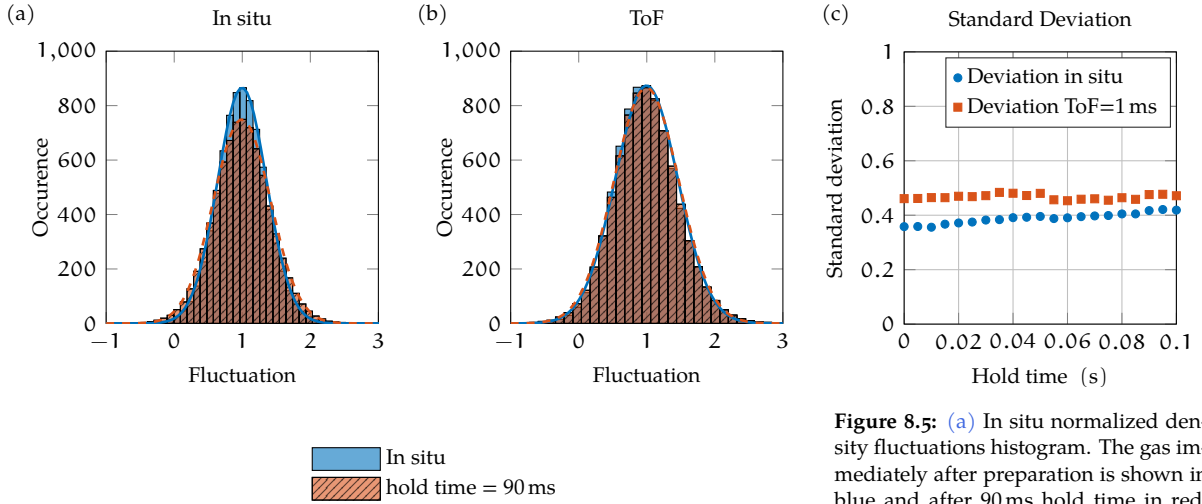


Figure 8.5: (a) In situ normalized density fluctuations histogram. The gas immediately after preparation is shown in blue and after 90 ms hold time in red. (b) Normalized density fluctuations histogram after 1 ms ToF. The gas immediately after preparation is shown in blue and after 90 ms hold time in red. (c) The density fluctuations standard deviation around the mean, in situ (blue circles) and after 1 ms ToF (red squares).

IN SITU DENSITY FLUCTUATIONS can be used to estimate the relative increase in internal energy of the gas. The measured values are normalized to unity density and plotted in a histogram, see Fig. 8.5. Since the optical resolution of our imaging system has been artificially reduced to increase the DoF, the absolute values do not represent true point like fluctuations per pixel but are averaged over the extent of our PSF, see Section 9.2.2. The images contain not only the atomic shot noise we are interested in, but also the Poisson noise contribution of the imaging light. The influence of the PSF limits the usefulness of this analysis to relative measurements without compensation. The photon shot noise contribution is strongly suppressed by averaging over a few pixel wide kernel. The extracted standard deviation around the mean density shows a slight increase of density fluctuations of 16.6 % in situ but only little change for the images taken after ToF, as can be seen in Fig. 8.5c.

The most prominent feature of the density correlation function is arguably the minimum since it indicates anticorrelation which – for long times – are expected to vanish in a thermal gas⁸⁴. A change in the position of the minimum would indicate a change in the dominant length scale of the correlations. As can be seen in Fig. 8.6, the location of the minimum does not change, whereas the absolute amplitude decreases, i. e. the minimum becomes much less pronounced.

BRIEF CONCLUSION OF THE MOSTLY THEORY-AGNOSTIC ANALYSIS

In the previous chapter, the result of the momentum-space analysis was that the gas might be driven out of degeneracy while being held in the dipole trap. With the introduction of non-equilibrium effects either globally or locally. The reduction of average density with an apparent increase in temperature does support the possibility of a phase transition during holding, analogous to the discussion in the prior chapter concerning the T/4-measurement. Additionally, the slight in-

⁸⁴ V. P. Singh and L. Mathey: *Phys. Rev. A*, vol. 89, (2014)

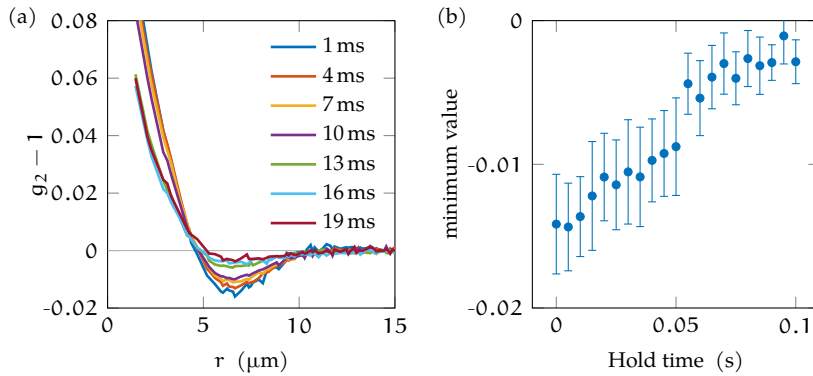


Figure 8.6: The absolute amplitude of minimum in the density correlation function decreases (a) Examples of density correlation functions during hold time. Note that the minimums decreases in depth (b) Amplitude of the minimum in the density correlation functions in dependence with hold time. The uncertainty given is the standard deviation over all realizations. The location stays approximately constant at $r_{\min} \approx (6.91 \pm 0.30) \mu\text{m}$.

crease of in situ density fluctuations indicates an increase in internal energy and hence equilibrium temperature, assuming all other excitations remain approximately equal. However, the approximately constant density fluctuations after ToF are rather puzzling. The heating process of ultracold 2D gases is often modeled as an increase of phase fluctuations in the quasi-condensate since those require the least amount of energy. This would, however, lead to an increase in density fluctuations after ToF, even considering that the in situ density fluctuations turn into phase fluctuations and hence escape our detection. The density correlations after ToF also hint at a more complex situation. The ansatz made in Section 8.1.2 indicates that the amplitude of the minimum in g_2 should increase. However, this holds true only if the heating process is indeed mostly phonon driven. If the heating is, alternatively, particle like, thus transferring atoms from the quasi-condensate to the thermal part, a vanishing minimum could indicate a growing non-degenerate fraction. To identify the degenerate and thermal state of the gas from the qualitative shape of the density correlations after ToF is not trivial. Their qualitative behavior is very similar and show the strongest differentiation in the time scales of the decay of anticorrelations. Due to the complexity of the problem, in order to extract in situ properties from the density correlation function, a methodical comparison with a sophisticated theory is more appropriate.

8.3.2 Model theory

It turns out that in situ excitations in density as well as phase have to be considered since phase excitations transform into density excitations and vice versa. How in situ density fluctuations are treated in the analysis is presented in more detail in Section 9.2.3. In the following it will be concentrated on phase fluctuations since on the one hand, density fluctuations are strongly suppressed for cold Bose gases and on the other hand, the BKT-physics of interest manifest in the correlation function g_1 and hence the phase interference. For the final quantitative analysis, the effects of in situ density fluctuations have been corrected for in first order.

The theoretical approach presented here, gaining insight into the

in situ phase fluctuations from the knowledge of density fluctuations, is based on the work of A. Imambekov⁸² and follows the additions of V. Singh⁷⁷. Also, the derivation will focus on the conceptual steps performed to arrive at the in situ phase to ToF density relationship, the interested reader can find the full, step by step, derivation in Appendix A. The formulas will be presented simplified, in order to focus on the used concept. Hence, all integrals are understood to span the interval $(-\infty, \infty)$, and all constants are set to unity, i. e. $\hbar \equiv \hbar \equiv m \equiv 1$. Additionally, this derivation is using the complex field approximation of the phase operator.

The onset of the derivation is the de facto default ansatz of the in situ wave function ψ_0 with constant density $\sqrt{n_0}$ and position dependent phase $\theta(\mathbf{x}, t)$ at time $t = t_0 = 0$,

$$\Psi_0(\mathbf{x}, t_0 = 0) = \sqrt{n_0} e^{-i\theta(\mathbf{x}, t_0)}. \quad (8.8)$$

Since the absorption image is taken after ToF, the knowledge of the wave functions at some later time $t > t_0$ is required. The straightforward application of the time evolution operator is simplified by the use of a Green's function propagator, since this approach yields much more accessible expressions. The wave function is propagated in time by

$$\Psi(\mathbf{x}, t) = \int G(\mathbf{x} - \mathbf{x}', t) \Psi_0(\mathbf{x}', t_0 = 0) d\mathbf{x}'. \quad (8.9)$$

Here, the Green's function G is taken to be the free particle propagator defined as

$$G(\mathbf{x}, t) = \frac{1}{it} e^{i\frac{\mathbf{x}^2}{2t}}. \quad (8.10)$$

Despite the fact that the sample is initially well in the many-body regime, this assumption is still reasonable since the fast expansion after release from the trap reduces interactions significantly.

With the wave function known at time t , the density after ToF $n(t) = \Psi^\dagger(t)\Psi(t)$ could in principle be calculated. Since the density-density correlation function, $\langle n(\mathbf{r}_1, t)n(\mathbf{r}_2, t) \rangle$, is constructed from two densities, it contains a quadruple integral over four wave functions Ψ and four exponentials – or phase rotations – from the Green's functions

$$\begin{aligned} \langle n(\mathbf{r}_1, t)n(\mathbf{r}_2, t) \rangle &= \iiint ds d\mathbf{S} d\mathbf{u} d\mathbf{U} e^{-\frac{i}{t}(\mathbf{S}-\mathbf{r}_1)\mathbf{s}} e^{-\frac{i}{t}(\mathbf{U}-\mathbf{r}_2)\mathbf{u}} \\ &\cdot \left\langle \Psi_0^\dagger\left(\mathbf{S} + \frac{\mathbf{s}}{2}\right) \Psi_0^\dagger\left(\mathbf{U} + \frac{\mathbf{u}}{2}\right) \Psi_0\left(\mathbf{S} - \frac{\mathbf{s}}{2}\right) \Psi_0\left(\mathbf{U} - \frac{\mathbf{u}}{2}\right) \right\rangle \\ &+ n_0 \delta(\mathbf{r}_1 - \mathbf{r}_2). \end{aligned} \quad (8.11)$$

The expression above has already been written in a center of mass reference frame with the centers \mathbf{S}, \mathbf{U} and the relative coordinates \mathbf{s}, \mathbf{u} . It is interesting to note that the independent variables $\mathbf{r}_1, \mathbf{r}_2$ only appear in the exponential and the in situ wave functions contain solely variables to be integrated over. The Dirac delta function in the last term results from the normal ordering of the wave functions. It represents an atomic shot noise contribution which will be ignored hereafter since

⁸² A. Imambekov et al.: *Phys. Rev. A*, vol. 80, (2009)

⁷⁷ V. P. Singh: *Probing Superfluidity of Ultracold Bose Gases via Laser Stirring and Noise Correlations*, (2017)

The Green's function takes the role of a transfer function in this expression. Analogous to the *amplitude transfer function (ATF)* in the treatment of the imaging as a linear invariant system in Section 9.2.2.

it impacts only the *origin* $r_1 \equiv r_2$ and thus can be removed easily in the numerical analysis.

The above expression already yields the connection between the in situ state and the measurement after ToF but is still unpractical since we have no knowledge of the in situ wave functions. To continue, the term in angle brackets can be identified as the density matrix $\rho(\ast) = \langle \Psi_0^\dagger \Psi_0^\dagger \Psi_0 \Psi_0 \rangle$. It can be simplified when realizing that it mostly contains exponentials of phase terms and we know from Section 4.1 in Chapter 4 that $\langle e^{i\hat{\phi}} \rangle = e^{\frac{1}{2}\langle \hat{\phi}^2 \rangle}$. With this, the expectation value of the density matrix ρ can be turned into the expectation value of the square of the phases

$$\begin{aligned} \rho(\mathbf{r}_a, \mathbf{r}_b, \mathbf{r}_c, \mathbf{r}_d) &= n_0^2 \langle e^{i[\theta(\mathbf{r}_a) + \theta(\mathbf{r}_b) - \theta(\mathbf{r}_c) - \theta(\mathbf{r}_d)]} \rangle \\ &= n_0^2 e^{\langle [\theta(\mathbf{r}_a) + \theta(\mathbf{r}_b) - \theta(\mathbf{r}_c) - \theta(\mathbf{r}_d)]^2 \rangle / 2}. \end{aligned} \quad (8.12)$$

Again, the coordinates \mathbf{r}_{a-d} in the arguments have been substituted to enhance readability. Since the first order correlation function is defined by the wave function's phase, the expectation value of the phase terms can be rewritten as an expression solely of g_1 ,

$$\rho(\mathbf{r}_a, \mathbf{r}_b, \mathbf{r}_c, \mathbf{r}_d) = n_0^2 \frac{g_1(\mathbf{r}_a - \mathbf{r}_c) g_1(\mathbf{r}_a - \mathbf{r}_d) g_1(\mathbf{r}_b - \mathbf{r}_c) g_1(\mathbf{r}_b - \mathbf{r}_d)}{g_1(\mathbf{r}_a - \mathbf{r}_b) g_1(\mathbf{r}_c - \mathbf{r}_d)}. \quad (8.13)$$

Substitution of the density matrix, a last center of mass transformation with $\mathbf{r}_1 - \mathbf{r}_2 = \mathbf{r}_{12}$ and $\frac{1}{2}(\mathbf{r}_1 + \mathbf{r}_2) = \mathbf{R}_{12}$, and exploiting the translational invariance to remove two of the four integrations, yields the final expression

$$\begin{aligned} g_2(\mathbf{r}_{12}, t) &= \frac{A^4}{4} \iint d\mathbf{r} d\mathbf{r}' e^{-\frac{im}{8\hbar t}(\mathbf{r}^2 - \mathbf{r}'^2 - 2\mathbf{r}_{12} \cdot (\mathbf{r} - \mathbf{r}'))} \\ &\quad \cdot \frac{g_1\left(\frac{1}{2}(\mathbf{r}' - \mathbf{r})\right)^2 g_1\left(\frac{1}{2}(\mathbf{r}' + \mathbf{r})\right)^2}{g_1(\mathbf{r}') g_1(\mathbf{r})}. \end{aligned} \quad (8.14)$$

Here $A = \sqrt{\frac{m}{2\pi\hbar t}}$, and all the constants have been re-substituted to form the full equation. One can see that the expression above connects the in situ phase correlation functions $g_1(\mathbf{r}, t_0 = 0)$ to the density correlation function $g_2(\mathbf{r}, t)$ at arbitrary time $t = \text{ToF}$.

Now, a first order correlation function – namely for a quasi-condensate or a thermal gas – can be inserted and compared to the measured density correlation function. To illustrate the effect of different decay, the following $g_{1,\ast}$ with algebraic and exponential decay are inserted in 1D in order to achieve a two-dimensional graphical representation and transfer some intuitive understanding of the expression above,

$$g_{1,\text{alg}}(\mathbf{r}) = \left(\frac{a^2}{a^2 + |\mathbf{r}|^2} \right)^{\frac{\eta}{2}} \quad g_{1,\text{exp}}(\mathbf{r}) = \left(\frac{c^2}{c^2 + 4 \sinh^2(|\mathbf{r}|/r_0)} \right)^{1/2}.$$

These functions are obtained from the ideal algebraic, $r^{-\eta}$, and exponential, e^{-r/r_0} , first order correlation functions. The parameters a and c are introduced to capture short-range physics, which are not included in the theoretical ansatz. In the case of the $g_{1,\text{exp}}$, it works in

After the center of mass transformation, the translational invariance leads to a free variable to be integrated over. This yields a delta function, which, in a second integration, eliminates a second coordinate.

conjunction with the smoothing of the exponential function towards $r = 0$ via the hyperbolic sine but also serves as a second fit parameter to ensure a fair comparison of the *goodness of fit* (GoF). The parameter c alters the shape of the correlation function drastically, for very small values of c and large r_0 it can even approach the shape of algebraic decay. Thus, the only physically viable value is approximately unity, as will be revisited in the comparison later on.

From Eq. (8.14), it is evident that the time evolution is independent of the in situ phase correlations and consists of two fast oscillating terms r^2, r'^2 and a distance term $r - r'$. For large r, r' , this effectively averages out the contributions of all values except $r = r'$. If the quotient term consisting of the algebraic or exponential g_1 is plotted over a Cartesian grid with the x -axis $\hat{=} r$ and y -axis $\hat{=} r'$, the images shown in Figs. 8.7 and 8.8 are produced. They demonstrate that only for $r = r'$ significant amplitude remains and differ mostly by how fast it decays beyond the diagonals. Since the quotient is positive, the minimum in g_2 can only originate from the multiplication with the oscillating exponential term. This explains the similar behavior of g_2 for short times, when only the value of g_1 on the diagonals is significant, which is almost identical for both g_1 . An appreciable qualitative difference is only observed for intermediate times when $g_{1,\text{exp}}$ has vanished but $g_{1,\text{alg}}$ is still finite. For very long times this difference persists since the algebraic decay is slow and also the oscillating exponential term starts to cease its averaging effect.

Hence, to better differentiate between algebraic and exponential decay, knowledge of the quantitative difference in the shape of the density correlation function is crucial. Fortunately, with Eq. (8.14) such a tool exists and a rigorous comparison of the density correlation function after hold time with theory is possible.

8.3.3 Quantitative analysis

The comparison of the measured density correlations with theoretical predictions which have been corrected for the systematic errors of the measurement procedure will be presented in the following. The analysis involves a computationally expensive integral equation. In order to ensure a feasible analysis, the theoretical g_2 data to compare to has been generated beforehand in large configuration space volumes on the local high performance computing cluster by V. Singh in the group of L. Mathey. Nevertheless, in a good approximation, one can think of the following plots as the result of the average of the fits to the autocorrelation of every single image with Eq. (8.14).

Since the images of the sample contain imperfections due to aberrations in the beams used to generate the trap potentials as well as vibrations of the used imaging optics, a suitable RoI is chosen to include as few imperfections as possible while maximizing the area to analyze. The chosen RoI can be seen in Fig. 8.9. Everything except the highlighted area is masked in every image prior to analysis. For all contained length scales, the effect of this mask is completely re-

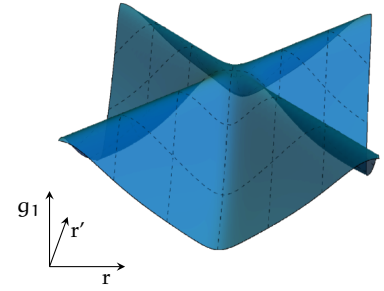


Figure 8.7: Plot of algebraic $g_1(r, r', \alpha, \eta)$ term in $g_2(r, t)$ expression with $\alpha = 3 \mu\text{m}$ $\eta = 0.25$.

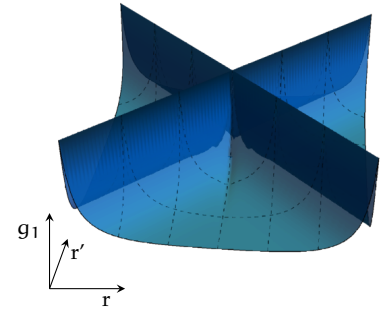


Figure 8.8: Plot of exponential $g_1(r, r', r_0, c)$ term in $g_2(r, t)$ expression with $r_0 = 1.6 \mu\text{m}$ $c = 1$.

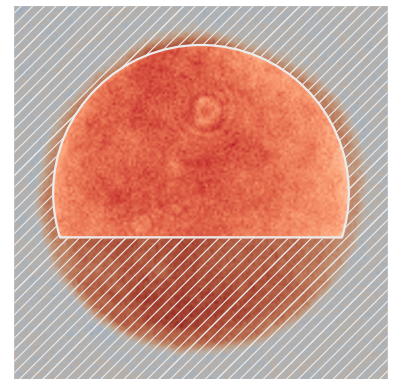


Figure 8.9: Representation of the region of interest. The highlighted part is selected for further study, the remainder is cut.

versible. This demonstrates the possibility to investigate samples locally which, however, comes at the cost of a reduced SNR.

Examples of the fits derived from different first order correlation functions $g_{1,\text{alg/exp}}$, ToF and hold times are shown in Fig. 8.10. Clockwise, it shows fits to the average in situ density correlation function (a), algebraic and exponential fits to g_2 after short time of flight for two different realizations for no additional hold time (b) and (d), as well as fits to a sample taken after 70 ms of hold time (c). The individual fits are discussed in this order in the following.

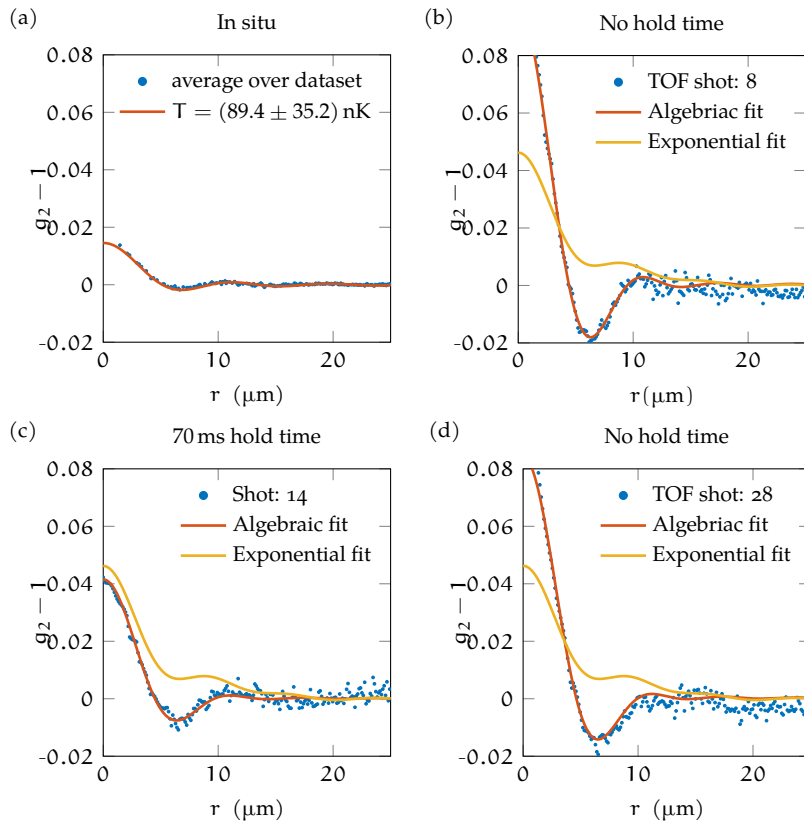


Figure 8.10: (a) Fit to the averaged in situ density-density correlation function g_2 with Eq. (8.15). The resulting temperature exhibits a significant error but is in reasonable agreement with the temperature obtained from the thermal wings. Nevertheless, only the shape of the curve is used in the short ToF analysis which shows acceptable agreement. (b) and (d) Fits to a single realization (shot no. 8 and 28) immediately after preparation with algebraically (red line) and exponentially (yellow line) decaying g_1 . Here, the parameter c is fixed at unity. Obviously, the algebraically decaying fit function yields much superior agreement. (c) Fits (same colors as previously) to a single realization (shot no. 14) after 70 ms hold time. Note the much reduced amplitude of g_2 .

FITTING g_2 TO IN SITU DENSITY-DENSITY CORRELATIONS

It is obvious that the second order correlation function taken from in situ (Fig. 8.10a) and ToF (Fig. 8.10b) images are very different for the two cases. In situ, only density fluctuations due to thermal fluctuations and quantum depletion are present and the most prominent feature is the broadened short range correlation up to approximately $r = 6 \mu\text{m}$.

At first sight, the sizable amplitude of the in situ density fluctuations of approximately 20% of the ToF data is surprising, since density fluctuations are expected to be strongly suppressed in ultracold two-dimensional gases. However, as the calculations below will show, the observed density fluctuations are in good agreement with the theoretical expectation. It is expected that for temperatures on the order of the critical temperature, thermally excited density fluctuations show

correlations on the order of the de Broglie wavelength, for our parameters $\lambda_{\text{dB}} \approx 1.6 - 1.9 \mu\text{m}$ ⁴². Even well below the critical temperature, the in situ density fluctuations are expected to be non-negligible due to the very low densities.

Within the Bogoliubov approximation for a radially symmetric system, the thermal and quantum in situ density fluctuations can be numerically computed by⁷⁷

$$\frac{\langle \delta n(r) \delta n(0) \rangle}{n_0^2} = \frac{\xi_h}{2\pi} \int_0^\infty dk \frac{k^2}{\sqrt{k^2 \xi_h^2 + 2}} J_0(kr) \cdot \left(\frac{2}{\exp\left(\frac{\beta \hbar^2 k}{2m\xi_h} \sqrt{k^2 \xi_h^2 + 2} - 1\right)} + e^{-k\xi} \right). \quad (8.15)$$

Here, $\beta = (k_B T)^{-1}$ is the inverse temperature and the healing length is defined as $\xi = 1/\sqrt{2m\mu}$ with the appropriate chemical potential μ . The first term in the parentheses is the temperature contribution whereas the second term represents the quantum contribution. In order to make the integral tractable a smooth momentum cut-off, $e^{-k\xi}$, has been introduced in the quantum term to limit the momenta to $k \leq 1/\xi_h$. The result from Eq. (8.15) is convolved with our imaging PSF and fitted to the averaged in situ density correlation data, see Fig. 8.10a. Two datasets have been taken, the first with hold times up to 30 ms and the second dataset with hold times up to 100 ms. These measurements will be referred to as the *30ms dataset* and the *100ms dataset*, respectively. The agreement is excellent for the data obtained from the *30ms dataset* and the fitted temperature of $T \approx (89.4 \pm 35.2)$ nK is compatible with the independent measurements made in momentum space in Chapter 7. Here the density is left as an independent fit parameter, which results in a good agreement to the measured average in situ density with $(2.75 \pm 0.90)/\mu\text{m}^2$. However, due to the strong influence of the imaging system, these fit parameters bear a relatively large error. Unfortunately, the agreement for the data obtained from the *100ms dataset* is significantly less good in comparison. The fitted parameters are still reasonable but the plot shows that the resultant curve deviates in shape and amplitude for very small radii, see Fig. 8.11. This might be an indication for a departure from equilibrium physics, which the Bogoliubov ansatz used above implies. Despite the partially excellent agreement, we do not use the fits to in situ density correlations in the current analysis since the momentum space measurement made in the prior chapter is a standard procedure for ultracold gases.

FITTING g_2 TO DENSITY-DENSITY CORRELATIONS AFTER SHORT TOF

The density-density correlation function g_2 after short ToF shows a remarkably high SNR which allows a fit to each single shot. The main features, the sharp rise towards small radii and the pronounced mini-

⁴² M. Naraschewski and R. J. Glauber: *Phys. Rev. A*, vol. 59, (1999)

⁷⁷ V. P. Singh: *Probing Superfluidity of Ultracold Bose Gases via Laser Stirring and Noise Correlations*, (2017)

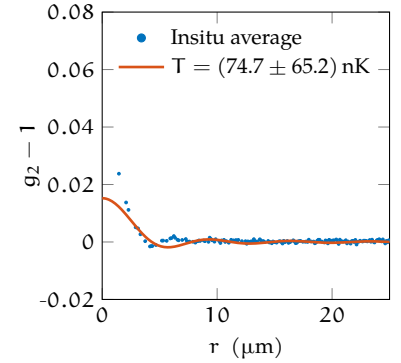


Figure 8.11: Fit to the in situ density fluctuations of the dataset with longer hold times. Density and temperature are reasonable with $n_0 \approx 2.9/\text{m}^2$ and $T \approx (75.0 \pm 65.2)$ nK but the quality is considerably worse compared to the fits to the dataset with shorter hold times.

imum around $7 \mu\text{m}$ are captured well by the fit functions for g_2 assuming algebraic g_1 , as can be seen from Fig. 8.10b and Fig. 8.10d. Even the predicted second maximum, which can be observed at $12 \mu\text{m}$, is fitted reasonably well. On the other hand, using a fit function for g_2 that assumes an exponentially decaying first order correlation function does not produce acceptable results. We point out that the exponentially decaying g_1 function used as an input to calculate g_2 also has two free parameters, namely the coherence length and a heuristic short-range cut-off c needed to prevent a divergence of g_1 at short distances. It reads

$$g_{1,\text{exp}}(\mathbf{r}) = \left(\frac{c^2}{c^2 + 4 \sinh^2(|\mathbf{r}|/r_0)} \right)^{1/2} \xrightarrow{\text{for large } |\mathbf{r}| \text{ and } c \approx 1} e^{-|\mathbf{r}|/r_0}. \quad (8.16)$$

Here, the ideal value $c \equiv 1$ has been chosen, which obviously does not capture the main features at all. If c is chosen to be a free fit parameter the fit quality naturally improves. However, the optimizer converges fast to very small values $c < 0.2$ and large correlation length r_0 which are unphysical and do not represent true exponential decay. In order to illustrate this, several g_1 functions with varying c parameters are plotted in Fig. 8.12.

Hence, the algebraic model for the first order correlation function produces superior results. However, even if c is not fixed to unity for the exponential model, the algebraic model outperforms at small hold times and becomes comparable in quality for hold times beyond $\approx 60 \text{ ms}$. The quality of the model is estimated by error coefficients collectively denoted by the **GoF**. In the following, the goodness of the exponential and algebraic fits are compared to each other using two measures that are depicted in Fig. 8.13.

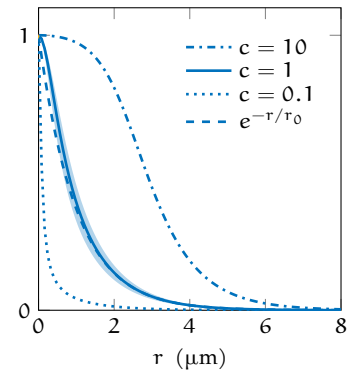


Figure 8.12: Comparison of different parameters for the exponentially decaying g_1 function as input to the fitting routine. True exponential decay (dashed) is compared with three values for c . For $c = 1$ (solid) the true exponential shape is well approximated, while for $c = 10$ (dash dotted) and $c = 0.1$ (dotted) large discrepancies become evident. Due to this behavior, only values close to unity produce physically reasonable results.

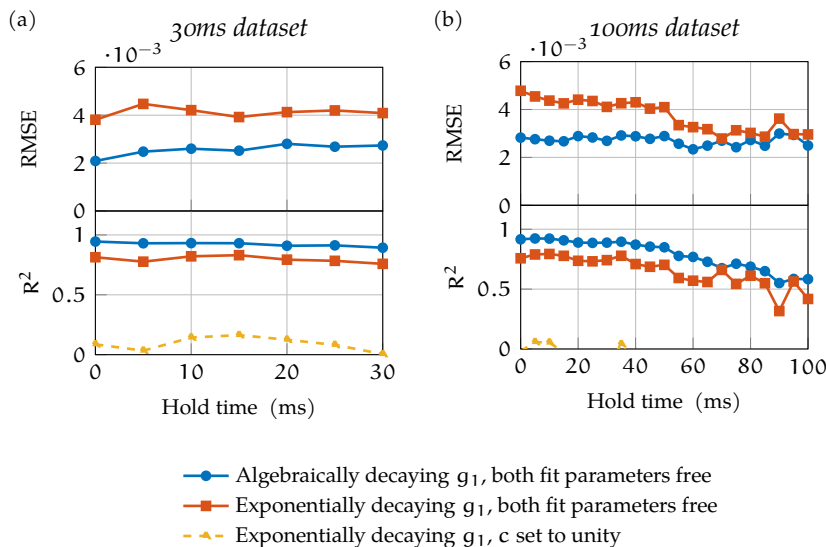


Figure 8.13: Comparison of the fit errors of the full numeric analysis of the density correlations measured after short **ToF**. Three options are compared, the algebraic (blue circles) and exponential (red squares) first order correlation functions with two free fit parameters and a physically reasonable exponential fit (yellow triangles) where the c parameter set to unity. The upper panel displays the *root-mean-square error* (**RMSE**) as described in the text whereas the lower panel shows the R^2 value. Note that the **RMSE** of the exponentially decaying fit always exceeds the algebraic fit. The **RMSE** for $c = 1$ is now shown since it is several times larger. Analogously, the R^2 coefficient of the algebraic decay is always closer to the ideal value of unity, although the quality of all fits diminishes towards longer hold times.

The first measure is the **RMSE**, given by

$$\text{RMSE} = \sqrt{\frac{1}{N} \sum_i (\hat{y}_i - y_i)^2}. \quad (8.17)$$

Here, y_i are all N values of $g_2(\Delta r_i)$ measured at each hold time for the N distances Δr_i and \hat{y}_i denotes the fitted value or prediction. From Fig. 8.13, it is clear that the algebraic model has a substantially smaller RMSE than the exponential model.

The second measure for the GoF is the coefficient of determination R^2 , which can be more easily compared across different fitting methods. R^2 ranges from $R^2 = 0$ for a bad fit to a $R^2 = 1$ for a perfect fit. A common definition is¹²²

$$R^2 = 1 - \frac{\text{RSOS}}{\text{TSOS}}, \quad (8.18)$$

where TSOS stands for the total sum of squares and RSOS for the residual sum of squares, given by

$$\text{TSOS} = \sum_i^N (y_i - \bar{y})^2, \quad \text{RSOS} = \sum_i^N \underbrace{(y_i - \hat{y}_i)^2}_{\text{residuals } r=y_i-\hat{y}_i} = \sum_i^N r_i^2, \quad (8.19)$$

with the mean of the data, $\bar{y} = \frac{1}{N} \sum_i^N y_i$. Thus, R^2 compares the fit of the model with that of a horizontal hyperplane, the null hypothesis. That means it compares the error RSOS assuming all predictors \hat{y}_i are simply given by the mean \bar{y} to the RSOS of a more sophisticated fit model. As can be seen in Fig. 8.13, the $c = 1$ model exhibits negative R^2 values which occur if the chosen model fits the data worse than a horizontal line. Note, that R^2 is a relative measure that relates the accuracy of the fit to the magnitude of the data. Thus if the data decreases in spread and the absolute error stays the same, the R^2 value decreases accordingly.

In summary, both measures show the algebraic model to be superior to the exponential model, especially if the physically motivated assumption of $c = 1$ is made for the latter.

THE MAIN RESULT OF THIS CHAPTER is contained in the plots of Fig. 8.14. If a first order correlation function $g_1 \propto r^{-\eta}$ with algebraic decay is assumed, which is a reasonable assumption as will be shown later, the scaling exponent η can be extracted from the fit with Eq. (8.14). Hence, the change of the scaling exponent can be shown in dependency of the hold time in Fig. 8.14a.

It can be seen that both datasets yield similar scaling exponents for the hold times where both are available. Since the datasets have been acquired more than two weeks apart, this increases our confidence in the measured data and demonstrates the reproducibility of the results. The specified error is the statistical error, i. e. given by one standard deviation of the mean of the fit parameter η . From the experimental setup, including mostly the effects of detuning and the treatment of in situ density fluctuations, we estimate the systematic error to be also approximately $\Delta\eta \approx \pm 0.025$. Both effects are presented in more detailed in Section 9.1. The remaining difference can be attributed to marginally different phase-space density caused by the drift of the dipole trap beams.

¹²² T. O. Kvalseth: *Am. Stat.*, vol. 39, (1985)

Conceptually R^2 can be thought of as:

$$R^2 = \frac{\text{RSOS}_{\text{null}}}{\text{TSOS}} - \frac{\text{RSOS}}{\text{TSOS}}.$$

With $\hat{y}_i \equiv \bar{y}_i$ for the null hypothesis, i. e.

$$\begin{aligned} \text{RSOS}_{\text{null}} &= \sum_i^N (y_i - \bar{y})^2 \\ &= \text{TSOS}. \end{aligned}$$

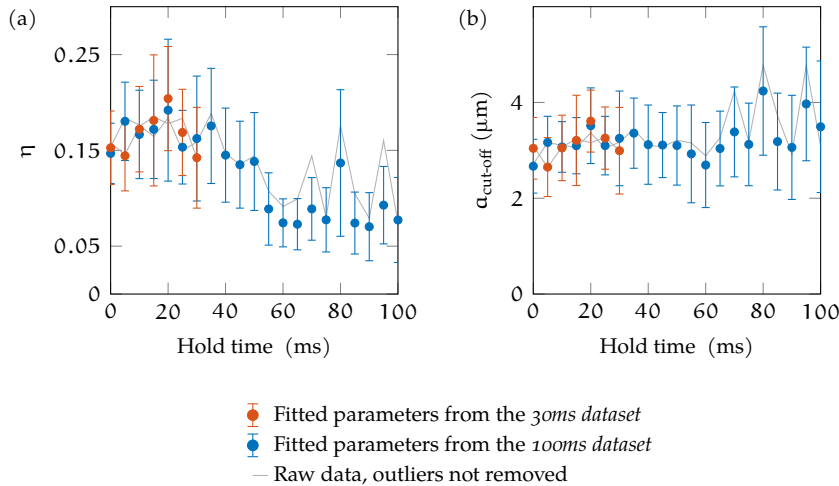


Figure 8.14: The main result of the full numerical analysis of the density correlations measured after short ToF (a) The scaling exponent η in dependency of the hold time for both, the 30ms dataset (red) and the 100ms dataset (blue). The error bars denote one standard deviation in the statistical average. Outliers greater than 3σ have been removed and the original dataset is plotted in gray in the background. Reasonable values for η can be observed for small hold times and a significant decrease beyond ≈ 40 ms. (b) The cut-off parameter $a_{\text{cut-off}}$ in dependence of the hold time. The same colors and style applies as in the prior plot. Apart from a slight increase in the statistical noise no remarkable feature can be observed. The average value is reasonable with $\approx 3 \mu\text{m}$.

Notwithstanding, a clear downward trend can be observed. The measured average scaling exponent decreases from initially $\eta \approx 0.2$ to approximately $\eta < 0.1$ during the holding period. Interestingly, the behavior of the data is incompatible with the assumption of heating a quasi-condensate of constant density, the regime to which our available theoretical predictions apply.

THE SECOND FIT PARAMETER, the short-range cut-off introduced in Chapter 4, does not show a significant change with increased hold time apart from a slight increase in noise. In fact, within the statistical error bounds, it remains approximately constant at $a_{\text{cut-off}} \approx 3 \mu\text{m}$. This is expected, since the cut-off is strongly coupled to the location of the minimum, which does not change as well. In principle, the cut-off could be connected to the healing length ξ_h in highly degenerate systems or the ratio of temperature to healing length for systems closer to the critical temperature via

$$\underbrace{a_{\text{cut-off}} \propto \xi_h}_{\text{cold gas}} \quad \text{--- ? ---} \quad \underbrace{a_{\text{cut-off}} \propto \frac{\lambda_{\text{dB}}^2}{\xi_h} \propto \frac{\sqrt{n}}{T}}_{\text{hotter gas}}. \quad (8.20)$$

Unfortunately, a meaningful result can not be extracted from the fit of this parameter to our data. However, considering the influence of the imaging system, the absolute value is reasonable for a system with our parameters.

For a single hold time, we find positive correlations for the fit parameters η and $a_{\text{cut-off}}$. Oddly, this does not correlate with the expectation for increasing temperature for the small range cut-off taken from Eq. (8.20), in clear disagreement with the expectation of Eq. (8.20) that with increasing temperature and hence increasing η the cut-off length $a_{\text{cut-off}}$ should – at least for hotter gases – decrease.

One explanation for this counterintuitive behavior stems from the fact the two fit parameters, η and $a_{\text{cut-off}}$, can result in similar changes to g_2 . This is illustrated by the density correlation functions plotted for

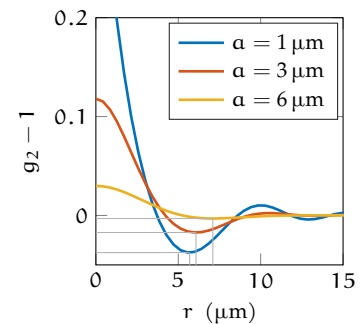


Figure 8.15: Comparison of g_2 for different short-range cut-offs. The density correlation function is computed from Eq. (8.14) for three different $a_{\text{cut-off}}$, 1 μm (blue), 3 μm (red) and 6 μm (yellow). The gray lines indicate the position of the minimum. Note how a change in the cut-off changes both amplitude and location on the r -axis.

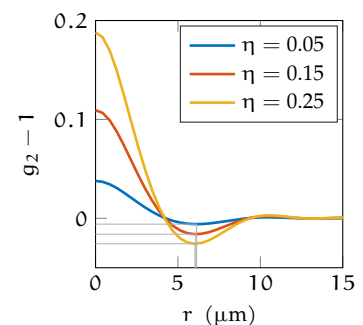


Figure 8.16: Comparison of g_2 for different scaling exponents. The density correlation function is computed from Eq. (8.14) for three different η , 0.05 (blue), 0.15 (red) and 0.25 (yellow). The gray lines indicate the position of the minimum. Note how a change in the scaling exponent changes only the amplitude.

increasing cut-off, Fig. 8.15, and increasing scaling exponent, Fig. 8.16. Although the location of the minimum is solely due to the cut-off, the amplitude degree of freedom depends on $\alpha_{\text{cut-off}}$ and η . With perfect data quality, the fit routine should still be able to discern the effect of the two different parameters very well. However, imperfect data quality and especially the fact that the imaging system blurs small scale structures can lead to undesired cross correlation between the two fit parameters. Due to this difficulty and the fact that we are mostly interested in the phase decay and hence η , the dependence of the short-range cut off on the temperature was ignored in the scope of this analysis.

Discussion of the results

The interpretation of these results is not straight forward since the decreasing scaling exponent presents a departure from the theoretical expectation that assumes thermal equilibrium and algebraically decaying *quasi-long-range order* (QLRO).

In the following, we discuss the interpretation under various assumptions. First, we assume that the system is in thermal equilibrium and subject to heating during the hold time, causing it to cross the transition from a BKT superfluid to a thermal gas. This interpretation is corroborated by the decrease of the occupation of low-momentum modes with hold time observed in the measurements described in Chapter 7. However, this interpretation is in direct disagreement with the decreasing scaling exponent that we extract from the data.

Next, we will discuss effects and limitations of the experimental realization that are not captured by the idealized theory with which we compare and fit the density fluctuations after ToF. These are finite-size effects, the occupation of higher vibrational levels due to temperature or collisions, and the effect of in situ density fluctuations. We find that neither finite size nor temperature induced occupation of higher levels can explain the observed behavior, whereas it is unclear how the occupation of higher levels would change the result.

The most likely explanation seems to be that the system is not in equilibrium, since the heating rates observed and the loss of low-momentum modes occur in only tens of milliseconds, which is on the same order as the time a sound wave needs to travel through the cloud, and hence a timescale for thermalization.

A PLAUSIBLE HYPOTHESIS is that the ultracold 2D gas crosses the phase transition from a quasi-condensate with algebraic quasi-long-range order to a thermal gas with exponentially decaying phase correlations due to heating processes. This hypothesis is also compatible with the observations made in situ and in momentum space although the observed increase in temperature is only small. Initially, the phase-space density $D = n_{2D} \lambda_{dB}^2 \approx 9$, determined via independent density and temperature measurements, is larger than the critical phase-space density $D_{\text{critical}} \approx \ln(380/\bar{g}) \approx 6$. This places the gas in the super-

fluid regime, in agreement with a fitted scaling exponent of $\approx 0.2 < 0.25 = \eta_{\text{critical}}$. As the temperature increases and the density decreases, the critical phase-space density is crossed and free vortices proliferate around density defects¹²³ caused by increased in situ density fluctuations, confer Fig. 8.5a. This process depopulates low-momentum modes rapidly which can also be observed in Fig. 7.9. However, in this case the scaling exponent extracted from the density correlations after short ToF should not decrease as observed but rather increase, at least if the theoretical approximations made are valid. Nonetheless, the obvious alternative – a fit with exponentially decaying correlations – exhibits significantly worse agreement with the measured data.

The hypothesis is not only at odds with the fitted scaling exponent but also with more agnostic and qualitative measures for the density correlations. Qualitative estimates suggest that the minimum in the second order correlation function becomes more pronounced as higher excitations in the Bogoliubov dispersion relation become populated in the quasi-condensate. In an intuitive picture, this can be understood in the following way. The increasing population of Bogoliubov modes leads to stronger phase fluctuations, which manifest themselves in regions of constructive and destructive interference, the latter give rise to the minimum in the correlation function. Yet, direct observation of the contrast as well as quantitative analysis of the scaling exponent indicate that this is not the case.

The considerations made above suggest that neither of the tested correlation functions fully describes the gas during the assumed heating process. However, the heating hypothesis fails to be rejected since the existence of heating is not only very plausible from a thermodynamic point of view but a series of independent measurements on our system, during which the *equation of state* (EOS) of the gas was determined by the application of a local potential, strongly corroborate a reduction in phase-space density during prolonged capture in a dipole trap. For details regarding this method see the work by K. Hueck et al⁸⁶.

8.4 POSSIBLE ISSUES WITH THE THEORETICAL DESCRIPTION

A possible solution lies in the possibility that we study a system that does not fulfill the conditions for the applicability of the model theory. The theoretical framework we use to compute the density correlation functions after time of flight is based on a Bogoliubov-type mean field approach. It assumes that the homogeneous gas is of infinite size, has very small density fluctuations and that the system is 2D, i. e. that no higher vibrational levels are excited. Finally, it is only valid for weak to moderate interactions. In the following, we explore the applicability of these assumptions in turn.

¹²³ A. L. Fetter: *Phys. Rev.*, vol. 138, (1964)

⁸⁶ K. Hueck et al.: *Phys. Rev. Lett.*, vol. 120, (2018)

8.4.1 Applicability of the used theoretical ansatz

This section will explore the most evident objections that could be raised against the suitability of the used theoretical ansatz.

The finite size of the sample has several consequences that are not captured by the theory. First of all, it introduces a definite upper limit to the correlation length: if the correlation length gets larger than the size of the system, true Bose-Einstein condensation can occur^{55,124}. However, this is clearly not an issue at our elevated temperatures and large interaction strength.

Secondly, phase fluctuations with wavelengths longer than the size of the system cease to exist, making BKT superfluids more robust against thermal fluctuations. Calculations by L. Mathey* suggest that algebraic order can persist up to scaling exponents that are twice as high as the critical scaling exponent for an infinite system of $\eta_c = 0.25$, i. e. superfluidity can exist even at higher temperatures. Again, this interesting fact does not seem relevant for the interpretation of our observation, since the extracted scaling exponent decreases rather than increases beyond the critical value.

The ansatz assumes a purely two-dimensional system, finite size effects in the strongly confined direction are thus not considered and are assumed to be negligible as is elaborated later. However, we point out that in our analysis certain finite-size effects are accounted for: We compensate for the finite size of the mask on which we evaluate g_2 by dividing the g_2 obtained from the masked regions by the correlation function of the mask itself. This approach coincides with the use of periodic boundary conditions and correlation functions of infinite systems in the computation of the fit functions, see Appendix B for details.

DENSITY FLUCTUATIONS ALREADY EXISTENT IN THE GAS before the short time of flight, i. e. in situ, present a further issue for the theoretical description. Zeroth order theory would only consider in situ phase fluctuations, since density fluctuations are expected to be strongly suppressed for repulsively interacting 2D systems. Within this approximation, any density correlations appearing in g_2 after short time of flight arise from phase fluctuations. However, initial density fluctuations can also give rise to density correlations after time of flight.

The fits in Section 8.3.3 show that our gas exhibits sizable in situ density fluctuations compared to the total density fluctuations after time of flight, which result from both the phase and the density. Unfortunately, it is very difficult to treat their combined effects after time of flight accurately. The reason is that density and phase fluctuations are usually treated additively as a small perturbation. When calculating the free time evolution, the complex amplitudes are squared to arrive at the density correlation. This gives rise to an interference term²⁷.

The theory of V. Singh and L. Mathey used here assumes that in situ phase and density fluctuations are small. In this case they show

⁵⁵ R. J. Fletcher et al.: *Phys. Rev. Lett.*, vol. 114, (2015), ¹²⁴ D. S. Petrov et al.: *Phys. Rev. Lett.*, vol. 84, (2000)

*Private communication, L. Mathey

²⁷ R. Desbuquois: *Thermal and superfluid properties of the two-dimensional Bose gas*, (2013)

that, to first order, the interference term can be omitted and the density fluctuations can be approximately compensated for by subtracting the in situ density power spectrum from the power spectrum observed after short TOF. The suggested subtraction of the power spectra is somewhat more involved when working in real space rather than in momentum space, as discussed in Section 9.2.3.

The alternative, ab initio simulation of the influence of the in situ density fluctuations is computationally prohibitively expensive and the analysis must still omit the interference term since the phase term is not initially known. In order to include the interference term, the implicit equations for $\delta\theta$ would have to be solved iteratively which is even less feasible.

Density fluctuations as well as vortices and other short scale effects also have an impact on the theoretically expected first order correlation function g_1 , leading to a more complicated decay³³. The effects are typically captured by the cut-off parameter $a_{\text{cut-off}}$ at short distances and by renormalizing the long-range algebraic decay by replacing $n_{\text{total}} \rightarrow n_{\text{superfluid}}$. Thus, for large distances, g_1 scales directly with the superfluid density n_s as

$$g_1 = \frac{n_s}{n_t} \left(\frac{\xi}{r} \right)^\eta. \quad (8.21)$$

At present, the algebraically decaying model employed does not account for the latter renormalization and the data is fitted with an algebraic model that effectively sets $n_s/n_{\text{total}} = 1$. We expect that at the critical point the ratio is lowest with $n_s/n_{\text{total}} \approx 0.66$. Thus, for a significant decrease in superfluid density, the dependence of g_1 on n_s could lead to a reduction of the observed interference visibility after ToF.

Although we compensate for in situ density fluctuations in first order phenomenologically, it is not clear what impact they may pose on the theoretical description. While repulsive interactions are expected to suppress density fluctuations for $r > \xi$, with ξ being the healing length, when $g_{2D}n_{2D}/k_B T \gg 1$ or equivalently $D \gg 2\pi/\tilde{g} \approx 7$, we do not fulfill these criteria very strongly. For our parameters, these values are $g_{2D}n_{2D}/k_B T \approx 1.5 - 2.5$, whilst the phase-space density D is approximately $4.5 - 9$. These estimates reaffirm that – at least for our hotter samples – also the theoretical considerations made might be improved by dropping the assumption of small density fluctuations, even when calculations by N. Prokof'ev et al.⁶⁸ show that they can be suppressed already for $D \gg 1$.

STRONG INTERACTIONS BETWEEN COMPOSITE BOSONS limit the integrity of a mean field approach when the system is dominated by a many-body state. An estimate of this regime yields an interaction parameter close to or above $\tilde{g} \approx 2\pi$ ³³. The gas is held in the dipole trap at a magnetic field of ≈ 690 G, this results in a dimer-dimer interaction parameter of $\tilde{g} \approx 0.87$. Hence, a mean field approximation is expected to yield acceptable results. Additionally, other groups have had much success with a mean field description at similar interaction parame-

³³ Z. Hadzibabic and J. Dalibard: *Riv. Nuovo Cimento*, vol. 34, (2011)

⁶⁸ N. Prokof'ev et al.: *Phys. Rev. Lett.*, vol. 87, (2001)

³³ Z. Hadzibabic and J. Dalibard: *Riv. Nuovo Cimento*, vol. 34, (2011)

ters, e. g. J. Selim's group has found reasonable agreement even up to $\tilde{g} \approx 2.76$.

EXCITED TRANSVERSE MODES in the strongly confined axial direction challenge the validity of the description of the gas as a low-dimensional system. As J. Kestner and L. Duan have shown⁸⁸, even for very dilute gases and/or very strong vertical confinement, a significant fraction of excited modes perpendicular to the 2D plane must be considered in strongly interacting systems when dealing with a wide Feshbach resonance as in the case of ⁶Li. Although this does not explicitly exclude the usage of an effective low-dimensional description, it is still an issue under discussion whether gases fulfilling $\hbar\omega_z \gg k_B T$ and $\hbar\omega_z \gg g_{2D}n_{2D}$ can be considered 2D close to a Feshbach resonance^{125–128}.

If we disregard this issue and only consider the mean-field energy of the composite bosons and their temperature, we find that the typical criterion used to determine whether an effective description via a 2D Hamiltonian is suitable is fulfilled. It states that the gas can be considered to be 2D if the energy spacing in the strongly confined direction exceeds the thermal energy and the mean-field interaction energy, i. e. as mentioned above

$$\hbar\omega_z \gg g_{2D}n_{2D}. \quad (8.22)$$

We find this requirement to be satisfied for our parameters,

$$\frac{\hbar\omega_z}{g_{2D}n_{2D}} \approx 6.8 \gg 1. \quad (8.23)$$

Additionally, thermal excitations should not be able to populate the higher transverse modes for the system to still be considered 2D. Thus, the trap spacing must exceed the thermal energy as well

$$\hbar\omega_z \gg k_B T. \quad (8.24)$$

Again, this is reasonably well satisfied, since a worst case estimate for our system yields

$$\frac{\hbar\omega_z}{k_B T} \approx 5. \quad (8.25)$$

Here, we have used a trap frequency of $\omega_z = 2\pi \cdot 12\,400$ Hz and our highest measured temperature of $T \approx 120$ nK.

Hence, a definitive conclusion can not be drawn. We have not observed high excited fractions in transverse modes but an argument for an *effective* Hamiltonian instead of the ansatz used in this analysis can certainly be made.

8.4.2 Probable necessity for non-equilibrium description

Collisions with particles of the background gas limit the measured $1/e$ lifetime of a non interacting gas to approximately (8.19 ± 0.62) s. During each collision, a particle is removed from the sample and either

⁸⁸ J. P. Kestner and L. M. Duan: *Phys. Rev. A*, vol. 74, (2006)

¹²⁵ J. P. Kestner and L. M. Duan: *Phys. Rev. A*, vol. 76, (2007), ¹²⁶ K. Merloti et al.: *Phys. Rev. A*, vol. 88, (2013), ¹²⁷ P. Dyke et al.: *Phys. Rev. A*, vol. 93, (2016), ¹²⁸ H. Hu et al.: *ArXiv*, (2018)

imparts energy into the gas via collisions or – especially when a low-momentum particle is removed – by the reorganization cascade of the remaining particles seeking equilibrium.

Additionally, if the gas is sufficiently dense – or strongly interacting – three-body collisions present an even faster loss channel with a timescale on the order of ≈ 100 ms for our parameters.

Since the equilibration at the final magnetic field is comparatively slow, two scenarios might ensue. Either the system is quenched during the magnetic field ramp from the evaporation state at strong interactions close to 834 G to relatively low interactions, which results in a super-heated 2D quasi-condensate similar to the observations made by A. Gaunt et al.¹²⁹ in 3D. This state would be topologically protected against thermalization, i. e. forming vortices, and hence rule out a quasi static description which assumes constant equilibrium.

Alternatively, the system might initially be in – global – thermal equilibrium but fast three-body decays impart energy into the system locally. If e. g. single vortices are allowed to nucleate at the density defects, thermal equilibrium is destroyed since vortex lifetimes are expected to be much longer than the timescales probed in the experiment. A super heated sample could be compatible with the observed superfluid fraction of $\approx 40\%$, if we assume that the extracted *peak fraction* approximates the true *superfluid fraction*, since for the measured phase-space densities, a much larger superfluid fraction of $\approx 80\%$ is expected.

Also, if thermal equilibrium is indeed absent, the hypothesis of heating during hold time can not be maintained. From this perspective, if constant equilibrium temperature is assumed, the decrease in the scaling exponent might be compatible with the observation of the depopulation of low-momentum modes. Low-momentum modes populate the linear region of the Bogoliubov dispersion and are dominantly phase excitations. Hence, a decrease in low-momentum modes corresponds to a decrease in phase excitations which in turn leads to a decrease of the scaling exponent η . Nonetheless, further studies are required to corroborate this qualitative description quantitatively.

8.4.3 Technical causes

Improper density calibration or an uncompensated imaging system could also be responsible for the observed discrepancy between experiment and theory. However, the analysis has been compensated for all systematic errors known to us and validated on synthetic data. The details of the employed procedure are expanded on in the following chapter.

¹²⁹ A. L. Gaunt et al.: *Nature Physics*, vol. 9, (2013)

9

MANAGING SYSTEMATIC ERRORS

- 9.1 Setting the experimental parameters 115
- 9.2 Compensation of systematic errors 123
- 9.3 Technical details of the implemented analysis 134
- 9.4 Advantages of analyzing g_2 instead of the PSD 141

Since the presented measurement is highly sensitive to the proper calibration of the apparatus, we present here the measures taken to minimize undesirable influences. Foremost, the sample must be centered in the *depth of field* (DoF) as experiments in the group of Y. Shin have demonstrated^{79,119}. Additionally, the detuning of the imaging laser light from the D2 line has strong impact on the measured density-density correlation function g_2 ²⁸ and hence needs to be set correctly. Since the focus lies on the *normalized* g_2 , the calibration of the density is of secondary importance but is vital to the interpretation of the results.

Following the presentation of the calibration of these critical parameters, the compensation of systematic errors which cannot not be averted is discussed. Here, the effect of the imaging system is presented in terms of the *point spread function* (PSF) and its Fourier transform the *amplitude transfer function* (ATF) alongside the introduction of the necessary theoretical background.

Finally, it is also explained why we have refrained from using the *power spectral density* (PSD) directly in the quantitative analysis.

9.1 SETTING THE EXPERIMENTAL PARAMETERS

9.1.1 Focus

It is imperative to ensure proper focus of the imaging apparatus onto the sample, which has been demonstrated by the group of Y. Shin⁵⁸. This is due to the fact that the free propagation of the imaging light through a gas out of focus can lead to very similar density modulation patterns compared to the free propagation of a matter wave field during *time of flight* (ToF). Hence, we employ a focusing technique developed in the group of I. Spielman¹²⁰, known to yield accurate results even if the extent of the cloud exceeds the DoF. This degree of robustness is advantageous since the gas of ^6Li expands quickly after release from the dipole traps and is additionally accelerated out of the plane of focus by absorption and reemission of the imaging light.

In order to obtain the optimal focus via the technique by I. Spiel-

⁷⁹ J.-Y. Choi et al.: *Phys. Rev. Lett.*, vol. 111, (2013), ¹¹⁹ S.-W. Seo et al.: *J. Korean Phys. Soc.*, vol. 64, (2014)

²⁸ S. Pres: *BKT - phase transition in a strongly interacting 2D Bose gas*, (2014)

⁵⁸ J.-Y. Choi et al.: *Phys. Rev. Lett.*, vol. 109, (2012)

¹²⁰ A. Putra et al.: *Rev. Sci. Instrum.*, vol. 85, (2014)

man et al., absorption images of the cloud are taken for varying distance from the imaging objective. In a gas with sufficiently random density fluctuations, the atomic shot noise serves as an imaging test target featuring a very small length scale. Imaging this atomic shot noise reveals the spatial frequencies which cannot be captured since they exceed the solid angle given by the *numerical aperture* (NA). From these absorption images, the PSD is computed of each image via 2D Fourier transform which displays pronounced minima and maxima in frequency space. A theoretical description and numerical simulations yield the result that optimal focus is achieved when the distance of said minima from the center of the frequency space is maximal.

The numerical simulation of the focusing procedure is presented in Fig. 9.1. It can be seen that the distance of the minima (white) from the origin diverges when in focus. For physical imaging systems, the maximal distance approaches the maximum observable frequency given by the NA, i. e. $k_{\max} = 2\pi NA/\lambda_{D2}$, with λ_{D2} being the optical wavelength of the imaging laser on the D2 line. Due to the limited range of the piezo actuators moving our imaging objective, even at maximum defocus only the first minimum could be resolved in our experiment. Fortunately, the distance of the first minimum from the origin is directly proportional to the width of the central peak in the PSD which is seen to also reach a maximum in focus. Hence, we achieve optimal focus of our imaging system when the actuators are set to protract by $(45 \pm 5) \mu\text{m}$. Note that this method compensates for the movement of the sample during the imaging and hence yields an *effective* focus position where the average influence of defocus is minimal.

This type of measurement yields excellent results, yet is very time consuming. A large number of images is required at each focusing step because the information is extracted only from the atomic shot noise. A traditional method to obtain optimal focus is based on reducing the apparent extent of an imaged feature which has a size below the resolution limit. Such an object is prepared in our elongated dipole trap. After evaporation, the trapping potential is abruptly increased for $420 \mu\text{s}$ during which the atoms perform exactly $1/4$ of the oscillation in the transverse direction. Hence, the atoms are compressed and the atomic sample has a final diameter on the order of the imaging resolution. This type of focusing procedure can be performed much faster since usually only a single image is required per focusing step due to the high density. However, this method can only be applied to particle clouds of axial extent well below the DoF and the error due to the movement of the sample during imaging is unclear. However, the extent of the compressed atom cloud in the direction of the imaging axis is also on the order of the imaging resolution and hence well below the DoF. The displacement due to our $5 \mu\text{s}$ imaging pulse is expected to be approximately $7 \mu\text{m}$ which is small compared to the DoF and hence can be neglected.

Both methods are measured to be in very good agreement as can be seen from Fig. 9.2. Due to the simplicity and time efficiency of the latter method, it is employed during day to day operation and calibrated

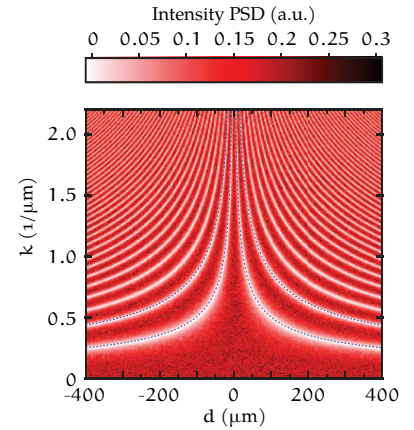


Figure 9.1: Example of the (simulated) result obtained via the Spielman focusing method. Here, the PSD (color) is plotted in dependence of the spatial frequency k (vertically) and the distance to the optimal focus position. The white lines indicate minima which move towards larger k when approaching the optimal focus position. The value of the color index is given above the data. Figure adapted from A. Putra¹²⁰.

¹²⁰ A. Putra et al.: *Rev. Sci. Instrum.*, vol. 85, (2014)

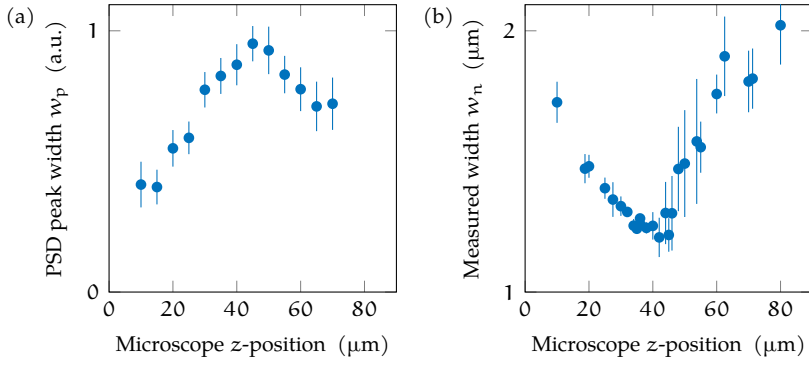


Figure 9.2: (a) The PSD main peak width in arbitrary units in dependence of the microscope z-position. Where the PSD shows the maximum, the optimal focus is obtained. The error bars indicate the statistical standard deviation. (b) Focusing imaging system via matter wave focus. Here, the width of the imaged cloud is plotted in dependence of the microscope z-position. When minimizing the width, the highest resolution and hence optimal focus is obtained. The error bars denote the width fitting error. Figure (b) adapted from K. Hueck¹³⁰.

¹³⁰ K. Hueck et al.: *Opt. Express*, vol. 25, (2017)

by the PSD based focusing method on longer time periods.

Additionally, the focus position is verified by measuring the ATF for the short ToF measurement in order to compensate for the influence of the imaging system. As in the method by I. Spielman et al. the images of the gas containing atomic shot noise are characterized in spatial frequency space via the ATF, which is the Fourier transform of the PSF. The PSF represents an accessible measure for the influence of the imaging apparatus in position space and describes the apparent image of a point source. Since every image can be thought of as a superposition of points, this PSF can be used to compensate for the non-ideal imaging, as discussed in detail in Section 9.2.2.

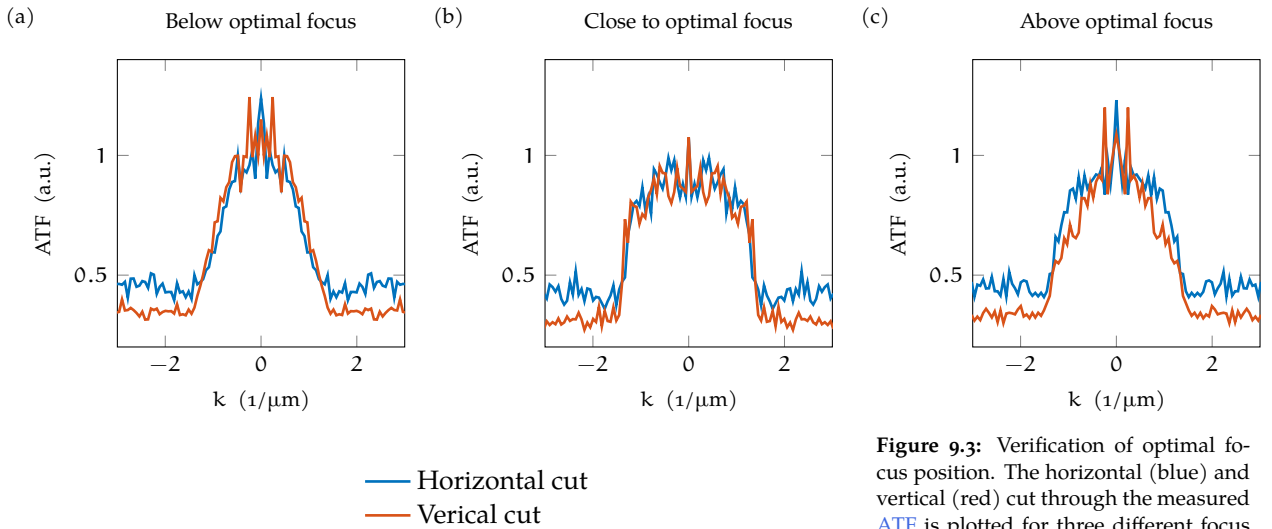


Figure 9.3: Verification of optimal focus position. The horizontal (blue) and vertical (red) cut through the measured ATF is plotted for three different focus positions. Ideal focus is represented by a Heaviside function, hence the closest resemblance is desired. (a) Microscope position below the optimal focus. (b) Microscope position close to the optimal focus position obtained with the aforementioned methods (see text). (c) Microscope position above the optimal focus. Note that the ATF exhibits the steepest transition when the microscope is close to the optimal focus position in figure (b).

If a point source is unavailable, a gas with a maximally random density distribution can also be used to obtain the independent response of the imaging system. Hence, the short ToF measurement was reproduced under identical imaging conditions but with an only weakly degenerate free Fermi gas at ≈ 530 G which exhibits no structure in frequency space, i. e. a flat measured spectrum for ideal imaging. Transforming the PSF into frequency space yields the ATF, which is expected to be uniform when in focus. Due to the limiting factor of the NA, the optimally achievable ATF takes the form of a unit-step function, vanishing at $\pm k_{\max} = 2\pi NA/\lambda_D$. Three examples of the

ATF for different positions of the objective are shown in Fig. 9.3. It can be seen that the ATF resembles a unit-step function best in the center image, Fig. 9.3b and becomes notably smoothed below and above the optimal focus position, see Fig. 9.3a and Fig. 9.3c respectively. Here, two cuts through the ATF are shown, one horizontal the other vertical, which indicate a symmetric ATF and hence proper alignment of the imaging apparatus, only Fig. 9.3c shows slight differences in vertical and horizontal dependence. In principle, images as these can be used to also align the microscope objective in addition to setting the optimal focus. However, the physical imaging characteristics are already very close to ideal and hence we have chosen to correct for remaining deviations numerically, as will be discussed in Section 9.2.2.

9.1.2 Detuning calibration and optimal intensity

The frequency of the imaging beam is optimal when the absorption of light by the atoms is maximized. To this end, we apply imaging pulses of different detunings and measure the imparted momentum. A $1\ \mu\text{s}$ long pulse of imaging light is applied in the z -direction and the displacement of the atoms is imaged after $80\ \mu\text{s}$ ToF via the auxiliary imaging perpendicular to the direction of motion. After determining the cloud's center of mass, it is obvious from Fig. 9.4 that a particular detuning yields the greatest displacement and hence indicates resonance with the D2 line of ${}^6\text{Li}$. Fits to the displacement in dependence of intensity yield a typical detuning within 4% of the natural linewidth of ${}^6\text{Li}$. Details of this process as well as most of the other calibration procedures can be found in our paper *Calibrating high intensity absorption imaging of ultracold atoms*¹³⁰. The advantage of measuring the displacement rather than the optical density via absorption is that it is independent of e. g. atom number fluctuations.

Since typical illumination times of our experiment are on the order of $5\ \mu\text{s}$, the displacement of the cloud for this imaging pulse is also measured and plotted in red in Fig. 9.4. Despite the five-fold illumination time, it is clear that the cloud has not been displaced five times further. The diminished absorption is due to the Doppler effect experienced by the accelerated atoms, which is more pronounced the longer the imaging pulse. In order to maximize the amount of scattered photons and hence the *signal-to-noise ratio* (SNR), shown in Fig. 9.5a, we compensate the Doppler shift by adjusting the frequency dynamically during the imaging time. To optimize this frequency chirp, the maximum displacement measurement is repeated, now in dependency of the chirp rate and yields approximately $1.5\ \text{MHz}/\mu\text{s}$ at saturation intensity.

The effect of the frequency chirp is illustrated in Fig. 9.5b. Here, the cloud velocity is determined after illuminating pulse lengths up to $15\ \mu\text{s}$ at 3.75 saturation intensity. The difference between the chirped and unchirped case is clearly visible. When the imaging is not frequency compensated (red squares), the atoms are shifted out of resonance and hence the velocity exhibits a sub-linear dependency instead

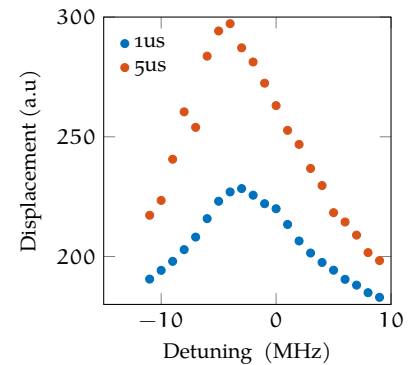


Figure 9.4: Example of the displacement of the atom cloud after illumination with (near) resonant laser light for the illumination times $1\ \mu\text{s}$ and $5\ \mu\text{s}$ in dependence of the detuning in arbitrary units. The maximal displacement indicates the greatest momentum transfer and thus optimal detuning. Note the reduction in relative displacement for longer illumination times due to the Doppler effect.

¹³⁰ K. Hueck et al.: *Opt. Express*, vol. 25, (2017)

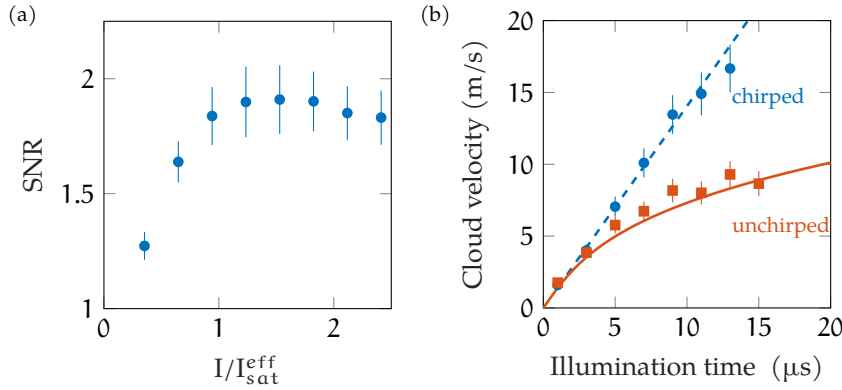


Figure 9.5: (a) signal-to-noise ratio evaluated as the standard deviation per pixel for all realizations and subsequently averaged over all pixels. Note the broad maximum between 1 to 2 $I/I_{\text{sat}}^{\text{eff}}$. The error bar indicates the standard deviation obtained from averaging over the pixels. (b) Velocity of the atom cloud in dependence of the illumination time at an intensity of $3.75I_{\text{sat}}^{\text{eff}}$. The effect of chirping the imaging light is clearly visible. In the unchirped case (red squares), the scattering rate decreases with illumination time and hence the velocity becomes sub-linear. When chirped (blue circles), the acceleration is constant. The theoretical expectations for the chirped (unchirped) case are given as red solid (blue dashed) lines. The error bars indicate the systematic error estimated for the auxiliary imaging. Figure adapted from K. Hueck¹³⁰.

¹³⁰ K. Hueck et al.: *Opt. Express*, vol. 25, (2017)

of the expected linear increase in velocity displayed when the imaging detuning is chirped (blue circles). The experimentally determined chirp rate yields excellent agreement with theoretical predictions as the plotted curves show. In summary, this method allows us to set the imaging light detuning and intensity quickly to optimal values before each measurement.

9.1.3 Density calibration

In order to discuss the density calibration procedure, the relations necessary to obtain an atomic density from two high intensity absorption images are introduced briefly in the following.

The usual Beer-Lambert law for absorption has to be extended for high intensity imaging where the effects of saturation have to be considered. According to G. Reinaudi et al.¹³¹, the optical density $od(x, y)$ and thus the 2D column density n_{2D} is then given by

$$\begin{aligned} od(x, y) &= \sigma_{\text{eff}} n_{2D}(x, y) \\ &= -\ln\left(\frac{C_{\text{out}}(x, y)}{C_{\text{in}}(x, y)}\right) + \frac{C_{\text{in}}(x, y) - C_{\text{out}}(x, y)}{C_{\text{sat}}^{\text{eff}}}. \end{aligned} \quad (9.1)$$

Here, the incident and final intensities I_{in} and I_{out} , which usually occur in this expression, are replaced by the count rates $C_* = \gamma I_*$ measured on the CCD camera, where γ is a – usually unknown – conversion parameter dependent on the precise parameters of the imaging apparatus but common to all measured intensities which hence cancels out. However, the effective scattering cross section $\sigma_{\text{eff}} = \alpha\sigma_0$ and the effective saturation counts $C_{\text{sat}}^{\text{eff}} = \alpha C_{\text{sat}} = \alpha\gamma I_{\text{sat}}$ had to be introduced, which capture the effects of non-perfect polarization or magnetic field orientation, hence reducing the ideal cross section $\sigma_0 = \frac{3\lambda}{2\pi}$ and the saturation intensity. At first, the formulation in terms of measured counts does not seem to be an improvement since the unknown factor has only been transferred from the measured intensity to the – previously known – saturation intensity. However, the effective saturation counts are readily measured which yield a calibration procedure unaffected by common error sources like fluctuating imaging beam power

A charge-coupled device, or CCD, converts the incident photons scattered by the atomic cloud into an electric signal suitable for digital analysis.

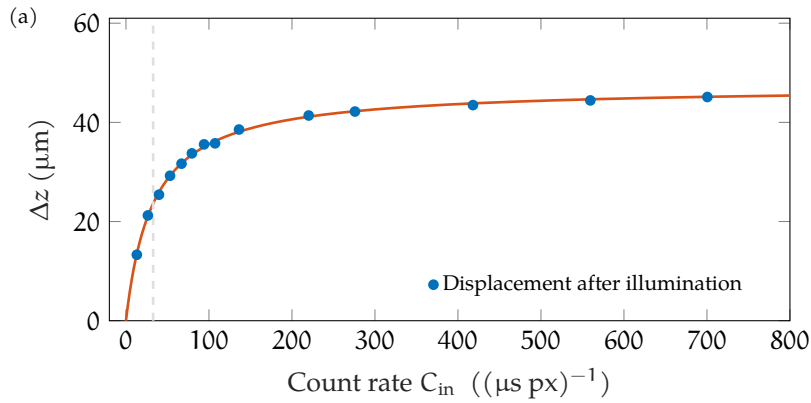
¹³¹ G. Reinaudi et al.: *Opt. Lett.*, vol. 32, (2007)

or atomic density.

The measurement of the effective saturation counts $C_{\text{sat}}^{\text{eff}}$ is based on the saturation of the photon scattering rate and hence displacement for higher beam intensities¹³⁰. Thus, a displacement measurement similar to the detuning determination detailed before exhibits a z -displacement which is described by

$$z(\nu_L, s) = z_0 + \kappa \frac{\Gamma}{2} \cdot \frac{s_0}{1 + s_0 + (2\Delta/\Gamma)^2}. \quad (9.2)$$

The displacement depends on the imaging laser detuning $\Delta = \nu_L - \nu_a$, with the laser frequency ν_L , atomic resonance frequency ν_a , and the natural linewidth of the imaging transition Γ . Here, κ is a factor converting the position difference to a scattering rate and $s_0 = I/I_{\text{sat}}^{\text{eff}} = C_{\text{in}}/C_{\text{sat}}^{\text{eff}}$ is the saturation parameter comparing the actual incident intensity I to the saturation intensity, both of which are left as free parameters.



Fitting the measured displacement in dependence of the incident intensity measured in terms of counts on the CCD camera with the above formula yields the parameters κ and $C_{\text{sat}}^{\text{eff}}$ to high precision. An example of the fit produced by this method is presented in Fig. 9.6a.

In summary, the measurement of the displacement after illumination in dependence of the measured count rate allows us to determine the atomic density without prior knowledge of the parameters of the imaging apparatus or camera efficiency. That the employed method yields indeed a proper density is demonstrated in Fig. 9.6b, where the unmodified Beer-Lambert law is compared to the saturation corrected formula which shows an approximately constant density over a wide range of incident imaging intensities.

9.1.4 Magnification calibration

The knowledge of the magnification of the imaging apparatus directly impacts all measurements of absolute length scales. Hence, a calibration in relation to a well known reference is required. No pre-calibrated target exists in our ultra high vacuum cell. Fortunately, the

¹³⁰ K. Hueck et al.: *Opt. Express*, vol. 25, (2017)

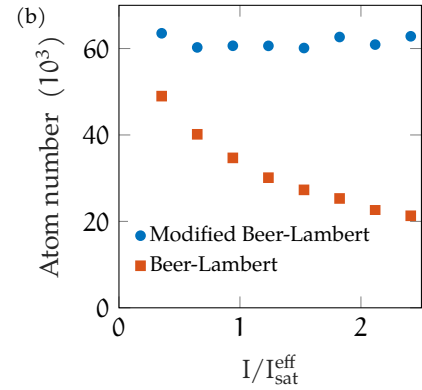


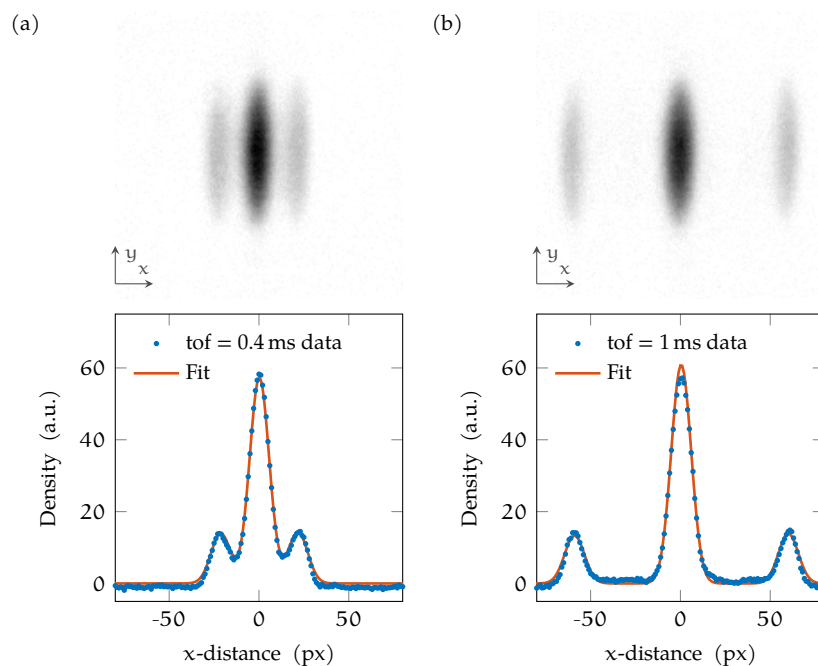
Figure 9.6: (a) The difference Δz in displacement for two ToF ($\Delta t = 10 \mu\text{m}$) as a function of the incident intensity and hence C_{in} . The line denotes a fit with Eq. (9.2) from which the saturation count rate $C_{\text{sat}}^{\text{eff}}$ can be determined (b) Measured atom number in dependence of the incident intensity determined with the modified Beer-Lambert law for high intensities used in this thesis (blue circles) and the unmodified relation (red squares). The measured atom number does not depend on the imaging intensity, hence validating the application of the modified Beer-Lambert law. Here, the errors bars are smaller than the symbol size. Figure adapted from K. Hueck¹³⁰.

¹³⁰ K. Hueck et al.: *Opt. Express*, vol. 25, (2017)

already present ultracold atom cloud can be used to create such a target, exploiting the Kapitza-Dirac effect, which is discussed in more detail in the masters thesis of K. Riechers¹³²

In order to create a known length scale from the atomic cloud, one of the *far off resonance traps* (FORTs) perpendicular to the imaging to be calibrated is temporarily retroreflected, hence producing a standing wave of light of known spacing at the position of the atoms. If the movement of the atoms during the interaction can be neglected, the interaction can be thought of as a diffraction of the atoms by the optical lattice, similar to how a laser beam is diffracted by an optical grating. During diffraction, a momentum of $\pm 2\hbar k_l$ is imparted onto the incident atom wave and hence a fraction of the atoms travel perpendicular to the optical axis of the imaging objective. Here, k_l is the wavenumber of the laser, in our case $k_l = 2\pi/\lambda \approx 2\pi/1064 \text{ nm}$. If the displacement measured in terms of pixels on the camera is compared to the theoretical prediction, the conversion factor and hence the magnification can be obtained.

Two average absorption images of the diffracted atom clouds for two different ToF are shown in the upper half and the corresponding projection onto the x -axis in the lower half of Fig. 9.7. The 1D density projection is fitted with an arbitrary spline in order to retrieve the maxima and thus the traveled distance. For longer flight times, the diffracted atoms are displaced a greater distance which allows the usage of the relative distance, therefore canceling out possible timing uncertainties.



¹³² K. Riechers: *Friedel oscillations and the Fermi wavevector in low-dimensional ultracold Fermi gases*, (2016)

Figure 9.7: A momentum of $\pm 2\hbar k_l$ has been imparted onto a fraction of the atoms which is visible in the displacement after time of flight. The density is given in arbitrary units since only the position of the peaks is of interest. The traveled distance is denoted in pixels (px) of the camera which is calibrated via this measurement. The magnification can be determined from comparing the measured relative distance and the expected relative distance traveled. (a) Average density and spline fit to sum in vertical direction after 0.4 ms ToF, the atoms have traveled only a short distance. (b) Average density and spline fit to sum in vertical direction after 1 ms ToF, the atoms have traveled a longer distance. Note that all density images are averages of approximately 50 individual images.

Since the atoms are subject to a harmonic potential during ToF, the

expected traveled distance is

$$\chi(t) = \frac{2\hbar k_l}{\omega_{\text{harmonic}} m_{\text{dimer}}} \cdot \sin(\omega_{\text{harmonic}} t). \quad (9.3)$$

Here, ω_{harmonic} denotes the trapping frequency of the harmonic potential and m_{dimer} is the mass of a molecular ${}^6\text{Li}$ dimer.

Thus, the desired magnification M is obtained by comparison with the measured relative distance Δ in camera pixels, for the relative time difference $\Delta t = \text{tof}_{\text{long}} - \text{tof}_{\text{short}}$ i. e. in this case for a pixel side length of $32 \mu\text{m}$ due to binning

$$M = \frac{32 \mu\text{m} \cdot \Delta}{x(\Delta t)} = 30.8 \pm 0.3. \quad (9.4)$$

To summarize, we have shown the methods applied to obtain reliable calibration of the focus position, imaging detuning, intensity, and magnification. These present the basis of a qualitative measurement. However, not all sources of uncertainty can be removed by calibration. A selection of relevant sources of systematic errors are the topic of the following chapter.

The actual pixel size of our camera is $16 \mu\text{m}$, however a common technique to increase the signal is to combine pixels into larger *bins*. We have chosen here a binning of 2 in each direction, i. e. four pixels are combined into one.

9.2 COMPENSATION OF SYSTEMATIC ERRORS

The central topic of this section is the treatment of systematic errors which even after careful calibration are not negligible.

The two most important systematic error sources are highlighted. The first is the limited resolution of the imaging system effectively smoothing out the density ripples appearing after ToF. The second is the presence of density fluctuations in the clouds before ToF despite the string repulsive interaction which also results in density fluctuations after ToF and which must be accounted for.

9.2.1 Absorption image acquisition procedure

In order to discuss the compensation of systematic errors, it is helpful to first illustrate the measurement procedure in our experiment.

At the end of each experimental cycle we illuminate a cloud of ultracold ${}^6\text{Li}$ dimers with resonant laser light and record the imaging light as well as the created shadow on a highly efficient CCD camera with fast vertical shift, which enables the acquisition of two images in fast succession*. In fact, a total of three images are taken in sequence

1. An image of the shadow cast by the illuminated atom cloud
2. After $460.8\ \mu\text{s}$, an image with identical parameters but without atoms in the observation volume
3. After a longer delay of 500 ms, two corresponding images with no incident imaging light or atoms in the observation volume.

* The model of the used camera is: Andor iXon DU-897 used here in *fast kinetics mode* to acquire two images in fast succession.

The third image contains the systematic noise of the camera imaging circuit such as dark currents and offset voltages and is thus subtracted from each of the first two images. Here, it is assumed that the characteristics of the camera are constant, which is a reasonable approximation for such short delays. Since the first and second image now contain only the measured counts which are proportional to the final and incident intensity, respectively, we insert the data from these images into the formula introduced in Section 9.1.3 to obtain the atomic density.

Despite the fact that this process has been calibrated carefully in order to minimize as many systematic errors as possible, one major systematic error cannot be eliminated, the limited resolution of the imaging apparatus.

9.2.2 Influence of the imaging system

A considerable theoretical framework has been developed over the years in the effort to compensate for non-ideal imaging systems. A complete treatment is beyond the scope of this thesis, thus we limit the

discussion to the core concepts relevant for the presented experiments. This discourse is based on the theory of Fourier optics and hence follows the excellent textbook of J. Goodman¹⁰⁹ in notation and reasoning. The treatment revolves around the model of a physical imaging apparatus as a *linear invariant system (LIS)*, a flexible concept also used for example in control theory or signal processing. Due to the linearity, the obtained image can be described as a result of a collection of point sources, where each point source is weighted by the *PSF* that describes the aberrations and limitations introduced by the imaging system. Especially in coherent fluorescent and absorption microscopy, a common technique involves the measurement of the *PSF* and the subsequent deconvolution of the raw image to compensate for said *PSF*. Even if the imaging system is taken to be free of aberrations, the finite aperture and wavelength still limit the resolution. In our case, the wavelength is not the limiting factor but the *NA*. In general, the *PSF* is dependent on all three spatial dimensions and only for a very thin sample of a thickness much smaller than the *DoF*, the *z*-dependency can be omitted. The *z*-extent of the gas during the $T/4$ measurement is on the order of millimeters while the *DoF* is on the order of micrometers. Hence, the gas is subject to different *PSFs* at different *z*-locations. To compensate for this, we average all contributions along the imaging axis, as will be explained in more detail in Section 9.2.2.

¹⁰⁹ J. W. Goodman: *Introduction to Fourier Optics*, (2005)

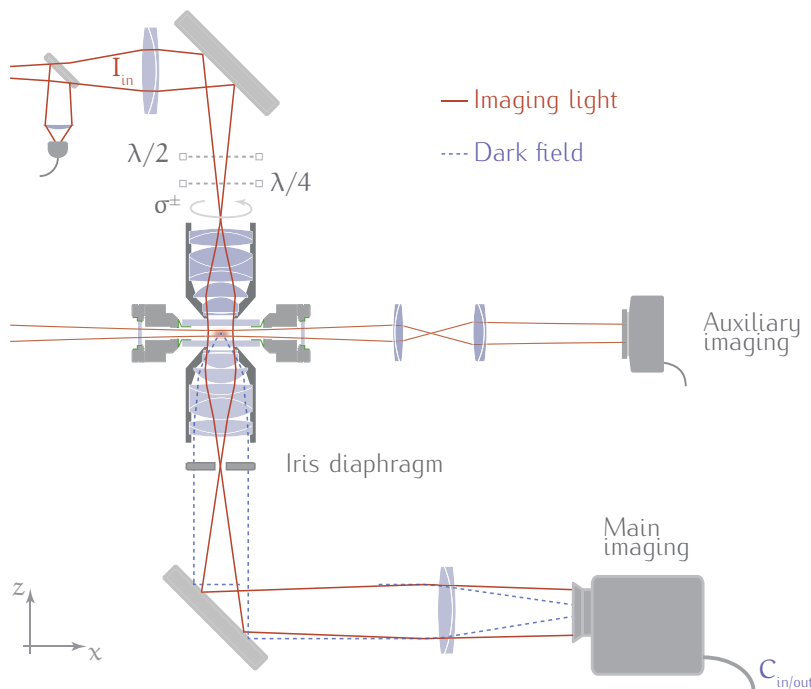


Figure 9.8: Sketch of the imaging setup. The atoms contained in the experiment cell in the center of the image are illuminated by a resonant laser beam of circular polarized light (red solid) and focused onto a highly efficient camera. The dark field emitted by the atoms (blue dashed) is apodized in Fourier space by an iris diaphragm and subsequently brought to interference with the imaging light on the camera where an intensity image is formed. The exact intensities I_{in} and I_{out} do not have to be known since the counts $C_{in/out}$ produced by the camera have been calibrated beforehand. The horizontal auxiliary imaging can be used to image the vertical displacement of the atomic cloud and is left uncorrected due to the diminished requirement on image fidelity.

Generalized treatment of imaging systems

A convenient way to represent the action of a system is via a mathematical mapping $\mathcal{S}\{*\}$ that acts on input functions and produces output functions. Hence, if $f_1(x_1, x_2)$ specifies an arbitrary input and

$f_2(x_2, y_2)$ the corresponding output, they are related by

$$f_2(x_2, y_2) = \mathcal{S}\{f_1(x_1, y_1)\}. \quad (9.5)$$

We aim to model an imaging apparatus as a linear invariant system which entails two simplifying assumptions. Linearity implies that the action of a system on all input functions f_1 and g_1 can be described by a map $\mathcal{S}\{*\}$ which satisfies the following superposition property for all complex constants a and b as

$$\mathcal{S}\{af_1(x_1, y_1) + bg_1(x_1, y_1)\} = a\mathcal{S}\{f_1(x_1, y_1)\} + b\mathcal{S}\{g_1(x_1, y_1)\}. \quad (9.6)$$

To study the action of the system it is helpful to think of the input functions as a composition of weighted basis functions, for example the Dirac δ functions

$$f_1(x_1, y_1) = \int_{-\infty}^{+\infty} \int_{-\infty}^{+\infty} f_1(\xi, \eta) \delta(x_1 - \xi, y_1 - \eta) d\xi d\eta. \quad (9.7)$$

Here, the Dirac δ functions are weighted by $f_1(\xi, \eta)$. Hereafter, all integral expressions are understood to span the entire space and thus explicit limits will be dropped for notational convenience. Since we are interested in the effect of the system on the input function, the map $\mathcal{S}\{*\}$ is applied and we use the linearity to pull it into the integral which yields

$$f_2(x_2, y_2) = \iint f_1(\xi, \eta) \mathcal{S}\{\delta(x_1 - \xi, y_1 - \eta)\} d\xi d\eta \quad (9.8)$$

Finally, we denote the response of the system at the output coordinates (x_2, y_2) to a Dirac δ function input at the object coordinates (ξ, η) by $h(x_2, y_2; \xi, \eta)$, i. e.

$$h(x_2, y_2; \xi, \eta) = \mathcal{S}\{\delta(x_1 - \xi, y_1 - \eta)\}. \quad (9.9)$$

The function h is in general called the impulse response or in optics the point-spread function of the system. It encodes the complete information about the action of the system and with it, the system can now be described by the following expression known as the *superposition integral* which demonstrates that the linear system is completely characterized by its responses to unit impulses

$$f_2(x_2, y_2) = \iint f_1(\xi, \eta) h(x_2, y_2; \xi, \eta) d\xi d\eta. \quad (9.10)$$

Frequency response in coherent imaging and the amplitude transfer function

The introduced concepts have been rather general in nature, here they will be applied to the case of coherent monochromatic imaging. An important distinction must be made, the formalism applies only to linear maps and hence we must determine what physical value to use as an input function. For incoherent imaging, the fast relative fluctuations of the light field E lead to the loss of coherence and thus an

This integral representation is reminiscent of the sifting property of the δ functions.

averaging effect even over small distances. Hence, interference can be neglected and incoherent imaging is linear in the intensities $I = |E|^2$. However, coherent imaging systems exhibit interference and are thus linear in complex amplitude. Therefore, the input functions must describe the amplitude and phase information of the incident light field. To find the resulting intensity, the absolute square of the complex output light field must be taken. Thus, the intensity mapping is nonlinear and if frequency analysis is to be applied, it must be applied to the *amplitude* mapping of the complex light field.

Previously, we have used the linearity of the model to simplify its description. The fact that the system is space invariant yields a second simplification. The concept of linear systems is generally applied to systems which are invariant in space as well as time. Here however, we consider a stationary system where time invariance is trivially satisfied. A system is said to be space-invariant, or isoplanatic, if its impulse response $h(x_2, y_2; \xi, \eta)$ depends only on the distances, e. g. $(x_2 - \xi)$, thus

$$h(x_2, y_2; \xi, \eta) = h(x_2 - \xi, y_2 - \eta). \quad (9.11)$$

In practice, an imaging system is only approximately invariant on small patches. However, if the particular portion of the object of interest is sufficiently small it often suffices to consider only the isoplanatic patch close to the optical axis of the imaging system, then the superposition integral takes the simple form

$$f_2(x_2, y_2) = \iint f_1(\xi, \eta) h(x_2 - \xi, y_2 - \eta) d\xi d\eta. \quad (9.12)$$

This is immediately recognized as a convolution $f_2 = f_1 \otimes h$. Thus, the output image f_2 can be thought of as a superposition of point spread functions h weighted by the original object space distribution f_1 . A convolution relation takes on a particularly simple multiplicative form after a Fourier transformation. Here, the Fourier transforms, or spectra, $\mathcal{F}\{f_2\} = F_2(k_x, k_y)$ and $\mathcal{F}\{f_1\} = F_1(k_x, k_y)$ of the output and input, respectively, are related by

$$F_2(k_x, k_y) = H(k_x, k_y) \cdot F_1(k_x, k_y) \quad (9.13)$$

where H is the Fourier transform of the impulse response

$$H(k_x, k_y) = \iint h(\xi, \eta) \exp[-i2\pi(k_x \xi + k_y \eta)] d\xi d\eta, \quad (9.14)$$

which is called the amplitude transfer function in the context of coherent imaging and k_x and k_y denote the frequency space coordinates.

This expression in itself yields only moderate insights since it still depends on the impulse response h . However, h can in turn be written as the Fraunhofer diffraction, i. e. Fourier transform, of the input pupil function $P(x, y)$ which describes the physically limiting aperture of the imaging system. The pupil function is usually of simple form, unity where light passes and zero otherwise since most apertures consist of a rectangular or circular hole.

Due to the fact that the Fourier transform of a Fourier transform is proportional to the original function, the ATF can be written in terms of a rescaled pupil function

$$H(k_x, k_y) = \mathcal{Ft} \left\{ \frac{A}{\lambda z_i} \iint P(x, y) \exp \left[-i \frac{2\pi}{\lambda z_i} (ux + vy) \right] dx dy \right\} \\ \sim P(\lambda z_i k_x, \lambda z_i k_y). \quad (9.15)$$

A is the constant amplitude and λ the wavelength of the imaging light, z_i denotes the distance from exit pupil to image plane. For notational convenience we have set $A/\lambda z_i = 1$ and omitted negative signs in the argument since almost all applications of interest are symmetrical in (x, y) .

As J. Goodman says, “This relation is of the utmost importance”¹⁰⁹, as it reveals very interesting information about diffraction-limited coherent imaging systems in the frequency domain. For a pupil which is indeed unity in some region and zero otherwise, a finite passband exists in which all frequency components are transmitted without amplitude or phase distortion. Only at the boundary of this passband, the pupil function and hence the frequency drops abruptly to zero, which implies that the frequency components outside the passband are completely eliminated. Note that this conclusion has been drawn for ideal imaging systems. For realistic imaging systems, the effects of aberrations are modeled as phase distortions within the passband.

Frequency response of incoherent imaging and the optical transfer function

An analogous derivation can be made for incoherent illumination. However, since all interference terms vanish for incoherent illumination, instead of being linear in the amplitude of the light field, the system is linear in the intensity. For perfectly incoherent illumination, the imaged intensity I_2 is found as a convolution of the *intensity impulse response* $|h|^2$ with the ideal image density I_1

$$I_2(x_2, y_2) \propto \iint |h(x_2 - \xi, y_2 - \eta)|^2 I_1(\xi, \eta) d\xi d\eta. \quad (9.16)$$

Therefore, this kind of system is analyzed as a linear mapping of intensity distributions. Additionally, one can see that the intensity impulse response is simply the squared absolute value of the amplitude impulse response h . And analogous to the coherent case, the transfer function of the incoherent system can be defined by

$$\mathcal{H}(k_x, k_y) = \iint |h(x_2, y_2)|^2 e^{-i2\pi(k_x x_2 + k_y y_2)} dx_2 dy_2. \quad (9.17)$$

Commonly, the incoherent transfer function \mathcal{H} is called the **OTF**, whereas its modulus or absolute value is called the *modulation transfer function* (**MTF**). Application of the convolution theorem then yields the frequency-domain relation quite similar to the coherent case.

$$\mathcal{F}_2(k_x, k_y) = \mathcal{H}(k_x, k_y) \cdot \mathcal{F}_1(k_x, k_y) \quad (9.18)$$

¹⁰⁹ J. W. Goodman: *Introduction to Fourier Optics*, (2005)

Extra 9.1: Transfer function examples

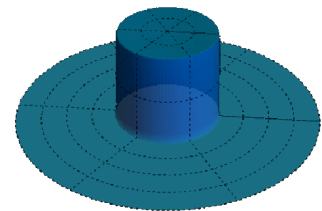
Example for the frequency response of a diffraction-limited coherent imaging system. The amplitude transfer functions of a circular pupil is given by

$$P(x, y) = \text{circ} \left(\frac{\sqrt{x^2 + y^2}}{w} \right).$$

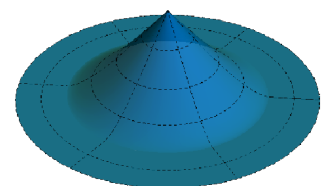
Thus with formula (9.15), the corresponding amplitude transfer function is

$$H(k_x, k_y) = \text{circ} \left(\frac{\sqrt{k_x^2 + k_y^2}}{w/\lambda z_i} \right).$$

A cut-off frequency can be defined as $f_0 = w/\lambda z_i$, beyond which all signal is suppressed. When plotting the ATF, which is simply the rescaled pupil function given above, an abrupt suppression at the cut-off frequency is visible:



The *optical transfer function* (OTF) for incoherent imaging, however, shows a gradual decrease that extends to twice the cut-off frequency of the coherent system:



Thus, the application of the linear systems framework yields analogous relations in both, the coherent as well as the incoherent case, highlighting the flexibility of this approach. However, the presented expressions act on the intensity and not the complex amplitude which is of significant consequence for the quality of the imaging.

A complete comparison is beyond the scope of this work and not relevant for the presented experiment. A short example of the impact the coherence of the illumination is presented for the interested reader in Extra 9.1. Since the amplitude impulse response function h occurs in both expressions, there is certainly a relation between the **OTF** and the **ATF** to be found and indeed, the **OTF** is precisely the autocorrelation of the **ATF**. In summary, ideal coherent and incoherent imaging can be conveniently described by a transfer function or its Fourier transform, the impulse response or **PSF**. The final image can thus be obtained by convolving the original image in a superposition integral with the **PSF** or in frequency space by multiplication with the appropriate transfer function. Since the convolution operation is rather involved, it is worthwhile for most practical purposes to eschew the superposition integral in favor of Fourier transforming, multiplication by the transfer function and reverse Fourier transforming, which is highly efficient on modern computer hardware.

Aberrations and their effect on the frequency response

If a system is not perfectly diffraction-limited it is said to have aberrations. Here, the wavefront of a point source on the exit pupil is not perfectly spherical. Aberrations can have many origins, from a simple error in focus to inherent properties of e. g. not perfectly spherical lenses.

In order to describe wavefront errors, one can imagine the exit pupil to be perfectly illuminated by a spherical wavefront but that a phase-shifting plate exists right at the aperture, thus deforming the wavefront that leaves the pupil. Let the phase error at (x, y) be denoted by $kW(x, y)$, where $k = 2\pi/\lambda$ and W is an effective path length error, then the effect of the phase-shifting plate can be described by the complex amplitude transmittance

$$\mathcal{P}(x, y) = P(x, y)e^{ikW(x, y)}. \quad (9.19)$$

How the departure from an ideal Gaussian wavefront is parameterized by the introduced path length error is illustrated in Fig. 9.9.

In the discussion of linear systems we found that as a consequence of Fourier transforming back and forth, the amplitude transfer function could be written in terms of a scaled pupil function, confer Eq. (9.15). Similarly, the amplitude transfer function of an imaging system with aberrations can be written with the *generalized pupil function* \mathcal{P} as

$$\begin{aligned} H(k_x, k_y) &= \mathcal{P}(\lambda z_i k_x, \lambda z_i k_y) \\ &= P(\lambda z_i k_x, \lambda z_i k_y) e^{ikW(\lambda z_i k_x, \lambda z_i k_y)}. \end{aligned} \quad (9.20)$$

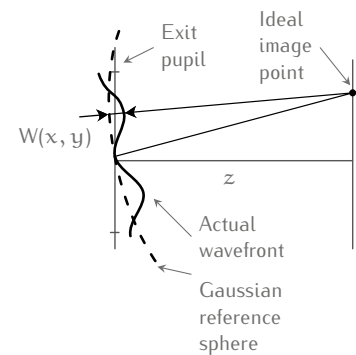


Figure 9.9: An illustration how imaging aberrations are modeled in terms of the effective path length error W . Here the deformation at the exit pupil is measured relative to an ideal Gaussian spherical wave emanating from an ideal image point. Figure adapted from J. Goodman¹⁰⁹.

¹⁰⁹ J. W. Goodman: *Introduction to Fourier Optics*, (2005)

The effect of aberrations can hence be modeled as the introduction of amplitude and phase distortions via the generalized pupil function. Thus, the knowledge of the aberration function W is pivotal to the compensation of imaging effects onto our measured density distributions.

Experimental determination of the generalized pupil function

There exist several possibilities to measure the generalized pupil function or the ATF of a physical system. Since we have no point source available in the observation volume, we chose to employ a technique presented by C. Ching¹³³ that only relies on uncorrelated density fluctuations which are conveniently obtained by preparing a thermal non-interacting Fermi gas.

The basic idea of the extraction of the ATF from perfectly random density fluctuations will be presented in brevity in the following.

As shown in the previous section, the experimentally measured density distribution $n_{\text{exp}}(\mathbf{r})$ is obtained by convolving the actual density distribution $n(\mathbf{r})$ with the PSF which contains the effect of the imaging apparatus. The same is true for the density fluctuations $\delta n(\mathbf{r}) = n(\mathbf{r}) - \bar{n}$, where \bar{n} denotes the mean density. Hence, on every pixel \mathbf{r} on the camera, we measure the density fluctuation

$$\delta n_{\text{exp}}(\mathbf{r}) \approx \int \delta n(\mathbf{r}') \text{PSF}(\mathbf{r}_j - \mathbf{r}') d\mathbf{r}'. \quad (9.21)$$

This convolution is transformed into a multiplication by Fourier transforming the expression, thus

$$\delta n_{\text{exp}}(\mathbf{k}) = \delta n(\mathbf{k}) \underbrace{\mathcal{Ft}\{\text{PSF}\}}_{\text{amplitude transfer function}}. \quad (9.22)$$

The second term on the right hand side is easily identified as the amplitude transfer function, which is the goal of this endeavor. However, the first term on the right hand side, the true density fluctuations in frequency space $\delta n(\mathbf{k})$, i. e. the PSD, is still unknown. In order to identify that term, a look at the density fluctuation correlations, which define the density-density correlation function $v(\mathbf{r}_1 - \mathbf{r}_2) = \langle \delta n(\mathbf{r}_1) \delta n(\mathbf{r}_2) \rangle / \bar{n}$ proves to be worthwhile. The Fourier transform of this correlation function is known as the static structure factor given by

$$S(\mathbf{k}) = \int v(\mathbf{r}) e^{-i\mathbf{k}\mathbf{r}} d\mathbf{r}. \quad (9.23)$$

Here, the normalization constant of the transform has been dropped for notational convenience. Now, we can pull the Fourier transform into the density fluctuations correlator and write the structure factor in terms of the Fourier transform of each of the density fluctuations $\delta n(\mathbf{k}) = \int \delta n(\mathbf{r}) e^{-i\mathbf{k}\mathbf{r}} d\mathbf{r}$ as

$$S(\mathbf{k}) = \frac{\langle \delta n(\mathbf{k}) \delta n(-\mathbf{k}) \rangle}{\bar{n}} = \frac{\langle |\delta n(\mathbf{k})|^2 \rangle}{\bar{n}}. \quad (9.24)$$

In the first step, the definition of $\delta n(\mathbf{k})$ was inserted and we made use of fact that $v(\mathbf{r}_1 - \mathbf{r}_2)$ depends only on the distance $\mathbf{r}_1 - \mathbf{r}_2$. The second

¹³³ C. L. Hung et al.: *New J. Phys.*, vol. 13, (2011)

step relies on the fact that the density fluctuations are real valued, i. e. $\delta n(-\mathbf{k}) = \delta n^*(\mathbf{k})$. Here, we have found the square of the sought after term and are now able to exploit the uncorrelated density fluctuations of the thermal Fermi gas in the following. In order to determine the structure factor of such a gas, it is instructive to write S in terms of the density-density correlation function g_2 , which is obtained by a few straight forward substitutions from Eq. (9.23) to be¹³⁴

$$S(\mathbf{k}) = 1 + \bar{n} \int (g_2(\mathbf{r}) - 1) e^{-i\mathbf{r}\mathbf{k}} d\mathbf{r}. \quad (9.25)$$

Since g_2 is unity for an uncorrelated gas we immediately find the structure factor to be unity as well. Thus, after taking the square of Eq. (9.22), solving for the ATF and inserting $S = 1$, the absolute value of the ATF* is found to be proportional to the measured density fluctuations, i. e.

$$|\text{atf}(\mathbf{k})| \approx \sqrt{\langle |\delta n_{\text{exp}}(\mathbf{k})|^2 \rangle}. \quad (9.26)$$

In order to employ this method experimentally, we produce an approximately uncorrelated gas by preparing a thermal gas of non-interacting ${}^6\text{Li}$ atoms at a magnetic field of $\approx 527\text{ G}$, which is close to the zero crossing of the 3D scattering length. Due to the large temperature, the fugacity $z = e^{\mu/(k_B T)}$ is small and the gas is in the non-degenerate regime which exhibits Poissonian density fluctuations¹³⁵. Hence, the structure factor is in good approximation constant and close to unity.

In general one has to compensate not only for the imaging system but also for the detection cell geometry. However, at the point where the total ATF vanishes due to the imaging aperture, $k_{\text{max}} = \frac{2\pi NA}{\lambda_D^2} \approx 0.9/\mu\text{m}$, the transfer function of a single pixel has only decayed by $\approx 3.4\%$ and thus will be ignored henceforth.

In summary, the measurement of the density-density correlations of a gas with Poissonian density fluctuations allows us to extract the influence of the imaging apparatus in form of the frequency representation of the characteristic PSF. For in situ imaging, where the extent of the sample is much smaller than the DoF, this result would be sufficient in order to compensate for the imaging apparatus. However, the size of the sample in direction of the imaging axis is on the order of a millimeter in case of the matter wave focusing technique and even for the shorter ToF used in the self-interference measurement, the extent is still on the same order as the DoF and hence cannot be neglected.

Effective transfer function

Due to the large extent of the atom cloud during imaging, not all parts of the sample are subject to the same transfer function. Each slice perpendicular to the imaging axis of the extended sample has a different distance to the focus position and thus picks up a unique wave front error. Since we cannot treat the object as two-dimensional, a two-dimensional transfer function fails to yield an adequate description of the imaging process.

¹³⁴ L. Pitaevskii and S. Stringari: *Bose-Einstein Condensation*, (2003)

* The absolute value is also called the *modulus*. However, the modulus of the OTF for incoherent imaging is usually named modulation transfer function, hence it is refrained here from using MTF as the designation for the modulus of the ATF, to avoid confusion. Furthermore, as the ATF is non-negative in all cases relevant, the *modulus* will be omitted and the absolute value $|\text{ATF}|$ will henceforth simply be referred to as ATF.

¹³⁵ J. J. Meineke: *Fluctuations and Correlations in Ultracold Fermi Gases*, (2012)

For extended objects, a three-dimensional transfer function in dependence of the z -direction along the imaging axis should be applied to the actual three-dimensional density distribution. However, the volume density is neither known nor measured since the imaging procedure effectively integrates along the imaging axis and thus produces a 2D column density. The process we use to account for the varying influence of the imaging apparatus is outlined in the following.

If multiphoton scattering is ignored, i. e. the imaging light incident on each slice is identical, the imaged density distribution can be approximated by an average over all 2D density slices convolved with their respective PSF

$$n_{\text{exp}}(x, y) \approx \sum_{z_i} n(x, y, z_i) \otimes \text{PSF}(x, y, z_i). \quad (9.27)$$

Note that the normalization constant has been dropped here for notational convenience. Since we are interested in the transfer function, we Fourier transform the above expression, hence turning the convolution \otimes into a multiplication

$$n_{\text{exp}}(k_x, k_z) \approx \sum_{k_i} n(k_x, k_y, k_z) \cdot \text{ATF}(k_x, k_y, k_z). \quad (9.28)$$

The arguments k_* represent momenta associated with the directions x, y, z . Now, we make use of the fact that the gas resides in the harmonic oscillator ground state in the z -direction $\Psi(z) \propto e^{-m\omega_z z^2/(\hbar^2)}$, with the vertical trap frequency $\omega_z = 2\pi \cdot \nu_z$. Therefore, the momentum space representation is also a Gaussian, i. e. $\Psi(k_z) \propto e^{-\hbar k_z^2/2m\omega_z}$. If we assume the density to be separable, $n(x, y, z) = n(x, y) \cdot n(z)$, we obtain

$$n_{\text{exp}}(k_x, k_z) \approx n(k_x, k_y) \underbrace{\sum_{k_i} e^{-\hbar k_z^2/m\omega_z} \text{ATF}(k_x, k_y, k_z)}_{\text{ATF}_{\text{eff}}}. \quad (9.29)$$

Here, the summation over the weighted amplitude transfer functions is denoted by the *effective amplitude transfer function* (ATF_{eff}). With the previously measured ATF in focus and the knowledge that imaging aberrations such as defocus can be described by a simple quadratic wavefront distortion¹³⁶ we are able to estimate the influence of the imaging apparatus also for extended samples.

An example of a number of ATFs for different positions along the imaging axis are shown in Fig. 9.10a. The sole influence of defocus is a change in the complex phase depicted in the bottom plot, the individual amplitudes are unaffected. The real part scaled to the relative density contribution for that distance is plotted in the upper part of Fig. 9.10a. In the summation, the imaginary parts cancel and a real ATF_{eff} remains that is plotted in Fig. 9.10b. This is not necessarily always the case, for example when the ATFs are not averaged symmetrically around the focus position. In this case, a constant complex phase remains indicating e. g. a misalignment. However, since we ultimately image the intensity which is obtained by taking the square of the light field amplitude, we would have obtained a real value regardless. In

Here, the factor 2 in the denominator of the exponential cancels out since the density is obtained by taking the square of the wave functions.

¹³⁶ E. Hecht: *Optics*, (2017)

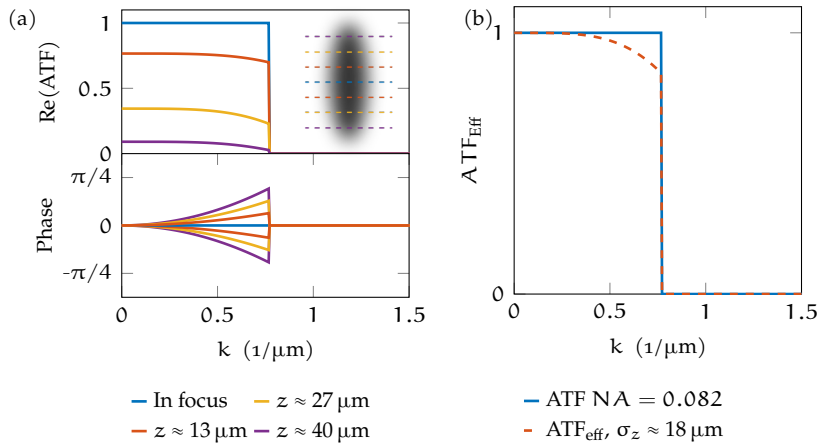


Figure 9.10: (a) Examples of the density weighted real part and the phase of ATFs for three distances to the focus position (blue to purple) which lies at the cloud center. The abscissa denotes the spatial frequency k . The location of the slice is indicated by lines of corresponding color in the sketched atomic cloud shown in the inset. The only effect of defocus is the introduction of a phase, the amplitude is not altered and thus not shown. Note that the phase changes sign when crossing the optimal focus. The imaginary part (not shown) shows a similar dependence which ultimately averages out in this situation. (b) Comparison of the resultant effective ATF (red dashed) for a cloud with $1/\sqrt{e}$ radius $\sigma_z \approx 18 \mu\text{m}$ and the ideal ATF (blue) of a diffraction limited imaging system with $\text{NA} = 0.082$ in dependence of the spatial frequency k . The vertical extent corresponds approximately to 1 ms ToF in the presented measurements.

general, the phase carries information about the position, for example a deflection by a wedge in the imaging path could be represented by a phase gradient.

Fitting of g_2 considering the imaging apparatus

The effective ATF we have estimated in this fashion can have strong influence on the lower resolution limit. The impact is illustrated in the following in the context of the density-density correlation function g_2 obtained during the short ToF measurement. We have seen that imaging out of focus results in a narrower ATF, i. e. higher frequencies are stronger suppressed compared to the case of ideal imaging. Nevertheless, also imaging free of aberrations is still restricted by the finite NA, which defines the largest obtainable frequency and thus the smallest resolved feature. The effect of the ideal ATF and two effective ATFs for two different cloud sizes on a theoretical estimate of $g_{2,\text{theory}}$ are plotted in Fig. 9.11.

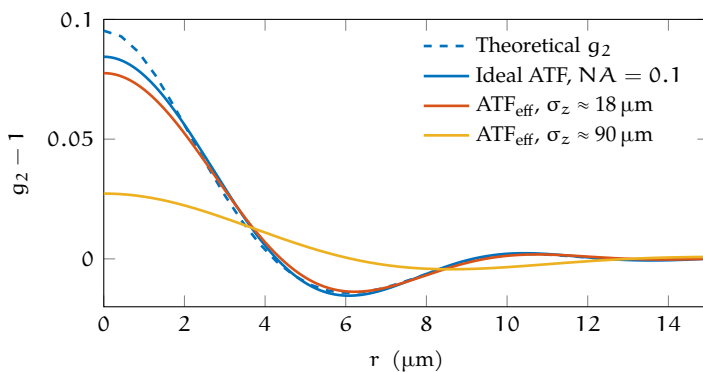


Figure 9.11: The effect of imperfect imaging on the measured density-density correlation function g_2 is demonstrated for various degrees of defocus. The theoretical g_2 is plotted in blue (dashed) and compared to diffraction limited imaging with $\text{NA} = 0.1$ and the effective ATF for $18 \mu\text{m}$ and $90 \mu\text{m}$ $1/\sqrt{e}$ cloud radii in blue, red and yellow, respectively. The imaged g_2 is still comparable to the theoretical values for small cloud extent. However, for the large cloud sizes reached in the matter wave focusing measurement, a strong deviation can be seen. The parameters η and $a_{\text{cut-off}}$ are 0.125 and $3 \mu\text{m}$ respectively.

The parameters of the theoretical g_2 are taken to be typical values for the expected temperature range, i. e. $\eta = 0.125$ and $a_{\text{cut-off}} = 3 \mu\text{m}$. It is immediately obvious that even aberration free imaging has visible impact on the shape of g_2 and especially the location and amplitude of the minimum. If fitted without compensation, significant errors

in the determination of η and $\alpha_{\text{cut-off}}$ must be expected, which can be significantly reduced by application of a suitable ATF as is discussed in Section 9.3.

9.2.3 Compensating for in situ density fluctuations

Not only the imaging apparatus introduces systematic errors which need to be compensated for in order to obtain a suitable density-density correlation function from the self-interference method. The basis of the extraction of g_2 from short ToF is that the phase information transforms into a density modulation which can be imaged. This process occurs simultaneously in reverse, i. e. the density fluctuations present in situ are rotated into phase space. After a quarter of the trapping period $T/4$, the phase has been completely transformed into density and vice versa. However, for the shorter expansion times like those used in the self-interference method, the process has not yet been completed. Thus, remnants of the in situ density fluctuations remain.

As discussed earlier, *ab initio* treatment of the in situ density fluctuations in the computation of the g_2 used for fitting is computationally prohibitively expensive. As an approximative alternative, we subtract the propagated in situ density-density correlation function $g_{2,\text{in situ}}(t = \text{ToF})$ from the density-density correlation function obtained after ToF $g_{2,\text{tof}}$, as suggested by V. Singh and L. Mathey⁸⁴. To this end, the time evolution operator is applied to an in situ wave function with fluctuating phase as well as fluctuating density, which ultimately yields the PSD after expansion of time t as

$$\begin{aligned} \text{psd}(\mathbf{k}, t) \approx & \cos^2\left(\frac{\hbar t \mathbf{k}^2}{2m}\right) \delta n(\mathbf{k})^2 \\ & + 4 \sin^2\left(\frac{\hbar t \mathbf{k}^2}{2m}\right) \delta \theta(\mathbf{k})^2 \\ & + 2 \delta n(\mathbf{k}) \delta \theta(\mathbf{k}) \sin\left(\frac{\hbar t \mathbf{k}^2}{m}\right). \end{aligned} \quad (9.30)$$

Details on the derivation of this relation can be found in the thesis of R. Desbuquois²⁷. Here, the first term contains the known density fluctuation δn whereas the second term describes the sought after phase fluctuation $\delta \theta$ after ToF. The third term describes the interference between the density and the phase fluctuations and is thus assumed to be small and is ignored. From the first term, it is immediately obvious that the in situ density fluctuations $\delta n(\mathbf{k})$ are modulated with time by the term $\cos^2\left(\frac{\hbar t \mathbf{k}^2}{2m}\right)$. Thus, the measured in situ density fluctuations cannot simply be subtracted but must first be propagated by multiplication with the *cosine term*.

The analysis sequence is as follows.

1. Measure the in situ density fluctuations and extract

$$g_{2,\text{in situ}}(t = 0).$$

⁸⁴ V. P. Singh and L. Mathey: *Phys. Rev. A*, vol. 89, (2014)

²⁷ R. Desbuquois: *Thermal and superfluid properties of the two-dimensional Bose gas*, (2013)

If the interference term would turn out to be significant, the analysis would have to be performed in an iterative self-consistent approach, further raising the computational cost.

2. Measure the density fluctuations after short **ToF** and extract

$$g_{2,\text{tof}}$$

3. Time propagate the in situ density-density correlation function by multiplication with the cosine term in frequency space, i. e. schematically:

$$g_{2,\text{in situ}}(t = \text{ToF}) =$$

$$\mathcal{Ft} \left\{ \mathcal{Ft} \left\{ g_{2,\text{in situ}}(t = 0) \right\}^2 \cdot \cos^2 \left(\frac{\hbar t k^2}{2m} \right) \right\}.$$

4. Subtract the time-propagated in situ density-density correlation function from the density-density correlation function acquired after short **ToF** to obtain,

$$g_2 = g_{2,\text{tof}} - g_{2,\text{in situ}}(t = \text{ToF}).$$

The effect of this time propagation on our measured in situ density fluctuations is illustrated in Fig. 9.12. It can be seen that although the in situ density-density correlation function has diminished, the change of shape is still significant and must be considered in the analysis of the density-density correlation function after **ToF**.

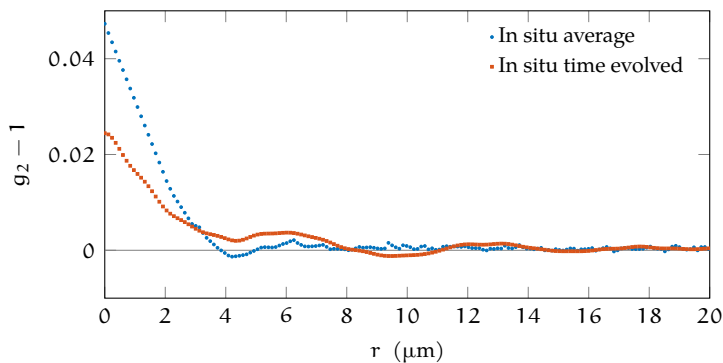


Figure 9.12: The azimuthal average of the in situ density-density correlation function of a single realization is plotted as blue circles whereas the time propagated g_2 is shown as red squares. Here, only the cosine term of Eq. (9.30) is considered. Note the diminished peak amplitude and increased oscillations at larger length scales.

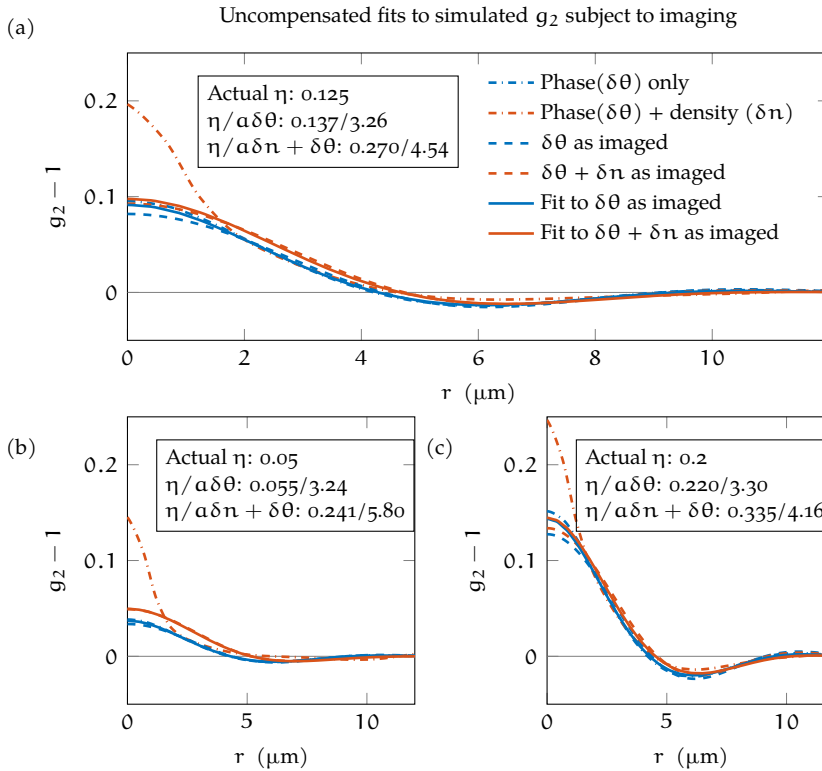
9.3 TECHNICAL DETAILS OF THE IMPLEMENTED ANALYSIS

When constructing a measuring device, it must be verified that it measures accurately. This is equally true for the numerical analysis presented here. Since no ultracold gas with known parameters exists we employ data simulated on a high performance cluster by V. Singh. The tests of two aspects of our numerical analysis are presented in the following. First, we verify that the compensation of in situ density fluctuations via the time propagation ansatz as well as the consideration of an imperfect imaging apparatus improves the fitted result. Second, the numerical image preparation, correlation and fitting sequence is verified. To this end, synthetic density images with noise according to the PSD supplied by V. Singh and L. Mathey⁸⁴ are created and fed into the analysis routines and hence treated identically to experimentally obtained images.

⁸⁴ V. P. Singh and L. Mathey: *Phys. Rev. A*, vol. 89, (2014)

9.3.1 Verification of compensation and fitting routines

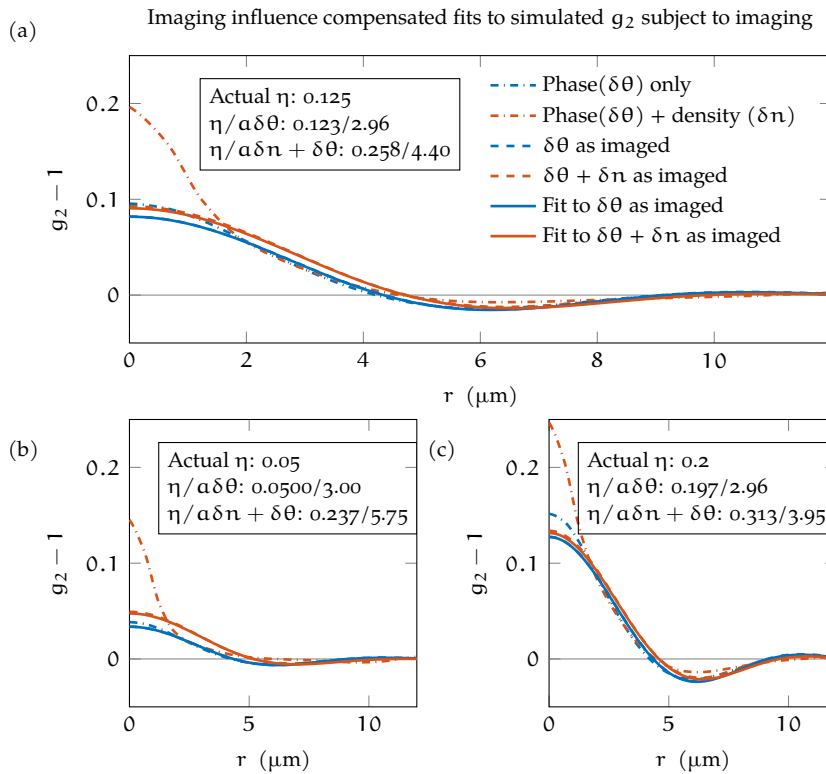
To establish a baseline, uncompensated fits to simulated data are presented first. Subsequently, the applied compensations are introduced iteratively to highlight their respective effects. The influence of the imaging apparatus has been simulated by a convolution with the PSF expected for our imaging system. Two simulated density-density correlation functions and their respective fits are presented in each of the following plots. An ideal correlation function for quasi-condensates with only phase fluctuations, $g_{2,\delta\theta}$, is plotted in blue and a realistic correlation function for a gas with additional thermal in situ density fluctuations, $g_{2,\delta\theta+\delta n}$, is plotted in red. The corresponding fits are colored accordingly. The thermal excitations are assumed to be Gaussian with a de Broglie wavelength of $\lambda_T \approx 1.9 \mu\text{m}$, which corresponds to a typical temperature of ultracold ${}^6\text{Li}$ gases of 70 nK. Furthermore, the results for three different scaling exponents η are given in order to compare the fitting performance close to $T = 0$ with temperatures approaching the critical point.



If the simulated density-density correlation functions are fitted without any compensation for the imaging system or in situ density fluctuations, the results plotted in Fig. 9.13 are obtained. Interestingly, the uncompensated fits to the phase-only g_2 yield reasonable results albeit with a systematic error of approximately 10%. The uncompensated fits fail, however, to yield acceptable results when in situ density fluctuations are present. This is especially obvious for small η , where

Figure 9.13: Uncompensated fitting of simulated data for three different scaling exponents η . The simulated correlation functions (dot dashed) are given in comparison to the data as imaged i.e. when subjected to our imaging system (dashed). Uncompensated fits are made to the data as imaged (solid lines). Two simulated g_2 are compared: only in situ phase fluctuations (blue) and including in situ density fluctuations $\delta n + \delta\theta$. The actual η_{act} is given in comparison to the fitted η_{fit} and $\alpha \equiv \alpha_{\text{cut-off}}$ for the phase only case $\delta\theta$ or in combination with in situ density fluctuations $\delta n + \delta\theta$. The cut-off is fixed at $\alpha = 3 \mu\text{m}$. The unit as well as the error which is always less than the difference to the input value is omitted. (a) $\eta_{\text{act}} = 0.125$: Phase only fits yield reasonable agreement with $\eta_{\text{fit}} = 0.137 \pm 0.003$ whereas not compensating for the in situ density fluctuations in the fit results in unacceptable discrepancy $\eta_{\text{fit}} = 0.270 \pm 0.005$. The cut-off likewise. (b) $\eta_{\text{act}} = 0.05$: Phase only fits yield excellent agreement with $\eta_{\text{fit}} = 0.055 \pm 0.001$ whereas not compensating for the in situ density fluctuations in the fit results in unacceptable discrepancy $\eta_{\text{fit}} = 0.241 \pm 0.004$. The cut-off likewise. (c) $\eta_{\text{act}} = 0.2$: Phase only fits yield reasonable agreement with $\eta_{\text{fit}} = 0.220 \pm 0.005$ whereas not compensating for the in situ density fluctuations in the fit results in unacceptable discrepancy $\eta_{\text{fit}} = 0.335 \pm 0.006$. The cut-off likewise.

the relative amplitude caused by the artificially introduced thermal excitations dominates.



The fits plotted in Fig. 9.14 show the effect of compensating for the imaging apparatus by convolving the model function prior to fitting with the PSF of the assumed imaging apparatus. As expected, the discrepancy due to in situ density fluctuations still persists but the relative error is seen to be significantly reduced. The fits to the phase-only density-density correlation function show excellent agreement within the statistical error bounds, as expected. The fits to the density-density correlation function with included in situ density fluctuations yield an improved discrepancy of $\Delta\eta_{\text{fit}}/\eta_{\text{act}} = 204.8\%$ compared to 216% when the imaging system has not been considered. However, these values as well as the cut-off $\Delta\alpha_{\text{cut-off}}/\alpha_{\text{cut-off, act}} = 151.3\%$ are well beyond acceptable, regardless of the small fit error on the order of 5% in each case.

The greatest discrepancy in the input parameters (η , $\alpha_{\text{cut-off}}$) and fitted output is caused by the introduction of in situ density fluctuations. However, since an ab initio treatment is computationally prohibitively expensive, we chose to subtract the in situ density-density correlation function after it has been time evolved to compensate for the ToF. The beneficial effect of this compensation can clearly be seen in Fig. 9.15. The fully compensated fits to the simulated density-density correlation function including in situ fluctuations yield excellent agreement for the scaling exponent with a discrepancy of 14.4% to the reference and a value of 0.107 ± 0.001 and much improved results for the cut-off with a discrepancy of up to $\Delta\alpha_{\text{fit}}/\alpha_{\text{act}} = 6.8\%$. These results show

Figure 9.14: Imaging compensated fitting of simulated data for three different scaling exponents η . The simulated correlation functions (dot dashed) are given in comparison to the data as imaged i.e. when subjected to our imaging system (dashed). Fits for which the influence of the imaging system is considered are made to the data as imaged (solid lines). Two simulated g_2 are compared: only in situ phase fluctuations (blue) and including in situ density fluctuations (red). The actual η_{act} is given in comparison to the fitted η_{fit} and $\alpha \equiv \alpha_{\text{cut-off}}$ for the phase only case $\delta\theta$ or in combination with in situ density fluctuations $\delta n + \delta\theta$. The cut-off is fixed at $\alpha = 3\mu\text{m}$. The unit as well as the error which is always less than the difference to the input value is omitted. (a) $\eta_{\text{act}} = 0.125$: Phase only fits yield reasonable agreement with $\eta_{\text{fit}} = 0.123 \pm 0.001$ whereas not compensating for the in situ density fluctuations in the fit results in unacceptable discrepancy $\eta_{\text{fit}} = 0.258 \pm 0.003$. The cut-off likewise. (b) $\eta_{\text{act}} = 0.05$: Phase only fits yield excellent agreement with $\eta_{\text{fit}} = 0.0500 \pm 0.0002$ whereas not compensating for the in situ density fluctuations in the fit results in unacceptable discrepancy $\eta_{\text{fit}} = 0.237 \pm 0.003$. The cut-off likewise. (c) $\eta_{\text{act}} = 0.2$: Phase only fits yield excellent agreement with $\eta_{\text{fit}} = 0.197 \pm 0.001$ whereas not compensating for the in situ density fluctuations in the fit results in unacceptable discrepancy $\eta_{\text{fit}} = 0.313 \pm 0.003$. The cut-off likewise.

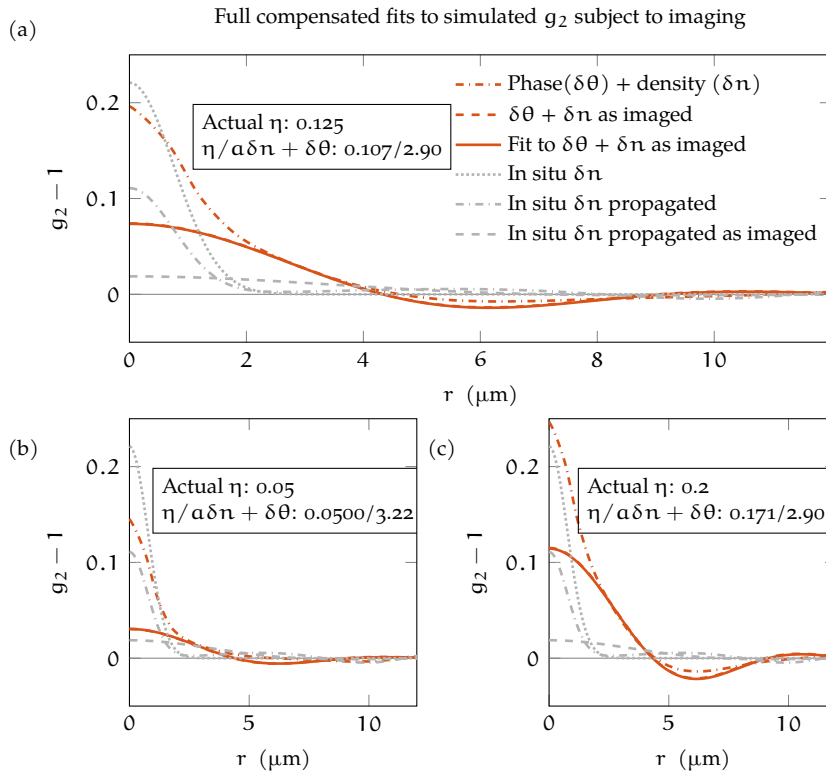


Figure 9.15: Imaging and in situ density fluctuations compensated fitting of simulated data for three different scaling exponents η . The simulated correlation functions (dot dashed) are given in comparison to the data as imaged i.e. when subjected to our imaging system (dashed). Fits for which the influence of the imaging system as well as in situ density fluctuations are considered are made to the data as imaged (solid lines). Only the case including in situ density fluctuations (red) is kept since the phase only case has been treated satisfactorily in the prior plot. Additionally, the expected in situ density fluctuations (dotted) are plotted as propagated (dot dashed) and propagated as images (dashed). The actual η_{act} is given in comparison to the fitted η_{fit} and $\alpha \equiv \alpha_{\text{cut-off}}$ for the phase only case $\delta\theta$ or in combination with in situ density fluctuations $\delta n + \delta\theta$. The cut-off is fixed at $\alpha = 3 \mu\text{m}$. The unit as well as the error which is always less than the difference to the input value is omitted. (a) $\eta_{\text{act}} = 0.125$: When compensating also for in situ density fluctuations, the fit results in acceptable agreement $\eta_{\text{fit}} = 0.107 \pm 0.001$. The cut-off likewise. (b) $\eta_{\text{act}} = 0.05$: When compensating also for in situ density fluctuations, the fit results in excellent agreement $\eta_{\text{fit}} = 0.0500 \pm 0.0003$. The cut-off likewise. (c) $\eta_{\text{act}} = 0.2$: When compensating also for in situ density fluctuations, the fit results in acceptable agreement $\eta_{\text{fit}} = 0.171 \pm 0.001$. The cut-off likewise.

that the compensation of the imaging apparatus and in situ density fluctuations are not only necessary but also that the employed measures successfully counteract the systematic errors introduced when applying the self-interference method under actual experimental conditions.

9.3.2 Verification of image preparation and correlation analysis routines

In addition to the compensation of the imaging system and the in situ density fluctuations, also the numeric analysis sequence as a whole must be tested in order to verify the numerical implementation.

In order to do so, we have produced synthetic density images with fluctuating noise of known spectrum, and hence known correlation, which can be fed into the analysis instead of actual experimental density images. The subsequent numerical analysis, however, is identical. The used routine relies on the inverse Fourier transformation of a known PSD which has been multiplied by a point symmetric random phase factor, hence distributing the power evenly over position space and yielding a real valued output. This process is implemented in the MATLAB programming language via the following excerpt.

```

1  N = 256; % The size of the required image in pixels
2  EffectivePixelSize = PixelSize * Binning / Magnification;
3  X = -N/2:N/2-1; % Create an array of length N
4  X = X * EffectivePixelSize; % Convert from px values to meter
5

```

```

6  [xx, yy] = meshgrid(X, -X);      % Create a grid of x,y values
7
8  [theta, rho] = cart2pol(xx, yy); % Convert from Cartesian to polar coordinates
9
10 % pointrand is a custom function that creates a point symmetric matrix of size N with random
    values [-1, 1] of uniform spectrum
11 randPhase = 1i*pi*pointrand(N);
12
13 % The magnitude is computed from the input power spectrum (psd) and the phase
14 magn = sqrt(psd) .* exp(randPhase);
15
16 % The magnitude is transformed to position space and masked by a heaviside function to emulate
    the shape of our sample. This is only done here for illustration. The *shift commands
    ensure proper positioning
17 img = heaviside(62- abs(rho)) .* (1 + N/(EffectivePixelSize) .* ifftshift(fftshift(magn))
    );
18
19 % The dominant real part is kept, however the imaginary part is only due to numeric errors and
    very small with abs(imag(img)) < 1e-20
20 img = real(img)

```

Here, the most important steps occur on line 14 and 17. The square root of the predefined PSD is multiplied by a random phase factor and Fourier transformed from frequency to position space. Since position information is encoded in the random phase, the resulting density image exhibits uniform density noise which obeys the defined power spectrum. For the PSD, we have chosen the analytical and numerical expressions for a system with algebraically decaying phase correlation function supplied by V. Singh and L. Mathey⁸⁴.

⁸⁴ V. P. Singh and L. Mathey: *Phys. Rev. A*, vol. 89, (2014)

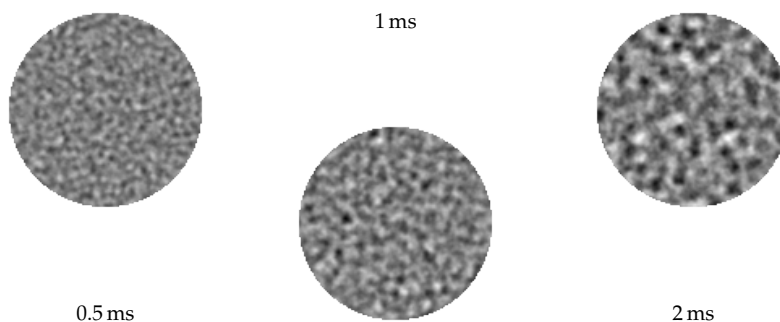


Figure 9.16: Examples of synthetic density ripple images for varying ToF. From left to right, the time of flight increases from 0.5 ms over 1 ms to 2 ms. Note, how the length scale of the density modulation changes.

Examples of images with algebraically decaying phase correlations for three different ToFs are shown in Fig. 9.16. Visual comparison indicates that the change in correlation length is qualitatively compatible with our experimentally acquired density images.

The results of the numerical analysis for 1 ms time of flight and varying η are shown in Fig. 9.17. Here, simulated data using the numerical expression for a phase fluctuating condensate without in situ density fluctuations are plotted in blue. Fits to the full numerical expression (analytical approximation) are shown in red (dashed). It is refrained from plotting data from both, numerical expression and analytical approximation, due to the fact that they are visually almost indistinguishable. The fitted value in the legend corresponds to fits to data generated from the full numerical expression. The examples shown and the overview of the fitted errors and mean in Fig. 9.18, in-

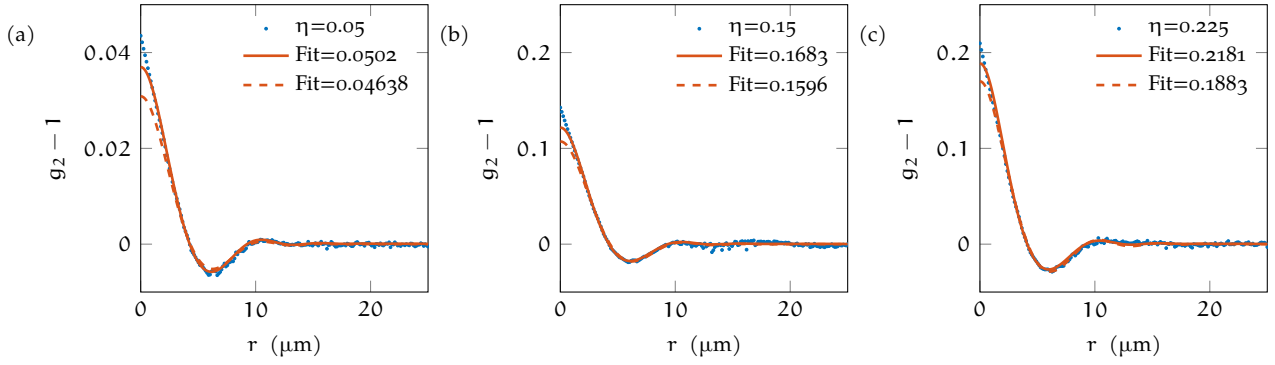


Figure 9.17: Examples of simulated density ripples images for varying η . From (a) $\eta = 0.05$ fitted $\eta_f \approx 0.0502$ over (b) $\eta = 0.15$ fitted $\eta_f \approx 0.1683$ to (c) $\eta = 0.225$ fitted $\eta_f \approx 0.2181$. Note the fivefold increase in the y-axis scale from (a) to (b). The data is fitted between 2–25 μm .

dicating that the numerical analysis reproduces the input parameters in good agreement, at least when input and fit rely on the same data. For smaller η , fitting the data created from the full numeric expression with the analytical expression still yields accurate results and vice versa. However, towards the critical point at $\eta = 0.25$ the cross fitted means begin to diverge by $\approx \pm 17\%$ from the ideal diagonal and the statistical error given by one standard deviation increases from approximately 2.5% to 13.6%. In contrast, when data and fit model are derived from the same data, the mean deviation is always less than 0.75% while the statistical spread increases from approximately 2.92% to 12.43%.

In conclusion, we have determined that the numerical analysis procedure yields excellent results for the average scaling exponent η , whereas fits to individual realizations suffers errors up to 12.43% when approaching the critical point, which we deem acceptable.

The short range cut-off $a_{\text{cut-off}}$ yields similar results but since a meaningful analysis showed to be impractical, we refrain from presenting detailed characteristics of the numerical analysis.

Nonetheless, the accuracy of the analysis is subject to a multitude of parameters, both technical and experimentally motivated. Two of these, the choice of the fit limits for the density-density correlation function and the size of the region of interest are summarized exemplarily in the following.

9.3.3 Fit limits

Due to the high sensitivity of the fitted model parameters to the shape of the data, the fit limits must be chosen carefully. Since the dominant signal occurs at small distances, we expect that the outer fit limit can be chosen freely in an interval larger than the main feature and small enough to not contain significant noise at large distances. The choice of the inner fit limit, however, is crucial. Towards $r = 0$, significant deviations in the experimental data from the expected functional form can be observed due to the finite resolution and the atomic shot noise contribution. Thus, the inner fit limit must be chosen such that small distances are excluded but sufficient signal is still contained in the in-

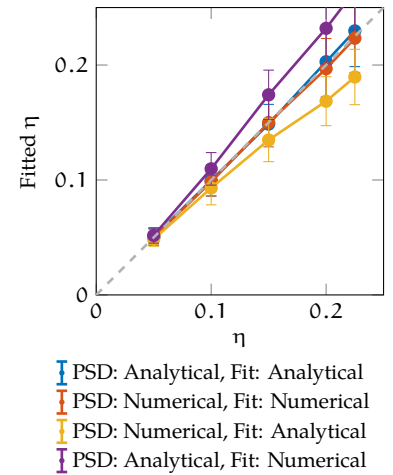


Figure 9.18: Comparison of the fitting errors of different implementations for generating the noise spectrum and fit model. The values represent the mean over 100 analyzed images where the error bar indicated one standard deviation. The colored lines are a guide to the eye and the ideal diagonal is marked with a gray dashed line. Note that the numerical analysis produces accurate results for both relevant cases where the noise spectrum and the fit model are determined from the same data. However, the statistical distribution increases towards the critical point $\eta_c = 0.25$.

terval to ensure a successful fit. To determine the optimal interval, the simulated data is fit with varying inner and outer fit limit and the fitted η_{fit} is compared to the input value of $\eta_{\text{in}} = 0.15$. The relative deviation, $\Delta\eta = \eta_{\text{fit}} - \eta_{\text{in}}$, from the input is plotted three-dimensionally in Fig. 9.19. Here, optimal parameters are depicted in white color, whereas too small (too large) values are plotted in blue (red) color. The dependence on the outer fit limit is given normal to the viewing plane. The almost constant relative deviation indicates that the outer limit can indeed be chosen freely in the interval 10–30 μm and most likely up to the maximum valid distance given by the size of the *region of interest (RoI)*. The dependence of the relative $\Delta\eta/\eta_{\text{in}}$ deviation on the inner fit limit is given on the horizontal axis, here a strong effect can be observed if the inner fit limit is chosen too small ($\lesssim 1 \mu\text{m}$) or too large ($\gtrsim 4 \mu\text{m}$). Examples of the used fit limits are given in the respective inset. Using this data, we have chosen the inner (outer) fit limit to be 2.5 μm (25 μm). Here, the dependence is minimal as indicated by the broad plateaus.

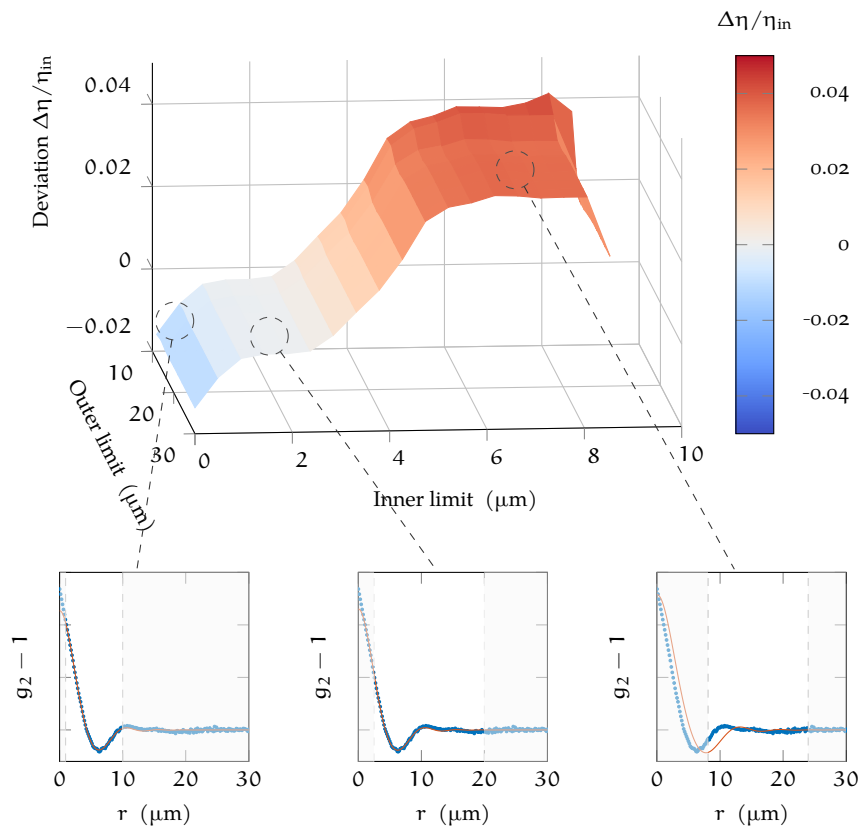


Figure 9.19: Comparison of the effect of different fit limits on the fitted η_{fit} . Here, the inner and outer fit limit are adjusted from 0–9 μm and 10–30 μm , respectively. The inner fit limit is given on the horizontal axis and the outer fit limit axis is normal to the viewing plane. The vertical axis and the color denote the relative difference of the fitted η_{fit} to the input of $\eta_{\text{in}} = 0.15$. Note that the outer fit limit has negligible effect and the existence of a plateau around inner fit limit values of approximately 1 μm . Example fits are shown as insets below, with dashed lines indicating the corresponding regime.

9.3.4 Size of the region of interest

In principle, the size and shape of the *RoI* can be compensated for by considering the correlation function of the created binary mask. However, there is no benefit from compensation, when the *RoI* does not contain sufficient signal on the relevant length scales. Clearly, there exists a lower size limit that generates acceptable results. In order to estimate the error introduced by the size of the *RoI*, we successively

increase the **RoI** and subsequently compare the fitted η with the input value. A plot of the relative difference $\Delta\eta/\eta_{\text{int}} = \eta_{\text{fit}} - \eta_{\text{in}}/\eta_{\text{in}}$ of the fitted value from the input is shown in Fig. 9.20. The error bars denote the statistical spread expected for the analysis of a single density image, whereas the error in the averaged η is always less than 3.3%. The vertical dashed line indicates the size of the **RoI** used in this experiment. Here, the uncertainty for a single realization is approximately 12.3% and the discrepancy of the mean to the expected value is less than 0.32%. Hence, we conclude that the **RoI** chosen in this experiment lies in a regime with acceptable accuracy for individual realizations and excellent results for the number of density images considered in the presented analysis.

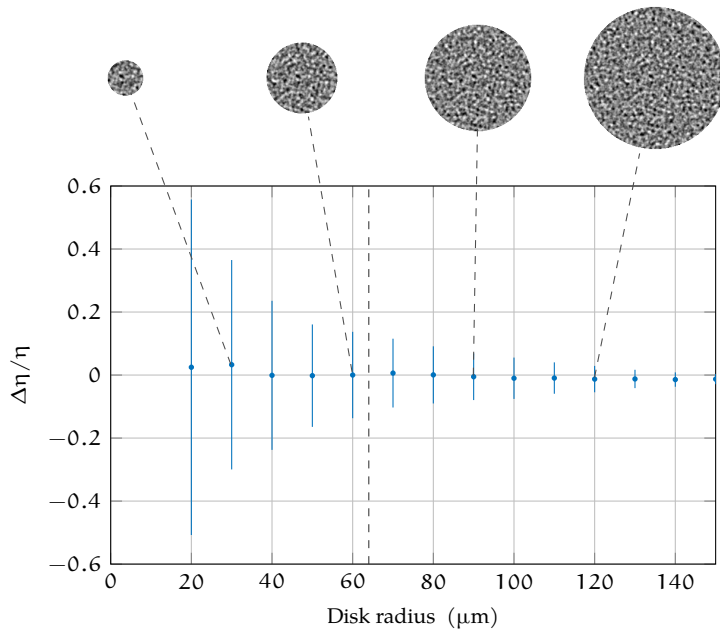


Figure 9.20: Effect of the size of the region of interest. The x-axis denotes increasing radius of a disk shaped **RoI**. The y-axis denotes the relative divergence of the average fitted value of η_{fit} to the input of $\eta_{\text{in}} = 0.15$. The error bars represent the statistical spread expected if a single image is analyzed. The vertical dashed line indicates the size of the **RoI** used in this experiment. In the presented analysis, we evaluate about a hundred images, which decreases the divergence from the true value considerably. Examples of the size of the **RoI** are shown as insets with dashed lines indicating the correspondence to the main plot.

9.4 ADVANTAGES OF ANALYZING g_2 INSTEAD OF THE PSD

In contrast to the aforementioned prior work, the focus of this thesis lies on the analysis of the density-density correlation function of ultracold gases. Theoretically, it is often advantageous to study coherence properties via the **PSD** in Fourier space instead of position space. This should also be true for the experiment presented in this thesis. An intermediary step of the computation of g_2 actually yields the **PSD** and V. Singh and L. Mathey have also presented an analytical expression in momentum space. However, the dependence of the introduced noise with distance made the analysis in Fourier space impractical. This is due to the fact that less data is present for correlations over larger distances, which causes the statistical error of the density-density correlation function to scale proportional with distance. A Fourier transform, however, eliminates the clear separation of the low-noise and high-noise regimes and yields a significant admixture of the statistical

noise to all momenta. The resultant PSD is ill suited for numerical fitting of the required accuracy. Since we ultimately rely on a numerical expression for either the PSD or g_2 , we chose to perform the analysis in position space where the noise can be easily separated from the signal.

This thesis reports on measurements of the coherence properties of 2D Bose gases. The fact that we have recently realized homogeneous gases is particularly advantageous, since it allows to measure global properties without averaging over an inhomogeneous density distribution. We have used two methods to study the phase coherence of ultracold bosonic ${}^6\text{Li}$ dimers, which are held in an optical dipole trap for a varying amount of time.

First, we have measured the momentum distribution via a matter wave focusing technique and observed that the population of low-momentum modes decreases significantly with hold time on the order of 50 ms. This behavior could be caused by heating. Yet, fits to the high-momentum modes indicate only a minor increase in temperature. Furthermore, the timescale of the low-momentum population decrease is fast, similar to the time a sound wave required to travel across the system, a process relevant for global thermalization. These observations suggest that the gas is not necessarily in thermal equilibrium.

The second method to investigate the phase properties relies on self-interference. When the gas is left to expand for a short time, in situ phase excitations transform into density fluctuations. After short time of flight, we have observed a density distribution reminiscent of a laser speckle pattern, which would not have occurred for a *Bose-Einstein condensate* (BEC) with true long-range order where the phase is constant. However, in a 2D gas only quasi-long-range order is maintained and, in a simplified picture, the gas can be thought of as a collection of patches with constant – but different – phase. During the time of flight, these matter wave fields begin to overlap and interfere constructively and destructively producing the aforementioned speckle pattern.

Analyzing the data from the short time of flight method, we find that the relative amplitude of the density fluctuations remains approximately constant for all hold times. However, destructive interference produces a pronounced minimum in the density-density correlation function, which is present immediately after the preparation but vanishes for hold times on the order of 50 ms. Following theoretical work by V. Singh and L. Mathey, the scaling exponent governing the algebraic decay of phase correlations is extracted from the density-density correlation function, assuming that we are in range of applicability of the theory and especially in thermal equilibrium. The scaling exponent determined in this fashion decreases with longer hold times.

Interestingly, the observations from the two methods are inconsistent with our theoretical expectation for a quasi-long-range ordered *Berezinskii-Kosterlitz-Thouless* (BKT) state being subject to heating. While the decrease of low-momentum modes is in agreement with this sce-

nario, the temperature extracted from the high-momentum modes and the scaling exponent do not increase as expected, rather, the scaling exponent even decreases. We argue that these discrepancies are most likely due to non-equilibrium effects, especially in view of the fast timescale on which low-momentum modes are lost. Yet, other assumptions of the theoretical model are also violated in our system which is of finite size, has strong interactions and experiences collisions during expansion. It is hence possible that reliable conclusions about the in situ phase coherence and its scaling exponent cannot be extracted using the short time of flight method.

In summary, we have presented the first measurements of the coherence properties of a strongly interacting homogeneous 2D gas of composite bosons with a high performance imaging system and have overcome issues experienced previously, such as strong systematic errors or density patterns caused by defocused or non-resonant imaging.

RECENT IMPROVEMENTS

The measurements presented in this thesis and summarized above suffer strongly from the very fast loss of low-momentum modes which potentially lead to a non-equilibrium state of the gas. Towards the end of the year 2017, the PhD students succeeding me, N. Luick and L. Sobirey, realized that the fast loss of low-momentum states might be caused by an insufficient vacuum pressure. The single particle atomic loss rate due to collisions with the background gas is only approximately 8 s, hence limiting the lifetime of the condensate fraction in 3D condensates to a maximum of 2 s and typically only 50–300 ms in the regime that we are interested in. Other groups have observed lifetimes an order of magnitude longer. The precise origin of the insufficient vacuum could not be determined conclusively. Leaks could not be found, but high background pressure can also be caused either by a high outgassing rate of the metallic experiment chamber combined with a very low pumping rate or alternatively outgassing from the getter foil placed in the tube connecting the experiment chamber to the main chamber. Ultimately, they have replaced the metallic chamber by a glass cell which has been previously commissioned and delivered already in 2011 but not used since the anti-reflection coatings had deteriorated substantially during manufacturing. With this glass cell, the aforementioned vacuum problem has been solved, now reaching lifetimes in excess of 130 s. Additionally, the condensate lifetime at ≈ 710 G has also been improved by a factor of more than 15.

Furthermore, they took this opportunity to implement improved coil holders and microscope mounts. By slitting the coil holders, the effect of eddy currents have been suppressed further. Furthermore, they removed superfluous conducting retaining rings used in the microscope mounts that may have caused vibrations and fringes in the images due to eddy currents. These improvements enable much faster changes of the magnetic field. This may allow us to study non-equilibrium effects in a more systematic fashion.

OUTLOOK

With the upgrades detailed above, it should now be possible to apply the methods developed in this thesis to perform improved studies of the coherence properties of 2D systems, with the important difference that the systems should now be in thermal equilibrium.

As I have shown here with proof of principle measurements, in equilibrium systems the self-interference method allows the extraction of the scaling exponent with high *signal-to-noise ratio* (SNR). The method is particularly attractive for inhomogeneous systems, since after a short time of flight the signal from regions of different density are still discernible since the atoms have not traveled far. This is in contrast to the case where the g_1 function is extracted from the trap averaged momentum distribution. While I have not discussed it extensively in the thesis, a substantial part of my dissertation work was devoted to extracting the scaling exponent from short time of flight images of harmonically trapped clouds in order to investigate the *Kosterlitz-Thouless* (KT) transition spatially. I found that the self-interference method is optimally suited to be applied locally and it is possible to extract a scaling exponent even from small patches. An example of the data quality possible is shown in Fig. 10.1 which demonstrates the capability to extract local phase properties from ultracold gases. However, these measurements have also been plagued by an unusually fast loss of coherence most likely caused by the insufficiently low background pressure.

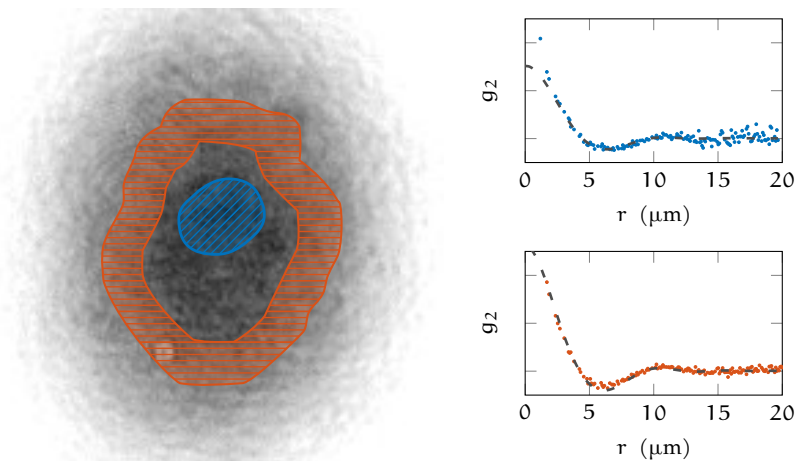


Figure 10.1: Example local analysis on two density intervals of an inhomogeneous gas of ultracold ${}^6\text{Li}$ dimers. The data represents 30 averaged realizations. Two patches of approximately constant density are highlighted, a patch around the center of the cloud and the corresponding density-density correlation function are shown in blue whereas a region of lower density towards the wings of the cloud and its corresponding density-density correlation function is shown in red. Note that the data quality remains high even for rather small sample patch sizes and a difference in the amplitude of g_2 is observable. Preliminary fits to g_2 with the tools presented in this thesis are plotted in gray (dashed).

Since a box potential and hence a homogeneous Fermi gas was realized during the time frame of this thesis, the advantage of the self-interference method, namely the ability to access the coherence locally in inhomogeneous clouds, is not so relevant anymore. Rather, in homogeneous systems, the momentum distribution, and hence g_1 , can be accessed directly via the momentum focusing technique since the undesirable averaging over different densities is eliminated. This was also recognized by the group of J. Dalibard, where such measurements are being performed with a homogeneous gas of bosonic ${}^{87}\text{Rb}$ atoms*.

* Private communication, H. Moritz

Thus, with the improvements that have been made, other directions have become more promising. For example, the group plans to investigate the buildup of coherence following a quench from a thermal gas in the weakly attractive fermionic regime to the strongly interacting bosonic regime. To this end, it is planned to use the matter wave focusing method established here to observe the increase of low-momentum modes as a function of hold time after the quench and determine the g_1 function via Fourier transform.

Also, measurements of completely different phenomena have become feasible. For example, the study of imbalanced Fermi gases in the homogeneous box potential might shed new light on the phase diagram of systems where theoretical studies propose a first order transition between a fully paired and a partially paired state, which would be observable in the formation of domains.

Furthermore, it would be fascinating to observe the Josephson effect in two dimensions, or even the propagation of second sound, which is an entropy wave predominantly mediated by oscillations between the normal and superfluid component. In both cases, the sudden jump of the superfluid density at the critical temperature of the KT transition might be observable. At the transition, both, the amplitude of the Josephson oscillations and the second sound mode should vanish. Hence, recent experimental advances indicate that the superfluid jump at the KT transition, which originally motivated this work, may finally be observed in ultracold atom systems in the near future.

A

DETAILED DERIVATION OF SIMULATED DENSITY-DENSITY CORRELATION FUNCTION AFTER TIME OF FLIGHT

Here, the detailed derivation of the expression for the density-density correlation function g_2 after *time of flight (ToF)* used in the numerical analysis is presented. This derivation follows the work of A. Imambekov et al.⁸² and V. Singh and L. Mathey⁸⁴. I have recreated the calculation in detail in order to gain an intuitive understanding of the resulting integral expression. It is presented here for the interested reader aiming to do the same. If not explicitly noted all integrals run from $-\infty$ to ∞ .

We begin with an expression for the single particle wave function of the bosonic gas and aim to obtain an expression relating the density-density correlation function after ToF $g_2(\mathbf{r}, t)$ to the in situ phase correlation function $g_1(\mathbf{r}, t = 0)$. To this end, the in situ wave function $\Psi(\mathbf{r}, t = 0)$ is propagated to arbitrary time t via application of a Green's function propagator $G(\mathbf{r}, t)$.

$$\Psi(\mathbf{r}, t) = \int G(\mathbf{r} - \mathbf{r}') \Psi(\mathbf{r}', 0) d\mathbf{r}'. \quad (\text{A.1})$$

Note that this expression bears great similarity to the way the light field was propagated in space in a superposition integral in the context of linear systems, see Section 9.2.2. The Green's function propagator is given as

$$G(\mathbf{r}, t) = \sqrt{\frac{m}{2\pi i \hbar t}} e^{i \frac{m \mathbf{r}^2}{2 \hbar t}}. \quad (\text{A.2})$$

Here, m denotes the mass of the studied particle and \hbar represents the reduced Planck constant. The prefactor, without the imaginary, unit will be abbreviated as $A = \sqrt{\frac{m}{2\pi \hbar t}}$ in the following, since the derivation is otherwise rather verbose. The imaginary unit is excluded as it will be eliminated shortly. Ultimately, we can only measure the density and not the wave function itself. With the time propagated in situ wave function, the density after ToF can be written as

$$n(\mathbf{r}, t) = \langle \Psi^\dagger(\mathbf{r}, t) \Psi(\mathbf{r}, t) \rangle \quad (\text{A.3})$$

$$= \frac{A^2}{i} \iint d\mathbf{v} d\mathbf{w} e^{-\frac{i m}{\hbar t} (\mathbf{r} - \mathbf{v})^2} \Psi^\dagger(\mathbf{v}, 0) e^{\frac{i m}{\hbar t} (\mathbf{r} - \mathbf{w})^2} \Psi(\mathbf{w}, 0). \quad (\text{A.4})$$

Here, the definition of $\Psi(\mathbf{r}, t)$ has simply been inserted and new coordinate names have been chosen for the \mathbf{r}' coordinate. To simplify the notation, we define $\Psi_0(\mathbf{r}) = \Psi(\mathbf{r}, 0)$ and perform a center of mass transformation, i. e. insert the relative distance $\mathbf{s} = \mathbf{v} - \mathbf{w}$ and the center of mass coordinate $\mathbf{S} = \frac{1}{2}(\mathbf{v} + \mathbf{w})$. When the exponents are combined, this results in

$$n(\mathbf{r}, t) = \frac{A^2}{i} \iint d\mathbf{s} d\mathbf{S} e^{-\frac{i m}{\hbar t} (\mathbf{S} - \mathbf{r}) \cdot \mathbf{s}} \Psi_0^\dagger\left(\mathbf{S} + \frac{\mathbf{s}}{2}\right) \Psi_0\left(\mathbf{S} - \frac{\mathbf{s}}{2}\right). \quad (\text{A.5})$$

⁸² A. Imambekov et al.: *Phys. Rev. A*, vol. 80, (2009)

⁸⁴ V. P. Singh and L. Mathey: *Phys. Rev. A*, vol. 89, (2014)

Although, we measure the density, we are actually interested in comparing the density-density correlations $\langle n(\mathbf{r}_1, t)n(\mathbf{r}_2, t) \rangle$. Combining two of the density expressions results in four integrals over 2D space in the expression for the density-density correlation. Here, \mathbf{u} and \mathbf{U} correspond to \mathbf{s} and \mathbf{S} in Eq. (A.5), respectively.

$$\begin{aligned}
\langle n(\mathbf{r}_1, t)n(\mathbf{r}_2, t) \rangle &= A^4 \iiint ds d\mathbf{S} d\mathbf{u} d\mathbf{U} e^{-\frac{im}{\hbar t}(\mathbf{S}-\mathbf{r}_1)\mathbf{s}} e^{-\frac{im}{\hbar t}(\mathbf{U}-\mathbf{r}_2)\mathbf{u}} \\
&\cdot \langle \Psi_0^\dagger \left(\mathbf{S} + \frac{\mathbf{s}}{2} \right) \Psi_0 \left(\mathbf{S} - \frac{\mathbf{s}}{2} \right) \Psi_0^\dagger \left(\mathbf{U} + \frac{\mathbf{u}}{2} \right) \Psi_0 \left(\mathbf{U} - \frac{\mathbf{u}}{2} \right) \rangle \\
&= A^4 \iiint \text{the same as above} \\
&\cdot \langle \Psi_0^\dagger \left(\mathbf{S} + \frac{\mathbf{s}}{2} \right) \Psi_0^\dagger \left(\mathbf{U} + \frac{\mathbf{u}}{2} \right) \Psi_0 \left(\mathbf{S} - \frac{\mathbf{s}}{2} \right) \Psi_0 \left(\mathbf{U} - \frac{\mathbf{u}}{2} \right) \rangle \\
&+ n_0 \delta(\mathbf{r}_1 - \mathbf{r}_2) \tag{A.6}
\end{aligned}$$

Here, the terms after the line break are understood to still be contained within the bounds of the integral, also the imaginary unit i drops out of the equation since two of the Green's functions appear complex conjugated and hence $i \cdot (-i) = 1$. In the second step, the wave functions Ψ and Ψ^\dagger have been reordered to be in so called *normal order*, i. e. all conjugates appear first in the expectation value $\langle * \rangle$. This step is necessary since the density correlations contain also the autocorrelation of the individual atoms with themselves, the $n_0 \delta$ term, where n_0 denotes the mean density. The second order correlation function g_2 , however, does not contain the aforementioned autocorrelations and thus they are subtracted from both sides. We can identify the density correlations on the left hand side minus the autocorrelation term as the sought after density-density correlation function $n_0^2 g_2$.

Now, we identify the term in angle brackets to be the density matrix $\langle * \rangle = \rho(1, 2, 3, 4)$ and perform another center of mass transformation. This time, we insert the relative distance $\mathbf{r}_{12} = \mathbf{r}_1 - \mathbf{r}_2$ and the center of mass coordinate $\mathbf{R}_{12} = \frac{1}{2}(\mathbf{r}_1 + \mathbf{r}_2)$,

$$\begin{aligned}
n_0^2 g_2(\mathbf{r}_1, \mathbf{r}_2, t) &= A^4 \iiint ds d\mathbf{S} d\mathbf{u} d\mathbf{U} \\
&\cdot e^{-\frac{im}{\hbar t}[(\mathbf{S}-\frac{\mathbf{r}_{12}}{2})\mathbf{s}+(\mathbf{U}+\frac{\mathbf{r}_{12}}{2})\mathbf{u}-\mathbf{R}_{12}(\mathbf{s}+\mathbf{u})]} \\
&\cdot \rho \left(\mathbf{S} + \frac{\mathbf{s}}{2}, \mathbf{U} + \frac{\mathbf{u}}{2}, \mathbf{S} - \frac{\mathbf{s}}{2}, \mathbf{U} - \frac{\mathbf{u}}{2} \right). \tag{A.7}
\end{aligned}$$

The center of mass transformation simplifies the expectation value but introduces additional complexity into the exponential term. However, since there is no dependence on \mathbf{R}_{12} in the wave functions, we are able to integrate over it and evaluate the integral $\int d\mathbf{R}_{12} = B$ on both sides. On the left hand side, this results in $B \cdot n_0^2 g_2(\mathbf{r}_1 - \mathbf{r}_2, t)$ since in homogeneous systems $g_2(\mathbf{r}_1, \mathbf{r}_2, t) = g_2(\mathbf{r}_1 - \mathbf{r}_2, t)$ and thus no dependency on the center of mass coordinate exists. On the right hand side, the evaluation of said integral results in a Dirac delta distribution

$$\left(\frac{m}{\hbar t} \right)^2 \int d\mathbf{R}_{12} e^{\frac{im}{\hbar t}(\mathbf{s}+\mathbf{u})\mathbf{R}_{12}} = (2\pi)^2 \delta(\mathbf{s} + \mathbf{u}). \tag{A.8}$$

When the delta distribution is inserted in the above equation, it now reads

$$\begin{aligned} B \cdot n_0^2 g_2(\mathbf{r}_1 - \mathbf{r}_2, t) &= A^2 \iiint ds d\mathbf{S} d\mathbf{u} d\mathbf{U} \\ &\cdot e^{-\frac{im}{\hbar t}[(\mathbf{S} - \frac{\mathbf{r}_1}{2})\mathbf{s} + (\mathbf{U} + \frac{\mathbf{r}_2}{2})\mathbf{u}]} \cdot \delta(\mathbf{s} + \mathbf{u}) \\ &\cdot \rho\left(\mathbf{S} + \frac{\mathbf{s}}{2}, \mathbf{U} + \frac{\mathbf{u}}{2}, \mathbf{S} - \frac{\mathbf{s}}{2}, \mathbf{U} - \frac{\mathbf{u}}{2}\right). \end{aligned} \quad (\text{A.9})$$

We integrate over \mathbf{u} so that the Dirac delta distribution yields the substitution $\mathbf{u} \rightarrow -\mathbf{s}$, thus

$$\begin{aligned} B \cdot n_0^2 g_2(\mathbf{r}_{12}, t) &= A^4 \iiint ds d\mathbf{S} d\mathbf{U} e^{-\frac{im}{\hbar t}(\mathbf{S} - \mathbf{u} - \mathbf{r}_{12})\mathbf{s}} \\ &\cdot \rho\left(\mathbf{S} + \frac{\mathbf{s}}{2}, \mathbf{U} - \frac{\mathbf{s}}{2}, \mathbf{S} - \frac{\mathbf{s}}{2}, \mathbf{U} + \frac{\mathbf{s}}{2}\right). \end{aligned} \quad (\text{A.10})$$

Yet another center of mass transformation is performed in order to exploit the translational invariance of the homogeneous wave function Ψ . Here, the relative coordinate is $\mathbf{x} = \mathbf{S} - \mathbf{U}$ and the center of mass coordinate is given by $\mathbf{X} = \mathbf{S} + \mathbf{U}$. Note, that unlike the earlier variable substitutions, this transformation does not include a division by two and hence introduces a Jacobian determinant of $1/2$ which is moved out of the integral. After the coordinate transformation, the expression for g_2 reads

$$\begin{aligned} B \cdot n_0^2 g_2(\mathbf{r}_{12}, t) &= \frac{A^2}{2} \iiint ds d\mathbf{x} d\mathbf{X} e^{-\frac{im}{\hbar t}(\mathbf{x} - \mathbf{r}_{12})\mathbf{s}} \\ &\cdot \rho\left(\frac{\mathbf{X}}{2} + \frac{1}{2}(\mathbf{x} + \mathbf{s}), \frac{\mathbf{X}}{2} - \frac{1}{2}(\mathbf{x} + \mathbf{s}), \frac{\mathbf{X}}{2} + \frac{1}{2}(\mathbf{x} - \mathbf{s}), \frac{\mathbf{X}}{2} - \frac{1}{2}(\mathbf{x} - \mathbf{s})\right). \end{aligned} \quad (\text{A.11})$$

Now, the translational invariance $\Psi_0(\mathbf{X} + \boldsymbol{\xi}) = \Psi_0(\boldsymbol{\xi})$ can be exploited which allows us to perform an integral over \mathbf{X} and thus obtain another B

$$\begin{aligned} B \cdot n_0^2 g_2(\mathbf{r}_{12}, t) &= B \frac{A^2}{2} \iiint ds d\mathbf{x} e^{-\frac{im}{\hbar t}(\mathbf{x} - \mathbf{r}_{12})\mathbf{s}} \\ &\cdot \rho\left(\frac{1}{2}(\mathbf{x} + \mathbf{s}), -\frac{1}{2}(\mathbf{x} + \mathbf{s}), \frac{1}{2}(\mathbf{x} - \mathbf{s}), -\frac{1}{2}(\mathbf{x} - \mathbf{s})\right). \end{aligned} \quad (\text{A.12})$$

The B on both sides of the equation cancel and a last coordinate transformation, $\mathbf{r}' = \mathbf{x} - \mathbf{s}$ and $\mathbf{r} = \mathbf{x} + \mathbf{s}$, reveals the simplified expression

$$\begin{aligned} n_0^2 g_2(\mathbf{r}_{12}, t) &= \frac{A^2}{4} \iint d\mathbf{r} d\mathbf{r}' e^{-\frac{im}{\hbar t}(\mathbf{r}^2 - \mathbf{r}'^2 - 2\mathbf{r}_{12}(\mathbf{r} - \mathbf{r}'))} \\ &\cdot \rho\left(\frac{\mathbf{r}'}{2}, -\frac{\mathbf{r}'}{2}, \frac{\mathbf{r}}{2}, -\frac{\mathbf{r}}{2}\right). \end{aligned} \quad (\text{A.13})$$

Note that the Jacobian determinant is again $1/2$ and has been moved out of the integral. Finally, no free variables remain and no additional integrals can be eliminated. Interestingly, the state of the gas, e. g. superfluid or normal, is solely encoded in the density matrix ρ , the time dependence, however, is identical in either case.

Since we wish to relate the density-density correlation function g_2 to the phase correlation function g_1 , all that remains is to write the density matrix ρ in terms of g_1 . With this, we can write the density matrix as

$$\rho(\mathbf{r}_a, \mathbf{r}_b, \mathbf{r}_c, \mathbf{r}_d) = n_0^2 \langle e^{i[\theta(\mathbf{r}_a) + \theta(\mathbf{r}_b) - \theta(\mathbf{r}_c) - \theta(\mathbf{r}_d)]} \rangle \quad (\text{A.14})$$

$$= n_0^2 e^{\langle [\theta(\mathbf{r}_a) + \theta(\mathbf{r}_b) - \theta(\mathbf{r}_c) - \theta(\mathbf{r}_d)]^2 \rangle / 2} \quad (\text{A.15})$$

$$= n_0^2 \frac{g_1(\mathbf{r}_a - \mathbf{r}_c) g_1(\mathbf{r}_a - \mathbf{r}_d) g_1(\mathbf{r}_b - \mathbf{r}_c) g_1(\mathbf{r}_b - \mathbf{r}_d)}{g_1(\mathbf{r}_a - \mathbf{r}_b) g_1(\mathbf{r}_c - \mathbf{r}_d)}.$$

To this end, we recall that $\langle e^{i\hat{\phi}} \rangle = e^{\frac{1}{2}\langle \hat{\phi}^2 \rangle}$, for details see Extra 4.1. Also, we have used the fact that g_1 can be written with as $g_1(\mathbf{r}_i - \mathbf{r}_j) \propto \exp(-1/2\langle \theta(\mathbf{r}_i)^\dagger \theta(\mathbf{r}_i) - \theta(\mathbf{r}_i)^\dagger \theta(\mathbf{r}_j) - \theta(\mathbf{r}_j)^\dagger \theta(\mathbf{r}_i) + \theta(\mathbf{r}_j)^\dagger \theta(\mathbf{r}_j) \rangle)$, which can be inserted after expanding the square in the exponent.

Insertion of the arguments $\mathbf{r}_a = \mathbf{r}'/2$, $\mathbf{r}_b = -\mathbf{r}'/2$, $\mathbf{r}_c = \mathbf{r}/2$, and $\mathbf{r}_d = -\mathbf{r}/2$ yields

$$\rho(\mathbf{r}'/2, -\mathbf{r}'/2, \mathbf{r}/2, -\mathbf{r}/2) = \quad (\text{A.16})$$

$$n_0^2 \frac{g_1(\frac{1}{2}(\mathbf{r}' - \mathbf{r})) g_1(\frac{1}{2}(\mathbf{r}' + \mathbf{r})) g_1(-\frac{1}{2}(\mathbf{r}' + \mathbf{r})) g_1(-\frac{1}{2}(\mathbf{r}' - \mathbf{r}))}{g_1(\frac{1}{2}(\mathbf{r}' + \mathbf{r}')) g_1(\frac{1}{2}(\mathbf{r} + \mathbf{r}))}.$$

Since g_1 is symmetric across the origin, i. e. $g_1(\frac{1}{2}(\mathbf{r}' - \mathbf{r})) = g_1(-\frac{1}{2}(\mathbf{r}' - \mathbf{r}))$, we can combine all functions of equal argument and obtain

$$\rho(\mathbf{r}'/2, -\mathbf{r}'/2, \mathbf{r}/2, -\mathbf{r}/2) = n_0^2 \frac{g_1(\frac{1}{2}(\mathbf{r}' - \mathbf{r}))^2 g_1(\frac{1}{2}(\mathbf{r}' + \mathbf{r}))^2}{g_1(\mathbf{r}') g_1(\mathbf{r})}. \quad (\text{A.17})$$

In conclusion, the expression to compute the density-density correlation function g_2 after time of flight for a given in situ phase correlation function g_1 is given as

$$g_2(\mathbf{r}_{12}, t) = \frac{\Lambda^4}{4} \iint d\mathbf{r} d\mathbf{r}' e^{-\frac{im}{\hbar t}(\mathbf{r}^2 - \mathbf{r}'^2 - 2\mathbf{r}_{12}(\mathbf{r} - \mathbf{r}'))} \cdot \frac{g_1(\frac{1}{2}(\mathbf{r}' - \mathbf{r}))^2 g_1(\frac{1}{2}(\mathbf{r}' + \mathbf{r}))^2}{g_1(\mathbf{r}') g_1(\mathbf{r})}. \quad (\text{A.18})$$

B

DETAILED NUMERICAL ANALYSIS PROCEDURE

This appendix presents three aspects of the numerical analysis procedure in more detail on the basis of its respective flowchart. First, the image preparation is discussed after the intensity images have been converted to density as outlined in Section 9.2.1. Next, the steps of the correlation analysis of the aforementioned density images are presented including a possible offset correction. Finally, the procedure of combining the density-density correlation functions from in situ and after *time of flight* (ToF) as well as the necessary steps involved in numerical fitting are discussed.

The flowcharts depict the flow of information passed along the arrows. Each node represents the numerical shape of the data, e. g. a vector or a matrix, or a process applied on one or more prior nodes.

A short description of the nodes used in the flowcharts follows:



Input or output from and to sources external to the flow chart



A three-dimensional array, i. e. a stack of two-dimensional images. The third dimension running over the number of realizations



A two-dimensional array, usually a two-dimensional image. In some cases also an array of vectors



A one-dimensional array in the third dimension, usually a value per realization. Thus, the "third" dimension runs over the number of realization



A one-dimensional vector, e. g. dependent on the radial distance. Distinct from the 1D-array since no dimension runs over the realizations, otherwise identical



A process applied on the prior nodes. If subject to two inputs, the input's role is labeled next to the incoming arrow



*A decision made in respect to user input. The data exits the node labeled *yes* or *no* respectively*



An arrow represents the flow of information, a junction is denoted by a filled circle. Here, the data flows out in both directions simultaneously

B.1 IMAGE PREPARATION

The first stage of the numerical analysis consists of the preparation of the measured density profiles in order to obtain a normalized density fluctuation signal. The process is sketched in Fig. B.1. Note that although this process is only strictly necessary for inhomogeneous gases and less so for the homogeneous gases used in this thesis, compensating for the mean density always yields a more manageable signal.

In order to isolate the density fluctuations, a region of interest is chosen by the user from which a binary mask is created. This mask is applied by element-wise multiplication with the `image` array, a stack of density images, yielding the `masked_images` array. Simultaneously, the `image` array is averaged over all realizations, yielding the mean density.

If it is chosen to scale the `masked_images` to the mean, the `masked_images` are piecewise divided by the `scale_factor`, which returns the `scaled_masked_images`. Regardless of scaling, the image arrays are piecewise divided by the mean density and all NaN are replaced by zero, which yields the `normalized_masked` or `normalized_scaled_masked_images`, respectively. The replacement of NaN is necessary since the `mean_density` might contain values of zero due to noise.

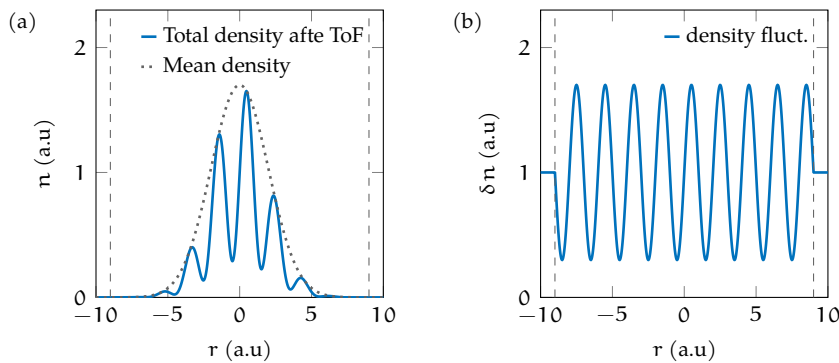
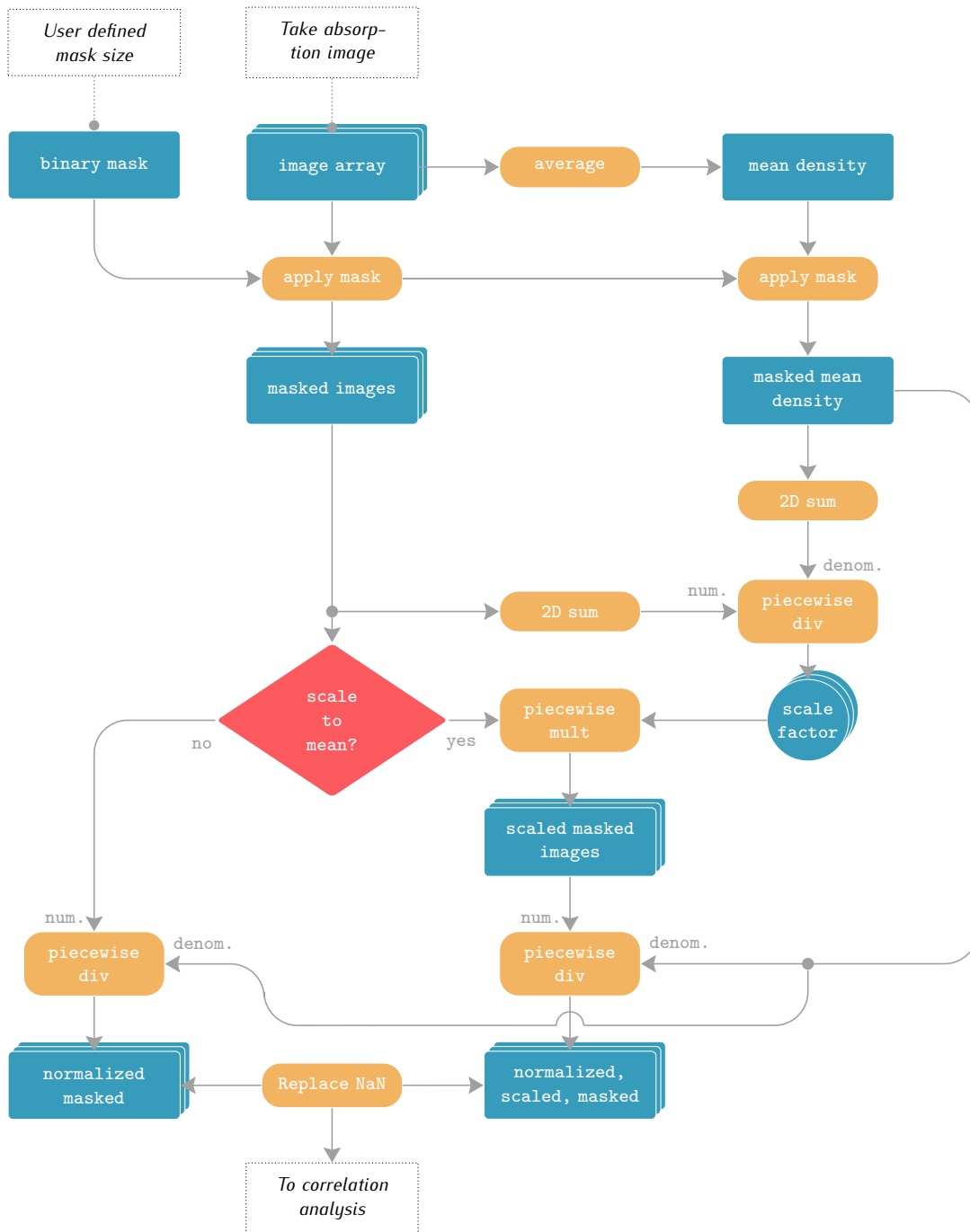


Figure B.1: (a) Sketch of the total density after ToF in an inhomogeneous system. Here, the density is modulated by the fluctuations according to $n(r) = \bar{n}(1 + \delta n(r))$ (a) After division by the mean density, the density fluctuations are isolated. The boundary of the sample is indicated by vertical dashed lines.

Image preparation



B.2 CORRELATION ANALYSIS

Extracting the density-density correlation function from the density modulation after ToF lies at the core of the self-interference method presented in this thesis. Thus, a detailed report of the steps involved follows.

The correlation analysis requires three inputs: The normalized – and possibly rescaled – density images from the image preparation step, the binary mask used in the previous step do define the region of interest, and a maximum radius restricting the evaluation of the measured g_2 . The latter parameter is necessary since we evaluate a finite area by setting the outer part to zero which is not considered by the correlation algorithm. Hence, we must eliminate the values of excessive noise or where divided by zero.

The normalized masked images as well as the binary mask are autocorrelated which is denoted by `xcorr`. The resultant density-density correlation function of the density images is divided by the density-density correlation function of the mask, which compensates for the suppression of long wavelength excitations.

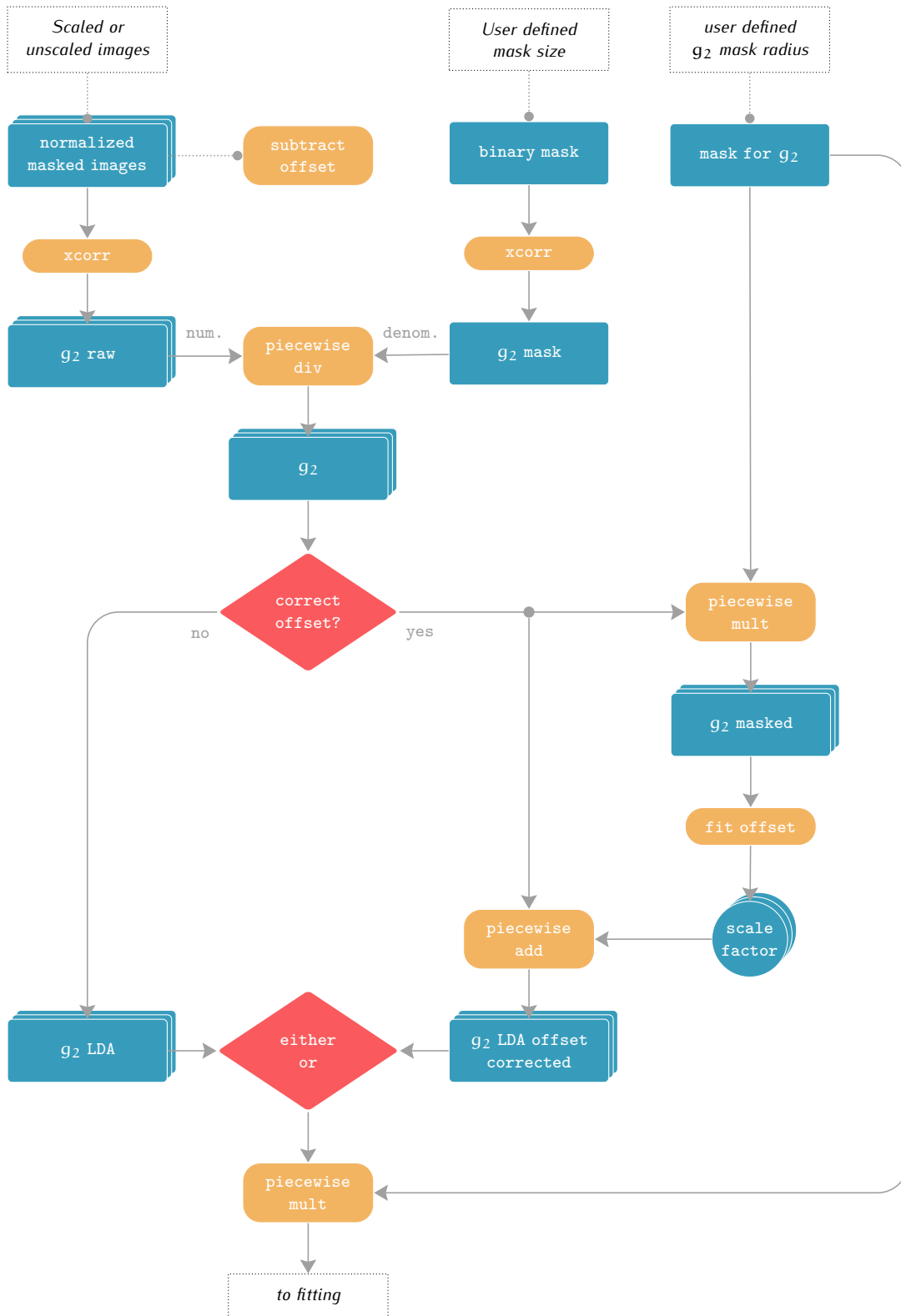
Subsequently, the user decides whether to correct for the offset of g_2 . This serves two purposes. On the one hand, it compensates for small errors in the imaging since for large distances all g_2 should approach unity. On the other hand, it simplifies the numerical analysis due to the fact that subsequent Fourier transforms do not produce large *zero frequency* peaks. Furthermore, the theoretical predictions by V. Singh and L. Mathey⁸⁴ yield also $g_2 - 1$ for comparison. Hence, the analysis almost always proceeds on that route, except when raw g_2 values are of interest.

Finally, the resultant g_2 is restricted to a well behaved domain by piecewise multiplication with the earlier defined binary mask for g_2

In practice, the autocorrelation is implemented as a Fourier transform pair due to the large advantage in performance, i. e. $\text{xcorr}(\langle \rangle) = \mathcal{Ft}\{(\mathcal{Ft}\{\langle \rangle\})^2\}$. This yields almost identical results apart from numerical rounding error, hence the intuitively much easier to understand autocorrelation function denoted as `xcorr(⟨⟩)` is used.

⁸⁴ V. P. Singh and L. Mathey: *Phys. Rev. A*, vol. 89, (2014)

Correlation analysis



B.3 IN SITU PROPAGATION AND FITTING OF g_2

The flowchart on the right illustrates the numerical fitting procedure used to extract the scaling exponent η and the short-range cut-off $a_c \equiv a_{\text{cut-off}}$. This process is identical when an exponentially decaying phase correlation function is used as an input to the fitting routine, then yielding the correlation length r_0 and the short-range parameter c .

Three inputs must be processed and combined in order to obtain the optimal fit. Two of which are the arrays of two-dimensional density-density correlation functions, for in situ and after ToF, $g_{2,\text{is}}(x, y)$ and $g_{2,\text{ToF}}(x, y)$ respectively. Both arrays are subsequently azimuthally averaged, which yields an array of $g_{2,*}(r)$, each row a different realization. From now, the in situ g_2 must be treated differently, since we require the in situ density correlation evolved to the point in time the ToF data is taken. Hence, we Hankel transform each row in order to multiply the in situ density-density correlation function by the cosine term, $\cos^2\left(\frac{\hbar t k^2}{2m}\right)$, in frequency space, for details confer Section 9.2.3. After an inverse Hankel transform, the time evolved in situ $g_{2,\text{is}}(r, \text{ToF})$ is subtracted from $g_{2,\text{ToF}}(r)$ which yields the compensated density-density correlation function $g_{2,\text{comp}}(r)$. This completes the preparation necessary for our fitting procedure which will be detailed next.

The fitting routine relies on the third input, which consists of a precomputed three-dimensional array of density-density correlation functions. Each dimension of the array contains samples for an independent parameter. The parameter intervals for the particular ToF investigated in this thesis, 1 ms, can be found in Table B.1.

Unit	Algebraic decay	Exponential decay
	$0.0025 \leq \eta < 1.25$	$0.5 \leq c < 3.5$
μm	$0.8 \leq a_{\text{cut-off}} < 8$	$0.5 \leq r_0 < 50$
μm	$0 \leq r < 25$	$0 \leq r < 20$

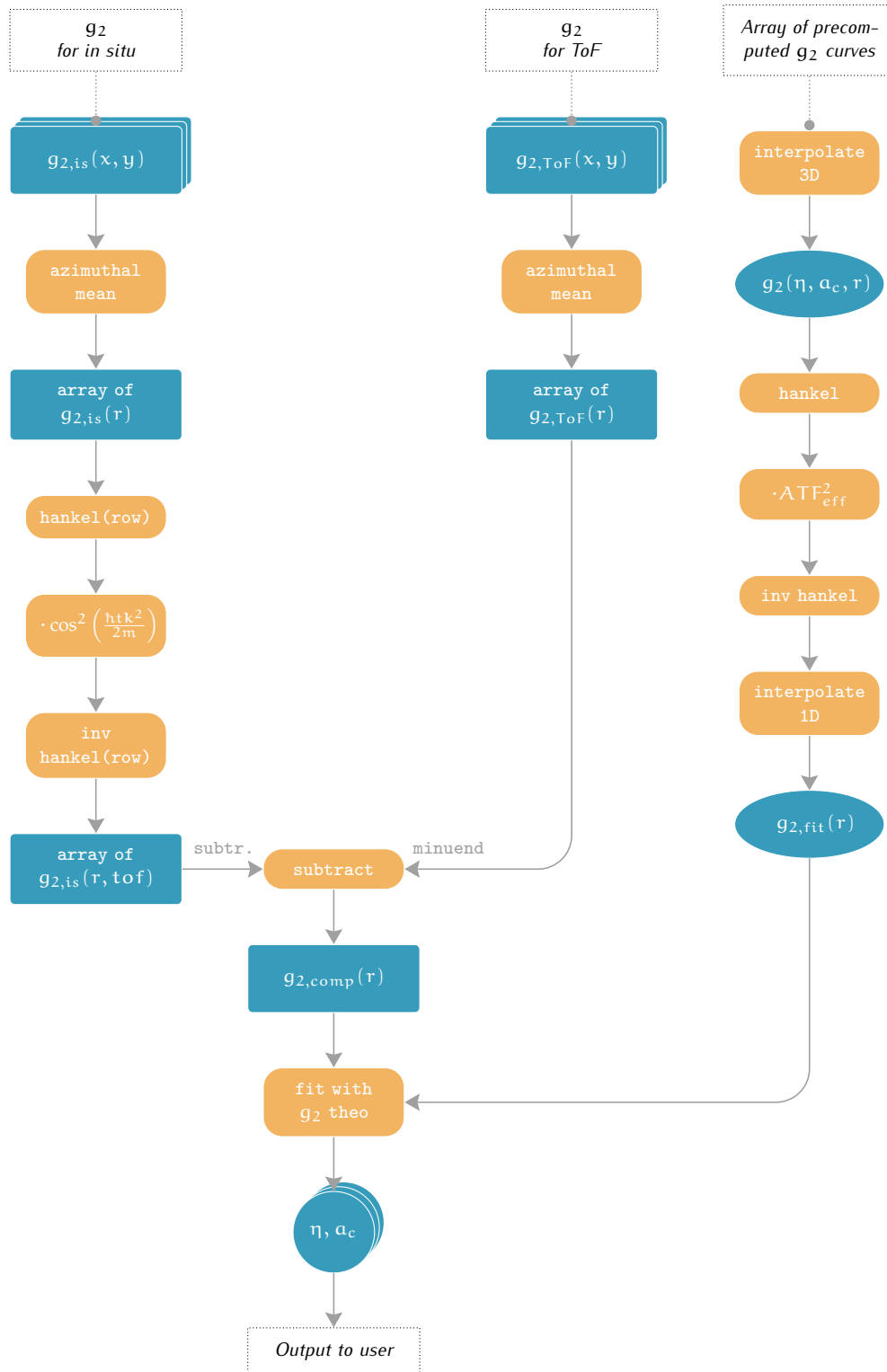
In advance to starting the fitting procedure, the density-density correlation functions have been simulated by V. Singh on a high performance cluster due to the high computational cost of solving a four dimensional integral for each η , $a_{\text{cut-off}}$ and r , refer Eq. (8.14). In order to use the step adaptive fitting routines of the MATLAB* computing environment we interpolate the three-dimensional g_2 array linearly. The resultant interpolant is evaluated by the fitting routine for a particular $(\eta, a_{\text{cut-off}}, r)$ tuple and subsequently Hankel transformed, since compensating for the imaging apparatus is most convenient in frequency space.

We have chosen to impart the effect of the imaging apparatus onto the theoretical prediction instead of trying to remove it from the measured density distribution. This is due to the fact that our imaging system is close to ideal, i.e. the *amplitude transfer function (ATF)* is similar to a Heaviside step function. The dominant effect of such a

Table B.1: Overview of the parameter space used for fitting g_2 for 1 ms time of flight.

*MATLAB and Statistics Toolbox Release 2018a, The MathWorks, Inc., Natick, Massachusetts, United States

In situ propagation and fitting of g_2



transfer function is the abrupt elimination of frequency components beyond a maximum spacial frequency k_{\max} . Since, these frequency components are permanently lost, a deconvolution technique, i. e. dividing the image spectrum by the ATF, would produce no noticeable image improvement. However, apodization of the theoretical g_2 by an abrupt ATF envelope does produce a signal that contains the same image imperfections as the measured density-density correlation. Note that since the density is contained twice in the density-density correlation function, the square of the ATF must be used. This process is completed by an inverse Hankel transform, which is linearly interpolated in the remaining independent variable r , since the MATLAB fitting routine requires a callable function and not a static vector of values.

Ultimately, the values for η and $\alpha_{\text{cut-off}}$ obtained for each realization are pruned for 3σ -outliers and averaged to yield the final result.

C | IN SITU TEMPERATURE DETERMINATION OF A HOMOGENEOUS GAS

Here, an in situ method to extract the temperature from a homogeneous gas is presented. It relies on the application of a potential gradient in order to exploit the fact that the degenerate part follows the gradient whereas the thermal part deviates. Unfortunately, we have not applied a sufficient gradient in the experiments performed in the context of this thesis to observe the deviation of the thermal part and hence could not extract a temperature. However, the method itself proved to be rather convenient for setups with high spatial imaging resolution since no expansion out of the *depth of field (DoF)* is necessary. For this reason, a short synopsis of our efforts is given in the following.

Since temperature is an intensive thermodynamic property of the gas, it is necessary to evaluate a finite partition of the sample. A common method to extract the temperature is to fit the density *equation of state (EOS)* which depends on chemical potential μ and temperature T , $n_{2D}(\mu, T)$, to a non-degenerate area of varying density. Since the in situ density distribution of a homogeneous disk does not offer a sufficient density gradient, we applied a linear magnetic field. While in principle viable, the analysis yielded insufficient deviation of the thermal density from the linear potential for accurate fitting in the acquired data. This can be seen as the absence of a non-linear density dependence on the potential in Fig. C.1. Unfortunately, no corresponding data with increased gradient is available, hence this method had to be abandoned.

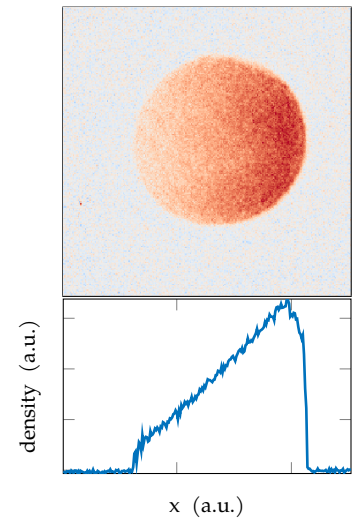


Figure C.1: (Above) Sample of a 2D in situ image with applied magnetic field gradient, not usable for temperature determination of a relatively cold gas. (Below) Density profile of the above image. Note that the profile is almost completely linear with negligible amount of thermal density expected on the left hand side.

ACRONYMS

2DEG two-dimensional electron gas. 3, 4

ATF amplitude transfer function. 83, 84, 85, 101, 115, 117, 118, 127, 128, 129, 130, 131, 132, 133, 156, 158

ATF_{eff} effective amplitude transfer function. 131

BEC Bose-Einstein condensate. 17, 22, 24, 25, 38, 47, 51, 75, 78, 82, 83, 84, 88, 90, 143

BKT Berezinskii-Kosterlitz-Thouless. 4, 74, 79, 84, 85, 90, 92, 93, 100, 109, 111, 143

DoF depth of field. 14, 60, 66, 71, 90, 95, 98, 99, 115, 116, 124, 130, 159

DoS density of states. 17, 20, 25, 75

EOS equation of state. 19, 72, 110, 159

FORT far off resonance trap. 121

FWHM full width at half maximum. 78

GoF goodness of fit. 103, 106, 107

GPE Gross-Pitaevskii equation. 28, 35, 45

KT Kosterlitz-Thouless. 4, 5, 37, 44, 46, 47, 50, 75, 78, 82, 89, 145, 146

LIS linear invariant system. 124

LRO long-range order. 17, 18, 23, 24, 27, 28, 29, 47

MOT magneto optical trap. 12

MTF modulation transfer function. 127

NA numerical aperture. 14, 116, 117, 124, 130, 132

OTF optical transfer function. 127, 128, 130

PSD power spectral density. 92, 115, 116, 117, 129, 133, 134, 137, 138, 141, 142

PSF point spread function. 15, 70, 84, 98, 99, 105, 115, 117, 124, 128, 129, 130, 131, 135, 136, 163

PSF_{eff} effective point spread function. 60, 71, 78

QLRO quasi-long-range order. 18, 109

RMSE root-mean-square error. 106, 107

RoI region of interest. 96, 97, 98, 103, 140, 141

SNR signal-to-noise ratio. [55](#), [91](#), [92](#), [95](#), [96](#), [98](#), [104](#), [105](#), [118](#), [145](#)

ToF time of flight. [4](#), [5](#), [14](#), [15](#), [55](#), [57](#), [65](#), [67](#), [69](#), [70](#), [76](#), [87](#), [88](#), [89](#), [90](#), [91](#), [92](#), [93](#), [95](#), [96](#), [97](#), [98](#), [99](#), [100](#), [101](#), [102](#), [104](#), [105](#), [106](#), [108](#), [109](#), [110](#), [112](#), [115](#), [117](#), [118](#), [120](#), [121](#), [123](#), [130](#), [132](#), [133](#), [134](#), [136](#), [138](#), [147](#), [151](#), [152](#), [154](#), [156](#)

LIST OF FIGURES

2.1	Trapping and cooling procedure overview	11
2.2	Lattice and ring setup	13
2.3	Kinematic confinement	13
2.4	Microscope setup	14
2.5	Effect on <i>point spread function</i> (PSF) when reducing the resolution	15
3.1	Mean occupancy comparison	19
3.2	Plot of the polylogarithm	21
3.3	Chemical potential and fugacity	22
3.4	Fraction of particles in the ground state vs. temperature	23
3.5	Interference and correlation function g_1 for interacting Bose gases	29
3.6	Second order correlation functions for an interacting Bose gas	30
3.7	Two atoms colliding	33
3.8	Feshbach resonance	33
4.1	Phase to density ripples during ToF	38
4.2	Comparison of phase decay, BEC, algebraic and exponential	44
4.3	Schematic of the KT transition	46
4.4	Illustration of topology change due to vortices	47
5.1	Probing the coherence across the KT transition	50
5.2	Stirring a 2D Bose gas	51
5.3	Local dynamics in a 2D Bose gas	52
5.4	First order correlation function via matter wave focusing	54
5.5	Phase to density for varying time of flight	54
6.1	Illustration gradient index lens	57
6.2	Sketch of the T/4 measurement method	58
6.3	Comparison of the methods to obtain the momentum distribution	60
7.1	Modeled vertical expansion and scattering rate	65
7.2	Azimuthal averages of $n(k)$ and $g_1(r)$	66
7.3	Comparison of the the measured $n(k)$ with and without brake pulse	68
7.4	Expansion during ToF with and without brake pulse	69
7.5	Modeled vertical expansion and scattering rate	70
7.6	Variations in momentum distributions	71
7.7	Variations in smoothed momentum distributions	71
7.8	Mean density during hold time	71
7.9	Azimuthal averages of bosonic momentum distributions $n(k)$ and peak amplitudes vs. hold time	72
7.10	Fitting the momentum distribution	73
7.11	Inverse phase-space density over time	74
7.12	Critical fraction in dependence on temperature	76
7.13	Two-body density decay	77
7.14	First and second sound in 2D	78
7.15	Theoretical momentum distributions and first order correlation functions	82
7.16	Comparison of momentum distributions and correlation functions for finite systems	83
7.17	Comparison of corrected momentum distribution and correlation function.	84
7.18	Comparison of corrected first order correlation functions vs. hold time.	85
8.1	Interference pattern during ToF	88

8.2	Normalized theoretical density-density correlation function g_2	94
8.3	Interference pattern after ToF=1 ms and ToF=2 ms	95
8.4	Outline of the image preparation used in the numerical analysis of g_2	97
8.5	Histogram contrast comparison	99
8.6	Minimum in density correlation function vs. hold time	100
8.7	Plot of algebraic g_1 term in $g_2(r, t)$ expression	103
8.8	Plot of exponential g_1 term in $g_2(r, t)$ expression	103
8.9	Region of Interest	103
8.10	Examples of fits, comparison between algebraic and exponential decay	104
8.11	In situ density fluctuations fit	105
8.12	Comparison of exponential g_1 functions as input to the fitting routine	106
8.13	Comparison of g_2 fit functions	106
8.14	Main result of short ToF analysis	108
8.15	Comparison of g_2 for different short-range cut-offs	108
8.16	Comparison of g_2 for different scaling exponents	108
9.1	Spielman focusing method	116
9.2	Focusing the imaging system	117
9.3	Verification of optimal imaging via ATF	117
9.4	Determining the detuning via atom displacement after illumination	118
9.5	Signal to noise ratio and chirp efficiency	119
9.6	Determining the saturation counts and verification of density stability	120
9.7	Determining the magnification	121
9.8	Sketch of imaging setup	124
9.9	Imaging aberrations as wavefront deformation	128
9.10	Effective amplitude transfer function	132
9.11	Comparison of the effect of imperfect imaging on the extracted g_2	132
9.12	Time propagation of in situ density fluctuations	134
9.13	Uncompensated fitting of simulated data	135
9.14	Imaging compensated fitting of simulated data	136
9.15	Fully compensated fitting of simulated data	137
9.16	Examples of synthetic density ripple images for varying ToF	138
9.17	Fits to simulated density ripples	139
9.18	Comparison of fitting errors on simulated data	139
9.19	Comparison of the result of different fit limits	140
9.20	Effect of the size of the region of interest	141
10.1	Self-interference locally measured	145
B.1	Density normalization after ToF	152
C.1	Density profile of in situ gradient	159

LIST OF TABLES

3.1	Overview of ideal 3D and 2D gas properties	27
4.1	Overview of interacting 3D and 2D gas properties	47
B.1	Overview of the parameter space used for fitting g_2	156

BIBLIOGRAPHY

- ¹D. Bishop and J. Reppy: *Study of the Superfluid Transition in Two-Dimensional ^4He Films*, “[Physical Review Letters](#)” vol. 40, no. 26, 1727–1730 (1978) (cited on pages 3, 4, 49).
- ²R. Peierls: *Bemerkungen über Umwandlungstemperaturen*, “[Helvetica Physica Acta](#)” vol. 7, 81–83 (1934) (cited on page 3).
- ³P. C. Hohenberg: *Existence of long-range order in one and two dimensions*, “[Physical Review](#)” vol. 158, no. 2, 383–386 (1967) (cited on pages 3, 18, 27).
- ⁴N. D. Mermin and H. Wagner: *Absence of ferromagnetism or antiferromagnetism in one- or two-dimensional isotropic Heisenberg models*, “[Physical Review Letters](#)” vol. 17, no. 22, 1133–1136 (1966) (cited on pages 3, 18, 27).
- ⁵V. L. Berezinskii: *Destruction of long-range order in one-dimensional and two-dimensional systems having a continuous symmetry group I. classical systems*, “[Soviet Journal of Experimental and Theoretical Physics](#)” vol. 32, no. 3, 2–9 (1971) (cited on page 3).
- ⁶J. M. Kosterlitz and D. J. Thouless: *Ordering, metastability and phase transitions in two-dimensional systems*, “[Journal of Physics C: Solid State Physics](#)” vol. 6, no. 7, 1181–1203 (1973) (cited on pages 3, 18, 49).
- ⁷P. Minnhagen: *The two-dimensional Coulomb gas, vortex unbinding, and superfluid-superconducting films*, “[Reviews of Modern Physics](#)” vol. 59, no. 4, 1001–1066 (1987) (cited on page 4).
- ⁸D. Snoke: *Spontaneous Bose coherence of excitons and polaritons*, “[Science](#)” vol. 298, no. 5597, 1368–1372 (2002) (cited on page 4).
- ⁹L. V. Butov: *Condensation and pattern formation in cold exciton gases*, “[Physica Status Solidi \(B\) Basic Research](#)” vol. 238, no. 3, 381–388 (2003) (cited on page 4).
- ¹⁰J. Kasprzak, M. Richard, S. Kundermann, A. Baas, P. Jeambrun, J. M. Keeling, F. M. Marchetti, M. H. Szymańska, R. André, J. L. Staehli, V. Savona, P. B. Littlewood, B. Deveaud, and L. S. Dang: *Bose-Einstein condensation of exciton polaritons*, “[Nature](#)” vol. 443, no. 7110, 409–414 (2006) (cited on page 4).
- ¹¹A. Amo, J. Lefrère, S. Pigeon, C. Adrados, C. Ciuti, I. Carusotto, R. Houdré, E. Giacobino, and A. Bramati: *Superfluidity of polaritons in semiconductor microcavities*, “[Nature Physics](#)” vol. 5, no. 11, 805–810 (2009) (cited on page 4).
- ¹²G. Situ and J. W. Fleischer: *Observation of all-optical Berezinskii-Kosterlitz-Thouless crossover in a photonic lattice*, in [Frontiers in Optics 2012/Laser Science XXVIII](#) (2012), FW2E.4 (cited on page 4).

- ¹³M. H. Anderson, J. R. Ensher, M. R. Matthews, C. E. Wieman, and E. A. Cornell: *Observation of Bose-Einstein Condensation in a Dilute Atomic Vapor*, “*Science*” vol. 269, no. 5221, 198–201 (1995) (cited on page 4).
- ¹⁴B. DeMarco and D. S. Jin: *Onset of Fermi degeneracy in a trapped atomic gas*, “*Science*” vol. 285, no. 5434, 1703 (1999) (cited on page 4).
- ¹⁵A. G. Truscott, K. E. Strecker, W. I. McAlexander, G. B. Partridge, G. Hulet, and R. G. Hulet: *Observation of Fermi Pressure in a Gas of Trapped Atoms*, “*Science*” vol. 291, no. 5513, 2570–2572 (2001) (cited on page 4).
- ¹⁶F. Schreck, G. Ferrari, K. L. Corwin, J. Cubizolles, L. Khaykovich, M. O. Mewes, and C. Salomon: *Sympathetic cooling of bosonic and fermionic lithium gases towards quantum degeneracy*, “*Physical Review A*” vol. 64, no. 1, 114021–114024 (2001) (cited on page 4).
- ¹⁷M. Greiner, I. Bloch, O. Mandel, T. W. Hänsch, and T. Esslinger: *Exploring phase coherence in a 2D lattice of Bose-Einstein condensates*, “*Physical Review Letters*” vol. 87, no. 16, 2–5 (2001) (cited on page 4).
- ¹⁸A. Görlitz, J. M. Vogels, A. E. Leanhardt, C. Raman, T. L. Gustavson, J. R. Abo-Shaeer, A. P. Chikkatur, S. Gupta, S. Inouye, T. Rosenband, and W. Ketterle: *Realization of Bose-Einstein Condensates in Lower Dimensions*, “*Physical Review Letters*” vol. 87, no. 13, 130402 (2001) (cited on page 4).
- ¹⁹K. Martiyanov, V. Makhalov, and A. Turlapov: *Observation of a two-dimensional fermi gas of atoms*, “*Physical Review Letters*” vol. 105, no. 3, 1–4 (2010) (cited on page 4).
- ²⁰Z. Hadzibabic, P. Krüger, M. Cheneau, B. Battelier, and J. Dalibard: *Berezinskii-Kosterlitz-Thouless crossover in a trapped atomic gas*. “*Nature*” vol. 441, no. 7097, 1118–21 (2006) (cited on pages 4, 37, 50, 89).
- ²¹P. Cladé, C. Ryu, A. Ramanathan, K. Helmerson, and W. Phillips: *Observation of a 2D Bose gas: From thermal to quasicondensate to superfluid*, “*Physical Review Letters*” vol. 102, no. 17, 170401 (2009) (cited on pages 4, 37, 53).
- ²²J.-Y. Choi, S.-W. Seo, and Y.-I. Shin: *Observation of thermally activated vortex pairs in a quasi-2D Bose gas*, “*Physical Review Letters*” vol. 110, no. 17, 22–26 (2013) (cited on page 4).
- ²³M. G. Ries, A. N. Wenz, G. Zürn, L. Bayha, I. Boettcher, D. Kedar, P. A. Murthy, M. Neidig, T. Lompe, and S. Jochim: *Observation of pair condensation in the Quasi-2D BEC-BCS Crossover*, “*Physical Review Letters*” vol. 114, no. 23, 1–5 (2015) (cited on pages 4, 53).
- ²⁴V. Schweikhard, S. Tung, and E. A. Cornell: *Vortex proliferation in the Berezinskii-Kosterlitz-Thouless regime on a two-dimensional lattice of Bose-Einstein condensates*, “*Physical Review Letters*” vol. 99, no. 3, 1–4 (2007) (cited on pages 4, 90).

- ²⁵T. Plisson, B. Allard, M. Holzmann, G. Salomon, a. Aspect, P. Bouyer, and T. Bourdel: *Coherence properties of a two-dimensional trapped Bose gas around the superfluid transition*, “*Physical Review A*” vol. 84, no. 6, 1–4 (2011) (cited on page 4).
- ²⁶P. A. Murthy, I. Boettcher, L. Bayha, M. Holzmann, D. Kedar, M. Neidig, M. G. Ries, A. N. Wenz, and S. Jochim: *Observation of the Berezinskii–Kosterlitz–Thouless phase transition in an ultracold Fermi gas*, “*Physical Review Letters*” vol. 115, no. 1, 1–9 (2015) (cited on pages 4, 37, 47, 53, 54).
- ²⁷R. Desbuquois: *Thermal and superfluid properties of the two-dimensional Bose gas*, PhD thesis, Université Pierre-et-Marie-Curie - Paris VI 2013 (cited on pages 4, 54, 90, 111, 133).
- ²⁸S. Pres: *BKT - phase transition in a strongly interacting 2D Bose gas*, MA thesis, University of Heidelberg 2014 (cited on pages 4, 91, 115).
- ²⁹W. Weimer: *Probing superfluid properties in strongly correlated Fermi gases with high spatial resolution*, PhD thesis, Universität Hamburg 2014 (cited on page 11).
- ³⁰K. H. Morgener: *Microscopy of 2D Fermi Gases Exploring excitations and thermodynamics*, PhD thesis, Universität Hamburg 2014 (cited on pages 11, 13, 14, 33).
- ³¹K. Hueck: *A homogeneous, two-dimensional fermi gas. Measurements in Position- and Momentum-Space*, PhD thesis, Universität Hamburg 2017 (cited on pages 11, 13).
- ³²A. Y. Cherny, J. S. Caux, and J. Brand: *Theory of superfluidity and drag force in the one-dimensional Bose gas*, “*Frontiers of Physics*” vol. 7, no. 1, 54–71 (2012) (cited on page 17).
- ³³Z. Hadzibabic and J. Dalibard: *Two-dimensional Bose fluids: An atomic physics perspective*, “*Rivista del Nuovo Cimento*” vol. 34, no. 6, 389–434 (2011) (cited on pages 17, 34, 75, 112).
- ³⁴L. Landau: *Theory of the superfluidity of helium II*, “*Physical Review*” vol. 60, no. 4, 356–358 (1941) (cited on pages 17, 31).
- ³⁵S. Coleman: *There are no Goldstone bosons in two dimensions*, “*Communications in Mathematical Physics*” vol. 31, no. 4, 259–264 (1973) (cited on page 18).
- ³⁶V. Berezinskii: *Destruction of Long-range Order in One-dimensional and Two-dimensional Systems Possessing a Continuous Symmetry Group. II. Quantum Systems*. “*Journal of Experimental and Theoretical Physics*” vol. 34, no. 3, 610 (1971) (cited on page 18).
- ³⁷J. J. Kelly: *Statistical Mechanics With Mathematica*, 2002 (cited on page 22).
- ³⁸K. Huang: *Statistical mechanics*, Wiley 1987 (cited on page 24).
- ³⁹C. J. Pethick and H. Smith: *Bose-Einstein Condensation in Dilute Gases*, Second Edition, Cambridge: Cambridge University Press 2008 (cited on page 28).
- ⁴⁰M. Holzmann, M. Chevallier, and W. Krauth: *Universal correlations and coherence in quasi-two-dimensional trapped Bose gases*, “*Physical Review A*” vol. 81, no. 4, 1–11 (2010) (cited on page 28).

- ⁴¹M. Andrews, C. G. Townsend, H.-J. Miesner, D. S. Durfee, D. M. Kurn, and W. Ketterle: *Observation of Interference Between Two Bose Condensates*, “*Science*” vol. 275, no. 5300, 637–641 (1997) (cited on page 29).
- ⁴²M. Naraschewski and R. J. Glauber: *Spatial coherence and density correlations of trapped Bose gases*, “*Physical Review A*” vol. 59, no. 6, 4595–4607 (1999) (cited on pages 29, 30, 81, 105).
- ⁴³R. Hanbury Brown and R. Q. Twiss: *A Test of a New Type of Stellar Interferometer on Sirius*, “*Nature*” vol. 178, no. 4541, 1046–1048 (1956) (cited on page 29).
- ⁴⁴M. Schellekens, R. Hoppeler, A. Perrin, J. Viana Gomes, D. Boiron, A. Aspect, and C. I. Westbrook: *Hanbury Brown Twiss Effect for Ultracold Quantum Gases*, “*Science*” vol. 310, no. 5748, 648–651 (2005) (cited on page 29).
- ⁴⁵G. Baym, J. P. Blaizot, M. Holzmann, F. Laloe, and D. Vautherin: *The transition temperature of the dilute interacting Bose gas*, “*Physical Review Letters*” vol. 83, no. 9, 1703–1706 (1999) (cited on page 30).
- ⁴⁶S. Pilati, S. Giorgini, and N. Prokof'ev: *Critical temperature of interacting bose gases in two and three dimensions*, “*Physical Review Letters*” vol. 100, no. 14, 1–4 (2008) (cited on page 30).
- ⁴⁷S. Giorgini, L. P. Pitaevskii, and S. Stringari: *Condensate fraction and critical temperature of a trapped interacting Bose gas*, “*Physical Review A*” vol. 54, no. 6, R4633–R4636 (1996) (cited on pages 30, 79).
- ⁴⁸F. Gerbier, J. H. Thywissen, S. Richard, M. Hugbart-Fouché, P. Bouyer, and A. Aspect: *Critical temperature of a trapped, weakly interacting Bose gas*, “*Physical Review Letters*” vol. 92, no. 3, 30405 (2004) (cited on page 30).
- ⁴⁹C. Raman, M. Kohl, R. Onofrio, D. S. Durfee, C. E. Kuklewicz, Z. Hadzibabic, and W. Ketterle: *Evidence for a critical velocity in a Bose-Einstein condensed gas*, “*Physical Review Letters*” vol. 83, no. 13, 4 (1999) (cited on page 31).
- ⁵⁰J. Dalibard: *Collisional dynamics of ultra-cold atomic gases*, in *Proceedings of the international school of physics 'Enrico Fermi'* (1999), pp. 321–349 (cited on pages 32, 68).
- ⁵¹E. Burt, R. Ghrist, C. Myatt, M. Holland, E. Cornell, and C. Wieman: *Coherence, Correlations, and Collisions: What One Learns about Bose-Einstein Condensates from Their Decay*, “*Physical Review Letters*” vol. 79, no. 3, 337–340 (1997) (cited on pages 32, 77).
- ⁵²J. J. Sakurai: *Modern Quantum Mechanics, Revised Edition*, Vol. 63, 1, Addison Wesley 1995 (cited on pages 32, 33).
- ⁵³R. J. Fletcher: *Bose-Einstein Condensation and Superfluidity in Two Dimensions*, PhD thesis, University of Cambridge 2015 (cited on page 33).
- ⁵⁴P. Krüger, Z. Hadzibabic, and J. Dalibard: *Critical point of an interacting two-dimensional atomic Bose gas*, “*Physical Review Letters*” vol. 99, no. 4, 040402 (2007) (cited on pages 37, 51).

- ⁵⁵R. J. Fletcher, M. Robert-de-saint-vincent, J. Man, N. Navon, R. P. Smith, K. G. H. Viebahn, and Z. Hadzibabic: *Connecting Berezinskii-Kosterlitz-Thouless and BEC Phase Transitions by Tuning Interactions in a Trapped Gas*, “[Physical Review Letters](#)” vol. 114, no. 1, 1–5 (2015) (cited on pages 37, 111).
- ⁵⁶R. Desbuquois, L. Chomaz, T. Yefsah, J. Léonard, J. Beugnon, C. Weitenberg, and J. Dalibard: *Superfluid behaviour of a two-dimensional Bose gas*, “[Nature Physics](#)” vol. 8, no. 9, 645–648 (2012) (cited on pages 37, 51).
- ⁵⁷C. De Rossi, R. Dubessy, K. Merloti, M. De Goër De Herve, T. Badr, A. Perrin, L. Longchambon, and H. Perrin: *Probing superfluidity in a quasi two-dimensional Bose gas through its local dynamics*, “[New Journal of Physics](#)” vol. 18 (2016) 10.1088/1367-2630/18/6/062001 (cited on pages 37, 52).
- ⁵⁸J.-Y. Choi, S.-W. Seo, W.-J. Kwon, and Y.-I. Shin: *Probing phase fluctuations in a 2D degenerate Bose gas by free expansion*, “[Physical Review Letters](#)” vol. 109, no. 12, 125301 (2012) (cited on pages 37, 54, 90, 115).
- ⁵⁹D. E. Miller, J. R. Anglin, J. R. Abo-Shaeer, K. Xu, J. K. Chin, and W. Ketterle: *High-contrast interference in a thermal cloud of atoms*, “[Physical Review A](#)” vol. 71, no. 4, 1–4 (2005) (cited on page 38).
- ⁶⁰L. Mathey: *Condensed matter and ultra-cold atoms*, 2015 (cited on page 38).
- ⁶¹C. Mora and Y. Castin: *Extension of Bogoliubov theory to quasicondensates*, “[Physical Review A](#)” vol. 67, no. 5, 053615 (2003) (cited on pages 38, 40).
- ⁶²Z. Hadzibabic, P. Krüger, M. Cheneau, S. P. Rath, J. Dalibard, P. Krüger, M. Cheneau, S. P. Rath, and J. Dalibard: *The trapped two-dimensional Bose gas: From Bose-Einstein condensation to Berezinskii-Kosterlitz-Thouless physics*, “[New Journal of Physics](#)” vol. 10, no. 045006, 22pp (2008) (cited on page 38).
- ⁶³J. O. Andersen, U. Al Khawaja, and H. T. C. Stoof: *Phase Fluctuations in Atomic Bose Gases*, “[Physical Review Letters](#)” vol. 88, no. 7, 070407 (2002) (cited on page 38).
- ⁶⁴M. G. Bulmer: *Principles of Statistics*, Dover Books on Mathematics, Dover Publications 2012 (cited on page 42).
- ⁶⁵Y. Kagan, B. V. Svistunov, and G. V. Shlyapnikov: *Influence on inelastic processes of the phase transition in a weakly collisional two-dimensional Bose gas*, “[Soviet Journal of Experimental and Theoretical Physics](#)” vol. 66, no. 2, 314 (1987) (cited on page 44).
- ⁶⁶A. J. Beekman: *Vortex duality in higher dimensions*, PhD thesis, Universiteit Leiden 2011 (cited on page 47).
- ⁶⁷D. S. Fisher and P. C. Hohenberg: *Dilute Bose gas in two dimensions*, “[Physical Review B](#)” vol. 37, no. 10, 4936–4943 (1988) (cited on page 47).

- ⁶⁸N. Prokof'ev, O. Ruebenacker, and B. Svistunov: *Critical point of a weakly interacting two-dimensional Bose gas*, "Physical Review Letters" vol. 87, no. 27, 270402 (2001) (cited on pages 47, 72, 79, 112).
- ⁶⁹N. Prokof'ev and B. Svistunov: *Two-Dimensional Weakly Interacting Bose Gas in the Fluctuation Region*, "Physical Review A" vol. 66, no. 4, 8 (2002) (cited on page 47).
- ⁷⁰V. Ambegaokar, B. I. Halperin, D. R. Nelson, and E. D. Siggia: *Dissipation in two-dimensional superfluids*, "Physical Review Letters" vol. 40, no. 12, 783–786 (1978) (cited on page 49).
- ⁷¹J. M. Kosterlitz: *The critical properties of the two-dimensional xy model*, "Journal Of Physics C: Solid State Physics" vol. 7, no. 6, 1046 (1974) (cited on page 49).
- ⁷²M. Chester and L. C. Yang: *Superfluid Fraction in Thin Helium Films*, "Physical Review Letters" vol. 31, no. 23, 1377–1380 (1973) (cited on page 50).
- ⁷³I. Rudnick: *Critical Surface Density of the Superfluid Component in ⁴He Films*, "Physical Review Letters" vol. 40, no. 22, 1454–1455 (1978) (cited on page 50).
- ⁷⁴Z. Hadzibabic, S. Stock, B. Battelier, V. Bretin, and J. Dalibard: *Interference of an array of independent Bose-Einstein condensates*, "Physical Review Letters" vol. 93, no. 18, 1–4 (2004) (cited on pages 50, 89).
- ⁷⁵S. Stock, Z. Hadzibabic, B. Battelier, M. Cheneau, and J. Dalibard: *Observation of phase defects in quasi-two-dimensional Bose-Einstein condensates*, "Physical Review Letters" vol. 95, no. 19, 2–5 (2005) (cited on page 50).
- ⁷⁶A. Polkovnikov, E. Altman, and E. Demler: *Interference between independent fluctuating condensates*, "Proceedings of the National Academy of Sciences of the United States of America" vol. 103, no. 16, 6125–9 (2005) (cited on pages 50, 92).
- ⁷⁷V. P. Singh: *Probing Superfluidity of Ultracold Bose Gases via Laser Stirring and Noise Correlations*, PhD thesis, Universität Hamburg 2017 (cited on pages 52, 101, 105).
- ⁷⁸R. Dubessy, C. De Rossi, M. D. G. De Herve, T. Badr, A. Perrin, L. Longchambon, and H. Perrin: *Local correlations reveal the superfluid to normal boundary in a trapped two-dimensional quantum gas*, "AIP Conference Proceedings" vol. 1936 (2018) 10.1063/1.5025465 (cited on page 53).
- ⁷⁹J.-Y. Choi, S.-W. Seo, W.-J. Kwon, and Y.-I. Shin: *Choi et al. Reply*: "Physical Review Letters" vol. 111, no. 15, 159602 (2013) (cited on pages 54, 90, 115).
- ⁸⁰S.-W. Seo, J.-Y. Choi, and Y.-I. Shin: *Scaling behavior of density fluctuations in an expanding quasi-two-dimensional degenerate Bose gas*, "Physical Review A" vol. 89, no. 4, 043606 (2014) (cited on pages 54, 90).
- ⁸¹N. Luick: *Local probing of the Berezinskii – Kosterlitz – Thouless transition in a two-dimensional Bose gas*, MA thesis, Universität Hamburg 2014, p. 80 (cited on page 55).

- ⁸²A. Imambekov, I. Mazets, D. Petrov, V. Gritsev, S. Manz, S. Hofferberth, T. Schumm, E. Demler, and J. Schmiedmayer: *Density ripples in expanding low-dimensional gases as a probe of correlations*, “*Physical Review A*” vol. 80, no. 3, 033604 (2009) (cited on pages 55, 90, 92, 101, 147).
- ⁸³L. Mathey, A. Vishwanath, and E. Altman: *Noise correlations in low-dimensional systems of ultracold atoms*, “*Physical Review A*” vol. 79, no. 1, 1–13 (2009) (cited on page 55).
- ⁸⁴V. P. Singh and L. Mathey: *Noise correlations of two-dimensional Bose gases*, “*Physical Review A*” vol. 89, no. 5, 053612–053622 (2014) (cited on pages 55, 91, 92, 99, 133, 134, 138, 147, 154).
- ⁸⁵P. A. Murthy, D. Kedar, T. Lompe, M. Neidig, M. G. Ries, A. N. Wenz, G. Zürn, and S. Jochim: *Matter-wave Fourier optics with a strongly interacting two-dimensional Fermi gas*, “*Physical Review A*” vol. 90, no. 4, 043611 (2014) (cited on pages 57, 59, 65).
- ⁸⁶K. Hueck, N. Luick, L. Sobirey, J. Siegl, T. Lompe, and H. Moritz: *Two-Dimensional Homogeneous Fermi Gases*, “*Physical Review Letters*” vol. 120, no. 6, 60402 (2018) (cited on pages 59, 110).
- ⁸⁷S. Tung, G. Lamporesi, D. Lobser, L. Xia, and E. a. Cornell: *Observation of the Presuperfluid Regime in a Two-Dimensional Bose Gas*, “*Physical Review Letters*” vol. 105, no. 23, 230408 (2010) (cited on page 65).
- ⁸⁸J. P. Kestner and L. M. Duan: *Conditions of low dimensionality for strongly interacting atoms under a transverse trap*, “*Physical Review A*” vol. 74, no. 5, 1–10 (2006) (cited on pages 67, 113).
- ⁸⁹D. S. Petrov, C. Salomon, and G. V. Shlyapnikov: *Weakly bound dimers of fermionic atoms*, “*Physical Review Letters*” vol. 93, no. 9, 1–4 (2004) (cited on page 68).
- ⁹⁰L. Salasnich, P. A. Marchetti, and F. Toigo: *Superfluidity, sound velocity, and quasicondensation in the two-dimensional BCS-BEC crossover*, “*Physical Review A*” vol. 88, no. 5, 1–7 (2013) (cited on pages 68, 78).
- ⁹¹W. Ketterle, D. S. Durfee, and D. M. Stamper-Kurn: *Making, probing and understanding Bose-Einstein condensates*, in *Proceedings of the international school of physics ‘Enrico Fermi’* (1999), pp. 67–176 (cited on pages 69, 74, 79).
- ⁹²V. P. Singh, C. Weitenberg, J. Dalibard, and L. Mathey: *Superfluidity and relaxation dynamics of a laser-stirred two-dimensional Bose gas*, “*Physical Review A*” vol. 95, no. 4, 043631–043641 (2017) (cited on pages 75, 79).
- ⁹³M. Born: *Physical Aspects of Quantum Mechanics*, “*Nature*” vol. 119, no. 2992, 354–357 (1927) (cited on page 75).
- ⁹⁴T. A. Savard, K. M. O’Hara, and J. E. Thomas: *Laser-noise-induced heating in far-off resonance optical traps*, “*Physical Review A*” vol. 56, no. 2, R1095–R1098 (1997) (cited on page 76).

- ⁹⁵D. S. Petrov, C. Salomon, and G. V. Shlyapnikov: *Scattering properties of weakly bound dimers of fermionic atoms*, “*Physical Review A*” vol. 71, no. 1, 1–15 (2005) (cited on page 76).
- ⁹⁶M. Weidemüller: *Cold Atoms and Molecules*, edited by M. Weidemüller and C. Zimmermann, Weinheim: Wiley 2009 (cited on page 77).
- ⁹⁷T. Lompe: *Effimov Physics in a three-component Fermi gas*, PhD thesis, Ruperto-Carola University Heidelberg 2011 (cited on page 77).
- ⁹⁸S. Nakajima, M. Horikoshi, T. Mukaiyama, P. Naidon, and M. Ueda: *Nonuniversal efimov atom-dimer resonances in a three-component mixture of Li_6* , “*Physical Review Letters*” vol. 105, no. 2, 6–9 (2010) (cited on page 77).
- ⁹⁹L. Verney, L. Pitaevskii, and S. Stringari: *Hybridization of first and second sound in a weakly interacting Bose gas*, “*EPL (Europhysics Letters)*” vol. 111, no. 4, 40005 (2015) (cited on page 78).
- ¹⁰⁰M. Ota and S. Stringari: *Second sound in 2D Bose gas: from the weakly interacting to the strongly interacting regime*, “*Physical Review A*” vol. 97, no. 3, 033604–033611 (2018) (cited on page 78).
- ¹⁰¹X. J. Liu and H. Hu: *First and second sound in a two-dimensional harmonically trapped Bose gas across the Berezinskii-Kosterlitz-Thouless transition*, “*Annals of Physics*” vol. 351, 531–539 (2014) (cited on page 78).
- ¹⁰²T. Ozawa and S. Stringari: *Discontinuities in the First and Second Sound Velocities at the Berezinskii-Kosterlitz-Thouless Transition*, “*Physical Review Letters*” (2014) (cited on page 78).
- ¹⁰³L. Mathey, K. J. Günter, J. Dalibard, and A. Polkovnikov: *Dynamic Kosterlitz-Thouless transition in two-dimensional Bose mixtures of ultracold atoms*, “*Physical Review A*” vol. 95, no. 5, 1–7 (2017) (cited on page 79).
- ¹⁰⁴P. O. Fedichev and G. V. Shlyapnikov: *Dissipative dynamics of a vortex state in a trapped Bose-condensed gas*, “*Physical Review A*” vol. 60, no. 3, R1779–R1782 (1999) (cited on page 79).
- ¹⁰⁵S. Prabhakar, R. P. Singh, S. Gautam, and D. Angom: *Annihilation of vortex dipoles in an oblate Bose-Einstein condensate*, “*Journal of Physics B: Atomic, Molecular and Optical Physics*” vol. 46, no. 12, 1–4 (2013) (cited on page 79).
- ¹⁰⁶S. J. Rooney, P. B. Blakie, B. P. Anderson, and A. S. Bradley: *Suppression of Kelvin-induced decay of quantized vortices in oblate Bose-Einstein condensates*, “*Physical Review A*” vol. 84, no. 2, 1–8 (2011) (cited on page 79).
- ¹⁰⁷P. C. Haljan, B. P. Anderson, I. Coddington, and E. A. Comell: *Use of surface-wave spectroscopy to characterize tilt modes of a vortex in a Bose-Einstein condensate*, “*Physical Review Letters*” vol. 86, no. 14, 2922–2925 (2001) (cited on page 79).
- ¹⁰⁸J. Eisert, M. Friesdorf, and C. Gogolin: *Quantum many-body systems out of equilibrium*, “*Nature Physics*” vol. 11, 124 (2015) (cited on page 80).

- ¹⁰⁹J. W. Goodman: *Introduction to Fourier Optics*, Second Edition, Englewood, Colorado: Roberts and Company Publishers 2005 (cited on pages 84, 124, 127, 128).
- ¹¹⁰P. Carruthers and M. M. Nieto: *Phase and angle variables in quantum mechanics*, “*Reviews of Modern Physics*” vol. 40, no. 2, 411–440 (1968) (cited on page 88).
- ¹¹¹H. Talbot: LXXVI. *Facts relating to optical science. No. IV*, “*Philosophical Magazine Series 3*” vol. 9, no. 56, 401–407 (1836) (cited on page 88).
- ¹¹²S. Dettmer, D. Hellweg, P. Ryytty, J. J. Arlt, W. Ertmer, K. Sengstock, D. S. Petrov, G. V. Shlyapnikov, H. Kreutzmann, L. Santos, and M. Lewenstein: *Observation of phase fluctuations in elongated Bose-Einstein condensates*, “*Physical Review Letters*” vol. 87, 160406 (2001) (cited on page 89).
- ¹¹³S. Hofferberth, I. Lesanovsky, T. Schumm, A. Imambekov, V. Gritsev, E. Demler, and J. Schmiedmayer: *Probing quantum and thermal noise in an interacting many-body system*, “*Nature Physics*” vol. 4, no. 6, 489–495 (2008) (cited on page 89).
- ¹¹⁴S. Manz, R. Bücker, T. Betz, C. Koller, S. Hofferberth, I. Mazets, A. Imambekov, E. Demler, A. Perrin, J. Schmiedmayer, and T. Schumm: *Two-point density correlations of quasicondensates in free expansion*, “*Physical Review A*” vol. 81, no. 3, 031610 (2010) (cited on page 89).
- ¹¹⁵B. Rauer, P. Grišins, I. E. Mazets, T. Schweigler, W. Rohringer, R. Geiger, T. Langen, and J. Schmiedmayer: *Cooling of a One-Dimensional Bose Gas*, “*Physical Review Letters*” vol. 116, no. 3, 1–5 (2016) (cited on page 89).
- ¹¹⁶D. R. Scherer, C. N. Weiler, T. W. Neely, and B. P. Anderson: *Vortex formation by merging of multiple trapped bose-einstein condensates*, “*Physical Review Letters*” vol. 98, no. 11, 1–4 (2007) (cited on page 90).
- ¹¹⁷I. Mazets: *Two-dimensional dynamics of expansion of a degenerate Bose gas*, “*Physical Review A*” vol. 86, no. 5, 055603 (2012) (cited on page 90).
- ¹¹⁸T. Langen: *Comment on “Probing Phase Fluctuations in a 2D Degenerate Bose Gas by Free Expansion”*, “*Physical Review Letters*” vol. 111, no. 15, 2012–2013 (2013) (cited on page 90).
- ¹¹⁹S.-W. Seo, J.-Y. Choi, and Y.-I. Shin: *Free expansion of quasi-2D Bose-Einstein condensates with quantized vortices*, “*Journal of the Korean Physical Society*” vol. 64, no. 1, 53–57 (2014) (cited on pages 90, 115).
- ¹²⁰A. Putra, D. L. Campbell, R. M. Price, S. De, and I. B. Spielman: *Optimally focused cold atom systems obtained using density-density correlations*, “*The Review of scientific instruments*” vol. 85, no. 1, 013110 (2014) (cited on pages 90, 115, 116).
- ¹²¹A. Imambekov, V. Gritsev, and E. Demler: *Mapping of Coulomb gases and sine-Gordon models to statistics of random surfaces*, “*Physical Review A*” vol. 77, no. 6, 1–5 (2008) (cited on page 92).

- ¹²²T. O. Kvalseth: *Cautionary Note about R^2* , “The American Statistician” vol. 39, no. 4, 279–285 (1985) (cited on page 107).
- ¹²³A. L. Fetter: *Vortices in an imperfect Bose gas. I. The condensate*, “Physical Review” vol. 138, no. 2A, 429–437 (1964) (cited on page 110).
- ¹²⁴D. S. Petrov, M. Holzmann, and G. V. Shlyapnikov: *Bose-Einstein Condensation in Quasi-2D Trapped Gases*, “Physical Review Letters” vol. 84, no. 12, 2551–2555 (2000) (cited on page 111).
- ¹²⁵J. P. Kestner and L. M. Duan: *Effective low-dimensional Hamiltonian for strongly interacting atoms in a transverse trap*, “Physical Review A” vol. 76, no. 6, 1–5 (2007) (cited on page 113).
- ¹²⁶K. Merloti, R. Dubessy, L. Longchambon, M. Olshanii, and H. Perrin: *Breakdown of scale invariance in a quasi-two-dimensional Bose gas due to the presence of the third dimension*, “Physical Review A” vol. 88, no. 6, 4–7 (2013) (cited on page 113).
- ¹²⁷P. Dyke, K. Fenech, T. Pepler, M. G. Lingham, S. Hoinka, W. Zhang, S. G. Peng, B. Mulkerin, H. Hu, X. J. Liu, and C. J. Vale: *Criteria for two-dimensional kinematics in an interacting Fermi gas*, “Physical Review A” vol. 93, no. 1, 1–5 (2016) (cited on page 113).
- ¹²⁸H. Hu, B. C. Mulkerin, U. Toniolo, L. He, and X. J. Liu: *Quantum anomaly in a quasi-two-dimensional strongly interacting Fermi gas*, “ArXiv e-prints”, 1–6 (2018) (cited on page 113).
- ¹²⁹A. L. Gaunt, R. J. Fletcher, R. P. Smith, and Z. Hadzibabic: *A superheated Bose-condensed gas*, “Nature Physics” vol. 9, no. 5, 271–274 (2013) (cited on page 114).
- ¹³⁰K. Hueck, N. Luick, L. Sobirey, J. Siegl, T. Lompe, H. Moritz, L. W. Clark, and C. Chin: *Calibrating High Intensity Absorption Imaging of Ultracold Atoms*, “Optics Express” vol. 25, no. 8, 8670–8679 (2017) (cited on pages 117–120).
- ¹³¹G. Reinaudi, T. Lahaye, Z. Wang, and D. Guéry-Odelin: *Strong saturation absorption imaging of dense clouds of ultracold atoms*. “Optics Letters” vol. 32, no. 21, 3143–5 (2007) (cited on page 119).
- ¹³²K. Riechers: *Friedel oscillations and the Fermi wavevector in low-dimensional ultracold Fermi gases*, MA thesis, Universität Hamburg 2016 (cited on page 121).
- ¹³³C. L. Hung, X. Zhang, L. C. Ha, S. K. Tung, N. Gemelke, and C. Chin: *Extracting density-density correlations from in situ images of atomic quantum gases*, “New Journal of Physics” vol. 13, no. 7, 075019 (2011) (cited on page 129).
- ¹³⁴L. Pitaevskii and S. Stringari: *Bose-Einstein Condensation*, Oxford: Clarendon Press 2003 (cited on page 130).
- ¹³⁵J. J. Meineke: *Fluctuations and Correlations in Ultracold Fermi Gases*, PhD thesis, ETH Zürich 2012 (cited on page 130).
- ¹³⁶E. Hecht: *Optics*, edited by M. Borthakur and V. Tiwari, 5th Edition, Essex: Pearson Education Limited 2017 (cited on page 131).

DANKSAGUNG

Diese Arbeit wäre nicht zustande gekommen, gäbe es nicht ein paar engagierte Menschen in meinem Leben, bei denen ich mich hier bedanken möchte.

Besonders dankbar bin ich Prof. Dr. Henning Moritz, ohne den dieses gesamte Unterfangen nicht möglich gewesen wäre. Du hast mich immer – auch in schwierigen Phasen – wertschätzend und hilfsbereit als Mentor und Doktorvater begleitet. Am Ende ist es deine optimistische und neugierige Art, die dieses Team an Menschen um dich geschart hat, dem ich so gerne angehört habe.

Dieses Team bestand aus Wolf und Kai, sowie Nils und Jan, die mich sofort zuhause haben fühlen lassen. Die Integrität von Wolf und das ästhetisch/praktische Verständnis von Kai sowie die Lebensfreude beider, haben mich in meiner Entwicklung als Forscher und Mensch maßgeblich geformt.

Während meiner Doktorarbeit hat sich das Lithium-Team ständig verändert und vergrößert. Keinen möchte ich missen. Nicht Klaus, der mich nicht nur unterstützt, sondern mir auch als Vorbild gedient hat; nicht Niclas, dessen Gewissheit und Geduld viele meiner Aha-Effekte geschuldet sind; auch nicht Lennart, der mich nicht nur darin antrieb meine Coding Skills zu verbessern, sondern auch gerne mit mir abnerdete; sowie nicht Thomas, quasi allwissend und zu jeder noch so späten Stunde bereit, mir mit kundigem Rat zur Seite zu stehen.

Auch ehemaligen Gruppenmitgliedern wie Keno, neuen Begleitern wie Bernd und auch dem Kalium-Team, Phillip, Martin und Alexandra, möchte ich danken. Oft habe ich mich zu später Stunde dankbar mit der einen oder anderen philosophisch-wissenschaftlich-gesellschaftlichen Diskussion von meiner Arbeit ablenken lassen.

Ich bedanke mich außerdem bei Prof. Dr. Ludwig Mathey. Erstens für seine Bereitschaft, ein Gutachten dieser Arbeit anzufertigen, sowie zweitens für sein und Vijays stets offenes Ohr, ihre unendliche Geduld sowie ihren Optimismus, wenn ich mal wieder mit demselben Datensatz und neuen Fragen vor der Tür stand.

Für seinen unermüdlichen Einsatz für unser Institut im Speziellen und die Physik im Allgemeinen danke ich Prof. Dr. Klaus Sengstock, ohne diesen es uns allen nicht annähernd so gut in Hamburg ginge.

Ich danke denen, ohne die es im Institut drunter und drüber ginge, im Besonderen, Reinhard Mielck, Ellen Gloy und Janina Neubert.

Nicht nur diese Arbeit, sondern auch mich hätte es ohne meine Eltern, Kristina und Joachim, nicht gegeben. Ihnen und meinen Schwestern, Ninja, Jenna und Janne, bin ich für viel mehr als diese Arbeit dankbar.

Meiner Freundin adequat zu danken, würde leicht noch einmal so viele Seiten füllen. Demnach sollen nach dem letzten Punkt nun Taten folgen. Danke Hannah.

EIDESSTATTLICHE VERSICHERUNG

Hiermit versichere ich an Eides statt, die vorliegende Dissertationschrift selbst verfasst und keine anderen als die angegebenen Hilfsmittel und Quellen benutzt zu haben.

Die eingereichte schriftliche Fassung entspricht der auf dem elektronischen Speichermedium.

Die Dissertation wurde in der vorgelegten oder einer ähnlichen Form nicht schon einmal in einem früheren Promotionsverfahren angenommen oder als ungenügend beurteilt.

Hamburg, Oktober 2018

Jonas D. Siegl